



Functional Materials of
Metal Hexacyanometallates

(Funktionelle Materialien aus Metall-Hexacyanometallaten)

Von der Fakultät für Mathematik und Naturwissenschaften der Carl von Ossietzky Universität
Oldenburg zur Erlangung des Grades

Doktor der Naturwissenschaften (Dr. rer. nat.)
angenommene Dissertation

von Frau **Lena Gerhards** (geb. Harms), M.Sc.
geboren am 24 Juli 1995 in Delmenhorst, Deutschland

Oldenburg, Mai 2024

The experimental research was conducted between January 2020 and October 2023 at the Carl von Ossietzky University of Oldenburg, School of Mathematics and Science, Department of Chemistry, under the guidance of Professor Dr. Gunther Wittstock.

This project received funding from the DFG (German Research Foundation) and was part of the Priority Program 1928 “Coordination Network: Building Blocks for Functional Systems”.

The results of this work have been published in scientific journals after peer review and are presented in Section 5.7 and Chapters 6 and 7 of this thesis. Additionally, this work has been enriched by collaborations with the working group of Prof. Thomas Bein at Ludwig-Maximilians-Universität of Munich. The collaborative results have been published or submitted to scientific journals. Parts of these papers are used as example data in the introductory Chapter 4.4 X-ray photoelectron spectroscopy.

Gutachter: Prof. Dr. Gunther Wittstock

Zweitgutachter: Prof. Dr. Rüdiger Beckhaus

Tag der Disputation: 21.06.2024

Abstract

Thin films of metal hexacyanometallates were investigated for their functionality in electrochemical environments or as layered solids, particularly iron hexacyanoruthenate and nickel hexacyanoferrate. Layered structures were prepared by electrochemical deposition of iron hexacyanoferrate as inner film and layer-by-layer deposition of nickel hexacyanoferrate as outer film or by drop-casting pre-synthesized nickel hexacyanoferrate nanoparticles onto electrodeposited iron hexacyanoruthenate. The electron flow can be manipulated in these systems to exhibit charge trapping or rectifying behavior. This is related to the redox states of the coordinated transition metal ions. The materials were characterized, among other methods, by X-ray photoelectron spectroscopy and polarization-modulation infrared reflection absorption spectroscopy. Voltammetry in electrolyte solutions and current-voltage curves in the solid state demonstrated the charge trapping / rectifying behavior of these films. A selected reference system, in which the transition metal ions are statistically distributed on the lattice sites, does not exhibit any rectifying behavior but behaves with similar electrochemical properties to the individual materials, thereby supporting the role of the layered systems for charge trapping and rectifying behavior.

An interesting effect is the protium/deuterium isotope effect observed in the voltammetry of iron hexacyanoruthenate-modified electrodes in electrolytes with light (H_2O) or heavy (D_2O) water. Two reduction peaks can be found in voltammetry with H_2O -based electrolytes, while only one peak was observed in D_2O -based solutions. Transferring the electrode between the electrolytes led to reversible changes in voltammetry. Temperature-dependent studies show the importance of transport processes for the observed phenomenon. The electrochemical investigations are accompanied by spectroscopic methods to characterize the materials. The observations are discussed regarding different structural forms of the material, the role of cations in charge compensation during the redox reaction, and the possible presence of an amorphous layer at the iron hexacyanoruthenate | electrolyte interface.

Zusammenfassung

Dünne Filme von Metall-hexacyanometallaten, insbesondere Eisen-hexacyanoruthenat und Nickel-hexacyanoferrat, wurden hinsichtlich ihrer Funktionalität in elektrochemischen Umgebungen oder als Schichtstrukturen untersucht. Bei der Präparation einer Schichtstruktur durch elektrochemische Abscheidung von Eisen-hexacyanoruthenat als inneren Film und ‚Schicht-für-Schicht‘-Abscheidung für Nickel-hexacyanoferrat als äußeren Film oder durch Drop-Casting präsynthetisierter Nickel-hexacyanoferrat-Nanopartikel auf einem elektrochemisch präparierten Eisen-hexacyanoruthenat Film, kann der Elektronenfluss in den Materialien manipuliert werden, sodass dieser gleichrichtend wird. Dies hängt mit den Redoxzuständen der koordinierten Übergangsmetallionen zusammen. Die Materialien wurden unter anderem mittels Röntgenphotoelektronenspektroskopie und polarisationsmodulierter Infrarot-Reflexions-Absorptionsspektroskopie charakterisiert. Die Voltammetrie in Leitelektrolytlösungen sowie Strom-Spannungs-Kurven von Festkörpern zeigten das gleichrichtende Verhalten der Filme. Ein gewähltes Referenzsystem aus denselben Metallionen mit statistischer Verteilung auf den Gitterplätzen zeigte keine gleichrichtenden Eigenschaften. Somit wird die Bedeutung der Schichtstruktur für das Auftreten der gleichrichtenden Eigenschaften unterstrichen.

Ein interessanter Effekt ist der Protium/Deuterium-Isotopeneffekt, der in der Voltammetrie von Eisen-hexacyanoruthenat-modifizierten Elektroden in Elektrolyten mit leichten (H_2O) und schweren (D_2O) Wasser auftritt. Zwei Reduktionspeaks werden in den Voltammogrammen mit H_2O -basierten Elektrolyt gefunden, während in D_2O -basierten Lösungen nur ein Peak sichtbar war. Der Transfer der modifizierten Elektroden zwischen den Elektrolyten führte zu reversiblen Veränderungen in der Voltammetrie. Temperaturabhängige Studien zeigen die Bedeutung von Transportprozessen für das beobachtete Phänomen. Begleitet werden die elektrochemischen Untersuchungen von spektroskopischen Experimenten, um die Materialien zu charakterisieren. Die Beobachtungen werden im Hinblick auf unterschiedliche Kristallstrukturen des Materials, die Rolle von Kationen für die Ladungskompensation während der Redoxreaktion und das mögliche Vorhandensein einer amorphen Schicht an der Eisen-hexacyanoruthenat|Elektrolyt-Grenzfläche diskutiert.

Danksagung

Während meiner Promotion haben mich viele Menschen unterstützt und standen mir mit Rat und Tat zur Seite. Zunächst gebührt mein herzlicher Dank Herrn Prof. Gunther Wittstock für die Möglichkeit, an diesem spannenden Thema zu arbeiten, sowie für seine hervorragende wissenschaftliche Betreuung. Besonders wertvoll waren die unterstützenden Gespräche und Diskussionen sowohl bei der praktischen Arbeit als auch während der Schreibprozesse, zusammen mit der Hilfe bei der Anfertigung der Publikationen, die maßgeblich zum Erfolg dieser Arbeit beitrugen. Mein Dank gilt ebenfalls Herrn Prof. Rüdiger Beckhaus für die Übernahme des Zweitgutachtens.

Hervorheben möchte ich Frau PD Dr. Izabella Brand, deren Unterstützung in Bezug auf PM IRRAS und mehr, diese Arbeit sehr positiv geprägt hat. Herrn PD Dr. Carsten Dosche danke ich für seine stets hilfreiche Unterstützung, insbesondere im Bereich der Röntgenphotoelektronenspektroskopie und für die dazugehörigen Diskussionen.

Nico Kuhlmann und Johann Fecht möchte ich für die technische Hilfe und Zusammenarbeit danken, durch die ich viele nützliche Dinge lernen konnte, die über die Chemie hinausgehen. Ein besonderer Dank gilt Frau Heike Hiller, die mir bei administrativen Fragen stets eine große Hilfe war.

Ein besonderer Dank geht auch an alle jetzigen und ehemaligen Mitglieder der Arbeitsgruppe Wittstock für die kollegiale und angenehme Arbeitsatmosphäre.

Mein Dank richtet sich auch an die Deutsche Forschungsgemeinschaft (DFG) für die Finanzierung des Projektes im Rahmen des Schwerpunktprogramms 1928 „Koordinationsnetzwerke als Bausteine für Funktionssysteme“ sowie an die Graduiertenschule OLTECH der Carl von Ossietzky Universität Oldenburg für die Reisekostenzuschüsse.

Abschließend danke ich meinem Partner Luca, meinen Eltern und meiner Schwester, sowie meinen Freunden für ihre ständige positive Energie und die unermüdliche Unterstützung, die sie mir während der letzten Jahre zuteilwerden ließen.

Table of Contents

| | | |
|-----|--|----|
| 1 | Introduction..... | 1 |
| 2 | A Brief History of Metal Hexacyanometallates..... | 4 |
| 2.1 | Crystal Structure of Metal Hexacyanometallates | 5 |
| 2.2 | Counterions in the Structure of Metal Hexacyanometallates | 8 |
| 2.3 | Electrochemistry of Metal Hexacyanometallates..... | 11 |
| 2.4 | Conductivity in Metal Hexacyanometallates | 15 |
| 3 | Thin Film Applications | 16 |
| 3.1 | Rectifying Behavior and Charge Trapping of Electrochemically Active Films..... | 18 |
| 3.2 | Thin-Film Preparation of Metal Hexacyanometallates | 21 |
| 4 | Applied Characterization Techniques for Metal Hexacyanometallates | 27 |
| 4.1 | Scanning Force Microscopy | 28 |
| 4.2 | Conductive Scanning Force Microscopy..... | 32 |
| 4.3 | Electrochemical Measurements of Metal Hexacyanometallates | 35 |
| 4.4 | X-ray Photoelectron Spectroscopy..... | 37 |
| 4.5 | X-Ray Diffraction of Metal Hexacyanometallates | 44 |
| 4.6 | Electron Microscopy for the Analysis of M-HCMs | 46 |
| 4.7 | Polarization Modulation Infrared Reflection Absorption Spectroscopy..... | 48 |
| 5 | Experimental Details..... | 51 |
| 5.1 | Chemicals and Materials..... | 51 |
| 5.2 | Preparation of Substrate Surfaces | 52 |
| 5.3 | Electrodeposition of Metal Hexacyanometallates | 52 |
| 5.4 | Ni-HCF Nanoparticle Synthesis..... | 54 |
| 5.5 | Fe-HCR Bulk Material Synthesis for PIGE Measurements | 54 |
| 5.6 | Layer-by-layer Deposition of M-HCMs | 55 |
| 5.7 | Dipping Robot for Layer-by-Layer Deposition..... | 55 |
| 5.8 | Instrumentation for Preparation and Characterization of M-HCMs..... | 59 |
| 6 | Investigations of Layered Metal Hexacyanometallates..... | 64 |
| 6.1 | Introduction | 64 |
| 6.2 | Structural characterization of Layered Material and Reference Compounds..... | 67 |
| 6.3 | XPS Investigations of Layered Material and Reference Compounds | 72 |
| 6.4 | Spectroelectrochemical and Voltammetric Analysis of the Materials | 78 |
| 6.5 | Conductivity in Solid State | 86 |
| 6.6 | Attempts on other Layered Metal Hexacyanometallates Systems..... | 90 |

| | | |
|------|---|-----|
| 6.7 | Conclusion | 92 |
| 7 | Isotope Effect in Metal Hexacyanometallates..... | 94 |
| 7.1 | Introduction | 94 |
| 7.2 | Electrodeposition of Fe-HCR Films in H ₂ O- and D ₂ O-Based Electrolytes..... | 96 |
| 7.3 | Voltammetry of Electrodeposited Fe-HCR Films in H ₂ O- and D ₂ O-Based Electrolytes | 98 |
| 7.4 | Voltammetry of Fe-HCR films in Electrolytes Made with H ₂ O-D ₂ O Mixtures..... | 103 |
| 7.5 | Voltammetry with Wave Clipping | 105 |
| 7.6 | Effect of Viscosity and Temperature | 106 |
| 7.7 | Voltammetry of Fe-HCR Crystals in H ₂ O- and D ₂ O-Based Electrolytes..... | 108 |
| 7.8 | XPS Investigations of the Material | 109 |
| 7.9 | Polarization Modulation Infrared Reflection Absorption Spectroscopy | 126 |
| 7.10 | Discussion on the H/D Isotope Effect | 131 |
| 7.11 | Summary and Conclusion | 133 |
| 8 | Summary and Outlook | 134 |
| 9 | Appendix..... | 137 |
| 9.1 | Software Modification of the Dipping Robot..... | 137 |
| 9.2 | Section Analysis of Fe-HCR, the layered Fe-HCR Ni-HCF material and the mixed material..... | 141 |
| 9.3 | H/D Exchange Experiments in Ni-HCF..... | 144 |
| 9.4 | List of Abbreviations | 145 |
| 9.5 | Symbols | 147 |
| 10 | Literature | 148 |
| 11 | Own Publications and Conference Contributions..... | 170 |
| 11.1 | Own Publications..... | 170 |
| 11.2 | Oral Presentations in National and International Conferences | 170 |
| 11.3 | Posters in National and International Conferences | 171 |
| 12 | Erklärung..... | 172 |

1 Introduction

Metal hexacyanometallates naturally existed on earth for about 3.5 billion years,¹ they can be considered as the first synthetic coordination compound.² They have been studied extensively for decades and are used in formulations³ (e.g., paints, lacquers, printing inks) and various applications (e.g., batteries^{4,5,1}, catalysis^{6,7} or sensors⁸⁻¹⁰). Additionally, metal hexacyanometallates can be used as precursors for other inorganic materials, for example, with high surface area, since the calcination of these materials leads to the removal of the cyanide linker and the formation of metal oxides.¹¹ For instance, Ti-containing Prussian blue analogue can be calcined to nanoporous Ti-Fe-based oxides, which preserve the original morphology of the metal hexacyanometallates.¹² Both metal oxides are promising materials for various applications such as chemical sensors, catalysts, batteries or medical applications.¹²

Prussian blue is the best-known member of the metal hexacyanometallate material class. It exhibits the empirical formula $\text{Fe}_4[\text{Fe}(\text{CN})_6]_3$, where $\underline{\text{Fe}}_4[\text{Fe}(\text{CN})_6]_3$ represents a N-coordinated high-spin Fe^{III} ion and $\text{Fe}_4[\underline{\text{Fe}}(\text{CN})_6]_3$ corresponds to a C-coordinated low-spin Fe^{II} ion.^{13,14} The transition metal ions linked by a cyanide ligand form open framework structures, enabling ion transport inside the coordination network compounds.¹⁴ The transport of alkali metal (or NH_4^+) ions is characterized by reversible intercalation into or extraction from the network and thus neutralizes the charge of a valence change in the transition metal ions within the material.¹⁵ The metal hexacyanometallates family is extended by the possibility of substituting both metal centers with other transition metal ions.¹⁴ Alongside the rich electrochemistry in this material class,^{14,15} the variety of metal hexacyanometallates leads to different physical and chemical properties. The choice of transition metal centers influences the stabilities, magnetic, optical or catalytic properties.¹⁶⁻¹⁸

Metal hexacyanometallates are mostly composed of inexpensive earth-abundant elements.^{19,14} The preparation can be conducted efficiently by different routes depending on the desired application.^{14,20} Alongside the synthesis of M-HCM powders, thin films of these materials can be prepared by electrodeposition,²¹ layer-by-layer deposition,²² precipitation methods, hydrothermal methods, sonication-assisted casting (SAC) or the SAC combined with

vapor-assisted conversion.^{14,23} Moreover, M-HCM crystals can be prepared in different sizes and shapes if desired.^{24,25}

Research on thin films of porous material with tunable chemical functionalities is a promising perspective for preparing smart membranes, catalytic coatings, chemical sensors or other nanotechnological devices.²⁶ In the case of M-HCMs, the deposition of thin films enabled extensive studies of the electrochemical properties and their use in nanodevices.^{27,28}

In this work, the electrochemical properties of layered M-HCMs were investigated in order to clarify the correlation between the electrochemical behavior, material composition, and structure. To improve the preparation of the material in the laboratory, a commercial 3D printer was converted into a programmable dipping robot, which reliably produced films of the material by layer-by-layer-deposition.

As shown in the literature, layered films of different redox-active thin films can show charge trapping and rectifying behavior under specific circumstances.²⁹ For thin films of M-HCMs, charge trapping behavior was demonstrated for iron hexacyanoferrate and nickel hexacyanoferrate systems.^{30,31} Since the electrode and the outer layer are not allowed to contact each other to prevent shortcuts, a polymer film was implemented in the system.³⁰ In this thesis, a system without a polymeric matrix was prepared to preserve the crystallinity of the layers. Moreover, a system with spectroscopically distinguishable transition metals was prepared. Stratified iron hexacyanoruthenate and nickel hexacyanoferrate layers were prepared by electrochemical deposition and layer-by-layer deposition, respectively. Cyclic voltammetry and *I-V* curve measurements indicated that this layered system shows charge trapping and rectifying behavior. A reference system was prepared with the same materials but with transition metal ions statistically distributed on the lattice sites. This so-called 'mixed system' did not show rectifying behavior but behaved similarly to the electrochemical properties of the individual materials.

A novel aspect of the versatile electrochemistry of iron- and ruthenium-containing metal hexacyanometallates was found by means of the protium/deuterium isotope effect in the voltammetry of the material. Iron hexacyanoruthenate showed interesting and unexpected differences in the voltammetry in protium- and deuterium-based electrolyte solutions. The difference in the voltammetry depending on the isotope composition of the aqueous electrolyte is only known for vanadium hexacyanoferrate, to the best of knowledge.³² In

vanadium hexacyanoferrate, water is stoichiometrically involved in the electrode reaction, which explains the effect. For iron hexacyanoruthenate this does not serve as an explanation.

Detailed investigations were carried out to study the structural properties of these materials. Cyclic voltammetry was used to study the electrochemical behavior in electrolyte solutions. Scanning force microscopy was used to investigate the topography of the samples. By using this method, the roughness of the thin films can be determined. Conductive scanning force microscopy was used to study the solid-state voltammetric behavior of the samples by using *I-V* curves. Scanning electron microscopy was used to study the morphology of the films. The size and shape of synthesized nanoparticles were determined using transmission electron microscopy. The structural characterization methods X-ray photoelectron spectroscopy, grazing incidence X-ray diffraction and polarization modulation infrared absorption spectroscopy were applied to study the samples' composition, structure, oxidation states and crystallinity.

The thesis first provides an overview of the fundamentals and history of M-HCMs. As this work focuses on electrochemistry and structural composition, these topics are discussed first, alongside the relationship between counter-cations in the structure of M-HCMs and the conductivity of the material. The basics of thin films and the requirements for current rectification in layered materials are discussed in Chapter 3. Selected examples are given for layered systems where rectifying behavior or charge trapping was observed. The fundamentals of thin film preparation, particularly electrochemical deposition and wet chemical layer-by-layer deposition are also described in this chapter. Chapter 4 gives an overview of the characterization techniques applied in this work using exemplary measurements of M-HCMs. In the case of X-ray photoelectron spectra of transition metal ions, the data treatment is illustrated by an example from collaborative work carried out as part of SPP 1928 with the group of Prof. Thomas Bein at Ludwig-Maximilians-Universität of Munich. In Chapter 5, the experimental details are given, and the developed dipping robot is described in detail. Chapter 6 presents the rectifying current in layered structures of metal hexacyanometallates. Chapter 7 describes the voltammetric H/D isotope effect in iron hexacyanoruthenate, an essential material for the publications in Chapter 6. Chapter 7 is followed by a summary of this work and an outlook giving further perspective for continuation on this research topic.

2 A Brief History of Metal Hexacyanometallates

As the first metal hexacyanometallates (M-HCM), iron hexacyanoferrate (Fe-HCF), discovered in the early 18th century,³³ marks a significant milestone for art and chemistry. During the discovery, Berlin was the capital of the Kingdom Prussia,³³ therefore, the material was named after the country of its discovery, Prussian Blue. The blue pigment has been the subject of a lot of publications.^{1,34} The published data focuses on its structure, electrochemical behavior, and potential applications, among others. The synthesis procedure remained a secret until it was published in 1724^{2,35} by J. Woodward. The process involved mixing crude alum ($\text{AlK}(\text{SO}_4)_2 \times 12 \text{H}_2\text{O}$) and green vitriol ($\text{FeSO}_4 \times x\text{H}_2\text{O}$) with potassium carbonate solution (K_2CO_3), which had been previously calcined with cattle blood (as source of cyanide groups). The greenish precipitate was washed with hydrochloric acid (HCl), yielding the deep blue Fe-HCF compound.^{2,35} Other recipes of other scientists from this century also consisted of the same ingredients but different amounts of reagents.³⁶ Soon after the discovery, one of the most essential uses of Fe-HCF was as a dye for coloration of textiles. As an important example, the blueprint or cyanotype process has to be mentioned, which was invented by Henschel in 1842.¹

Almost 200 years after the first synthesis, the first structural characterization was achieved in 1936.³⁷ Until today, in 300 years of research, various applications have been found for Fe-HCF and numerous analogues. Fe-HCF is used in battery research, sensors and optically switchable films in electrochromic devices and is a Food and Drug Administration (FDA) approved drug as a poison antidote.^{14,38,39} In 1994, selective hydrogen peroxide detection was shown for Fe-HCF-modified electrodes by the electroreduction in the presence of oxygen.^{6,40} The activity of Fe-HCF is three orders of magnitude higher for H_2O_2 reduction and oxidation in neutral media than for platinum, which is the most widely used material for H_2O_2 detection. Thus, the field of M-HCMs is versatile.⁴¹

2.1 Crystal Structure of Metal Hexacyanometallates

Over the last decades, the structures of M-HCMs have been intensively investigated. In these structures, transition metal centers are bonded to cyanide ligands. Their general formula is $A_xM^I[M^2(CN)_6]_z\Box_{1-y}\cdot nH_2O$.¹ Here, with M^I representing a N-coordinated high-spin metal center (such as Fe, Ni, Cu, Co), M^2 is a C-coordinated low-spin metal center (e.g., Fe, Ru) and A denotes a monovalent cation or NH_4^+ .^{1,42,43} Anionic vacancies in the structure, represented by \Box , arise from the loss of $[M^2(CN)_6]$ groups. Various combinations of A , M^I and M^2 are known, leading to more than 100 compounds.¹ These materials exhibit diverse crystal phases, including cubic, monolithic, rhombohedral, tetragonal or hexagonal crystal structures.¹

The C and N atoms form a strong triple bond, with one lone pair of electrons at each side of the ligand.¹⁹ These lone pairs of electrons facilitate the coordination of the ligand with transition metal centers. The highest occupied molecular orbital (HOMO) exhibits σ character, while the lowest unoccupied orbital (LUMO) has π^* character. Donating electrons from the metal to the ligand imparts an antibonding character to the π^* orbital, thereby weakening the $C\equiv N$ bond. Even though the $C\equiv N$ ligand is a simple ligand consisting of two atoms, the interaction with metal centers reveals a large diversity of coordination modes. The strongest bond is formed at the C end due to the σ -donation ability.¹⁹ This is evident in terminal coordination modes observed in metal cyanide complexes, such as $K_{6-m}[M^m(CN)_6]$.¹⁹ Cyanides exclusively form low-spin complexes. Therefore all precursor building blocks for metal hexacyanometallates are in this spin state.⁴⁴ Additionally, the cyanide ligand can act as a linear bridging ligand with a second transition metal center.

In 1936, Keggin and Miles³⁷ contributed significantly to the understanding of M-HCMs, especially Fe-HCF, by reporting on its crystal structure, as determined by X-ray powder diffraction, of the alkali metal-containing and the alkali metal-free compounds as shown in Figure 1. They identified the structure as belonging to the cubic $Fm\bar{3}m$ space group, with a crystal lattice parameter of $a = 10.2 \text{ \AA}$. The CN^- groups are located at the edges, while $Fe^{II/III}$ ions are positioned in the corners of the cubic lattice. In 1939, Emel us and Anderson found that the CN^- group acts as a bridging unit along the edges of the lattice.³⁴ Furthermore, Keggin and Miles³⁷ hypothesized that in alkali metal-free Fe-HCF, additional iron ions might be present, occupying interstitial spaces rather than being replaced by alkali metal ions. 1977 Buser et al.⁴⁵

published the currently accepted crystal structure for alkali metal-free Fe-HCF. They demonstrated that the alkali metal-free form does not contain interstitial Fe ions but has anionic $\text{Fe}^{\text{II}}(\text{CN})_6^{4-}$ -vacancies. Unsaturated metal ions at the anionic vacancy sides are bound to coordinated water molecules and additionally, the amount of counter cations in the structure will be reduced.¹⁴ It is worth noting that the vacancies are distributed randomly in the framework. For single crystals of M-HCMs, the symmetry is found to be $\text{Pm}\bar{3}\text{m}$, whereas $\text{Fm}\bar{3}\text{m}$ is usually observed in fine powders.⁴³

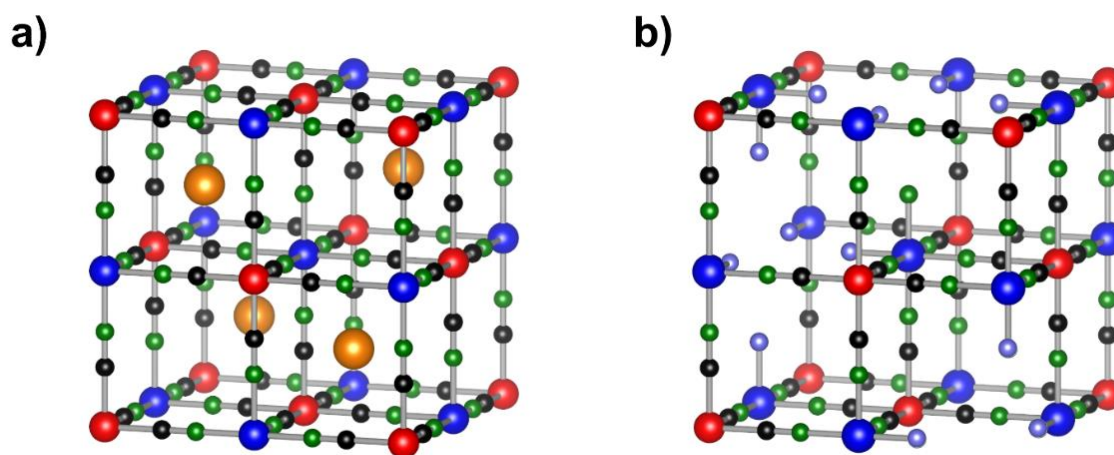


Figure 1. a) ‘soluble’ form with the formula $\text{AM}^1[\text{M}^2(\text{CN})_6]$, b) ‘insoluble’ form with the formula $\text{M}^{14}[\text{M}^2(\text{N})_6]_3$. Color code blue – M^1 , red- M^2 , black- C, green- N, orange- A, purple- H_2O . The schematic was created with VESTA³⁴⁶ and data of Ref.⁴³ for copper hexacyanoferrate adapted for Fe-HCF.

In scientific literature, these different forms of M-HCMs, depicted in Figure 1, are also referred to as the ‘soluble’ form, which contains alkali metals with the ideal formula $\text{AM}^1[\text{M}^2(\text{CN})_6]$, and the ‘insoluble’ form, characterized by vacancies, with the formula $\text{M}^{14}[\text{M}^2(\text{CN})_6]_3$. The terms ‘soluble’ and ‘insoluble’ are historical, originating from the common use of Fe-HCF as a dye. They are not related to the (water) solubility.³⁴ The terms were first found in the book by Liebig⁴⁷ as “*lösliches Berlinerblau*”, which is believed to refer to the ability of the compounds to form colloidal solutions.³⁴

It is important to note that metal hexacyanometallates are typically synthesized as non-stoichiometric compounds.³⁴ These materials can be understood as solid solutions,³⁰ representing a statistical distribution of building blocks on the network. The term ‘solid solution’ in M-HCMs was first mentioned by Ellis et al.⁴⁸ who described partially reduced and

partially oxidized Fe-HCF as a two-component system. Others referred to the term 'solid solution' as the mixture of 'soluble' and 'insoluble' forms of M-HCMs, where the anionic vacancies may have a fractional number rather than a whole number, these structures may be written as $\text{Fe}_4^{\text{III}}[\text{Fe}^{\text{II}}(\text{CN})_6]_{3 \times n} \text{MFe}^{\text{III}}[\text{Fe}^{\text{II}}(\text{CN})_6]$.^{34,49} Widmann et al.⁵⁰ referred to solid solutions by means of M-HCM compounds, where the N-coordinated metal ion is substituted by other metal ions e.g., $\text{K}_2\text{Cu}_{1-x}\text{Ni}_x[\text{Fe}(\text{CN})_6]$, $\text{K}_2\text{Ni}_{1-x}\text{Pd}_x[\text{Fe}(\text{CN})_6]$, but also where the C-coordinated metal ion is substituted as in case of $\text{KCu}^{\text{II}}[\text{Fe}^{\text{III}}(\text{CN})_6]_{1-x}[\text{Co}^{\text{III}}(\text{CN})_6]_x$.⁵⁰

In the insoluble structure, the anionic vacancies at the M^{I} transition metal centers (as shown in Figure 1b) are occupied by coordinated water molecules. In addition to the coordinated water on the vacancy sides, zeolitic water is also present in the cavities of the structure.⁴³ Since the zeolitic water is only physically absorbed in the interstitial sites, it can be removed easily in contrast to the chemically bonded coordinated water.¹⁴

Even trace amounts of alkali metal ions are absorbed into the framework during preparation.⁴⁵ These ions can enter the structure through the diffusion channels for the embedding in the interstitial sites of the framework and play an important role in charge compensation.³⁴ The role of alkali metal ions will be further discussed in Section 2.2.

2.2 Counterions in the Structure of Metal Hexacyanometallates

M-HCMs are in constant exchange with their environment and can absorb even trace amounts of counterions from liquids.⁴⁵ Alkali metal ions (or NH_4^+ ions) can diffuse through the network channels for charge neutralization. Particularly noteworthy are the voltammetric shapes of M-HCMs during electrochemical processes, which vary depending on the cation present in the electrolyte solution.⁵¹

Investigation of the electrochemical deposition using cyclic voltammetry (CV) of iron hexacyanoruthenate (Fe-HCR) on a glassy carbon electrode in different electrolyte solutions (LiCl, NaCl, KCl, RbCl, CsCl and TlCl) were performed by Chen et al.⁵² The film could be successfully synthesized in all electrolyte solutions. For all experiments, the deposited Fe-HCR film could be characterized by a single, rather broad, redox peak couple between 0.0 V and 0.4 V, which were attributed to the $\text{Fe}^{\text{III}}[\text{Ru}^{\text{II}}(\text{CN})_6]/\text{Fe}^{\text{II}}[\text{Ru}^{\text{II}}(\text{CN})_6]$ redox couple. An additional experiment was performed using a Fe-HCR film deposited in an electrolyte solution of KCl. The Fe-HCR film was transferred to aqueous solutions of 0.1 M LiCl, NaCl, KCl, RbCl, and CsCl to calculate the formal potentials ($E^{\circ'}$) of the redox couple, which can be found in Table 1.

Table 1. Calculated formal potentials of Fe-HCR thin film in 0.1 M electrolyte solution of LiCl, NaCl, KCl, RbCl and CsCl.⁵²

| Electrolyte / aqueous solution of 0.1 M | $E^{\circ'} / \text{V}$ |
|---|-------------------------|
| LiCl | 0.13 |
| NaCl | 0.16 |
| KCl | 0.18 |
| RbCl | 0.29 |
| CsCl | 0.34 |

The results suggest an increase of $E^{\circ'}$ with increasing ionic radii (Li = 76 pm < Na = 102 pm < K = 138 pm < Rb = 152 pm < Cs = 167 pm).

Itaya et al.⁵³ studied the electrochemical behavior of Fe-HCF in cyclic voltammetry with electrolyte solutions of 0.1 M NaCl, RbCl, NH_4Cl , CsCl, LiCl and 0.05 M BaCl_2 . They reported the easy intercalation of K^+ , Rb^+ , Cs^+ and NH_4^+ , while the uptake of Li^+ , Na^+ and Ba^+ into the framework was hindered. These results were initially explained by the Stokes radii, which are

2.88 Å (Ba²⁺), 2.37 Å (Li⁺), 1.83 Å (Na⁺), 1.25 Å (K⁺ / NH₄⁺), 1.18 Å Rb⁺ and 1.19 Å (Cs⁺). They suggested that the radii for Ba²⁺, Li⁺ and Na⁺ are too large to enter the network of Fe-HCF. However, it is now understood that the Stokes radii are erroneous for alkali metal ions, with some being smaller than the ionic radii.^{34,54} Consequently, they should not be considered as a definitive guide.

In contrast to Itaya et al.⁵³, Lundgren and Murray⁵¹ observed stable voltammograms of Fe-HCF in 0.5 M NaCl electrolyte. Similar to Itaya et al.,⁵³ 0.5 M LiCl produced unstable cyclic voltammograms.^{51,53} On the other hand, other groups reported successful cyclic voltammetry in LiCl.^{55,56} Taken together, these results indicate that the kinetics of the electrode are influenced by a diffusion process, where the movement of the cation of the electrolyte into the lattice of Fe-HCF is affected, rather than the electron transport between the Fe centers.⁵⁶

Bocarsly et al.⁵⁷ investigated the electrode charge transfer properties of a Ni electrode derivatized with [Fe(CN)₆]^{3-/4-} in electrolyte solutions of 1 M LiClO₄, NaNO₃, KNO₃ and CsNO₃. Reversible electrochemical responses were found for Li⁺, Na⁺, K⁺, and Cs⁺. They note particularly fast insertion kinetics for Cs⁺ and comparatively slow insertion kinetics for Li⁺. The results were also discussed in context of the hydration radius and the sizes of the cations.

Malik et al.⁵⁸ investigated Ni-HCF in various electrolytes containing Li⁺, Na⁺, K⁺, Rb⁺ and Cs⁺ and reported well-defined voltammograms without any evidence of blocking effects.

Schneemeyer et al.⁵⁹ found that only Li⁺ and Na⁺ can intercalate into the Ni-HCF lattice. Cyclic voltammograms performed in K⁺-containing electrolytes demonstrated an irreversible behavior. The insertion of larger ions was impossible.

The varying results reported by different research groups may be reasonably explained by the transformation of the crystal structure of Fe-HCF or Ni-HCF during reduction or oxidation. For instance, Rudola et al.⁵ and Wang et al.⁶⁰ described a phase transition in Fe-HCF from a cubic to either a monoclinic or a rhombohedral crystal structure during reduction and Na⁺ intercalation. Structural differences in the soluble and insoluble material may also play a crucial role in the electrochemical analysis of Ni-HCF. For instance, in Ni-HCF, these structural differences could result in distinct diffusion behavior of the cations; this may explain the divergences in the results of the research groups.⁵⁷⁻⁵⁹ A low number of anionic vacancies, as shown Figure in 1a, might inhibit the intercalation of larger ions. As shown in Figure 1b, anionic vacancies in the structure create the space needed for larger ions to intercalate.³⁴

Furthermore, the mechanism by which the ions enter the network is not satisfactorily explained. Some researchers explained their results using hydration radii, but electrochemical quartz crystal microbalance (EQCM) studies of M-HCMs do not support the theory. Data from studies of Ni-HCF⁶¹ and cobalt hexacyanoferrate (Co-HCF)⁴⁹ imply that the intercalation of hydrated cations is unlikely - the values in Table 2 support this.

Table 2. Number of water molecules transferred by one cation (Li⁺, Na⁺ and K⁺) in nickel hexacyanoferrate and cobalt hexacyanoferrate given in literature.^{49,61}

| Compound | Cation/electrolyte solution | Transferred water molecules |
|----------------------|---|-----------------------------|
| Ni-HCF ⁶¹ | Li ⁺ / Li ₂ SO ₄ | 1.47 |
| | Na ⁺ / Na ₂ SO ₄ | 0.56 |
| | K ⁺ / K ₂ SO ₄ | 0.23 |
| Co-HCF ⁴⁹ | Li ⁺ / LiCl | 1.4 |
| | Na ⁺ / NaCl | 0.5 |
| | K ⁺ / KCl | 0.3 |

In studies measuring the ion sorption in poly(tetracyanoquinodimethane) electrodes, hydration numbers were given by 12, 7 and 5 H₂O molecules for Li⁺, Na⁺ and K⁺ ions, respectively.⁶² In other measurements, similar values were found.⁶³

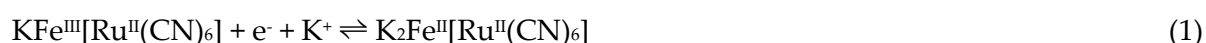
In EQCM studies focusing on the redox processes of Fe-HCF, mass changes of 23.2 g mol⁻¹ for the reduction process and 23.5 g mol⁻¹ for the oxidation process were found. These values approximately agree with the mass change expected from exchanging a potassium ion with one water molecule (39.10 g·mol⁻¹ – (2·1.01 g·mol⁻¹ + 16.00 g·mol⁻¹) = 21.08 g·mol⁻¹).⁶⁴ These findings suggest that K⁺ is primarily involved during charge compensation in the electrochemical processes and also agree with the values in Table 2.

Although the exact mechanisms of cation uptake/withdrawal are not entirely understood, the strong ability of M-HCMs to absorb cations supports their application for removing Cs⁺ from human bodies.¹⁹ For instance, Fe-HCF capsules, approved by the FDA, are used to treat contaminations of human bodies of ¹³⁷Cs. Moreover, a magnetic composite of Fe-HCF has been prepared as a supportive material to treat radioactive wastewater.^{19,65}

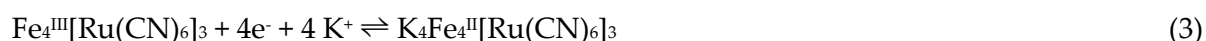
2.3 Electrochemistry of Metal Hexacyanometallates

M-HCMs exhibit rich electrochemistry due to diverse possible combinations of transition metal centers. Depending on the amount of redox-active sites, M-HCMs can facilitate single-electron transfer or dual-electron transfer.¹ Single-electron transfer is observed in $M^I\text{-HCM}^2\text{s}$ with $M^I = \text{Zn, Ni, Fe}$ and $M^2 = \text{Fe, Co, Mn, Ru}$ ($M^I \neq M^2$) transition metal centers. Dual electron transfer was found in M-HCMs of M^I and $M^2 = \text{Mn, Fe, Co}$, with Fe-HCF as the best-known example. In Ni-HCF, only the C-coordinated low-spin Fe metal center is involved in the redox process, in iron hexacyanoruthenate (Fe-HCR) the N-coordinated high-spin Fe undergoes redox reactions.⁶⁶ The redox processes of high-spin Fe or low-spin Fe can be found at different potentials. High-spin Fe is oxidized and reduced at ~ 0.2 V, whereas low-spin Fe is oxidized and reduced at ~ 0.9 V (vs. saturated calomel electrode (SCE) in 1 M KCl) in Fe-HCF.⁵³ The presence of other transition metal ions in the structure may slightly influence the potential of the redox reaction. In Ni-HCF, low-spin Fe undergoes the redox reaction at ~ 0.6 V vs. SCE.⁶⁷

As discussed in Chapter 2.2, counterions in the structure and the number of anionic vacancies directly influence the redox chemistry of M-HCMs. The exchange of counterions accompanies the electrochemical changes to the M-HCM system to maintain the electroneutrality.^{64,68} The electrochemical behavior of Ni-HCF in electrolyte solutions of alkali metal ions can vary, as already described in Chapter 2.2. The redox reaction of the ‘soluble’ forms of Fe-HCR (Eq. 1)⁷ and Ni-HCF (Eq. 2)⁶⁹ can be written as:



These reactions are simplified since vacancies in the compound may change the uptake of counterions. The ‘insoluble’ forms can be written as follows for Fe-HCR (Eq. 3)⁷ and Ni-HCF (Eq. 4)⁶⁹:



In Ni-HCF, the soluble and insoluble structures can be distinguished at slightly different potentials in cyclic voltammograms.⁶⁹ The redox potential of ‘soluble’ Ni-HCF (Figure 1a, Eq.

2) is shifted towards more positive potentials in comparison to the ‘insoluble’ structure (Figure 1b, Eq. 4).⁶⁹ Similar discussions can be found regarding cyclic voltammograms of high-spin Fe in Fe-HCR but also in Fe-HCF in literature.

Abe et al.⁷ identified two distinct reduction peaks of Fe-HCR in NaH₂PO₄, separated by a potential difference of 0.1 V, which they assigned to two structural forms of Fe-HCR: the ‘soluble’ form (Figure 1a, Eq. 1) at more negative potentials and the ‘insoluble’ form (Figure 1b, Eq. 3) at more positive potentials. They noted that the redox peak associated with the ‘insoluble’ structure shows a pH-dependent behavior, in contrast to the pH-independent reduction peak of the soluble structure. These results imply that the redox processes of the two peaks are compensated by H⁺ and Na⁺, respectively.⁷ This explanation is plausible, as for each vacant Ru-site, there may be six water molecules coordinated to the six adjacent high-spin Fe^{III} ions. The coordinated water forms a network with zeolitic water, facilitating fast proton conduction.⁷⁰

Feldman and Murray⁷¹ attributed two different peaks in cyclic voltammograms to the high-spin Fe in Fe-HCF with different coordination:

- I. High-spin iron coordinated by four cyanide ligands and two water molecules.
- II. High-spin iron coordinated by six cyanide ligands.

The peak at more positive potentials is believed to correspond to species with vacancies (Figure 1b), while the peak at more negative potentials may display the reduction of the species without vacancies (Figure 1a).⁷¹ The conclusion drawn for the high-spin Fe species with vacancies was reasoned by analogy with [Fe(H₂O)₆]³⁺.

The findings of Feldman and Murray⁷¹ for high-spin Fe in Fe-HCF are in good agreement with those of Abe et al.⁷ for high-spin Fe in Fe-HCR. Other groups offered other explanations for the peak splitting of high-spin Fe in Fe-HCMs.

Tian et al.⁸ also reported on peak splitting of the cathodic peak during the electrochemical deposition of Fe-HCR on a gold electrode. In the phosphate buffer solution, they detected two pairs of redox peaks. In experiments with different ratios of K⁺ and Na⁺, the redox pair at higher potentials (at $E^{0'} = 0.14$ V vs. Ag|AgCl|sat. KCl) remained stable. In comparison, the second redox peak pair at lower potentials showed a positive shift with the increment of Na⁺ concentration. The authors assigned the peak pair at more positive potentials to the redox

equation in Eq. 3, while the peak pair at more negative potentials was referred to as a cation-related process, as shown in Eq. 5:



Mortimer and Varley⁷² reported that the redox reaction of Fe-HCR includes one oxidation peak but two reduction peaks. These two reduction peaks were assigned to two different charge compensation processes: the negative charge from the reduction of high-spin Fe^{3+} is balanced either by interstitial $\text{Fe}^{3+}/\text{Ru}^{3+}$ or by intercalating potassium ions, each process having a slightly different peak potential.

Similarly, peak splitting in the redox process of the high-spin Fe is observed in Fe-HCF. Liu et al.⁷³ reported peak splitting in the N-coordinated high-spin Fe in nanosized Fe-HCF, which was self-assembled on a cysteine-modified gold electrode. In their study, a single cathodic peak at 0.200 V (vs. SCE) was observed in CVs in 1 M KCl at low scan rates of 1 mV s^{-1} . However, as the scan rates increased to 5 mV s^{-1} , 10 mV s^{-1} and 25 mV s^{-1} , a second reduction peak appeared at 0.226 V (vs. SCE). At scan rates higher than 100 mV s^{-1} , the peak at lower potential merged with the peak at higher potential. The cathodic peak at lower potentials was associated with the redox reaction of the inner atoms of the network, while the peak at higher potentials was ascribed to the reduction of the surface atoms.

In a related study, Hu et al.⁴ investigated Fe-HCF as a potential cathode material for sodium-ion batteries, focusing on samples with varying water content. CV measurements on these samples revealed peak splitting in the reduction peaks of high-spin Fe^{2+} for the samples with medium and low water content. The peak separation was approximately 0.01 V (at 2.77 V and 2.87 V for medium water content and at 2.74 V and 2.86 V for low water content, with potentials measured vs Na/Na^+) using a NaClO_4 in ethylene carbonate: diethyl carbonate (Vol = 1:1) with 5% fluoroethylene carbonate. However, in samples with high water content, a single reduction peak was observed at 2.82 V, which did not correspond clearly to either of the split peaks found in the other samples.

Different factors influence the kinetics of the reduction from Fe-HCR films.⁷⁴ Rajan and Neff⁷⁴ found a linear increase in peak currents at low scan rates (<20 mV s^{-1}). Between scan rates of 20 mV s^{-1} and 1 V s^{-1} , the peak current increased with the square root of the scan rate. This square root dependence is typically indicative of diffusion control. Since stirring of the

solution or concentration differences had little effect on the voltammetry, it was suggested that diffusion from the bulk solution to the film surface is not the rate-determining step. Instead, the authors suggest that the observed behavior is due to the resistance of the film, which is influenced by the concentration of the compounds within the film.

2.4 Conductivity in Metal Hexacyanometallates

M-HCMs are known for their ionic and electronic conductivity.³⁰ Improvements of conductivity in M-HCMs can be achieved by enhancing the crystallinity of the material and reducing the number of grain boundaries.^{1,70} High ionic conductivities from M-HCMs arise from wide channels in the crystal structure, which enable fast ion movement.⁴² For instance, M-HCMs like $\text{Co}[\text{Cr}(\text{CN})_6]_{2/3} \times z\text{H}_2\text{O}$ and $\text{V}[\text{Cr}(\text{CN})_6]_{2/3} \times z\text{H}_2\text{O}$ exhibit high proton conductivities (1.2×10^{-3} and 1.6×10^{-3} , respectively), a phenomenon explainable by Grotthuss mechanism involving a three dimensional (3D) hydrogen-network of zeolitic water molecules.⁷⁵

The electric conductivity of these compounds has been a subject of investigation since the late 1920s.^{76,77} This research was further advanced through electrochemical studies of Fe-HCF-modified electrodes, facilitating the analysis of oxidized and reduced forms. Both electrochemical and solid-state measurements have highlighted significant differences in the conductivity of Fe-HCF in the three oxidation states ($\text{Fe}^{2+}/\text{Fe}^{2+}$, $\text{Fe}^{2+}/\text{Fe}^{3+}$, $\text{Fe}^{3+}/\text{Fe}^{3+}$). Notably, in vacuum-dried Fe-HCF the $\text{Fe}^{2+}/\text{Fe}^{3+}$ oxidation state acts as an insulator, and the oxidized and reduced forms exhibit semiconducting properties. The nature of the electronic conductivity in M-HCMs was addressed by the work of Hurlbutt et al.⁴², where systems like $\text{Na}_x\text{Mn}[\text{Fe}(\text{CN})_6]$, $\text{Na}_x\text{Fe}[\text{Fe}(\text{CN})_6]$ and $\text{Na}_x\text{Co}[\text{Fe}(\text{CN})_6]$ (referred to Mn-HCF, Fe-HCF and Co-HCF, respectively) were investigated. In Fe-HCF, electron transport is believed to occur by electron hopping also referred to as electron self-exchange between neighboring oxidized and reduced Fe-sites.⁷¹ The reduction of Fe-HCF, for instance, depends on the concentration of ferric ions in the structure.⁷⁴ The concentration of ferric ions decreases during reduction, and the resistance is expected to increase.

Local humidity and water content in the structure significantly influence the conductivity. In the absence of water vapor, with only dry N_2 , no detectable currents are observed, indicating that water content is essential for the electron conduction.⁷¹ Rajan and Neff⁷⁴ hypothesized that during reduction, Fe-HCF behaves as an electronic conductor due to the varying concentration of ferric ions, whereas in the oxidation phase, it acts more like an ionic conductor, with K^+ ion concentration in the film dominating the conduction mechanism.

3 Thin Film Applications

Thin films play a crucial role in the functionalization of substrates and can be used in optics, optoelectronic applications, magnetic devices, quantum engineering applications or microelectronic applications. Thin films consist of solid materials built up on a substrate.⁷⁸ The deposition process varies depending on the desired material, material properties and substrate. Generally, thin film fabrication can be categorized into two approaches. In the bottom-up process, atomic or molecular components are built into complex nanoscale assemblies or directed self-assemblies. The top-down process seeks to produce nanostructures starting from larger dimensions and reducing them to the required size.⁷⁹

The thin film growth involves three steps:

- i) Production of the appropriate atomic, molecular or ionic species.
- ii) Transport of the material through the medium to the substrate.
- iii) Condensation on the substrate, for example, through (electro-) chemical reactions.

The process can be summarized as a statistical process of nucleation, surface-diffusion, film growth of 3D nuclei, forming a network structure and the subsequent filling of cavities and holes to form a continuous film. The thin film growth (without modification of the substrate by a self-assembled monolayer (SAM)) can be described as follows:

- i) In contact with the substrate, the material loses its velocity and is physically absorbed onto the substrate surface.
- ii) The adsorbed species, out of thermal equilibrium, can move and form larger clusters through interaction among themselves.
- iii) Due to thermodynamic instability, these nuclei (or clusters) tend to desorb over time, depending on the deposition parameters. Successful film growth requires parameters that support collision and adsorption of the clusters before desorption occurs. As the clusters reach a specific crystal size, they become thermodynamically stable.
- iv) The nucleus can grow lateral and perpendicular to the surface. Generally, lateral growth is favored, leading to the formation of so-called islands on the substrate.

- v) To minimize the surface area, these islands start to merge. This agglomeration is enhanced by increasing the surface mobility of the absorbed species.
- vi) As larger islands grow, holes and channels are left on the uncovered substrate. A complete continuous film is built by filling these gaps of the sample surface.

During the growth process, grain boundaries and point and line defects may be incorporated into the film by randomly distributed islands.

For modern technology applications, thin film devices are required.⁸⁰ Fabrication of thin films allows easier integration of materials into different devices of various types. Thin films need to be used for micro miniaturization of devices. Thin film devices have been used in e.g., rectifiers, integrated circuits, transistors and solar cells.⁸⁰ For molecular electronic devices, well-defined assemblies of well-ordered supramolecular architectures are crucial.⁸¹ Additionally, control over the directionality of electron transfer is essential.

3.1 Rectifying Behavior and Charge Trapping of Electrochemically

Active Films

Rectifying behavior found in diodes allows an electrical charge to flow in one direction but not in the reverse direction.⁸² Diodes are defined as two-terminal circuit elements with asymmetrical current-voltage (I - V) characteristics.⁸³ In an ideal case, a diode has an infinite conductance when forward-biased and contrastingly infinite resistance when reversed-biased. Rectifying behavior in bulk semiconductor materials has been well-known and understood. Besides this research topic, reports on molecular⁸² and thin film rectifiers are available^{29-31,81,84,85}.

The combination of two (or more) redox active species or films of two different redox potentials (as shown in Figure 2) can lead to rectifying behavior (in solid state) or charge trapping (in contact with electrolyte solution). In this phenomenon, the electron transfer between the electrode and the outer layer is mediated by the redox states of the inner redox-active layer, resulting in a unidirectional current, similar to electronic devices such as Zener diodes. Essential criteria for successful production of materials for unidirectional current flow are the following²⁹:

- i. The contact between the outer layer and the electrode must be inhibited, allowing the system to undergo redox processes where the inner layer mediates the electron transfer between the electrode and the outer layer.
- ii. The counterion flow required by the redox reactions of the inner layer should be facilitated by the permeability of the outer layer.
- iii. There should be a minimal overlap of charge distributions of redox levels of inner and outer redox-active films.

The following paragraph summarizes results from the literature where rectifying behavior (or charge trapping) was observed for redox-active thin films. There are two primary differences in system preparation that promote a unidirectional current. In the first group, unidirectional currents are achieved through a monolayer which is in contact with a solution containing a redox-active material (Figure 2a). In the other group, the unidirectional current flow is mediated through a bilayer system of two redox-active films (as shown in Figure 2b).

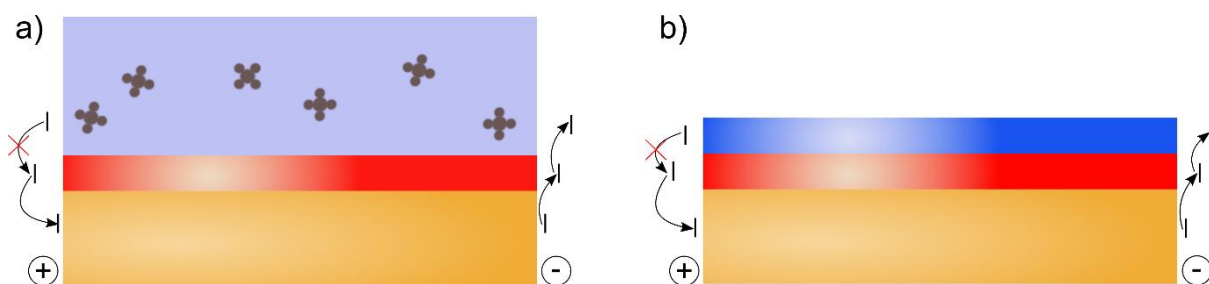


Figure 2. Examples of rectifying behavior of redox-active films, a) a monolayer in contact with redox-mediator containing solution and b) rectifying behavior of redox-active layered bilayer system.

3.1.1 Organic Redox-Centers

Azzaroni et al.⁸¹ presented a strategy to construct redox-active molecular platforms that can function as molecular rectifiers and provide amplifiable electronic readout. Their approach involved chemisorbing a binary mixed SAM on an Au substrate as a first step, followed by creating a multilayer assembly using ferrocene-labeled streptavidin and biotin-labeled polyallylamine due to strong ligand-receptor biological interactions. This redox-active interfacial architecture successfully mediated and rectified electron transfer between redox donors in the solution ($[\text{Fe}(\text{CN})_6]^{4-}$) and the Au electrode, acting as a tunable bio-supramolecular diode.

Another example of electrochemical current rectification at bio-functionalized electrodes was achieved using $[\text{Fe}(\text{CN})_6]^{3-/4-}$ in solution and a gold electrode functionalized with microperoxidase-11, a biomolecular redox-mediator.⁸⁵ Here, direct electron transfer between the electrode and the redox probe was inhibited by an insulating undecanethiol monolayer. This barrier is overcome by immobilizing the redox-active microperoxidase-11 on the passivated electrode. This allows controlled electron transfer due to selective electron transport between the bio-functionalized electrode and the redox mediator in the solution. Notably, the redox potential of microperoxidase-11 and the ferricyanide only allows the electron flow of the cathodic Faraday current.

Oh et al.⁸⁴ constructed a dendrimer-based electrochemical rectifier using a biomaterial monolayer composed of redox-active ferrocenyl dendrimers and *n*-hexadecanethiol. This assembly exhibited excellent blocking properties, enabling electrochemical current rectification. It was shown that the oxidation of solution-phase $[\text{Fe}(\text{CN})_6]^{4-}$ occurred exclusively

through electron transfer mediated by the ferrocenyl groups attached to the dendrimers, while the reduction of $[\text{Fe}(\text{CN})_6]^{3-}$ was not possible.

Abruña et al.²⁹ demonstrated a unidirectional current in an electrochemically polymerized bilayer system of vinylpyridine and vinylbipyridine. This bilayer electrode exhibited different behavior than the monolayers of the same materials. In the bilayer, the outer layer does not directly oxidize at certain potentials; instead, it undergoes oxidation through electron transfer from the inner layer at specific potentials. This behavior is observable in cyclic voltammograms, where even a small population of oxidized sites in the inner layer is sufficient to initiate the reduction of the outer layer, leading to unidirectional electron transfer across the bilayer.

3.1.2 Coordinated Metal Redox-Centers

Kulesza and co-workers³⁰ prepared a rigid bilayer structure from M-HCMs on an electrode. The system consisted of the electrochemically deposited inner layer of Fe-HCF and an outer layer containing Ni-HCF and poly(*N*-methylpyrrole). The layered system exhibits unidirectional current, as shown by cyclic voltammetry. The inner Fe-HCF layer serves as a mediator as described in the work of Abruña et al.²⁹ Here, the outer layer can only be oxidized once the inner Fe-HCF layer is oxidized, and the reduction only takes place if the reduction of the inner layer starts. Additionally, the rectifying effect was examined under solid-state voltammetric conditions using a two-electrode sandwich configuration. The powders were pressed separately and then introduced into the cell set-up. The electrons and ions were forced to flow in response to the applied potential. Since Ni-HCF can only be reduced to $\text{Ni}^{\text{II}}\text{-HCF}^{\text{II}}$, the fully oxidized $\text{Ni}^{\text{II}}\text{-HCF}^{\text{III}}$ acts as an insulator.

Similar to the work of Kulesza et al.,³⁰ the group of Kurihara and co-workers³¹ prepared stratified layers of Fe-HCF as the inner layer and Ni-HCF as the outer layer. The outer layer was spin coated onto the Fe-HCF film in this approach. The authors address the thickness of the inner layer and the influence of it on the rectifying behavior of the final material. The emergence of a unidirectional current required a minimum thickness of 20 nm for the inner layer. Additionally, the thickness dependence of the second layer was studied, leading to the result that the peak currents in cyclic voltammetry depend on the outer layers' thickness. This

result indicates that the trapped charge density of the layered films can be accumulated as the top layer increases in thickness.

3.2 Thin-Film Preparation of Metal Hexacyanometallates

Various methods are known for producing thin films of coordination network compounds. Since rapid development and diverse applications of coordination network compounds, a wide array of preparation techniques has emerged for creating porous networks.⁸⁶ The functionalization of surfaces and interfaces is important for technological advancements. Modifying a surface with regard to its electrical, optical, wetting or biological properties is a key to successfully imparting a desired functionality to an object.⁸⁶ For M-HCMs, the preparation can be conducted efficiently in different ways depending on the desired application.^{14,20} Alongside the synthesis of M-HCM powders, thin films of these materials can be prepared by electrodeposition,²¹ layer-by-layer deposition,²² precipitation methods, hydrothermal methods, sonication-assisted casting (SAC) or the SAC method with vapor-assisted conversion.^{14,23}

3.2.1 Electrochemical Deposition

Electrochemical deposition is a versatile and widely used process in which materials are deposited onto a conductive substrate from a precursor solution and plays a significant role in the functionalization of substrates.⁸⁷ Campagnol et al.⁸⁷ demonstrated the electrochemical deposition of metal-organic frameworks. Similarly, other coordination networks, such as M-HCMs, can be easily prepared on electrode surfaces through electrochemical reduction. This method increases the spectrum of possible deposition techniques for coordination network compounds. In 1978, Neff²¹ first demonstrated the preparation of modified electrodes with Fe-HCF. This involved cathodizing a platinum foil for 1 h at 1 mA in 1 M HCl, followed by placing the electrode in a solution of 0.01 M $\text{FeCl}_3 \cdot 6 \text{H}_2\text{O}$ + 0.01 M $\text{K}_3[\text{Fe}(\text{CN})_6]$, resulting in the precipitation of the Fe-HCF film on the electrode.

The electrochemical deposition technique of M-HCMs under galvanostatic conditions, as used today, was reported by Itaya et al.⁸⁸ for Fe-HCF. For this, a current density of about $20 \mu\text{A cm}^{-2}$ in a solution of previously prepared $\text{K}_3[\text{Ru}(\text{CN})_6]$ and $\text{Fe}_2(\text{SO}_4)_3$ was applied. This

technique remains popular for producing thin films of M-HCMs. Film growth can be achieved during the execution of a cyclic voltammogram,⁸⁹ or using chronoamperometric conditions.^{51,90} For the deposition of M-HCMs, cathodic potentials reduce the precursors at the electrode to the M-HCM film. Bácskai et al.⁶¹ investigated the film growth of Ni-HCF by cyclic voltammetry with an EQCM. They observed an increase in current and mass with each cycle. In the range where Ni-HCF was deposited (0.00 V – 0.85 V vs. SSCE), only $[\text{Fe}(\text{CN})_6]^{4-/3-}$ is redox-active, for the redox reaction of Ni^{2+} much more negative potentials are required (-1.00 V vs. SSCE).⁶¹ The measurements show, that the film growth proceeds during the reductive scan (from 0.85 V to 0.00 V vs. SSCE). In this step, $[\text{Fe}(\text{CN})_6]^{3-}$ is reduced to $[\text{Fe}(\text{CN})_6]^{4-}$. $[\text{Fe}(\text{CN})_6]^{4-}$ precipitates with Ni^{2+} . This leads to the formation of Ni-HCF, which is deposited on the electrode surface.⁶¹ During the first cycles, only a small amount of Ni-HCF is electrodeposited, which can be explained by poor adherence of the film to the substrate. After several cycles a decrease in film growth rate was described by the authors, which may be explained by the dissolution of thicker films. The presence of K^+ ions in the precipitation process suggests the formation of not only $\text{Ni}_2^{II}[\text{Fe}^{II}(\text{CN})_6]$ but also of $\text{K}_2\text{Ni}^{II}[\text{Fe}^{II}(\text{CN})_6]$ or $\text{KNi}_{1.5}^{II}[\text{Fe}^{II}(\text{CN})_6]$. It was found that both forms of Ni-HCF, as already shown in Eq. 2 and Eq. 4, are formed during deposition.⁶¹

Besides other electrochemical methods, recent publications mostly use cyclic voltammetry for electrodeposition of Fe-HCR on different conductive substrates, as shown in Table 3. These examples from literature indicate that cyclic voltammetry is a versatile tool for depositing Fe-HCR on various substrates in different electrolyte solutions.

Table 3. Literature overview for electrochemical deposition of Fe-HCR using cyclic voltammetry.

| | Brief description | Working electrode | Preparation: Potential range / scan rate |
|----------------------|---|-----------------------------|---|
| Fe-HCR ⁸ | FeCl ₃ +K ₄ [Ru(CN) ₆]+KCl | Au electrode | 0.1 – 1.0 V (vs. Ag AgCl sat. KCl) / 0.05 V s ⁻¹ |
| Fe-HCR ⁹¹ | FeCl ₃ +K ₄ [Ru(CN) ₆]+KCl | Carbon fiber microelectrode | -0.2 - 1.0 (vs. Ag AgCl) / 0.05 V s ⁻¹ |
| Fe-HCR ⁹² | FeCl ₃ +K ₄ [Ru(CN) ₆]+KCl | Glassy carbon electrode | -0.3 – 1.0 V (vs. SCE) / 0.05 V s ⁻¹ |
| Fe-HCR ⁷² | FeCl ₃ +K ₄ [Ru(CN) ₆]+RuCl ₃ +KCl | ITO | -0.2 – 0.6 V (vs. Ag AgCl 3 M NaCl) 0.05 V s ⁻¹ |
| Fe-HCR ⁵² | Fe ³⁺ + [Ru(CN) ₆] ⁴⁻ + KCl (or LiCl, NaCl, RbCl, CsCl) | Glassy carbon electrode | -0.2 – 0.9 V (or 1.0V) (vs. Ag AgCl) / 0.1 V s ⁻¹ |

3.2.2 Layer-by-Layer Deposition

Layer-by-layer (LbL) deposition is a versatile method to build functional thin films on substrates.⁹³ It has been improved to be a useful tool for many applications, e.g., catalysis,^{94,95} optics,^{96,97} and biomedicine.⁹⁸ Substrates can be coated with polymers, nanoparticles as well as biomolecules like proteins or lipids. The original principle is based on oppositely charged ions alternatingly deposited onto a substrate with implemented washing steps.⁹³ One cycle creates a single bilayer, which can be repeated and lead to several micrometer thick films. However, covalent, hydrogen-bonding, or other molecular interactions can also be considered and achieve continuous development of the technique. LBL assembly can be performed by spray or spin coating, immersion, fluidic, or electromagnetic techniques.⁹³

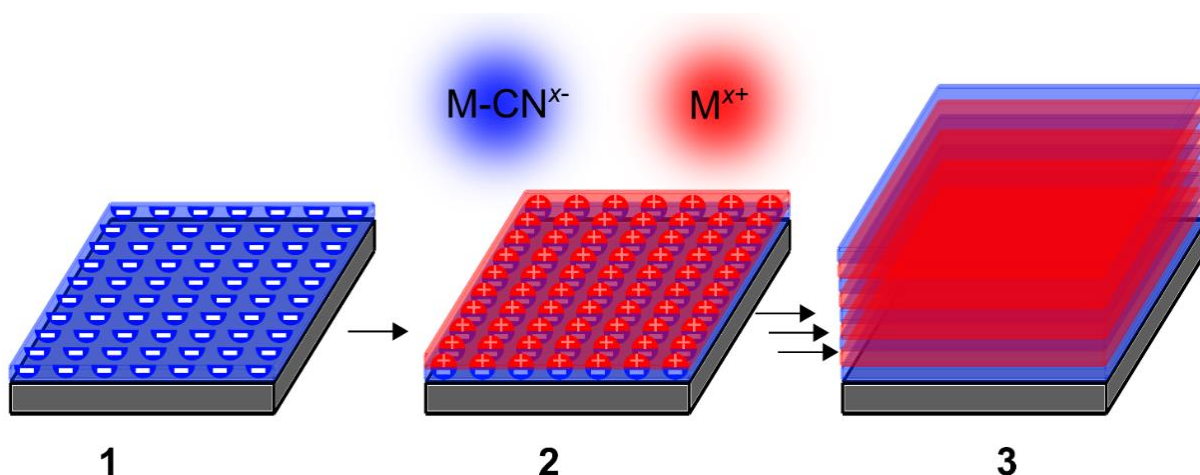


Figure 3. Schematic illustration of layer-by-layer principle. 1) Modified electrode with negatively charged surface, 2) immersion into solution of positively charged ions, 3) multilayered material after alternating steps in positively and negatively charged precursor solutions.

Thin films can be formed by an alternative immersive “dipping” assembly of a (planar) substrate into separated precursor solutions, as shown in Figure 3. Immersive LBL assembly is often performed manually, robotics are also used, facilitating longer immersion times and automated processing of many cycles.⁹³ The thickness of the resulting film can be controlled by the number of deposition cycles. Layer-by-layer assembly techniques can be successfully performed for coordination network compounds.⁹⁹ The synthesis of surface-mounted metal-organic frameworks (SURMOFs) is conventionally based on hydrothermal or solvothermal methods. Layer-by-layer assembly facilitates the fabrication of SURMOFs at room or low temperatures. A requirement for the fabrication of SURMOFs is the functionalization of the substrate to expose a specific functional group like $-\text{COOH}$, $-\text{OH}$ or thiol groups.⁹⁹ Consequently, the layer-by-layer deposition of SURMOFs consists of i) selection of the substrate, ii) functionalization of the substrate and iii) layer by layer deposition by subsequent immersion.

The first publication related to LbL deposition of M-HCMs was published by Millward et al.²² in 2001. Thin films of Fe-HCF and Fe-HCR were prepared by alternately immersing a gold substrate into $[\text{Fe}(\text{CN})_6]^{4-}$ (or $[\text{Ru}(\text{CN})_6]^{4-}$) and Fe^{3+} . The Fe-HCR films were prepared by cycles consisting of 60 s in the Fe^{3+} precursor solution, 30 s rinsing with deionized water, 60 s in $[\text{Fe}(\text{CN})_6]^{4-}$ precursor solution followed by an additional rinsing step of 60 s. In the deposition process, Fe^{3+} cations are absorbed on the substrate, and during the subsequent

immersion into $[\text{Fe}(\text{CN})_6]^{4-}$ (or $[\text{Ru}(\text{CN})_6]^{4-}$), the anions react with the cations and absorb, and thus, a monolayer of Fe-HCF or Fe-HCR is formed.²² The deposited films showed the expected voltammetric peaks of the material at +0.2 V (vs. Ag|AgCl), indicating the reduction and oxidation of the material even for the first accomplished deposition cycle. With increasing number of deposition cycles, the peak positions change, and the charge under the peaks increases, indicating each layer to be deposited on a slightly different substrate.

Pyrasch et al.¹⁰⁰ expanded the area of M-HCMs deposited by LbL deposition on pretreated quartz or indium tin oxide (ITO)-coated glass substrates with poly(diallyldimethylammonium chloride) (PDADMA) or poly(styrene sulfonate) (PSS) and poly(allylamine hydrochloride) (PAH). In a broad CV and IR spectroscopic study, investigations of Fe-HCF, Ni-HCF, Co-HCF and iron hexacyanocobaltate (Fe-HCC) in different oxidation states were performed. The oxidation state of the material was tuned by using the precursor salts in different oxidation states, the concentration of all transition metal precursors was 10 mM. The substrates were kept in each solution for 30 min, with a rinsing step in between. For instance, $\text{Ni}^{\text{II}}\text{-HCF}^{\text{III}}$ was prepared by using $\text{NiCl}_2 + \text{K}_3[\text{Fe}(\text{CN})_6]$, and the preparation of $\text{Ni}^{\text{II}}\text{-HCF}^{\text{II}}$ was achieved by using $\text{NiCl}_2 + \text{K}_4[\text{Fe}(\text{CN})_6]$. From scanning force microscopy (SFM) studies it was found that $\text{Fe}^{\text{III}}\text{-HCF}^{\text{II}}$ films consist of multiple small crystallites of 50-150 μm in diameter. After 10 dipping cycles, the surface was not fully covered with $\text{Fe}^{\text{III}}\text{-HCF}^{\text{II}}$, whereas after 20 dipping cycles a dense, defect-free layer was achieved. Moreover, it was found that the substrate precoating plays a crucial role in the nucleation process. As shown for Ni-HCF, the thin films prepared on the PDADMA- and PSS/PAH-pretreated substrates indicate the same redox peaks of Ni-HCF (Eq. 2, Eq. 4) but with different relative heights of the two peaks. The studies show that the LBL method is a tool that easily forms thin films of metal hexacyanometallates. By using precursor solutions of different oxidation states, the oxidation states of M-HCMs can be tuned during deposition.

Fitta et al.¹⁷ found a complete coverage of Ni-HCF on a silicon substrate modified with PDADMA after 10 dipping cycles. The time for cycles used for this deposition was 120 s in each precursor solution, with a rinsing step in between. The concentration of both transition metal precursor solutions was 20 mM. This result is contrary to the result of Pyrasch et al.¹⁰⁰ and underlines the diverse parameters for layer-by-layer deposition. For instance, Pyrasch et al. used longer dipping times than Fitta et al. (30 min vs. 120 s), but the concentration of the

precursor solutions varied (10 mM vs. 20 mM). These differences may influence the time needed to build up a thin film.

4 Applied Characterization Techniques for Metal Hexacyanometallates

Various techniques can be used to investigate M-HCM samples. In this work, the following experimental methods were applied:

- (i) Scanning force microscopy (SFM) is used to investigate the topography of the samples. By this technique, the roughness and thickness of the samples can be determined. Conductive-SFM (C-SFM) can be used to study the solid state voltammetric behavior of the samples by measuring I - V curves.
- (ii) Cycling voltammetry (CV) is used to study the electrochemical behavior in electrolyte solutions.
- (iii) X-ray photoelectron spectroscopy (XPS) provides insights into the material's composition and the oxidation state of the transition metal centers.
- (iv) Grazing incidence X-ray diffraction (GI-XRD) yields information about the crystal structure of the material.
- (v) Scanning electron microscopy (SEM) was used in addition to SFM measurements to study the morphology of the samples.
- (vi) Transmission electron microscopy (TEM) to determine the size and shape of synthesized nanoparticles.
- (vii) More detailed information about the bonding within the structure and the electrochemical behavior at the metal|air interface and metal|electrolyte can be gained by polarization modulation infrared reflection absorption spectroscopy (PM IRRAS) measurements.

In this chapter, the working principles of the methods are explained, along with the interpretation of the data relevant to this thesis.

4.1 Scanning Force Microscopy

SFM, often also referred to as atomic force microscopy (AFM), is a versatile tool to obtain images of a sample by deflection of a tip at a cantilever on the nanometer scale.^{101,102} Besides others, information about the topography, conductivity (including *I-V* characteristic curves), adhesion and stiffness of a sample can be gained using this method. There are no specific requirements for the sample, such as conductivity (for tapping or conductive mode) or opaqueness, nor are specific measurement environments needed.¹⁰¹ This is the main advantage over scanning tunneling microscopy (STM), where only conductive surfaces can be imaged.¹⁰³ SFM can be conducted in air, vacuum or liquid environments. The principle of SFM is a line-wise scan of a selected area of sample surfaces with a small, sharp tip attached to a flexible cantilever (Figure 4). The SFM probe (consisting of a chip, cantilever and tip) is the heart of the SFM. The cantilever is rectangularly or triangularly shaped and can be found at the end of the chip.¹⁰⁴ At the end of the cantilever, the tip is formed, which is in mechanical interaction with the sample surface. The shape of the tips can commonly be found as a pyramidal structure, but depending on the applied technique and the sample, spherical, pillar or conical shapes are also commercially available. Tips are most often made of silicon or silicon nitride. Due to the crystal structure, forming a sharper tip with silicon is easier than with silicon nitride (≤ 10 nm vs. ≤ 20 nm).¹⁰⁴ However, silicon nitride is more wear-resistant than silicon. The cantilever is typically coated with a thin reflective film (e.g., Al, Au) on its backside. The forces between the tip and the sample displace the cantilever from its equilibrium position, from which it can be seen as a force sensor.¹⁰⁴ The displacement is measured using a laser beam that is deflected on the backside of the cantilever and detected on a photodiode (Figure 4). The attractive and repulsive forces between the tip and sample are measured.¹⁰³

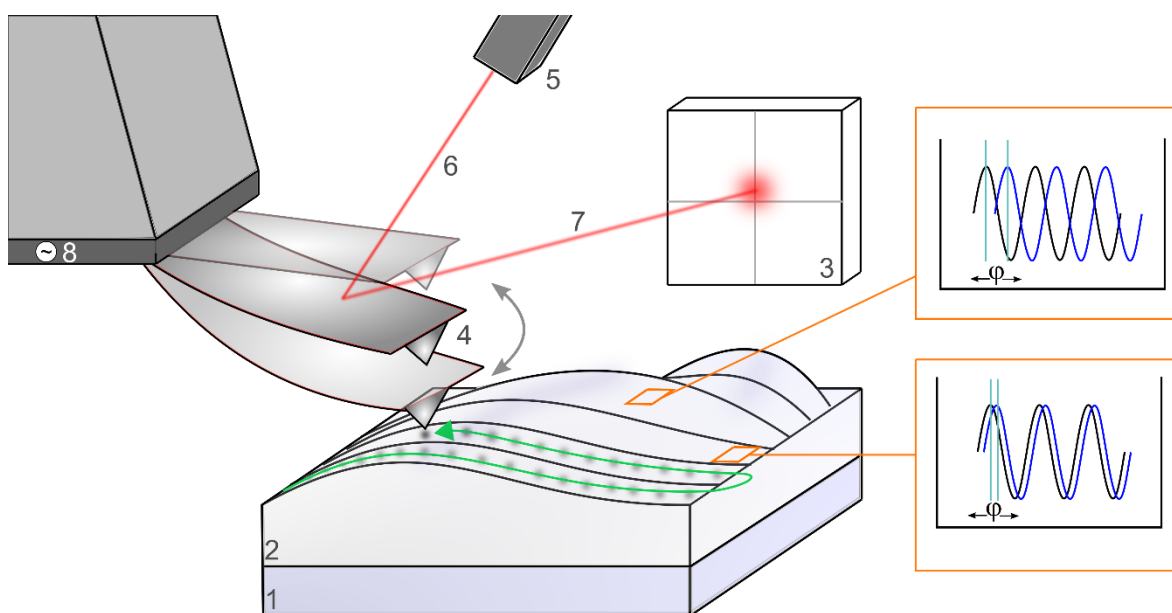


Figure 4. Schematic illustration of tapping mode AFM. 1) Sample stage; 2) sample; 3) quadrant photodiode; 4) cantilever and probe tip; 5) laser diode; 6) laser beam; 7) deflected laser beam; 8) piezo element.

In contact mode, the cantilever exerts a constant force on the sample surface.^{102,103} Low-spring constants should be used for this technique. Depending on the sample stiffness, the probe may be deformed and may exert a local force that damages the sample. Such unintended alterations of the sample should be avoided. The contact between the probe and the sample appears in the blue regime of the force-distance curve in Figure 5, where repulsive interaction force occurs. The cantilever approached the surface and bends due to an elastic deformation. As the scanning is performed on different surface locations, the deflection of the sample changes.

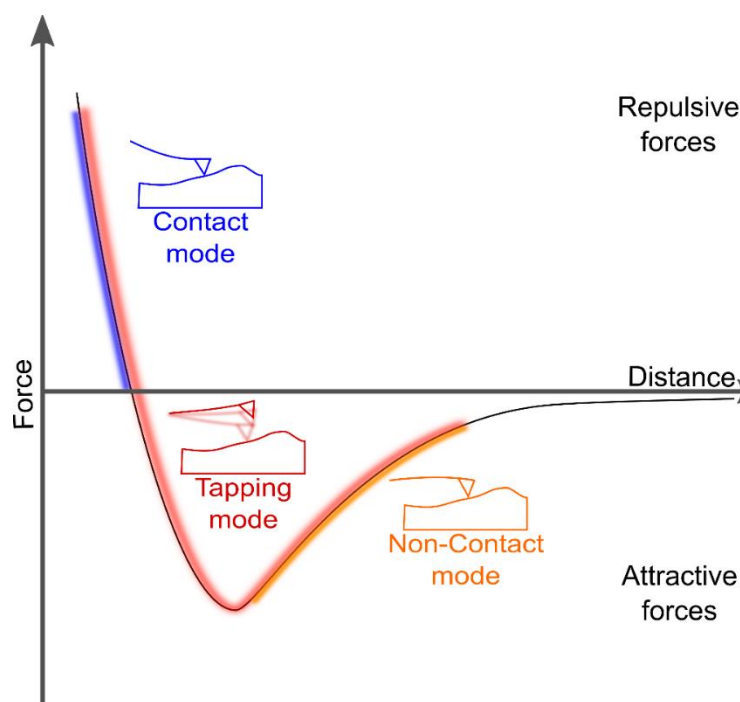


Figure 5. Schematic illustration of the Lennard-Jones potential (Force-Distance curve) with inserted interatomic forces between the tip and the sample in dependence of their distance. Different forces between tip and sample imply three different SFM modes. The figure was adapted from ref 102.

SFM measurements can also be performed in a dynamic mode with an oscillating tip, which is referred to as tapping or intermittent contact mode,^{103,105} in which the tip is in intermittent contact with the surface of the sample. This mode is used in the regime of attractive and repulsive forces (red region in Figure 5). It is often used when imaging soft and sensitive samples (e.g., polymers or biological samples) since strong repulsion and lateral forces applied to the surfaces in contact mode may destroy them. Tapping mode is also helpful in cases of loosely attached particles on a sample. The cantilever constantly oscillates close to its free resonance frequency.¹⁰³ This oscillation can be generated from the piezo element by applying an AC signal (Figure 4). This technique prevents the tip from being trapped by the adhesive forces and causing damage to the sample surface. The amplitude of the cantilever oscillation is used as a feedback signal for topography.¹⁰⁶

The force between the tip and the sample can be even more reduced using non-contact SFM. The mode is located in the orange region shown in Figure 5. This mode is usually conducted at tip-sample distances larger than 0.6 nm.¹⁰⁷ The tip is placed in attractive force regions, and force gradients are detected either from shifts of the resonance frequency of the cantilever or of the amplitude and phase of the cantilever.

M-HCMs are soft materials, often producing a granular film structure, therefore SFM measurements of this material class are often conducted in tapping mode.^{108,109}

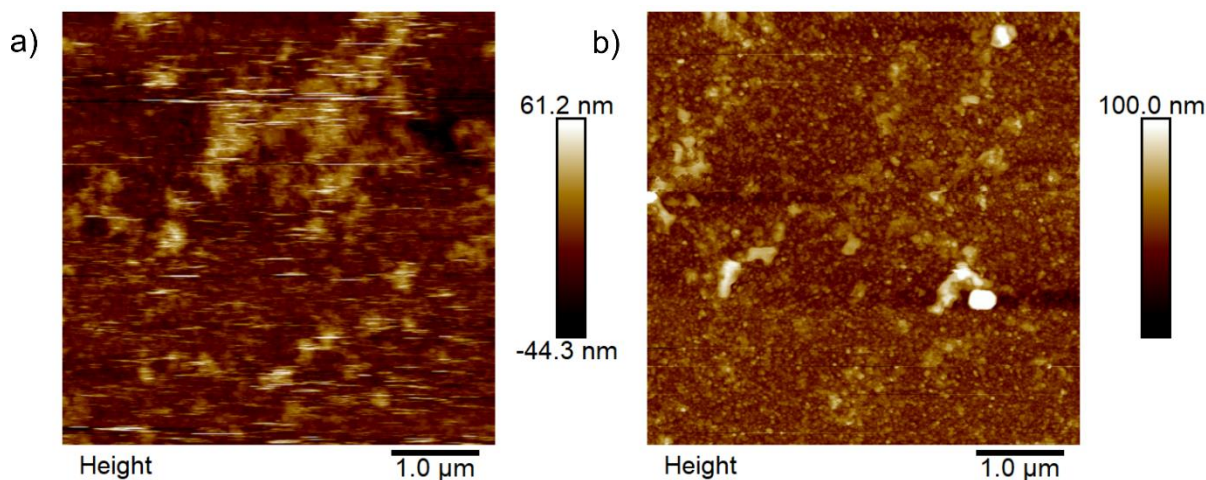


Figure 6. SFM from M-HCM samples on deposited Au-electrodes recorded in a) contact mode and b) tapping mode of a scan area of $5 \times 5 \mu\text{m}$. Own measurements.

While scanning in contact mode, stripes can be found in the image (Figure 6a), whereas the image in tapping mode of M-HCMs remains stripe-less (Figure 6b). As shown in Figure 6b, the intermittent mode also allows high-resolution images from soft samples.¹⁰³ For this reason, all SFM images of M-HCMs were conducted in tapping mode.

Determination of thickness can be achieved through SFM measurements, which involve scratching the surface and subsequently scanning the surface in contact or tapping mode (Figure 7a). In literature, various approaches have been documented for this procedure. Ono et al.⁷⁰ investigated a thin film of Fe-HCF (7.0 nm). In this case, the area was forcibly peeled by an SFM probe-polishing technique.⁷⁰ For this method, a tip in contact mode with a strong probe force was used, which gradually removed the film from the substrate sequentially (scan-by-scan). Afterwards, the resulting rectangle, which uncovers the substrate, can be utilized for further thickness analysis. For thickness ranges of a few nanometers, forcibly peeling surfaces using SFM is a practical technique. Nevertheless, other methods may be more recommended for thicker films. In some publications, knife edges were employed to scratch the surfaces for measuring the thickness of polyaniline ($>100 \text{ nm}$)¹¹⁰ or polypyrrole ($>30 \text{ nm}$) polymeric films, with subsequent scanning of the area in tapping mode and contact mode, respectively.¹¹¹ Cho¹¹² used Teflon® tape to mask parts of the substrate during the deposition of polypyrrole

(>130 nm), thus creating a substrate|polymer edge that facilitated the study of film thickness by scanning the area in contact mode.

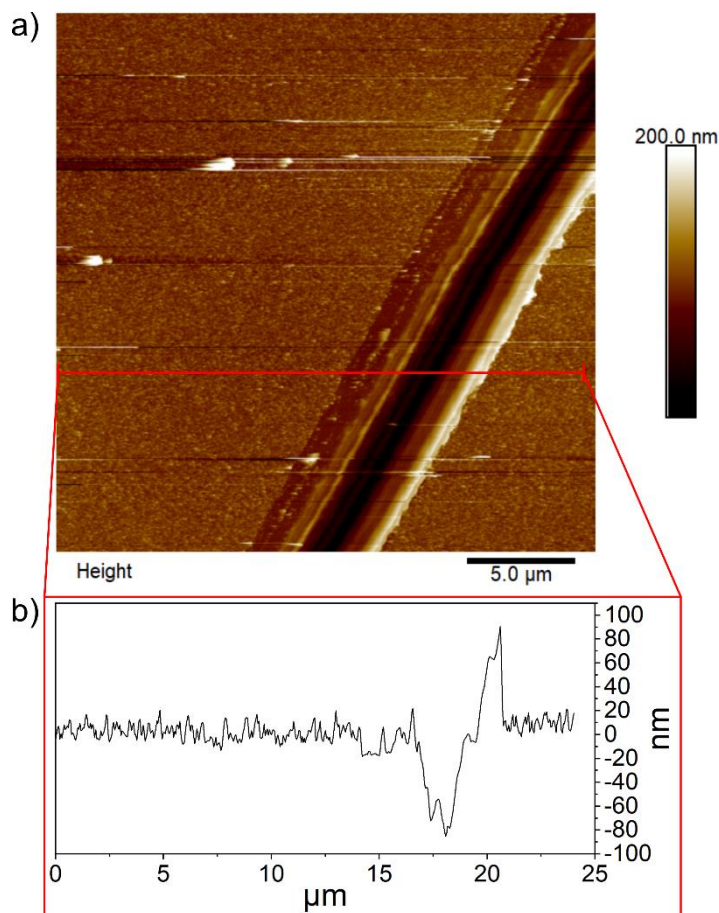


Figure 7. a) SFM measurement of a Fe-HCR film deposited on an Au electrode. A thin cannular was used to create a scratch and uncover the substrate, to determine the film thickness. b) Thickness analysis of the marked section using the software NanoScope (Bruker Corporation, USA).

Using the ‘section analysis’ tool in the NanoScope Software (Bruker Corporation, USA), the height between the sample surface and the bottom of the scratch (Figure 7b), usually the substrate surface, can be determined.

4.2 Conductive Scanning Force Microscopy

Conductive SFM (C-SFM) is based on contact mode and was developed in the 1990s.¹¹³ For this method, a bias voltage is applied between the conductive cantilever and the sample, and the

resulting current is detected. The topography of the sample and the current distribution are measured simultaneously with C-SFM.

A current amplifier connected to the SFM is required for C-SFM. Besides an SFM with scanner and cantilever detection technique, a conductive SFM probe, and an external voltage source are needed.¹¹³ The amplification is needed for samples with high resistance or even with insulating behavior.¹¹³ In some cases the measured currents can range from several femto- to picoamperes. In contrast to STM, C-SFM measures the current completely independent of the sample topography, which is obtained simultaneously by the cantilever deflection.

With C-SFM, I - V characteristics can also be recorded, which can evaluate the electrical properties by measuring the current between the sample and the cantilever while sweeping the sample bias voltage. The widely used abbreviation ' I - V characteristics', it is intended to distinguish cyclic voltammograms from I - V characteristics clearly. Here, ' V [V]' stands for the bias voltage applied between both contacts (rather than the electrode potential E [V] vs. a reference electrode in voltammetry).

Even though all conductive SFM tips can be used for C-SFM measurements, attention has to be paid regarding to the stability of the geometry and electrical properties of the tips.¹¹³ Several types of SFM probes that are specifically designed for C-SFM measurements can be found. The best results have been found with doped diamond tips.¹¹³ There are p- (doped with boron) and n-doped (doped with nitrogen) diamond tips. By doping, the Fermi-level gets altered due to the introduction of newly occupied and unoccupied states within the band gap. By this, the tip can be made with nearly metallic conductivity. Since tips with Au or PtIr coatings are much softer, the doped diamond tips have a higher lifetime.

Local I - V characteristics can be measured by approaching the tip on a certain sample position and applying sufficient force. Then, the voltage is ramped within the desired range. Since I - V characteristics can be recorded in air, they complement CV measurements performed in electrolyte solution. Figure 8a shows the I - V curve of a microscope glass slide measured with a conductive doped diamond tip. No currents were detected in this sample since the sample is non-conductive. Contrary to this, a sample of ITO deposited on a microscope glass slide is shown in Figure 8b, the I - V curve shows an almost linear behavior indicating ohmic behavior as expected for conductive samples. M-HCMs are ionically and electronically conductive due to their mixed-valent centers and mobile potassium ions.³⁰ In solid state

measurements, the mobility of counterions depends on the amount of structural water. The transport of electrons is based on hopping and is coupled to the displacement of counterions.^{30,68}

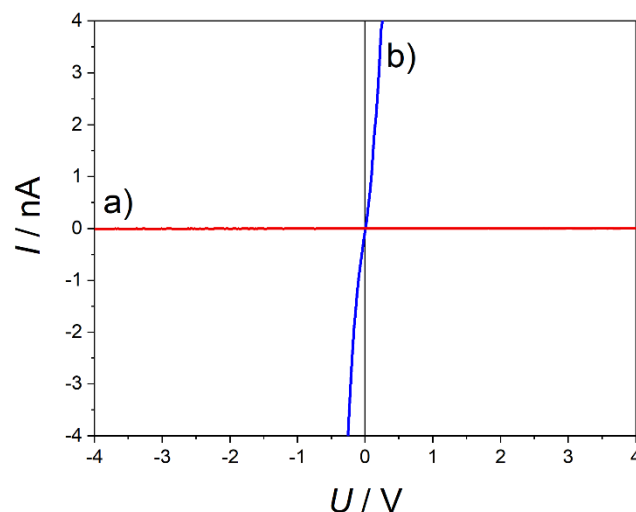


Figure 8. *I-V* characteristics of a) a glass microscope glass slide (non-conductive) and b) ITO substrate (conductive).

The *I-V* characteristic curves of diodes are non-linear and asymmetric and can be divided into three parts: the forward-biased, reversed-biased, and breakdown regions.

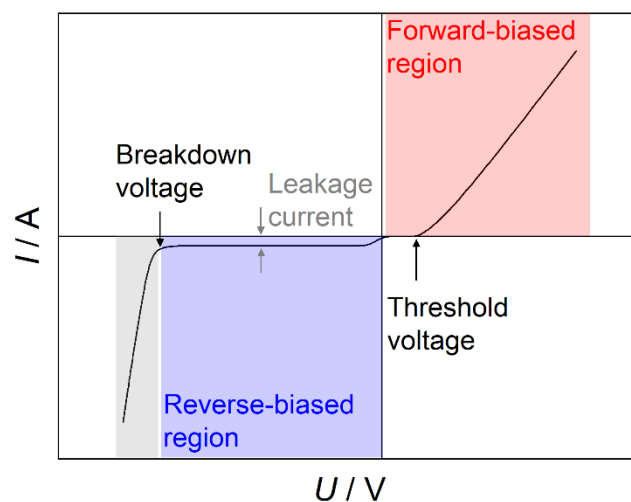


Figure 9. *I-V* characteristic curve of a diode in forward-biased and reverse-biased voltage regions. The image was adapted from ref. 114.

When an AC voltage is applied to a diode, the current flows in the forward-biased region, whereas a threshold voltage needs to be reached for significant conductivity in the reverse-

bias region.¹¹⁴ When the diode is reverse-biased (negative voltage is applied to the anode), the anode is non-conductive in the ideal case. Nevertheless, a small leakage current can be detected in this part of the I - V characteristic curves. At a certain reverse-biased voltage, the diode starts to conduct in the reversed direction; in most cases, the device is destroyed by reaching this point. This region is known for the breakdown voltage.

4.3 Electrochemical Measurements of Metal Hexacyanometallates

Since M-HCMs exhibit rich electrochemistry due to various combinations of transition metal centers in the structure, cyclic voltammetry is a preferred technique to analyze the materials.¹ This is a widely used technique because of its versatility. In cyclic voltammetry, a three-electrode setup is used to apply a triangular voltage $E(t)$ as an input signal, which has two limit values (Figure 10a).¹¹⁵ The scan is carried out by switching the direction of the scan at the maximum (or minimum) value at $t = \lambda$. Applying the potential triggers several electrochemical processes. As an output signal, the current response $I(t)$ is measured (Figure 10b), which is directly influenced by the redox chemistry of the sample. To gain the typical shape of a cyclic voltammogram, the curve is usually plotted as $I = I(E)$, as shown in Figure 10c.

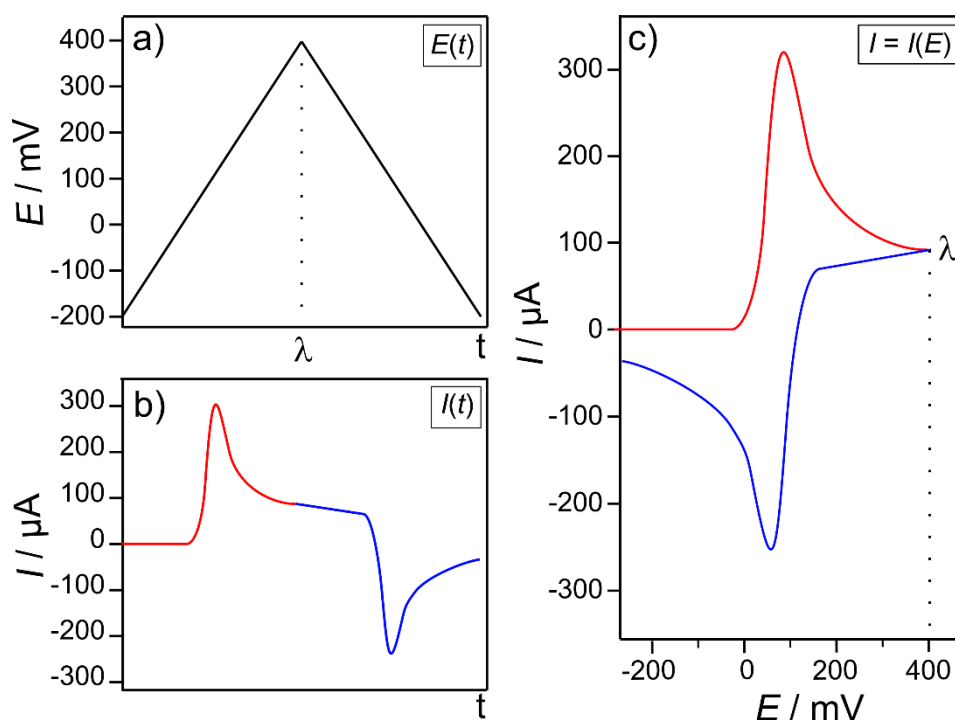


Figure 10. a) Input signal applied potential to the working electrode (triangle potential) $E(t)$; b) output signal, the current response $I(t)$, c) cyclic voltammogram in a typical format where $I = I(E)$. The image was adapted from Ref. 116.

The three-electrode setup consists of a working electrode (WE), a reference electrode (RE) and an auxiliary electrode (Aux). The reaction to be investigated takes place at the WE. The potential of the WE is controlled by the RE, the electric circuit is closed by the Aux. Electrolyte solutions in which the analyte is solved are an important component of cyclic voltammetry to ensure good conductivity.

Cyclic voltammograms of deposited thin films are more complicated than those of dissolved species (Figure 10). Strong or irreversible absorptions of a species a conductive substrate may change the electrochemical behavior of the material.¹¹⁵ The ideal case is a system of a redox-active film O, which undergoes a reversible redox reaction to R without desorption into the electrolyte solution. In this system, the peak current is given by Eq. 6:

$$I_p = \frac{n^2 F^2}{4RT} v A \Gamma_0^* \quad (6)$$

with n as a stoichiometric number of electrons involved in the electrode reaction, F as Faraday constant [C], R as a gas constant [$\text{J mol}^{-1}\text{K}^{-1}$], T as temperature [K], v as scan rate [V s^{-1}], A as area and Γ_0^* as surface excess (Eq. 7), which can be described as the sum of the surface excess Γ_O and Γ_R of the species O and R, respectively:

$$\Gamma_0^* = \Gamma_O + \Gamma_R \quad (7)$$

In contrast to diffusing species, where the current is proportional to $v^{1/2}$, the current for these systems is proportional to v . The charge required for the total reduction of the thin film can be obtained by Eq. 8.

$$Q = nFA\Gamma_0^* \quad (8)$$

Under Langmuir isotherm conditions (no interactions between the adsorbed species on the substrate surface) for a Nernstian Reaction $E_{pa} = E_{pc}$, the total width at half-height at 25 °C is described by Eq. 9:

$$\Delta E_{p,1/2} = 3.53 \frac{RT}{nF} = \frac{90.6}{n} mV \quad (9)$$

The equation can be extended by the Frumkin-Isotherm to describe the behavior of a thin film adsorbed on an electrode. The isotherm also describes the lateral interactions of the adsorbates.

As discussed in Chapter 3.2 M-HCMs can be easily prepared as thin films on working electrodes and undergo redox reactions accompanied by the insertion/ejection of counter cations. Cyclic voltammetric studies of modified working electrodes with M-HCMs are a technique that is often used in literature.^{21,30}

In this study, cyclic voltammetry is used as a technique for investigating the deposited M-HCMs and studying the charge trapping behavior in the layered materials. In addition, the electrochemical control of CV is coupled to in-situ PM IRRAS to study the spectroelectrochemical behavior of the redox-active M-HCM thin films.

4.4 X-ray Photoelectron Spectroscopy

XPS is a widely used method to analyze the elemental composition and chemical environment of constituting elements.¹¹⁷ Analysis of surfaces can provide qualitative and quantitative information on the atoms in the material. Measurements are performed in an ultra-high vacuum (UHV); the sample is irradiated with photons. Consequently, electrons (also referred to as photoelectrons) are emitted from the irradiated atoms due to the complete energy transfer of the photons to core-level electrons. The photoelectrons are emitted from atoms close to the sample surface to the vacuum. They are separated according to their kinetic energy and then detected. From the difference of the kinetic energy (E_{kin}), which depends on

the atom and the chemical environment, and the energy of the X-ray source (h - Planck constant, ν -photon frequency), the binding energy (E_B) can be calculated by Eq. 10. Additionally, the work function ϕ_{spec} of the instrument must be overcome, this constant is related to the difference of the Fermi level of sample and detector. The terms $h\nu$ and ϕ_{spec} are known, the parameter E_{kin} is measured in the XPS experiment.¹¹⁸

$$E_B = h\nu - E_{\text{kin}} - \phi_{\text{spec}} \quad (10)$$

Every electron with a binding energy less than the energy of the X-ray source should be emitted from the sample and measured with the XPS.¹¹⁸

The binding energy of the core-level electrons is specific for the atom and the orbital from which the electron is emitted (except for H and He) and is independent from the X-ray source (even though the kinetic energy will vary as described in Eq. 11).^{117,118}

Small shifts of E_B are also referred to as chemical shifts.¹¹⁷ The chemical shift is connected to the change of the initial state of the atom, this can happen, for example, due to bonds with other atoms. As the formal oxidation state of an atom increases, the E_B of the photoelectrons also increases. The nomenclature of the photoelectron peaks depends on the element and the orbital from which the electrons are emitted. 'C 1s' describes electrons emitted from the 1s orbital from carbon.¹¹⁸

All XPS lines except those of the s orbitals appear as doublets due to spin-orbit coupling.¹¹⁸ The doublet (peak-to-peak) separation trend is $p > d > f$ within a given atom.¹¹⁷ Doublets are notated with the quantum number j as subscript. Table 4 shows the XPS notation depending on the quantum numbers n - principal quantum number, l - angular momentum quantum number, and j - total angular momentum quantum number.¹¹⁷

Table 4. Nomenclature of XPS peaks, with n – principal quantum number, l – angular momentum quantum number, and j – total angular momentum quantum number.¹¹⁷

| n | Quantum numbers | | XPS Notation |
|-----|-----------------|-----|-------------------------|
| | l | j | |
| 1 | 0 | 1/2 | 1s (1s _{1/2}) |
| 2 | 0 | 1/2 | 2s (2s _{1/2}) |
| 2 | 1 | 1/2 | 2p _{1/2} |
| 2 | 1 | 3/2 | 2p _{3/2} |
| 3 | 0 | 1/2 | 3s (3s _{1/2}) |
| 3 | 1 | 1/2 | 3p _{1/2} |
| 3 | 1 | 3/2 | 3p _{3/2} |
| 3 | 2 | 3/2 | 3d _{3/2} |
| 3 | 2 | 5/2 | 3d _{5/2} |

In some cases, splitting of the s photoemission peak into a doublet can also be observed for some transition metal ions. This phenomenon requires unpaired orbitals in the valence shell.¹¹⁷ Mn 3s signal is one example of those elements displaying a doublet. The peak-to-peak separation is a helpful tool to differentiate between oxidation states of Mn.^{119,120} This was demonstrated in cooperation with the working group of Prof. Thomas Bein from the Ludwig-Maximilians-University of Munich in Ref 120. A manganese containing ethyne-anthracene-based MOF-74 was synthesized, and XPS measurements were performed, to determine the oxidation state of Mn.

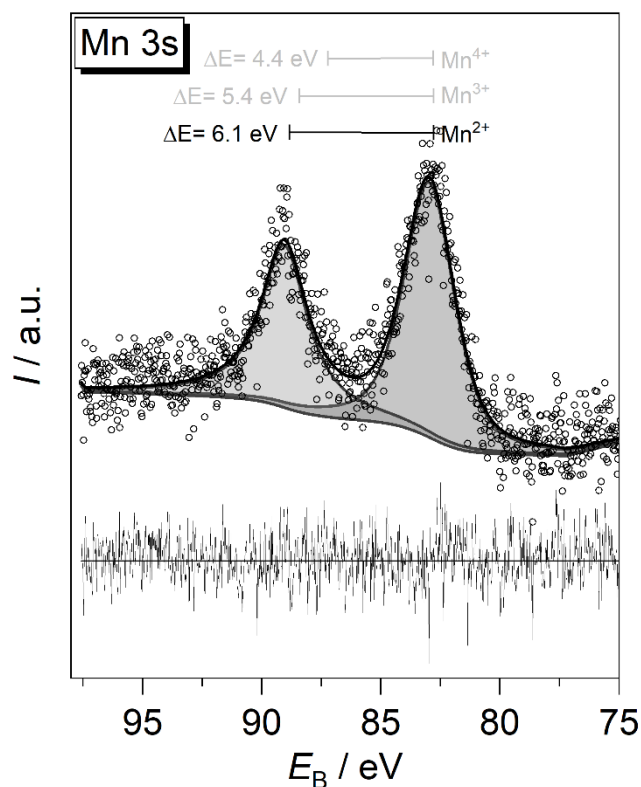


Figure 11. High-resolution Mn 3s XP spectra. Based on the peak-to-peak separation, the oxidation state of Mn can be determined to be Mn^{2+} .^{119,120}

The peak-to-peak separation in Mn 3s spectra allows an assignment of the Mn oxidation states: ~ 6 eV is found in MnO (corresponding to Mn^{2+})¹¹⁹, ~ 5.4 eV is found in MnO(OH) (corresponding to Mn^{3+})¹¹⁹ and ~ 4.4 eV is found in MnO_2 (corresponding to Mn^{4+}).¹¹⁹

Multiplet structures appear due to exchange interactions between the unpaired electron in the core level, where the photoemission takes place, and unpaired electrons in the valence shell. Another contributing factor is the reorganization of valence electrons, which occurs due to an increased effective nuclear charge after the emission of a core electron.^{121–123} The reorganization process can excite ligand-metal charge transfer in transition metal complexes with partially filled d-orbitals. The energy associated with this multi-electron process may influence the kinetic energy of the photoelectron, resulting in a shake-up satellite. Shake-up satellites and multiplet splitting have diagnostic value for geometries and oxidation states of transition metal complexes.¹²³

For example, complex multiplet splitting can be found in the XP spectra of MnO, where high-spin Mn^{2+} is present. As an example, a spectrum is shown from a contribution in cooperation with the working group of Prof. Thomas Bein of the Ludwig-Maximilians-

University of Munich to Ref. 120. The fitting of the spectra was performed in accordance with Biesinger et al.,¹²⁴ who performed multiplet fitting for transition metal oxides and hydroxides.

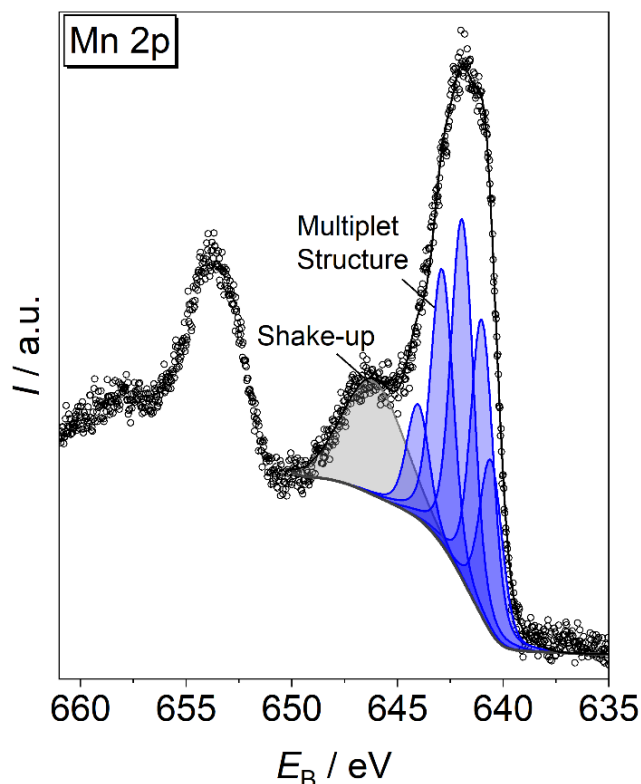


Figure 12. High-resolution Mn 2p XP spectra of Mn^{2+} . The multiplet structure and the shake-up satellite were obtained by the fitting process. Parameters and fitting procedures follow the example of Biesinger et al.¹²⁴

In Figure 12, a Mn 2p doublet is shown. Each doublet component is further subject to multiplet splitting into five spectral compounds. Additionally, a shake-up satellite can be found at ~ 646 eV. Each multiplet compound was fitted with FWHM of 1.26 eV and Lorentzian / Gaussian mix of 26.12 %. These values are close to those reported by Biesinger et al.¹²⁴. Also other transition metals show multiplet splitting. For open-shell ions like high-spin Fe^{2+} , Fe^{3+} and low-spin Fe^{3+} , XPS analysis is complicated by the appearance of multiplet structures and shake-up satellites.¹²³ The fitting of Fe 2p XP-spectra is a non-trivial task which is often the subject of discussion in the literature.^{123,122,125}

Gupta and Sen¹²⁶ have conducted theoretical calculations on multiplet splitting using Hartree-Fock approximation for free ions. The intensity ratios for the multiplets are shown in Figure 13.

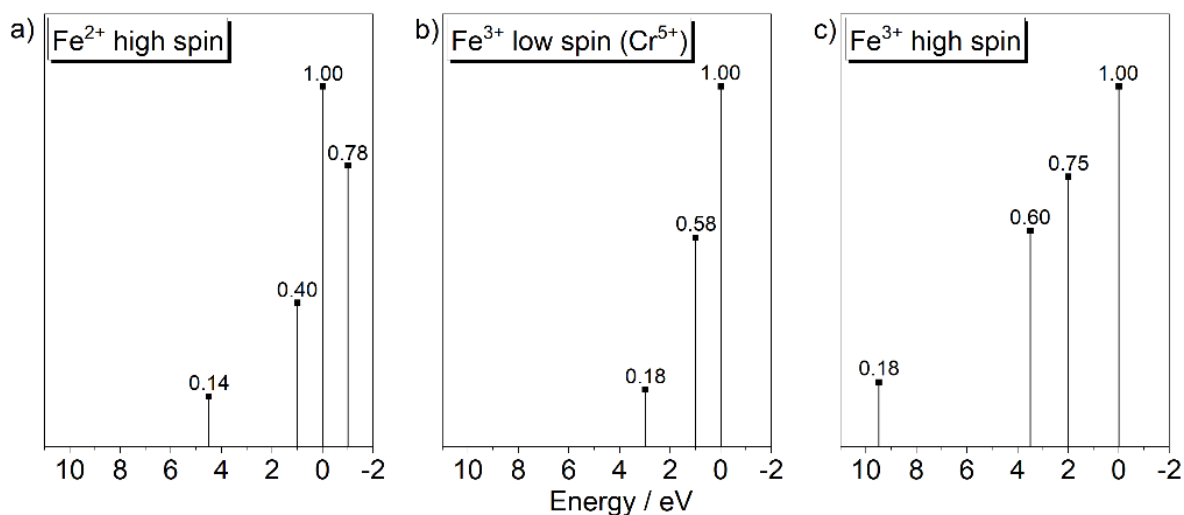


Figure 13. Intensity ratios and approximate separation of a) multiplet peaks of high-spin Fe²⁺, b) low-spin Fe³⁺ (Cr⁵⁺), and c) high-spin Fe³⁺ according to Gupta and Sen.¹²⁶

Since all six d-electrons are spin-paired in low-spin Fe²⁺, no multiplet splitting must be considered.¹²² However, multiplet patterns can be found in XP spectra for low-spin Fe³⁺, high-spin Fe²⁺, and high-spin Fe³⁺. For Fe³⁺ low-spin, the calculation of a free metal ion with the same number of unpaired 3d electrons was carried out by Gupta and Sen,¹²⁶ in this case Cr⁵⁺.

An example of high-spin Fe³⁺ is shown in Figure 14. This spectrum was measured in cooperation with the working group of Prof. Bein from LMU Munich from a metal-organic framework comprised of a hexahydroxy-cata-hexabenzocoronene and Fe³⁺ ions.¹²⁷ The multiplet structure can be determined according to the paper by Gupta and Sen.¹²⁶ Additionally, satellite, surface and pre-peaks were added for a good fit according to Grosvenor et al.¹²²

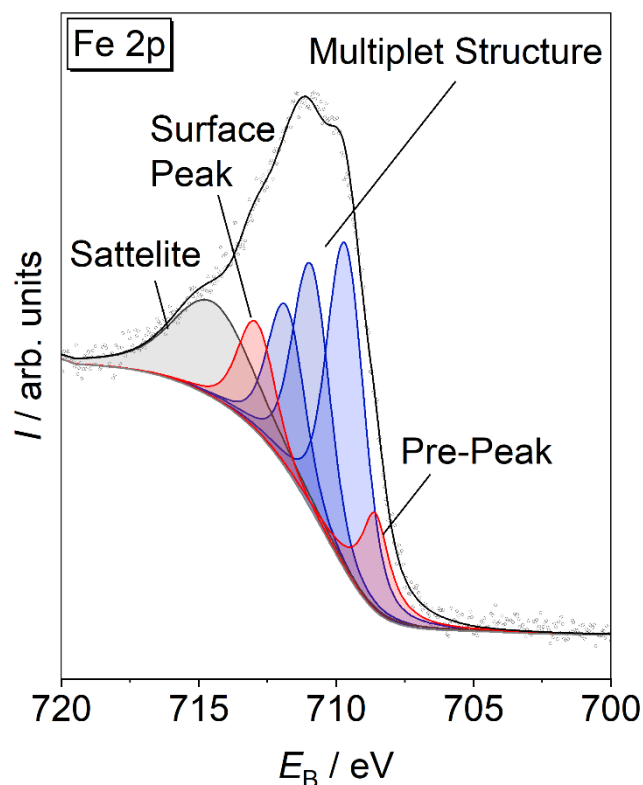


Figure 14. High-resolution Fe 2p XP spectra indicate a high-spin Fe³⁺ multiplet structure with additional satellite, surface, and pre-peak.

Since metal hexacyanometallates and hexacyanometallates consist of transition metal centers and CN⁻ ligands, XP spectroscopy is a helpful tool to determine the oxidation states of the metal centers. Additionally, qualitative analysis of the spectra gives information about the structure of the M-HCMs. Detailed publications report the Fe 2p spectra of M-HCF materials.^{125,123} Also, XPS can be used as a sensor for electron density redistribution related to the π -back donation and the σ -bond formation at the C \equiv N site.¹²⁸ The electron density at the metal center is removed and located at the N end of the ligand. This effect can be observed in XPS since the electron density at an atom reduces the binding energy for its core-level electrons. The highest binding energy for the N 1s signal can be found for KCN, the peak values in the N 1s spectra of K₄[Os(CN)₆] and K₂[Pt(CN)₆] remain below this value because the π -back donation is absent in KCN. For K₄[Os(CN)₆] and K₂[Pt(CN)₆], the lower chemical shift shows the increased electron density at the N atom. The sensitivity of the N 1s spectra was also demonstrated by shifts in the oxidation state of the metal center. As Cano et al.¹²⁹ found, the peak difference of the N 1s peak is 0.2 eV in spectra of K₃[Fe(CN)₆] and K₄[Fe(CN)₆] × 3H₂O. For K₄[Fe(CN)₆] × 3H₂O, the electron density is removed from the metal center and

accumulated at the N-end is higher and therefore found at lower binding energy in the N 1s spectra.

4.5 X-Ray Diffraction of Metal Hexacyanometallates

Materials in which the atoms, molecules or ions occupy fixed positions, forming a periodic arrangement, are crystalline.¹³⁰⁻¹³² X-ray diffraction (XRD) is a non-destructive technique which allows the characterization of crystalline bulk material to determine the atomic and molecular structure.¹³⁰ The interaction between the incident X-ray beam and crystalline material causes the X-rays to diffract in different directions as they interact with multiple planes within the solid. Constructive and destructive interferences cause the intensity to be higher or lower (negligible) than the incident X-rays. Constructive interferences only occur when the Bragg condition is satisfied:

$$2d \sin\theta = n\lambda \quad (11)$$

Where d is the spacing between the crystal planes scattering the X-rays, θ is the angle of incidence, n is an integer describing the order of reflection, and λ is the wavelength of the incident X-rays.

For M-HCMs, powder XRD (PXRD) or grazing incidence XRD (GIXRD) measurements are reported.^{72,133,134,9} The materials show characteristic patterns, which may shift several degrees depending on the transition metal centers since the sizes of the metal atoms influence the lattice. Therefore, diffraction is influenced as well. Behera et al.¹³⁴ reported in Fe-HCF, Fe-HCR, and ruthenium hexacyanoruthenate (Ru-HCR) PXRD. The data revealed a slight Fe-HCR diffraction pattern shift towards lower degrees compared to Fe-HCF. Ru-HCR showed quite broad peaks, which were associated with smaller crystallites of the material compared with those of Fe-HCF and Fe-HCR. As-synthesized Fe-HCR powder was confirmed by XRD by Jain et al.¹³³ The main peaks that were found are summarized in Table 5, the material was indexed as pure face-centered cubic (fcc) lattice.

Table 5. Positions of the XRD pattern and the assignment of the as-synthesized Fe-HCR powder indices.¹³³ The formation of pure fcc is confirmed.

| Position / ° | Identified peaks |
|--------------|--|
| 16.9 | 200 |
| 23.8 | 220 |
| 34.1 | 400 |
| 38.2 | 420 |
| 44.3 | 420 (422, corrected on the basis of ref 134) |

Another report on the powder XRD pattern of Fe-HCR by Behera et al.¹³⁴ also indicates the same positions and indices as reported by Jain et al.¹³³, except for the pattern at $\sim 44.0^\circ$. Behera et al.¹³⁴ assigned this pattern to the 422 indices. From this result, it can be concluded that Jain et al.¹³³ probably inserted a typing error in the evaluation of the reflection pattern. While XRD determines the average positions of atoms within a bulk sample, GIXRD is a technique to study crystallinity as well as the positions of atoms at surfaces or in thin films. Since the substrate under the film can be neglected in GIXRD, this technique is commonly used to study thin films. Measurements of thin Fe-HCR films on ITO substrates revealed similar patterns, the results from Fe-HCR as thin film are shown in Table 6.^{9,72}

Table 6. Positions of the XRD pattern and the assignment of the indices of thin film Fe-HCR samples, both synthesized by electrochemical deposition protocols.^{72,9} The formation of pure fcc is confirmed.

| Position / °, ref 72 | Position / °, ref 9 | Identified peaks |
|----------------------|---------------------|------------------|
| 17.0 | 16.9 | 200 |
| 24.5 | 23.9 | 220 |
| 34.1 | 34.4 | 400 |
| 44.8 | 38.2 | 420 |

As can be seen from the XRD pattern positions shown in Table 6, both groups found similar positions for the pattern caused by X-rays interacting with Fe-HCR material.^{72,9} The Fe-HCR materials were assigned to an fcc phase in both examples. Since the crystallinity of the materials plays an important role in this work, GI-XRD was applied to the modified electrodes.

4.6 Electron Microscopy for the Analysis of M-HCMs

Electron microscopy is one of the most commonly used microscopy techniques besides light and probe microscopy.¹³⁵ As the name suggests, electrons are used as an excitation source. They interact with the sample, and the resulting emissions cause different signals.

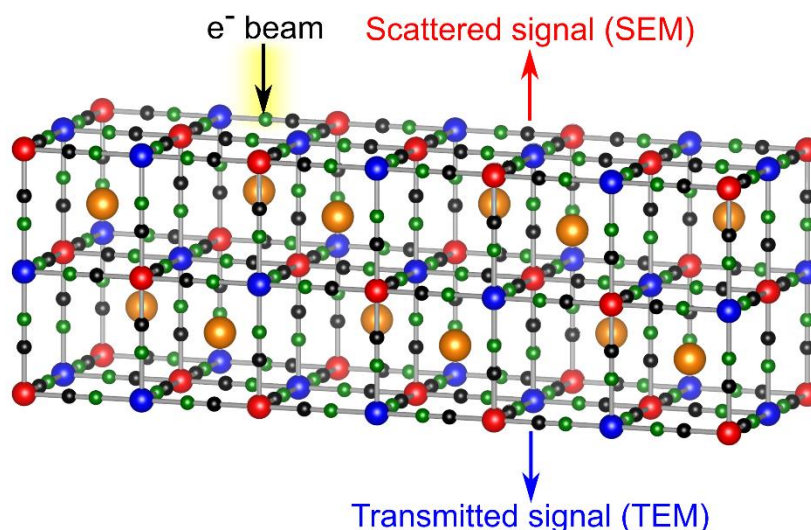


Figure 15. Schematics of electron microscopy. The electron beam interacts with the sample, in SEM, the scattered electrons are processed, whereas in TEM, the transmitted electrons are processed. This figure was adapted from ref 135.

SEM is a technique often used for imaging samples and to gain information about the topography of a sample. The method can be used versatily for materials like alloys, metals, ceramics, porous materials, biological samples, etc. The most important part of the instrument is the electron column. The electron gun can be found on top of the column, which generates the electron beam.^{136,135} At a cathode, electrons are formed by applying a voltage between the cathode and the anode, these electrons are accelerated.¹³⁷ The beam is focused by electromagnetic lenses in the column into a small diameter (ranging within a few nanometers) probe. The gun, column and specimen chamber, where the sample is placed, are kept under a high vacuum due to the generation and advancement of the electron beam. The electrons penetrate the sample by a few microns and interact with the atoms in the material. By this, signals of secondary electrons (topographic contrast) and backscattered electrons (topographic + compositional contrast) are collected and processed to obtain images of the sample.

The limitations of SEM are that the sample must be solid, and the sample sizes are limited. Additionally, conductivity is essential for this technique, non-conductive samples must be coated.¹³⁶ SEM has often been used to study thin films of metal hexacyanometallates.¹³⁸ For electrodeposition studies of Fe-HCF, SEM is a complementing method to study the films' structural evolution, grain size and morphology. As Baggio et al.¹³⁸ demonstrated, SEM images can support XRD measurements. Six different crystalline thin Fe-HCF films deposited at different potentials (0.4 V, 0.3 V, 0.2 V, 0.1 V, 0.0 V, -0.1 V) were analyzed by XRD. XRD indicates that in the range of 0.3 to -0.1 V, the film growth started with a cubic structure, evolved to a pyramidal structure, and returned to a cubic crystal structure. The observations were accompanied by SEM images, showing crystallites of cubic structures and crystallites with pyramidal structures. SEM is also a helpful tool for biosensor development, as demonstrated by Chi et al.¹⁰ Ruthenium purple nanowire arrays (RPNA) were prepared as substrate layers to immobilise glucose oxidase. The presence of nanowire arrays in SEM confirmed the formation of RPNAs. Moreover, a smooth, closely packed and highly uniform appearance was found.¹⁰ According to the images, the density of the wires as nanowire/cm² could be determined.

TEM high-energy electrons are transmitted through nanometer-thick materials.¹³⁹ Information about the material size and shape can be gained. The bright-field TEM mode is commonly used to study the size, shape and dispersity of nanometer-sized material. Here, the images are generated by transmitted electrons. Due to the ability of TEM to image specimens on an atomic level, the crystallinity of materials can also be studied. The dark-field mode can be used to study the crystal structure and defects, this is done by diffracted electrons. Besides determining the size of metal hexacyanometallates nanomaterials by TEM,⁷³ the influence of different preparation protocols on metal hexacyanometallates can be studied. Liu et al.²⁵ studied the impact of HCl in the synthesis of Fe-HCF nanoparticles. Whereas particles in one sample with even contrast were determined as solid cubic structures, transparent centers and sides in the other sample indicate a concave center of the nanoparticles. The shape of the nanoparticles was confirmed by SEM images. Nie et al.¹⁴⁰ used SEM and TEM to study Co₃[Co(CN)₆]₂ nanoparticles. By SEM, the size and form of the nanoparticles were studied, and the SEM images were used to determine the size of the material. Further insights were gained by TEM analysis, where the cube-size structure was also determined. From the contrast of the

nanoparticles in the TEM images, a solid and dense structure of the material was derived. In this work, TEM is primarily used to study the size of synthesized nanoparticles, information gained about the contrast of the material is additionally helpful.

4.7 Polarization Modulation Infrared Reflection Absorption

Spectroscopy

Infrared (IR) spectroscopy is a powerful method for the analysis of different material classes.¹⁴¹ Different sampling methods for IR measurements bring a vast versatility.¹⁴¹ IR measurements can be conducted independently from the surrounding atmosphere, temperature and pressure, which allows the study of solid | solid, solid | liquid, solid | gas and liquid | gas interfaces.¹⁴¹ In-situ IR measurements offer the advantage that the sample can be analyzed while it remains under direct exposure to liquid or gaseous environments.¹⁴¹ By this, electrochemical-related studies can be conducted using an external potentiostat.¹⁴²

PM IRRAS is a highly sensitive method to investigate thin films or molecules absorbed on a reflecting surface. The surfaces used for this technique have to be reflective, e.g., gold, aluminum, or manganese. IR spectroscopy based on reflection enables measurements of absorbed thin films.¹⁴² By this technique, information can be gained about the structure, conformation, orientation and packing of the sample absorbed to the surface.¹⁴² Golden et al.¹⁴³ developed PM IRRAS in the 1980s, based on the work of Greenler¹⁴⁴ in the 1960s, for infrared studies by reflection of absorbed molecules on metal surfaces. The advantage of reflection-based IR techniques depends on the polarization selectivity of the surface absorption.^{142,144} In PM IRRAS, the IR-light is modulated between two orthogonal directions, namely parallel (p-polarized) and perpendicular (s-polarized) light, by a polarization modulator (PEM), which is commonly a ZnSe crystal mechanically deformed by a piezoelectric element by applying alternating voltage. When p-polarized light encounters a thin film-modified metallic electrode at large angles of incident, the reflected beam interacts strongly with the molecules.¹⁴² The interaction results in the absorption of the radiation by the surface species. Greenler found that the interaction of p-polarized light with a metal surface causes constructive interference with the incoming and reflected light at the surface.^{142,144} Contrastingly and under the same

experimental conditions, the s-polarized is not interacting with absorbed molecules and is, therefore, not absorbed by the species on the electrode surface.^{142,144} The beam causes destructive interference and cancels the electric field at the surface.

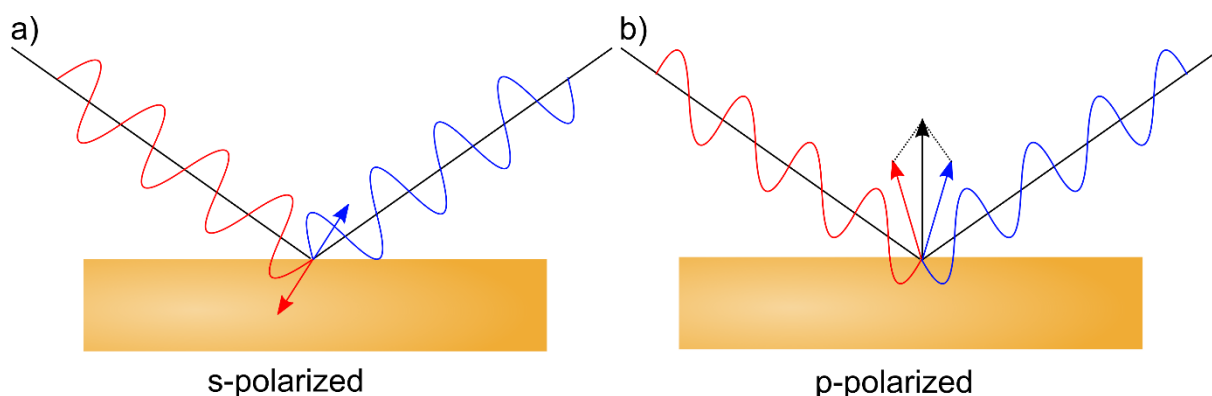


Figure 16. Polarization modulated IR beam at the metal | air interface, a) s-polarized light incident (red) and reflected (blue) waves cause destructive interferences; b) p-polarized light at the metal | air interface, incident and reflected waves overlap and cause constructive interferences. The figure was adapted from Ref. 142.

In PM IRRAS, the p- and s-polarized light is detected by the difference of $|R_s - R_p|$ and the averaged median of both $(R_s + R_p)/2$. The reflection absorption spectrum is obtained as follows:

$$\frac{\Delta R}{\langle R \rangle} = \frac{|R_s - R_p|}{(R_s + R_p)/2} \quad (12)$$

PM IRRAS measurements can be conducted at the air | metal (ex-situ) interface as well as the electrolyte | metal (in-situ) interface. In situ PM IRRAS measurements can be coupled with a three-electrode setup and spectroelectrochemical measurements can be performed.

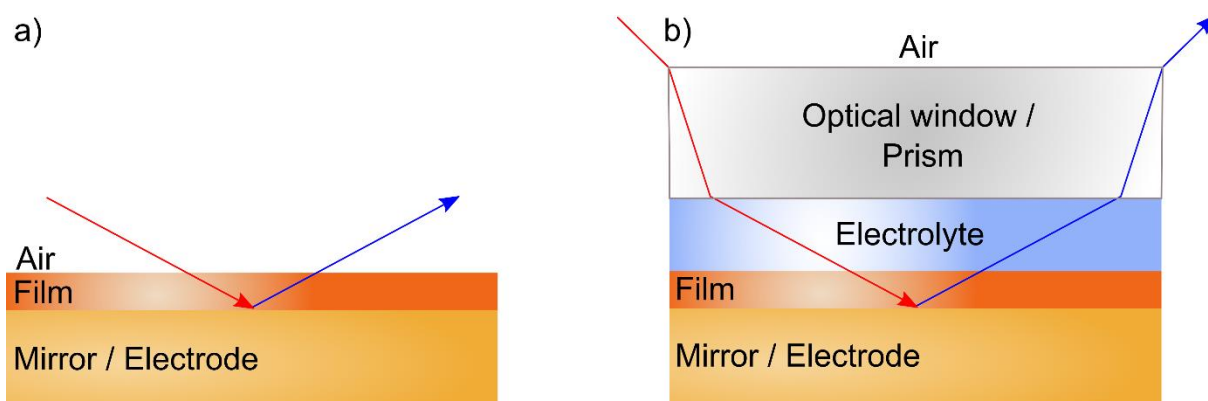


Figure 17. Schematics showing the IR beam at an angle of incidence interacting with a planar film in a) an ex-situ setup and b) an in-situ setup. The figure was adapted from Ref. 142.

The detected signal intensity is proportional to the mean squared electric strength magnitude, which is influenced by the angle of incidence.

For M-HCMs and hexacyanometallates, IR spectroscopy is a widely used technique. With this method, the water content and origin in the samples and the $\nu(\text{CN})$ absorption modes can be studied.¹²⁹ The $\nu(\text{CN})$ absorption mode is the most important IR sensor for the coordination chemistry of M-HCMs. The oxidation of the metal centers involves a frequency shift in the IR spectra. For the low-spin $\text{Fe}^{2+/3+}$ oxidation, a shift of about $+75 \text{ cm}^{-1}$ is reported in the literature.¹²⁹ For the N-coordinated transition metal, namely the high-spin metal center, charge donation from the N-end to the metal center favors strengthening the $\text{C}\equiv\text{N}$ bond. This phenomenon is detected as a higher frequency for the $\nu(\text{CN})$ absorption mode. For the oxidation of $\text{Mn}^{2+/3+}$ at the N-coordinated transition metal center, a shift of $\pm 14 \text{ cm}^{-1}$ was found.¹²⁹ Contrastingly, Erasmus and Gerber¹²⁵ found a peak shift upon oxidation of the N-coordinated metal (in this case Fe) of 35 cm^{-1} . For the oxidation of $\underline{\text{M}}\text{-HCF}$ ($\text{M} = \text{Co}, \text{Ni}, \text{Cu}$), the peak shifts were found to be 33 cm^{-1} , 23 cm^{-1} and 18 cm^{-1} , respectively.

Also, the shift of the $\nu(\text{CN})$ absorption mode correlates with the hydration of the sample. For hydrated samples of M-HCFs the vibration mode is found at $\sim 2066 \text{ cm}^{-1}$, whereas the peak position shifts about -34 cm^{-1} upon dehydration of the sample.¹²⁹ In M-HCR, the peak shift by dehydration is even higher and was found to be 40 cm^{-1} . Since thin films of M-HCMs can be deposited on reflective Au electrodes, PM IRRAS is a well-suited sensitive technique for investigating these samples.

5 Experimental Details

Chapter 5 provides the experimental details are given for the preparation and measurements of the samples studied in this work.

5.1 Chemicals and Materials

All chemicals are listed in Table 7 and were used without further purification. Deionized water (ELGA LabWater, Celle) with a resistance of 18.2 M Ω cm at 296 K was used to prepare aqueous solutions. For the experiment in Figure 42, shown in Chapter 7, deionized water for high-pressure liquid chromatography (HPLC) was used as a reference H₂O-base for the electrolyte solution to exclude impurities of the deionized water purified in the laboratory.

Table 7. Chemicals used in the experiments of this work.

| Product | Formula | Purity / % | Supplier |
|---|--|------------|---|
| Potassium hexacyanoferrate(III) | K ₃ [Fe(CN) ₆] | ≥99 | Alfa Aesar, Massachusetts, USA |
| Potassium hexacyanoruthenate(II) | K ₄ [Ru(CN) ₆] × x H ₂ O | N/A | Sigma - Aldrich, Missouri, USA |
| Nickel(II) chloride hexahydrate | NiCl ₂ × 6 H ₂ O | 99.9 | Sigma - Aldrich |
| Iron(III) chloride hexahydrate | FeCl ₃ × 6 H ₂ O | ≥99 | Sigma - Aldrich |
| Copper chloride | CuCl ₂ | ≥98 | Merck Schuchardt, Hohenbrunn, Germany |
| Potassium chloride | KCl | ≥99.5 | Carl Roth GmbH & Co. KG, Karlsruhe, Germany |
| 4'-mercapto-[1,1'-biphenyl]-4-carbonitril | C ₁₃ H ₉ NS | 97 | Sigma-Aldrich |
| Ethanol | | | Sigma-Aldrich |
| Deuterium oxide | D ₂ O | 99.9 | Deutero GmbH, Kastellaun, Germany |
| Deionized water for HPLC | H ₂ O | | Sigma-Aldrich |

5.2 Preparation of Substrate Surfaces

Microscope glass slides. The microscope glass slides were cleaned with ethanol and deionized water in an ultrasonic bath (Emmi-40HC, EMAG AG, Mörfelden-Walldorf, Germany) for 5 min each and dried under Ar stream. Additionally, the surfaces were cleaned by UV/O₃ for 10 min using the UV TipCleaner (UV.TC.EU.003, Bioforce Nanosciences, Inc., Ames, IA, USA).

Indium Tin Oxide. ITO was cleaned by acetone, ethanol and deionized water in an ultrasonic bath for 5 minutes each. Subsequently, the substrates were dried in an Ar stream.

Polycrystalline Gold Electrode. The polycrystalline gold electrode was polished with 0.05 μm and 0.3 μm alumina slurry (Buehler, IL, USA) and sonicated in water afterwards.

Evaporated Gold Substrate. Au surfaces were prepared onto a cleaned microscope glass surface by depositing 0.5 nm Cr and 150 nm Au using an evaporation chamber (tecta Mini-Coater, Tecta GmbH, Frankfurt am Main, Germany). An integrated quartz crystal balance (EM-Tec 6 MHz, gold electrode quartz crystals for thickness monitor, Micro to Nano, Haarlem, Netherlands) allows to measure the thickness of the deposited gold layers. The Au substrates were cleaned with acetone, ethanol and deionized water and dried in an Ar stream. Afterwards, the surfaces were cleaned by UV/O₃ using the UV TipCleaner for 10 min.

SAMs of 4′mercaptobiphenyl-carbonitrile (MBC). An Au substrate was immersed in a solution of ethanol and 10 mM MBC under Ar atmosphere in the dark for 24 h. Afterwards, the SAM|Au|glass substrate was rinsed with ethanol and dried in an Ar stream.

5.3 Electrodeposition of Metal Hexacyanometallates

The electrochemical deposition was performed with a CH660A potentiostat (CH Instruments, Austin, TX, USA) in a three-electrode cell setup with (evaporated) Au / ITO electrodes as WE. A Pt foil served as Aux ($A = 3.15 \text{ cm}^2$) and an Ag|AgCl|3 M KCl as RE to which all potentials were referenced to. All solutions were deoxygenated by purging with Ar for 30 min.

Fe-HCR (Figure 18a) and Ni-HCF (18b) were electrochemically deposited by 15 potential cycles with a scan rate of $40 \text{ mV}\cdot\text{s}^{-1}$ between -0.2 V and 0.6 V for Fe-HCR and 0 V and 0.75 V for Ni-HCF. For Fe-HCR, the preparation method from Mortimer and Varley was adjusted.⁷² An aqueous solution of $1 \text{ mM K}_4[\text{Ru}(\text{CN})_6] \times x\text{H}_2\text{O} + 1 \text{ mM FeCl}_3 \times 6 \text{ H}_2\text{O} + 70 \text{ mM KCl}$ was

prepared. For Ni-HCF, the aqueous precursor solution contained 1 mM $\text{NiCl}_2 \times 6 \text{H}_2\text{O}$ + 0.5 mM $\text{K}_3[\text{Fe}(\text{CN})_6]$ + 0.5 M KCl. After electrochemical deposition, the samples were rinsed with deionized water.

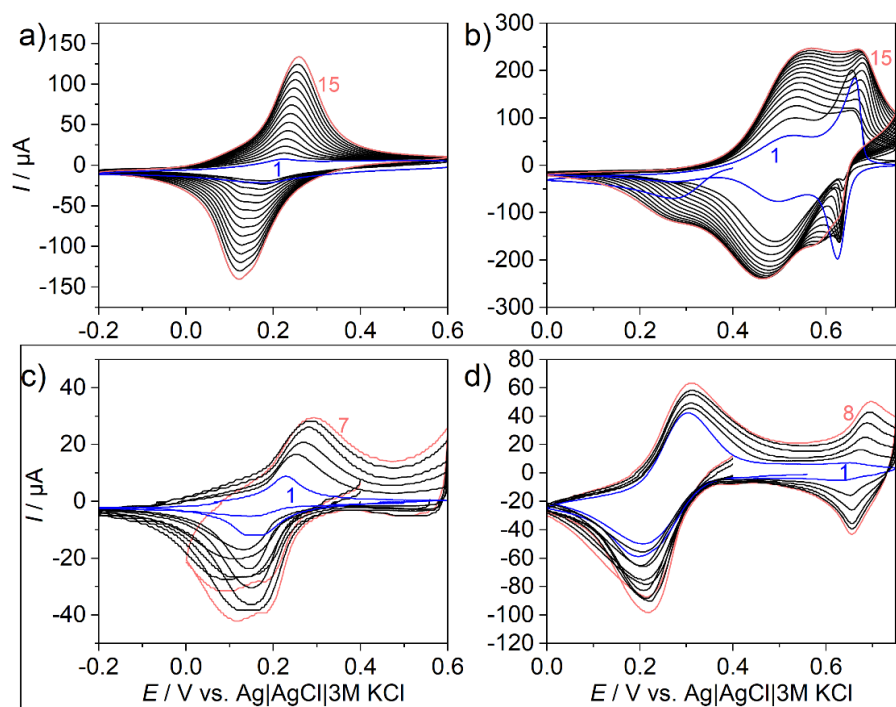


Figure 18. Electrochemical deposition of a) Fe-HCR in an aqueous solution of 1 mM $\text{K}_4[\text{Ru}(\text{CN})_6] \times x\text{H}_2\text{O}$, 1 mM $\text{FeCl}_3 \times 6 \text{H}_2\text{O}$ and 70 mM KCl, b) Ni-HCF in an aqueous solution of 1 mM $\text{NiCl}_2 \times 6 \text{H}_2\text{O}$, 0.5 mM $\text{K}_3[\text{Fe}(\text{CN})_6]$ and 0.5 M KCl and c) and d) the mixed material of Fe-HCR and Ni-HCF by alternatingly depositing the material in aqueous solutions of 1 mM $\text{K}_4[\text{Ru}(\text{CN})_6] \times x\text{H}_2\text{O}$ + 1 mM $\text{FeCl}_3 \times 6 \text{H}_2\text{O}$ + 70 mM KCl (c) and 1 mM $\text{NiCl}_2 \times 6 \text{H}_2\text{O}$ + 0.5 mM $\text{K}_3[\text{Fe}(\text{CN})_6]$ + 0.5 M KCl (d). $v = 40 \text{ mV} \cdot \text{s}^{-1}$.

The mixed material containing Fe-HCR and Ni-HCF was obtained by alternatingly electrodepositioning the material over one cycle in the respective potential window as well as precursor solution as for the pure materials (for Fe-HCR 1 mM $\text{K}_4[\text{Ru}(\text{CN})_6] \times x\text{H}_2\text{O}$ + 1 mM $\text{FeCl}_3 \times 6 \text{H}_2\text{O}$ + 70 mM KCl; for Ni-HCF 1 mM $\text{NiCl}_2 \times 6 \text{H}_2\text{O}$ + 0.5 mM $\text{K}_3[\text{Fe}(\text{CN})_6]$ + 0.5 M KCl) for 8 times each (Figure 18c and d).

For samples referred to in Chapter 7 the electrochemical deposition of Fe-HCR was performed in H_2O - or D_2O -based electrolyte solutions and Fe-HCR 1 mM $\text{K}_4[\text{Ru}(\text{CN})_6] \times x\text{H}_2\text{O}$ + 1 mM $\text{FeCl}_3 \times 6 \text{H}_2\text{O}$ + 70 mM KCl. For subsequent spectroscopic measurements, three different samples were studied, which showed significant differences from each other in cyclic voltammetry. The codes given to these samples depend on the preparation method and treatment afterwards (CV in 1 M KCl in the respective electrolyte), which are listed in Table 8.

Table 8. Sample codes for the Fe-HCR samples discussed in Chapter 7, with a short description of the procedure.

| Sample code | Electrolyte used for | |
|-------------|----------------------|-----------------------------------|
| | Electrodeposition | Treatment after electrodeposition |
| Fe-HCR-H | H ₂ O | H ₂ O |
| Fe-HCR-H-D | H ₂ O | D ₂ O |
| Fe-HCR-D | D ₂ O | D ₂ O |

Electrodeposition of Fe-HCF was performed on a cleaned Au electrode in a solution of 0.002 M FeCl₃ + 0.002 M K₃[Fe(CN)₆] + 0.1 M KCl + 0.1 M HCl in a potential window of 0.4 to 0.75 V at $v = 40 \text{ mV s}^{-1}$.

Electrodeposition of Zn-HCF was performed on a cleaned ITO electrode in a solution of 0.1 M ZnCl₂ + 0.05 M K₃[Fe(CN)₆] + 0.5 M KCl + 0.1 M HCl in a potential window of 0 to 1.2 V at $v = 50 \text{ mV s}^{-1}$.

5.4 Ni-HCF Nanoparticle Synthesis

Ni-HCF nanoparticles were synthesized according to the procedure of Li et al.²⁴ Briefly, 100 mL aqueous solution of 80 mM NiCl₂ and an equal volume of 73.5 mM K₃[Fe(CN)₆] were mixed by simultaneously dropwise addition (10 mL h⁻¹ of each solution) to 200 mL of deionized water. After complete addition, the solution was stirred for 18 h. The nanoparticles were centrifuged four times for 15 min at 4200 rpm (Megafuge 16, Thermo Scientific, USA) and stored in an aqueous solution in a fridge at 4 °C for further use.

5.5 Fe-HCR Bulk Material Synthesis for PIGE Measurements

Fe-HCR microcrystals were obtained by drop-wise addition of equal volumes of 0.25 M FeCl₃ and 0.2 M K₄[Ru(CN)₆] × *x*H₂O into deionized water under constant stirring over 1 h at 60°C under Ar atmosphere. Afterwards, the precipitate and mother liquid were separated by centrifugation, washed several times with distilled water and dried under Ar at 60°C. The paraffin-impregnated graphite electrode (PIGE) was prepared according to Scholz et al.¹⁴⁵ Finely distributed Fe-HCR was obtained by using an agate mortar and added onto filter paper.

The PIGE was gently rubbed on the material to collect the Fe-HCR powder. Afterwards, the electrode was transferred as a working electrode into a voltammetric cell setup as described in Chapter 5.8.

5.6 Layer-by-layer Deposition of M-HCMs

Layer-by-layer deposition was performed using a computer-controlled in-house made dipping robot; details of the robot are given in Section 5.7. The substrates were mounted to a clip at the dipping robot, which provided a vertical alignment of the substrate.

For the deposition of nickel hexacyanoferrate, an aqueous solution of 20 mM $\text{NiCl}_2 \times x\text{H}_2\text{O}$ and an aqueous solution of 20 mM $\text{K}_4[\text{Fe}(\text{CN})_6]$ were kept in separate compartments. The modified substrate was dipped in each solution for 20 min, the sample was rinsed with distilled water in a third compartment to remove non-adsorbed species. The term cycle refers to the substrate dipped into $\text{NiCl}_2 \times x\text{H}_2\text{O}$ for 20 min + rinsing + $\text{K}_4[\text{Fe}(\text{CN})_6]$ for 20 min + rinsing. The deposition cycles depended on the desired thickness of the Ni-HCF thin film. The cycles for the samples were adjusted depending on the experiment: 30 cycles in Figure 29c, 18 cycles in Figure 24b, Figure 27c and d, Figure 28b, Figure 26d, 14 cycles in Figure 23b left, 2 cycles in Figure 23b right and 4 cycles in Figure 29d.

For the LbL deposition of copper hexacyanoferrate (Cu-HCF), an aqueous 20 mM CuCl_2 and aqueous 20 mM $\text{K}_3[\text{Fe}(\text{CN})_6]$ were kept in separate compartments. The samples were exposed to each solution for 20 min, followed by 30 s rinsing with water. In total, 18 cycles were performed.

LbL deposition of Zn-HCF was conducted using 20 mM ZnCl_2 and 20 mM $\text{K}_3[\text{Fe}(\text{CN})_6]$ for 10 cycles from an aqueous solution. The samples were rinsed with water for 30 s in between the immersion.

5.7 Dipping Robot for Layer-by-Layer Deposition

LBL deposition was performed using a homemade dipping robot.¹⁴⁶ The setup was assembled as an important side project for this thesis. The details were published as technical note:

Harms, L.; Roth, N.; Wittstock, G. A New Programmable Dipping Robot. *Electrochem. Sci. Adv.* **2022**. <https://doi.org/10.1002/elsa.202100177>.

This specialized robot facilitates LbL preparations by automatically executing essential chemical preparation processes. It can be easily integrated into the workflow of a scientific laboratory. Moreover, the dipping robot stands out due to its versatility and cost-efficiency compared to existing commercial models.

The objectives of the publication were collaboratively established by L. Gerhards and G. Wittstock. L. Gerhards determined the requirements of the dipping robot and was responsible for initiating the dipping robot within the laboratory and optimizing the system components. N. Roth provided technical expertise, aiding in the successful realization of the project. L. Gerhards wrote the initial draft of the manuscript, and corrections and modifications were made in collaboration with G. Wittstock.

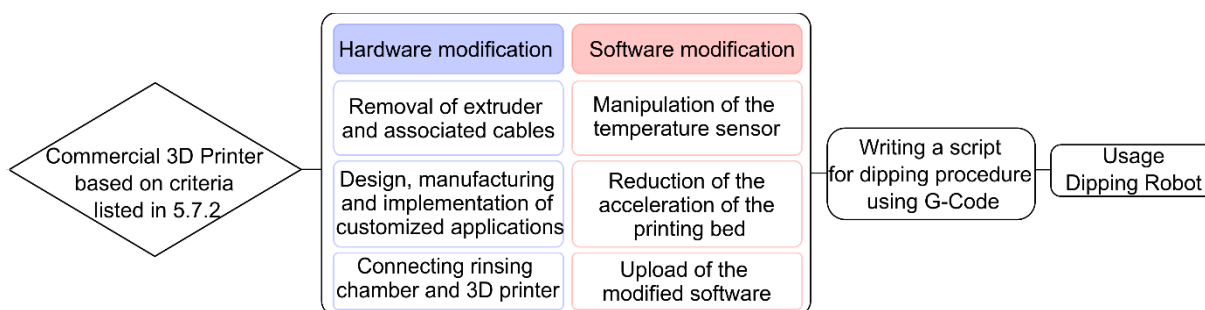


Figure 19. Flow chart of steps to transform a commercial 3D printer into a dipping robot.

5.7.1 Dipping Robot

By processing the protocol, a reliable and versatile dipping robot can be built by modifying a conventional 3D printer.

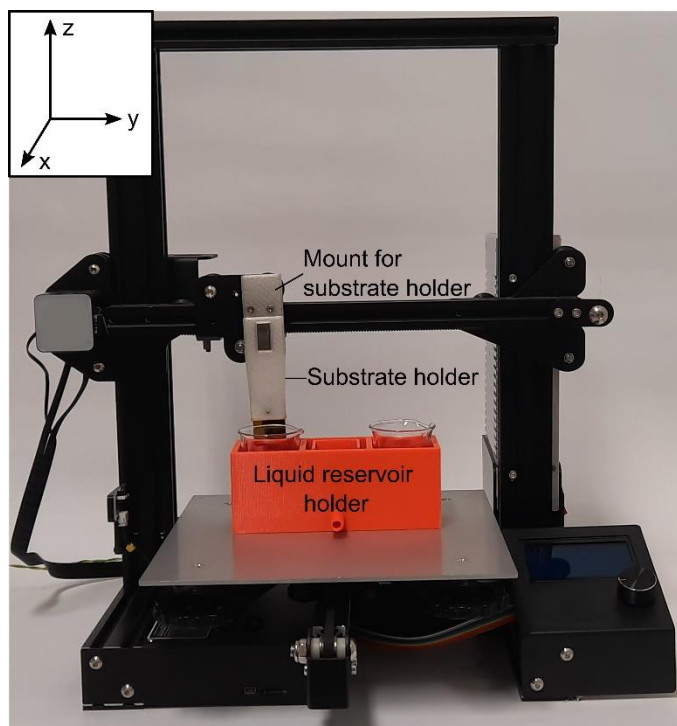


Figure 20. The modified 3D printer for dipping procedures.

The dipping routine can be modified and executed simpler than standard 3D printing procedures by operating in x -, y - and z - directions. Three solution reservoirs were placed in the same line along the x -coordinate. Thus, no positioning in the x -direction is required. The printing bed has space for more sets of liquid reservoirs that could be arranged in the x -direction to allow simultaneous preparation of more samples or more complex procedures. Furthermore, the setup can be extended by using an additional output line for controlling a heater for a solution, an ultraviolet light source for polymerization reactions or a magnetic stirrer.

5.7.2 Hardware Modification

A commercial 3D printer was used to execute the movements of the sample in three dimensions. A 3D printer consists of a horizontal arm with an attachment plate (normally used for the extruder) that can perform movements in the y -direction. The horizontal arm can also be moved in the z -direction, allowing height-positioning. Additionally, the printing bed, a platform at the bottom of the 3D printer, allows positioning in the x -direction.

A suitable 3D printer for dipping robot procedures needs to fulfill the following criteria:

1. It must allow movements in the y and z directions. The movement in the x direction is embedded into commercially available 3D printers, but it is only necessary for more complex procedures.
2. There is a need for a heated printing bed.
3. The main board of the 3D printer must be compatible with a small single-board computer.
4. The software of the 3D printer must be open source and thus editable.
5. The main board of the 3D printer must provide the physical possibility to upload a modified firmware. This can be an ISP port on the mainboard of the printer.
6. Operation of G-code instructions is a requirement.

Many commercially available 3D printers from different suppliers fulfill these conditions. The desired product can be chosen freely.

The sample holder, the reservoir holder, and the rinsing chamber were 3D printed in-house. For layer-by-layer deposition, the extruder is not needed. Therefore, it was removed from the setup as well as the cables for heating the filament and other components not required for the LbL process. Instead, the attachment plate on the horizontal arm was used to mount the in-house-made sample holder using neodymium magnets. This allows fast attachment/detachment of the sample holder to exchange samples between different preparation units. Direct contact of the Nd magnets would be too strong for convenient handling; therefore, a 3D-printed layer is needed between the magnets. A similar technique is used to connect the reservoir holder and the printing bed. The magnets are embedded into the 3D printed parts, and additionally, magnets are placed underneath the printing bed at the desired horizontal position. In this case, two magnets were used to enhance the force on each side. The reservoir holder was a helpful tool in the dipping procedure. Two glass beakers with precursor solution can be placed inside the holder. It also allows precise positioning of the beaker on the printing bed for sample preparations over several days. The defined geometric arrangement is necessary during position calibration of the 3D printer (homing, *vide infra*). The rinsing chamber may consist of a third beaker filled with deionized water for short dipping cycles. For more prolonged procedures, an in-house-made rinsing chamber can be included. The design of the rinsing chamber enables a laminar flow of the rinsing liquid parallel to the surface of the modified substrate from the inlet to the outlet. In the case of the

samples used in this work, the liquid was deionized water. Therefore, stability against organic solvents is not required in this thesis. Due to this, polyethylene terephthalate, modified with glycol, was used as printing material. Studies of Thermo Fisher Scientific show that this material is also compatible with diluted or weak acids and a range of organic solvents as rinsing liquid.¹⁴⁷ The freshwater enters the rinsing chamber at the bottom and leaves the chamber by flowing down one sidewall. The sidewall is designed to be lower than the other sidewalls to provide an outlet for the liquid reservoir.

Since the heating bed of the original 3D printer is not needed for the dipping procedure, its power supply is utilized to control a relay that switches on and off a pump, which supplies fresh water for the rinsing reservoir. This can be done directly on the circuit board of the 3D-printer.

To switch on the pump, the G-code must instruct the controller in the same way as to heat the temperature of the original printing bed to 100 °C. The voltage is supplied until the heating bed reaches the target temperature, which is measured by a temperature sensor. This sensor was removed from the setup, and the software was modified to emulate the temperature sensor to record a constant temperature of 25°C. The pump can be switched off by setting the target temperature of the heating bed to 0 °C. Details on the modified software can be found in Chapter 9.1.

5.8 Instrumentation for Preparation and Characterization of M-HCMs

Electrochemical measurements of whole M-HCM thin films. CVs were recorded using a CH660A potentiostat in a three-electrode setup assembled of M-HCM film (or microcrystals) on the WE, a Pt sheet as CE and an Ag|AgCl|3M KCl RE. The electrolyte solution of 1 M KCl was purged 30 min in advance.

Electrochemical measurements of M-HCM thin films on specified areas. Localized electrochemical measurements of M-HCM thin films were performed using a droplet cell. This cell configuration is schematically shown in Figure 21. For this purpose, an Ag wire (as RE) ($\varnothing = 0.25$ mm) and a Pt wire (as CE) ($\varnothing = 0.25$ mm) were inserted into a glass pipette. The RE was prepared by chloridizing an Ag-wire in aqueous solution of 3 M KCl and 0.1 M HCl.

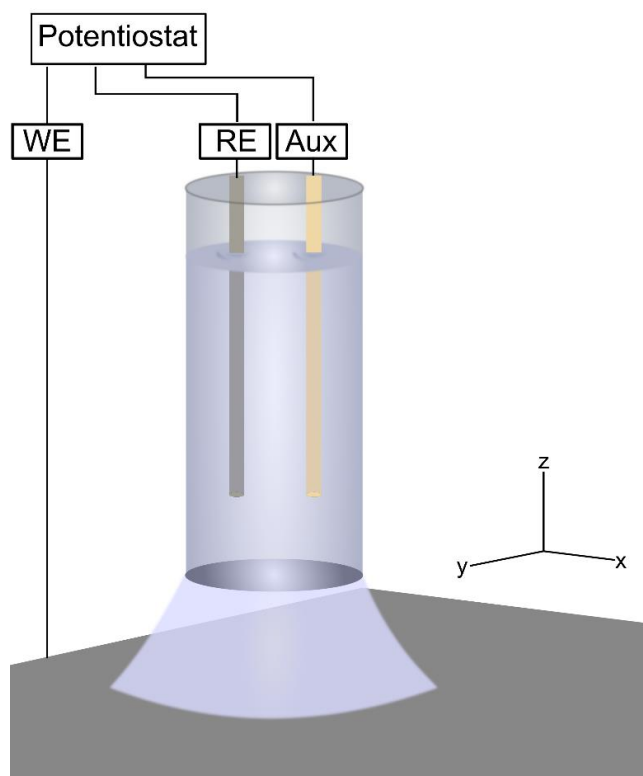


Figure 21. Schematic illustration of the droplet cell setup (three-electrode configuration). Including the WE, RE and Aux.

For this purpose, the electrolyte solution was purged with Ar for 30 min. Then, 2 V were applied to the Ag wire for 600 s in a two-electrode setup in 3 M KCl solution. The electrode on which the M-HCM material was deposited was connected to the potentiostat by a crocodile clip (Farnell, U.K.) orthogonal to the droplet cell. For electrochemical measurements, 1 M KCl solution was raised in the pipette. Subsequently, the pipette was approached to the sample surface to form a meniscus of electrolyte solution between the sample surface and the pipette.

Scanning force microscopy. SFM (Nanoscope IIIA controller with a Dimension 3100 stage, Nanoscope Software V5.3r3s3, Veeco Instruments Inc., CA, USA) was carried out with NCHV-A cantilevers (42 N m^{-1} , $f_0 = 320 \text{ kHz}$, Bruker, CA, USA) in tapping mode. The images were taken with 512×512 pixels resolution and a scan rate of 0.2 – 3.5 Hz. C-SFM mode was performed to measurements I - V characteristic curves in the air. For this purpose, conductive tips of doped diamond (CDT-FMR, Nano and more, Wetzlar, Germany) were used. Before measurement, the tip was approached to the sample and left there for 1 - 2.5 h. This step allowed the setup to equilibrate. Additionally, the sample was electrically connected to the SFM stage with conductive carbon tape (Plano GmbH, Wetzlar, Germany). For each sample,

several *I-V* curves were recorded, details are given in Table 9. The individual *I-V* curves were averaged. The averaged curve is displayed as bold solid lines in the respective plots for the samples in Figure 34 and 38. The measurement current showed an offset, quantified by taking the current reading when the tips were placed on a non-conductive microscope glass slide and subtracting this current from all measurements.

Table 9. Number of replicate *I-V* curves recorded for each sample shown in Figure 34.

| Sample | Number of Measurements |
|--|------------------------|
| Fe-HCF (Figure 34a) | 4 |
| Fe-HCR Ni-HCF nanoparticles (Figure 34b) | 10 |
| Mixed Material (Figure 34c) | 110 |
| Fe-HCR Ni-HCF (Figure 34d) | 100 |

For thickness measurements, scratching was manually performed on the substrate with thin cannulas (33G × 1.6", 0.20 mm × 4 mm, meso-relle®, Gallini S.R.L, Italy) and low forces on the surface, before the SFM measurements were conducted.

For analysis of the images, the software NanoScope Analysis 1.50 (Build R3.119069, Bruker, Billerica, Massachusetts, USA) was used. All samples were processed using the 'Flatten' option. For analysis of the film thickness, the 'Section' tool was used.

X-ray photoelectron spectroscopy. XPS was performed using an ESCALAB 250 Xi instrument (Thermo Fischer, East Grinstead, UK). Monochromatized Al K α radiation ($h\nu = 1486.6$ eV) was focused on a spot size of 500 μm . The pass energy was 200 eV for survey spectra and 10 eV for high-resolution spectra of individual lines. Conductive carbon tape (Plano GmbH, Wetzlar, Germany) was used to connect the sample and the sample holder electronically. All thin film spectra were measured on evaporated gold electrodes since the Sn 3p and In 3p signals of ITO substrates overlap with the Fe 2p signal of the deposited M-HCM materials.

Data was evaluated with the software Advantage 5.932 (Thermo Scientific™, Thermo Fisher Scientific Inc., Waltham, Massachusetts, USA). Since some measurements for internal references were performed with powder samples, the spectra were referenced to remaining adventitious carbon in the high-resolution C 1s spectra at 284.8 eV. The spectra were fitted with a "Smart Shirley background" and a convolution of Lorentzian and Gaussian functions. For

fitting of Fe 2p XP spectra, the calculations by Gupta and Sen were used,^{148,126} and followed the procedure of Sauter et al.¹²³ Additionally, satellite, surface and pre-peaks were added for a good fit according to Grosvenor et al.¹²² More details on the fitting of multiplett splitting of Fe 2p signals are given in Chapter 4.4.

Scanning Electron Microscopy. SEM was performed using a Helios Nanolab 600i system (FEI Company). As a conductive bridge between the sample surface and the sample holder, carbon tape (Plano GmbH, Wetzlar, Germany) was used.

Transmission Electron Microscopy. TEM analysis was conducted using a Zeiss EM 900N (Carl Zeiss AG, Oberkochen, Germany), operating at an acceleration voltage of 80 kV. 8 μ L of nanoparticles suspension was drop-casted on a copper grid with formvar film (300 mesh, Plano GmbH, Wetzlar, Germany). The mean diameter of the nanoparticles was determined by the analysis of 469 particles using the software ImageJ.^{149,150}

Grazing Incidence X-ray Diffraction. GI-XRD analysis was carried out using a PANalytical Empyrean diffractometer (Malvern Panalytical Ltd, Malvern, UK), operated with Cu K α ($\lambda = 1.54 \text{ \AA}$). The angle of incidence depended on the analyzed material. For the measurements in Figure 26, the angles of incidence were set as follows: 2° for ITO, 0.15° for Fe-HCR, 2° for Ni-HCF nanoparticles, 0.5° for the Fe-HCR | Ni-HCF layered material and 0.7° for the mixed material of Fe-HCR and Ni-HCF.

Polarization Modulation Infrared Reflection-Absorption Spectroscopy. PM IRRA spectra were recorded using a Vertex 70 spectrometer with an external reflection unit (Bruker, Ettlingen, Germany) containing a photoelastic modulator with a frequency of 50 kHz and a PMA 50 demodulator (Hinds Instruments, Hillsboro, OR, USA).

For the ex-situ PM IRRA spectra, recorded in a dry state at the gold | air interface, the angle of incidence of the IR light was set to $\phi = 80^\circ$ versus the normal surface. The resolution was 4 cm^{-1} . At each half-wave retardation (1600, 2200 and 3500 cm^{-1}), 400 scans were accumulated.

In situ PM IRRA spectra were recorded using an in-house-built spectroelectrochemical cell with a thin electrolyte layer. A polycrystalline gold electrode served as WE, Ag|AgCl|3 M KCl as RE and an in-house-built Pt ring as Aux. A CaF₂ prism served as an optical window. Before measurement, the prism was washed with water and ethanol and was cleaned in an ozone chamber for 15 min. The spectroelectrochemical cell was filled with H₂O- or D₂O-containing 1 M KCl electrolyte solution. The half-wave retardation was set to 2100 cm^{-1} (for measurements

in Figure 30-33) or 2200 cm^{-1} (for measurements in Figure 57) to monitor the changes in the $\text{C}\equiv\text{N}$ stretching mode. For the measurements at the gold | electrolyte interface, the angle of incidence of the IR light was set to $\phi = 60^\circ$ versus normal surface. The spectra were recorded with a resolution of 4 cm^{-1} , and 200 PM IRRA spectra were recorded and averaged at each potential step.

All PM IRRA spectra were processed using Opus software v5.5 (Bruker, Ettlingen, Germany).

6 Investigations of Layered Metal Hexacyanometallates

This chapter is based on the previously published peer-reviewed paper: **Gerhards, L.**; Wittstock, G. Unidirectional Current in Layered Metal Hexacyanometallate Thin Films: Implications for Alternative Wet-processed Electronic Materials, *ACS Omega* **2023**, *8*, (46), 44139-44147.¹⁵¹

L.G. conducted the experiments, analyzed the results, and wrote the first draft of the manuscript. G.W. analyzed the results and wrote the final vision of the manuscript.

The rectifying properties of alternative electronic materials are presented using layered structures of a crystalline coordination network, whose mixed ionic and electronic conductivity can be adjusted by altering the redox state of the coordinated transition metal ions. These transition metal ions can introduce additional functionalities, such as (redox)catalysis and electrochromism. Experiments are conducted with layered films of Fe-HCR and Ni-HCF to achieve rectifying behavior and charge trapping. The samples in this Chapter were prepared by a combination of different deposition procedures: electrodeposition during voltammetric cycles of both Fe-HCR and Ni-HCF, LbL deposition for Ni-HCF without redox chemistry, and drop casting of pre-synthesized Ni-HCF nanoparticles. The materials are then structurally examined using XRD, XPS, SEM, TEM and SFM. Studies using voltammetry in 1 M KCl and *I-V* curves, recorded via C-SFM, reveal these films' charge trapping and rectifying behavior, attributed to the differing formal potentials of the redox centers of Fe-HCR and Ni-HCF.

6.1 Introduction

The layering of redox-active materials, including M-HCMs, to investigate rectifying / charge trapping behavior described in Chapter 3.1 is challenging since the conditions outlined by Abruña et al.²⁹ must be met. Existing literature shows the influence of the preparation method on the final electrochemical behavior of the material. Long et al.¹⁶ studied films containing $\text{Cu}_x\text{Ni}_y\text{-HCF}$ with varying stoichiometries of Cu and Ni, which were tuned by adjusting the

molar ratio of the reactants. Electrochemical measurements of these materials reveal the redox features of Cu-HCF and Ni-HCF films. The intensities of the respective voltammetric signals depend on the concentration of Cu or Ni transition metal centers in the material. Additionally, it was observed that the cycling stability of the material improves with an increased Ni content.

Karpova et al.¹⁵² investigated a bilayer system containing Fe-HCF and Ni-HCF to enhance the performance of Fe-HCF as an electrocatalyst of H₂O₂ reduction. This system was prepared by electrodeposition of Fe-HCF followed by the subsequent electrodeposition of Ni-HCF directly on the first layer. The catalytic activity of the material remained comparable to that of the pure Fe-HCF film, but the stability showed significant improvement. Notably, the electrochemical responses were unaffected by the preparation method.

Interestingly, the fine-tuning of the synthesis of two-component systems can yield a system exhibiting charge trapping / rectifying behavior. The term 'charge trapping' is used when the outer layer of a layered sample, in contact with an electrolyte solution, retains its redox state even if the supporting electrode reaches a potential where a redox reaction of the outer layer should occur.³⁰ Contrastingly, 'rectifying behavior' refers to solid-state measurements like current-voltage characteristics, where the layered sample is contacted by two metallic conductors in the absence of a liquid electrolyte solution. Both phenomena are based on the same internal processes occurring at the interface between the two layers.

Miecznikowski et al.³⁰ demonstrated a system containing Fe-HCF as the inner layer and Ni-HCF as the outer layer, separated by a matrix of conducting poly(N-methylpyrrole). This matrix prevented direct contact between the outer layer and the electrode, which, as stated by Abruña et al.,²⁹ should be avoided. Additionally, the matrix inhibited the exchange of transition metal ions at the interface. The layered system was prepared using two different approaches: *i*) as a modified electrode in contact with an electrolyte solution and *ii*) as layered thick films composed of pressed powders of Fe-HCF and Ni-HCF, arranged in a two-electrode arrangement without a supporting electrolyte solution. The system exhibited charge trapping behavior in cyclic voltammetry and solid-state rectifying behavior.

Ono et al.³¹ also investigated the same system as ref 30. Their approach involved obtaining the system by spin-coating the outer layer onto the inner layer. Charge trapping was analyzed using cyclic voltammetry.

Miecznikowski et al.³⁰ successfully demonstrated a layered system that exhibited both charge trapping and rectifying behavior. In their work, a polymeric binder was employed to ensure the separation of inner and outer layers.

In this work, the aim was to develop a crystalline system following these rules: *i*) no (polymeric) binders should be used to separate the layers; instead, a careful selection of preparation methods would ensure a suitable interphase, *ii*) both layers should be distinguishable spectroscopically by an element exclusive to one of the two layers. Alongside the promising position of the redox centers, iron hexacyanoruthenate (Fe-HCR) and nickel hexacyanoferrate (Ni-HCF) were chosen as materials. These materials exhibit four completely different transition metal centers. Since the Fe in Fe-HCR is N-coordinated and therefore in a high-spin state, and the Fe in Ni-HCF is C-coordinated and therefore in a low-spin state (Chapter 2.1), also these ions can be distinguished using CV (Chapter 2.3), XPS (Chapter 4.4) or PM IRRAS (Chapter 4.7).

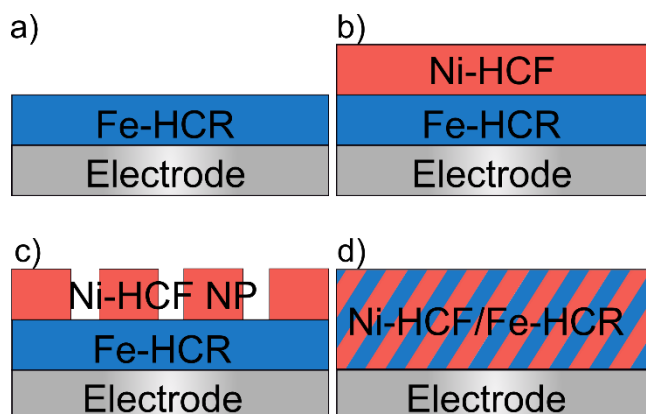


Figure 22. Schematic of the samples investigated in this chapter. a) pure film of Fe-HCR deposited on an electrode, b) layered material of Fe-HCR (inner layer) and Ni-HCF (outer layer), also referred to as Fe-HCR|Ni-HCF, c) Fe-HCR deposited on an electrode, with Ni-HCF nanoparticles (NPs) drop-cast on top of the inner film and d) mixed material of Fe-HCR and Ni-HCF, deposited in an alternating arrangement. The figure was adapted from Ref. 151.

Besides retaining the rules for the layered material of Fe-HCR|Ni-HCF, a reference system should also be prepared, which exhibits both materials but not as stratified layers but with a statistical distribution of the transition metals on the lattice sites.

6.2 Structural characterization of Layered Material and Reference Compounds

The SEM images in Figures 23a and 23b display continuous films of Fe-HCR and the layered material on the ITO surface. The cubic crystal morphology of the Fe-HCR film is discernable in the inset of the zoomed image in Figure 23a. In Figure 23b, the zoomed image reveals a flaky structure, cubes cannot be identified. This difference may be attributed to the layer-by-layer deposition process of Ni-HCF, as the substrate on which the material is deposited can significantly influence its morphology and, consequently, the topography. Figure 23c shows the Fe-HCR film coated with Ni-HCF nanoparticles. In Figure 23d, the mixed material is displayed, where the cubic particles similar to those in the Fe-HCR film (as shown in Figure 23a) can be identified. Notably, the film does not entirely cover the substrate.

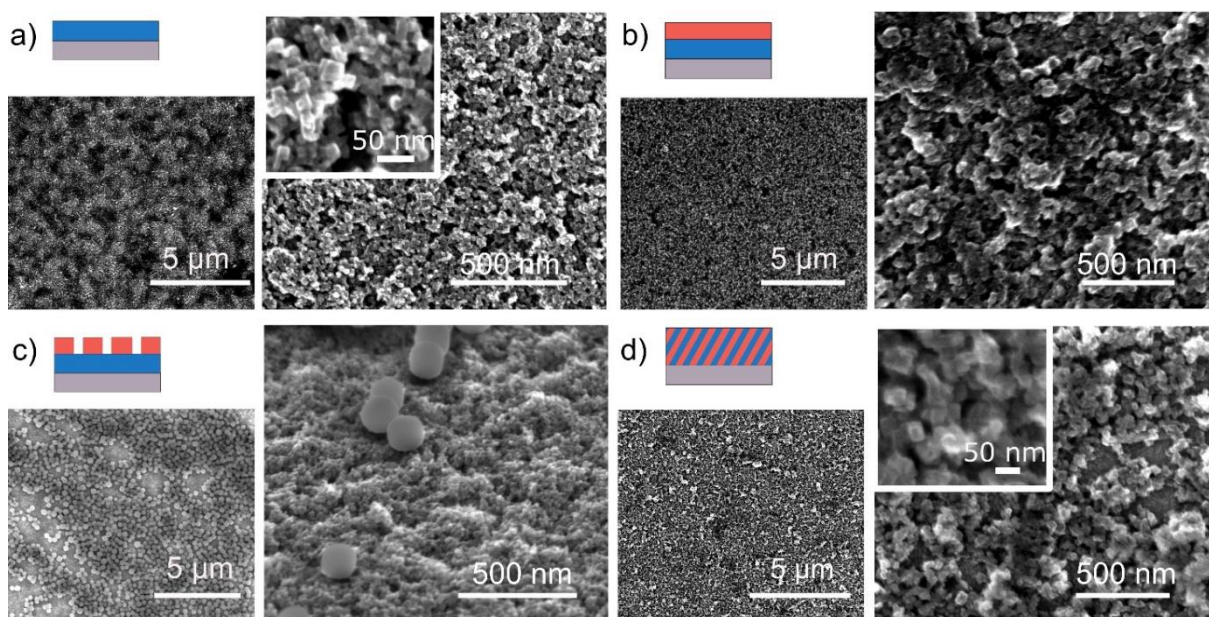


Figure 23. Scanning electron microscopy of M-HCM layers. a) Fe-HCR, b) Fe-HCR|Ni-HCF layered material, c) Fe-HCR|Ni-HCF nanoparticles layered material and d) mixed material from alternating deposition of Fe-HCR and Ni-HCF thin films. The figure was adapted from Ref. 151.

SFM images in Figure 24a indicate that Fe-HCR forms a continuous film composed of small crystals. The image roughness (root mean-square roughness R_q on $10 \mu\text{m} \times 10 \mu\text{m}$) is 32 nm, as shown in Table 10 (details are given in Appendix Figures A1-A3 and Tables A4-A6). The film thickness is approximately 80 nm. Figure 24b displays the layered material consisting of

Fe-HCR as the inner layer and Ni-HCF as the outer layer. Ni-HCF grows into larger crystals than the Fe-HCR film, with a roughness R_q of 21 nm on a $10\ \mu\text{m} \times 10\ \mu\text{m}$ area. The film thickness of the layered sample is 190 nm. By subtracting the thickness of Fe-HCR film from the thickness of the layered material, the approximate thickness of the Ni-HCF layer can be determined as $190\ \text{nm} - 80\ \text{nm} = 110\ \text{nm}$.

Figure 24c presents Ni-HCF nanoparticles on the Fe-HCR film. Analysis of their height, measured as the difference between the z-coordinate on top of the particle vs the z-coordinate on the Fe-HCR film, yields a mean value of 120 nm ($N = 12$).

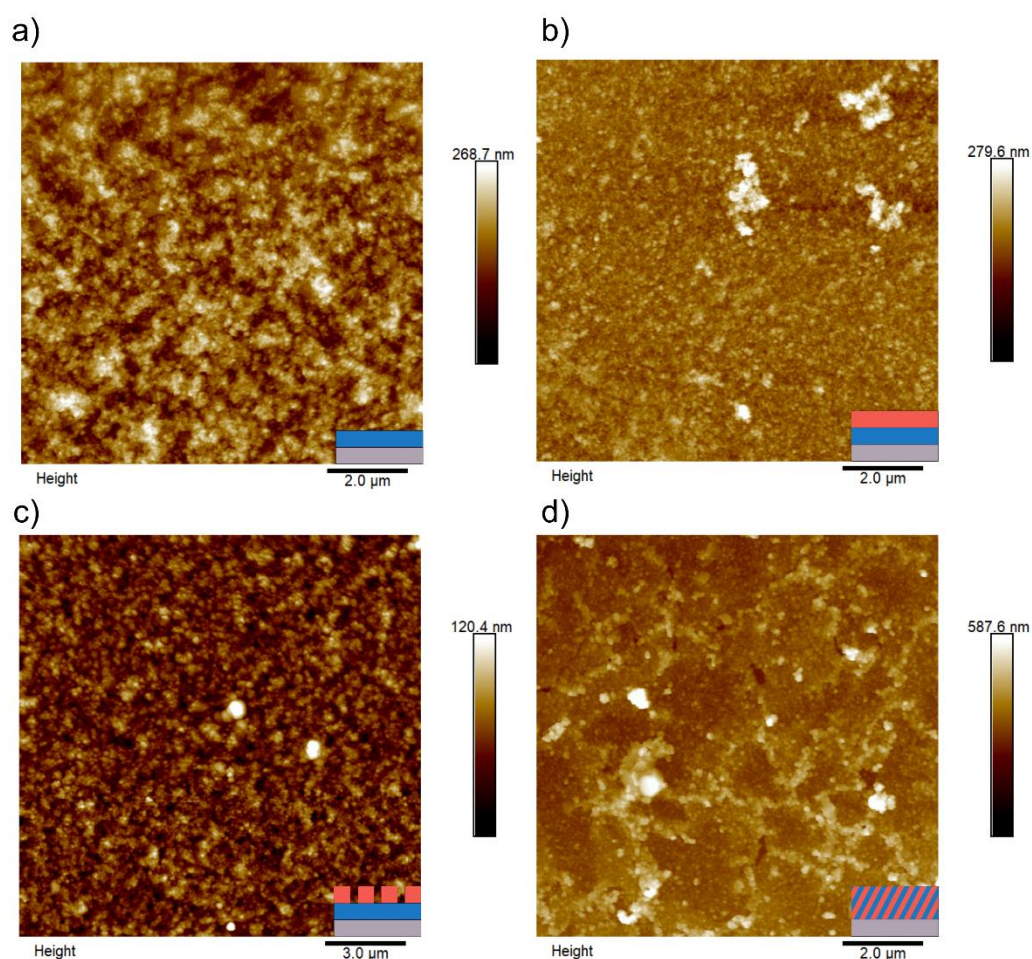


Figure 24. SFM measurements of a) Fe-HCR, $10\ \mu\text{m} \times 10\ \mu\text{m}$; b) layered Fe-HCR|Ni-HCF material, $10\ \mu\text{m} \times 10\ \mu\text{m}$; c) Ni-HCF nanoparticles on Fe-HCR thin film, $15\ \mu\text{m} \times 15\ \mu\text{m}$; d) mixed material of Fe-HCF and Ni-HCF in $10\ \mu\text{m} \times 10\ \mu\text{m}$. The figure was adapted from Ref. 151.

The SFM image of the mixed sample in Figure 24d shows a rougher film than the other samples, with $R_q = 45\ \text{nm}$ over a $10\ \mu\text{m} \times 10\ \mu\text{m}$ area, as shown in Table 10. This increased

roughness may result from the alternating electrochemical deposition, with varying average amounts of Fe-HCR and Ni-HCF deposited in each cycle.

Table 10. Root mean square roughness (R_q) measured by SFM on a $10\ \mu\text{m} \times 10\ \mu\text{m}$ area. The data was taken from Ref. 151.

| Sample | Roughness (R_q)/nm | Film thickness/nm |
|--------------------------------------|------------------------|-------------------|
| Fe-HCR | 32 | 80 |
| Fe-HCR Ni-HCF layered | 21 | 190 |
| Fe-HCR Ni-HCF layered - Ni-HCF layer | - | 110 = 190-80 |
| Mixed material | 45 | 240 |

TEM images of the Ni-HCF nanoparticles and their size distribution are shown in Figure 25. The nanoparticles are cubic, with edge lengths ranging from 170 to 300 nm. These particles, identifiable by their shape, can also be observed after drop-casting on the electrochemically deposited Fe-HCR film by SEM, as shown in Figure 23c. The nanoparticles exhibit uniform contrasts and indicate solid cubic morphology.²⁵

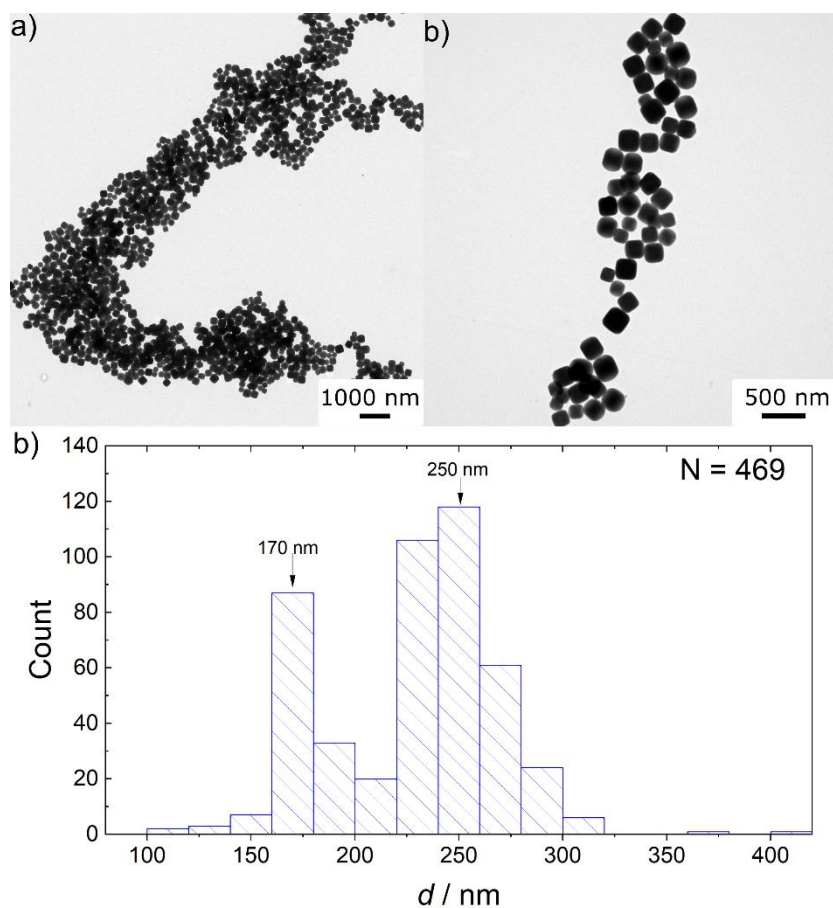


Figure 25. TEM images of Ni-HCF nanoparticles a), b) at different spots of the formvar copper grid, and c) the size analysis of 469 nanoparticles by ImageJ.^{149,150} The figure was adapted from Ref. 151.

Figure 26 shows the XRD patterns of ITO, Fe-HCR, Ni-HCF nanoparticles, the layered material Fe-HCR | Ni-HCF, and the Fe-HCR and Ni-HCF mixed material. Both Fe-HCR and Ni-HCF materials possess a face-centered cubic crystal structure.^{133,153}

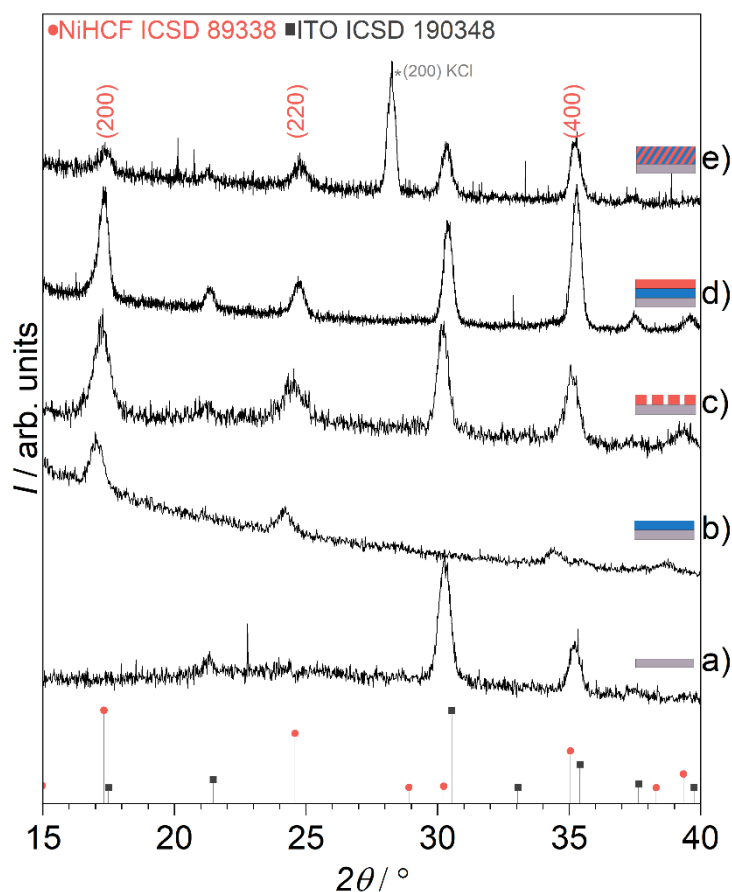


Figure 26. Grazing Incidence X-ray diffraction (GI-XRD) patterns of a) ITO; b) Fe-HCR thin film; c) Ni-HCF nanoparticles; d) layered material of Fe-HCR and Ni-HCF; e) mixed material of Fe-HCR and Ni-HCF. Symbols indicate the position of reflections according to literature (Ni-HCF ICSD 89338 and ITO ICSD 190348). The figure was adapted from Ref. 151.

According to the ICSD 89338 data for Ni-HCF, the main peaks can be assigned to the (200), (220) and (400) reflections of these materials. As already discussed in Chapter 4.5, these reflections can also be found for Fe-HCR thin films, but the patterns are shifted towards lower 2θ in comparison to Ni-HCF due to larger lattice parameters caused by Ru metal centers.^{72,9}

Table 11. Positions of the XRD pattern (200), (220) and (400) for the measurements shown in Figure 26.

| Sample | pattern position / ° (200) | pattern position / ° (220) | pattern position / ° (400) |
|-----------------|-------------------------------|-------------------------------|-------------------------------|
| Fe-HCR | 17.0 | 24.2 | 34.4 |
| Ni-HCF NPs | 17.2 | 24.6 | 35.1 |
| Fe-HCR Ni-HCF | 17.3 | 24.7 | 35.3 |
| Mixed material | 17.4 | 24.7 | 35.2 |

The positions of the pattern agree well with the values reported in the literature for Fe-HCR.^{72,9} It is noteworthy that the ITO patterns overlap with the M-HCM patterns, although the intensities are negligible in the regions of the (200) and (220) crystal planes of the studied M-HCMs. The patterns from Fe-HCR appear at lower angles compared to those of Ni-HCF, which can be attributed to the slightly larger unit cell of Fe-HCR.

6.3 XPS Investigations of Layered Material and Reference

Compounds

The valence states of the transition metal ions in the material were analyzed by XPS, as shown in Figure 27. The Fe 2p_{3/2} signal was fitted with a multiplet, as theoretically calculated by Gupta and Sen¹²⁶ using Hartree-Fock approximation for free ions. This approximation is based on the same number of unpaired 3d electrons as in the emitter atom, corresponding to isolated Fe²⁺ for Fe²⁺ high-spin and isolated Fe³⁺ for Fe³⁺ high-spin and Cr⁵⁺ for Fe³⁺ low-spin. More information is given in Chapter 4.4. Detailed peak positions of the fitted peaks in the Fe 2p_{3/2} spectra are listed in Table 12.

The Fe 2p_{3/2} spectrum of Fe-HCR, as shown in Figure 27a, reveals the presence of high-spin Fe²⁺ with three components at $E_B = 709.5, 710.8, 711.9$ eV with an intensity ratio of 78 : 100 : 40. Additionally, a surface peak and a satellite peak are included (assignment can be found in Table 12).¹²² This assignment aligns with previous findings indicating that the N-coordinated transition metal (i.e., Fe in Fe-HCR, as depicted in Figure 27a) predominantly exists in the high-spin configuration,^{154,66} while the C-coordinated metal ion typically assumes a low-spin configuration as found for Fe²⁺ in Ni-HCF (Figure 27c, 27e, 27g, Table 12). With all six Fe 3d electrons paired, this single Fe 2p_{3/2} component at $E_B = 708.5$ eV is fitted, showing no multiplet splitting.¹²³

In the layered material, there are two distinct iron centers: one in Ni-HCF and the other in the covered film of Fe-HCR (Figure 27c). The spectrum shown in Figure 27c displays only the signal for Fe in Ni-HCF. This can be concluded from the complete absence of the signal for Ru 3d_{5/2} at $E_B = 281.0$ in Figure 27d. This conclusion is consistent with the film thickness of the Ni-HCF layer (approximately 110 nm, as shown in Table 10), which exceeds the information

depth of XPS. The Fe $2p_{3/2}$ signal in Figure 27c features a single component from low-spin Fe^{2+} (also observed in Figure 27e, 27g). The peak at $E_B = 710.2$ eV and its associated multiplet components in Figure 27c are likely attributable to Fe^{3+} species within the material, which may originate from a partial oxidation during the preparation in an extended layer-by-layer procedure.

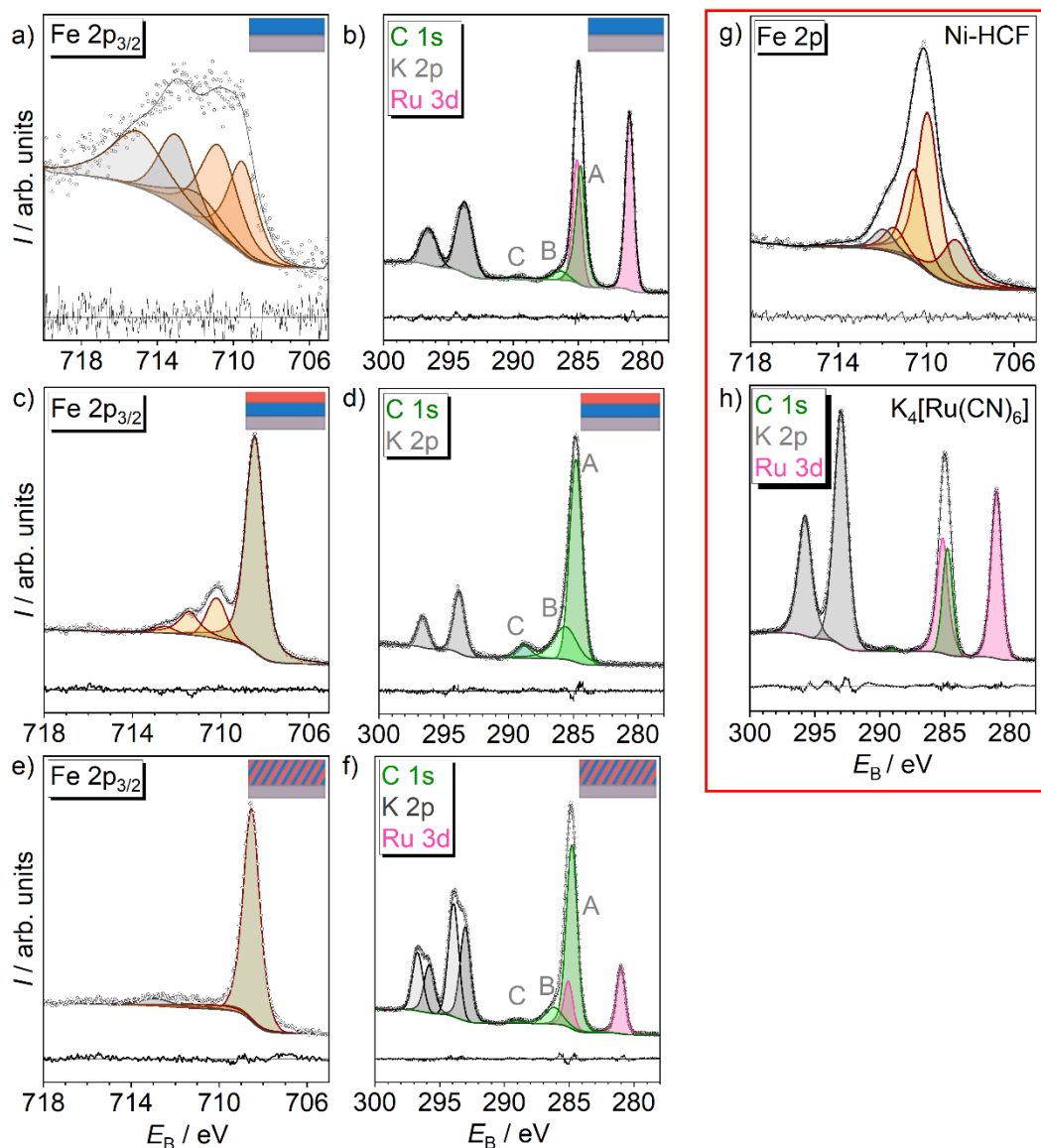


Figure 27. Fitting of the high-resolution Fe $2p_{3/2}$, C 1s, K 2p and Ru 3d XP spectra. a) and b) Fe-HCR; c) and d) layered material; e) and f) mixed material. The reference spectra g) Fe $2p_{3/2}$ XP spectra of Ni-HCF nanoparticles; and h) C 1s, K 2p and Ru 3d XP spectra of $\text{K}_4[\text{Ru}(\text{CN})_6] \times x\text{H}_2\text{O}$ are optically separated by a red box for better clarification. The figure was adapted from Ref. 151.

Due to the low intensity of the high E_B components, it is challenging to distinguish Fe^{3+} and high-spin Fe^{2+} with certainty in this overlaid signal.

The expected valence state of iron in the mixed material is Fe^{2+} , as the electrochemical deposition cycle was stopped after reduction (-0.2 V vs $\text{Ag}|\text{AgCl}|3\text{ M KCl}$). Notably, the expected high-spin Fe^{2+} from Fe-HCF is only visible as a small signal in Figure 27e. There could be several reasons for this. The electrodeposition experiments suggest that the Ni-HCF films grow more rapidly than the Fe-HCF films, as can be derived from Figure 18. This potentially leads to rapid material coverage, resulting in only a few high-spin Fe^{2+} ions being located within the information depth of XPS. Moreover, there may be a transition from high-spin to low-spin configuration in the mixed materials, where the coordination environment is less defined than in a pure material.

Table 12. Peak positions of the fitted peaks of Fe 2p high-resolution XP spectra of Fe HCF, layered material, mixed material and Ni-HCF. The data was taken from Ref. 151.

| Sample | E_B / eV | Assignment | Reference |
|------------------|------------|----------------------------|-----------|
| Fe-HCF | 709.5 | High-spin Fe^{2+} | 126,122 |
| | 710.8 | High-spin Fe^{2+} | 126,122 |
| | 711.9 | High-spin Fe^{2+} | 126,122 |
| | 713.0 | Surface peak | 126,122 |
| | 715.0 | Satellite | 122 |
| Layered Material | 708.5 | low-spin Fe^{2+} | 122,125 |
| | 710.2 | Fe^{3+} species | 126,125 |
| | 711.4 | Fe^{3+} species | 126,125 |
| | 712.6 | Fe^{3+} species | 126,125 |
| Mixed Material | 708.5 | low-spin Fe^{2+} | 122,125 |
| | 709.4 | high-spin Fe^{2+} | 126,122 |
| | 710.4 | high-spin Fe^{2+} | 126,122 |
| | 711.4 | high-spin Fe^{2+} | 126,122 |
| | 712.9 | Satellite / surface peak | 122 |
| Ni-HCF | 708.7 | low-spin Fe^{2+} | 122,125 |
| | 710.0 | low-spin Fe^{3+} | 126,125 |
| | 710.6 | low-spin Fe^{3+} | 126,125 |
| | 711.5 | low-spin Fe^{3+} | 126,125 |
| | 711.9 | Satellite | 125 |

The signal for low-spin Fe^{2+} of the layered material and the mixed material (Figure 27c and 27e, respectively) is also found for a pure Ni-HCF sample (Figure 27g). In addition, the Fe $2p_{3/2}$

spectrum in Figure 27g contains a multiplet indicative of additional low-spin Fe^{3+} in the Ni-HCF sample.

Ru $3d_{5/2}$ signals can be found in Figure 27b at 281.03 eV (Ru $3d_{3/2}$ at 285.10 eV overlapping with C 1s) and in Figure 27f at 281.0 eV (Ru $3d_{3/2}$ at 285.08 eV), the values are also given in Table 13. The Ru $3d_{5/2}$ signal from $\text{K}_4[\text{Ru}(\text{CN})_6] \times x\text{H}_2\text{O}$ powder in Figure 27h is detected at 281.01 eV (Table 13). Within the accuracy of the method, all these binding energies are consistent with each other (Table 13) and with the reported value of 280.9 eV.¹⁵⁵ The Ru 2p signal indicates whether the outer layer in the stratified-layer sample provides complete coverage of the inner layer. The absence of Ru $3d_{5/2}$ at $E_B = 281.0$ eV in Figure 27d suggests that the outer Ni-HCF film is thicker than the information depth of XPS and likely does not contain significant pinholes.

Figures 27b, 27d and 27f also display doublets for K $2p_{3/2}$ and K $2p_{1/2}$ photoemissions, detailed values are given in Table 13. Two distinct doubles are evident for the mixed material in Figure 27f, with K $2p_{3/2}$ binding energies of 293.0 eV and 293.9 eV. While only one doublet is identifiable in Figure 27b and 27d, the slightly broader K $2p_{3/2}$ peak in Figure 27b (with a full width at half maximum (FWHM) of 1.49 eV, compared to 1.05 eV in Figure 27d) might indicate the presence of two different species, whose photoemission peaks are not resolved spectroscopically. The E_B value in Figure 27d is 293.8 eV and matches the high binding energy component in Figure 27f. Typical values reported in the literature are around 293.9 eV.^{23,121} The second K $2p_{3/2}$ signal in Figure 27f likely originates from Fe-HCR. The K $2p_{3/2}$ binding energy for $\text{K}_4[\text{Ru}^{\text{II}}(\text{CN})_6] \times x\text{H}_2\text{O}$ is 293.00 eV, as shown in Figure 27h. Slight variations in the binding energies for the charge balancing K^+ ions could also be attributed to different hydration states of the material, especially in the vicinity of defects. Such defects are potentially more prevalent in mixed materials.

The C 1s spectra in Figures 27b, 27d and 27f feature the signals A, B, and C. The signal C is associated with the $\pi \rightarrow \pi^*$ shake-up process in the cyanide ligand. They are not considered for the analysis of the material because of the difficulty in reliably distinguishing signals originating from CN^- , from those of adventitious carbon contamination, which is present on all samples handled under ambient conditions.

Table 13. Peak positions of the fitted peaks of Ru 3d, K 2p and C 1s high-resolution XP spectra of the Fe HCF, layered material and mixed material samples as well as the $K_4[Ru(CN)_6] \times xH_2O$ as reference sample. For brevity, $K_4[Ru(CN)_6] \times xH_2O$ is shortened as $K_4[Ru(CN)_6]$. The data was taken from Ref. 151.

| Component | Binding Energy / eV | | | | Assignment | Ref. |
|----------------------|---------------------|------------------|----------------|-----------------|-------------------------|--------|
| | Fe HCR | Layered Material | Mixed Material | $K_4[Ru(CN)_6]$ | | |
| Ru 3d _{5/2} | 281.0 | - | 281.0 | 281.0 | Ru ²⁺ | 155 |
| Ru 3d _{3/2} | 285.1 | - | 285.1 | 285.2 | Ru ²⁺ | 155 |
| K 2p _{3/2} | - | - | 293.0 | 293.0 | K ⁺ | 128,23 |
| K 2p _{1/2} | - | - | 295.7 | 295.8 | K ⁺ | 128,23 |
| K 2p _{3/2} | 293.8 | 293.8 | 293.9 | - | K ⁺ | 23 |
| K 2p _{1/2} | 296.5 | 296.6 | 296.7 | - | K ⁺ | 23 |
| C 1s (A) | 284.8 | 284.8 | 284.8 | 284.8 | CN, adv. Carbon | 129 |
| C 1s (B) | 286.4 | 285.6 | 286.2 | - | sp ² | 129 |
| C 1s (C) | 289.7 | 288.8 | 289.0 | 289.1 | $\pi \rightarrow \pi^*$ | 129 |

The component A in the N 1s spectra is the most intensive signal. The binding energies are equal for the three samples within the method's accuracy. The exact values are 397.9 eV (Figure 28a), 397.8 eV (Figure 28b), 397.8 eV (Figure 28c) and 397.8 (Figure 28d). The slight variation is likely due to the different coordination environments of the CN⁻ ligand, e.g., Ru^{II}-CN-Fe^{II}, Fe^{II}-CN-Ni^{III}. The component B occurs at 398.5 eV (Figure 28b) and 398.2 eV (Figure 28c) and is likely caused by N-atoms in Fe^{III}-CN-Ni^{III} coordination in agreement with the Fe 2p spectra in Figure 27. Differences in binding energies result from differences in π -back bonding from the transition metal cation to the CN ligand for different metals and oxidation states.¹²⁹ On the other hand, also the high-resolution spectra of Fe-HCR (Figure 28a) and $K_4[Ru(CN)_6] \times xH_2O$ (Figure 28d) show a third component. This peak was also found for $K_2[Pd(CN)_4]$,¹⁵⁶ KCN¹⁵⁶ and films of $In_4[Fe(CN)_6]_3$.¹⁵⁷ The peak was attributed to decomposition products in the material, whose composition remained unidentified.^{156,157} The assignment of component C is not clear. It could be a shake-up satellite for a $\pi \rightarrow \pi^*$ excitation in the cyanide ligand upon photoemission from N,¹²⁸ or due to oxidized nitrogen species that may be formed at the surface of samples when in contact with air.^{158,159}

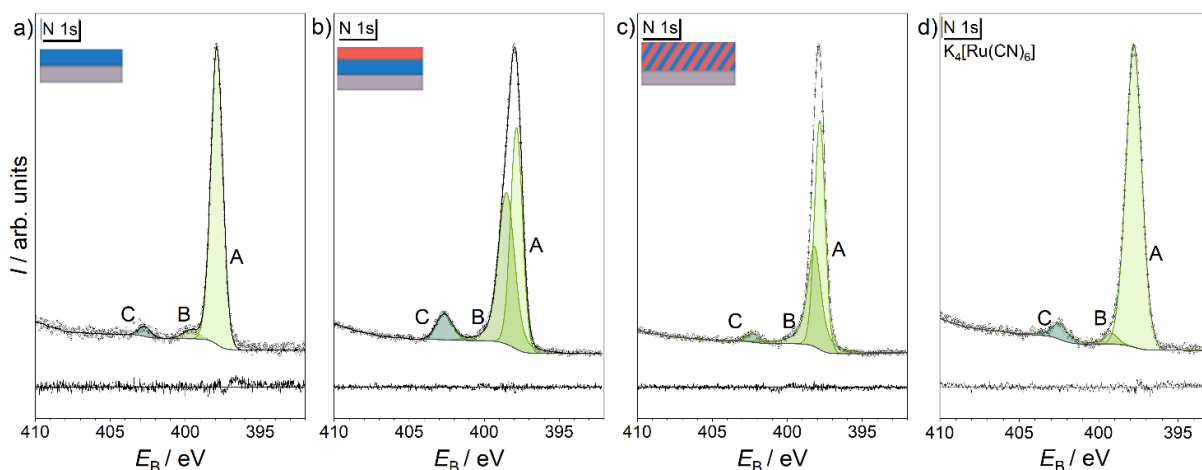


Figure 28. High-resolution N 1s XP spectra of a) Fe-HCR, b) layered material Fe-HCR|Ni-HCF, c) mixed material of Fe-HCR and Ni-HCF, d) $K_4[Ru(CN)_6] \times xH_2O$. The figure was adapted from Ref. 151.

The detailed peak positions of the fitted peaks of high-resolution N 1s XP spectra with assignment are given in Table 14.

Table 14. Peak positions of the fitted peaks of N 1s high-resolution XP spectra of the Fe HCF, the layered Fe-HCR|Ni-HCF and mixed material samples as well as the $K_4[Ru(CN)_6] \times xH_2O$ as reference sample. For brevity, $K_4[Ru(CN)_6] \times xH_2O$ is shortened as $K_4[Ru(CN)_6]$. The data was taken from Ref. 151.

| Compound | E_B / eV | Assignment | Reference |
|------------------|------------|--|-------------|
| Fe-HCR | 397.9 | $Ru^{II}\text{-CN-Fe}^{II}$ | 129 |
| | 399.6 | $Ru^{II}\text{-CN-Fe}^{III}$ / decomposition product | 129,156,157 |
| | 402.7 | shake-up satellite $\pi \rightarrow \pi^*$ or \underline{NO} | 128,23,159 |
| Layered Material | 397.8 | $Fe^{II}\text{-CN-Ni}^{II}$ | 129 |
| | 398.5 | $Fe^{III}\text{-CN-Ni}^{II}$ | 129 |
| | 402.6 | shake-up satellite $\pi \rightarrow \pi^*$ or \underline{NO} | 23,128,159 |
| Mixed Material | 397.8 | $Fe^{II}\text{-CN-Ni}^{II}$, $Ru^{II}\text{-CN-Fe}^{II}$ | 129 |
| | 398.2 | $Fe^{III}\text{-CN-Ni}^{II}$ | 129 |
| | 402.3 | shake-up satellite $\pi \rightarrow \pi^*$ or \underline{NO} | 128,23,159 |
| $K_4[Ru(CN)_6]$ | 397.8 | $Ru^{II}\text{-CN}$ | 129 |
| | 399.2 | Decomposition product | 129,156,157 |
| | 402.4 | shake-up satellite $\pi \rightarrow \pi^*$ or \underline{NO} | 128,23,159 |

6.4 Spectroelectrochemical and Voltammetric Analysis of the

Materials

Cyclic voltammograms of the M-HCM thin films recorded at 10 mV s^{-1} in 1 M are shown in Figure 29. Figures 29a-c display the typical redox responses of Fe-HCR and Ni-HCF. The redox reactions Fe-HCR (Figure 29a) exhibit redox peaks ($E_{\text{pa}} = 0.31 \text{ V}$ and $E_{\text{pc}} = 0.20 \text{ V}$) with $E^{\circ} = 0.26 \text{ V}$. These peaks can be assigned to the redox reactions in Eq. 1 and Eq. 3. The main peak of the electrochemically deposited Ni-HCF (Figure 29b), marked as $E_{\text{pa},1}$ and $E_{\text{pc},1}$ has a $E^{\circ} = 0.68 \text{ V}$ ($E_{\text{pa},1} = 0.71 \text{ V}$ $E_{\text{pc},1} = 0.63$), this peak may be attributed to the soluble form of Ni-HCF (Eq. 2). The redox signals at more negative potentials are found at $E_{\text{pa},2} = 0.57 \text{ V}$ and $E_{\text{pc},2} = 0.52$ and can be attributed to different stoichiometric forms including vacancies (Eq. 4).⁶⁹

In Figure 29c, the electrochemical behavior of Ni-HCF is shown for a sample prepared by LbL deposition on a nitrile-terminated SAM on an Au electrode. This experiment was a control experiment on how the preparation method may influence the redox behavior. Redox peaks at higher potentials are observed at $E_{\text{pa}} = 0.66 \text{ V}$ and $E_{\text{pc}} = 0.62 \text{ V}$, and those at lower potentials at $E_{\text{pa}} = 0.51 \text{ V}$ and $E_{\text{pc}} = 0.48 \text{ V}$. Indeed, the signals in Figure 29c are shifted to less positive potentials than those of the electrochemically deposited Ni-HCF in Figure 29b.

Ni-HCF can be considered as solid solutions of the soluble (Eq. 2) and insoluble form (Eq. 4).³⁰ As Zamponi et al.⁶⁹ and Chen et al.¹⁶⁰ discussed, these different forms in the structure of Ni-HCF are oxidized and reduced at slightly different potentials. The redox peaks at more positive potentials can be assigned to the K^+ -rich (soluble) form of Ni-HCF, whereas the peaks at more negative potentials can be attributed to the vacancy-containing (insoluble) form.^{69,160} The different deposition processes may yield different fractions of these forms in the resulting material, leading to varying voltammograms. Small signal contributions may also result from different redox responses from redox centers at the surface and in the bulk material.⁷³ Figure 29a-c demonstrates that the redox potentials of Fe-HCR and Ni-HCF are well separated from each other, which mainly depends on the N- or C-coordinated transition metals.¹⁵

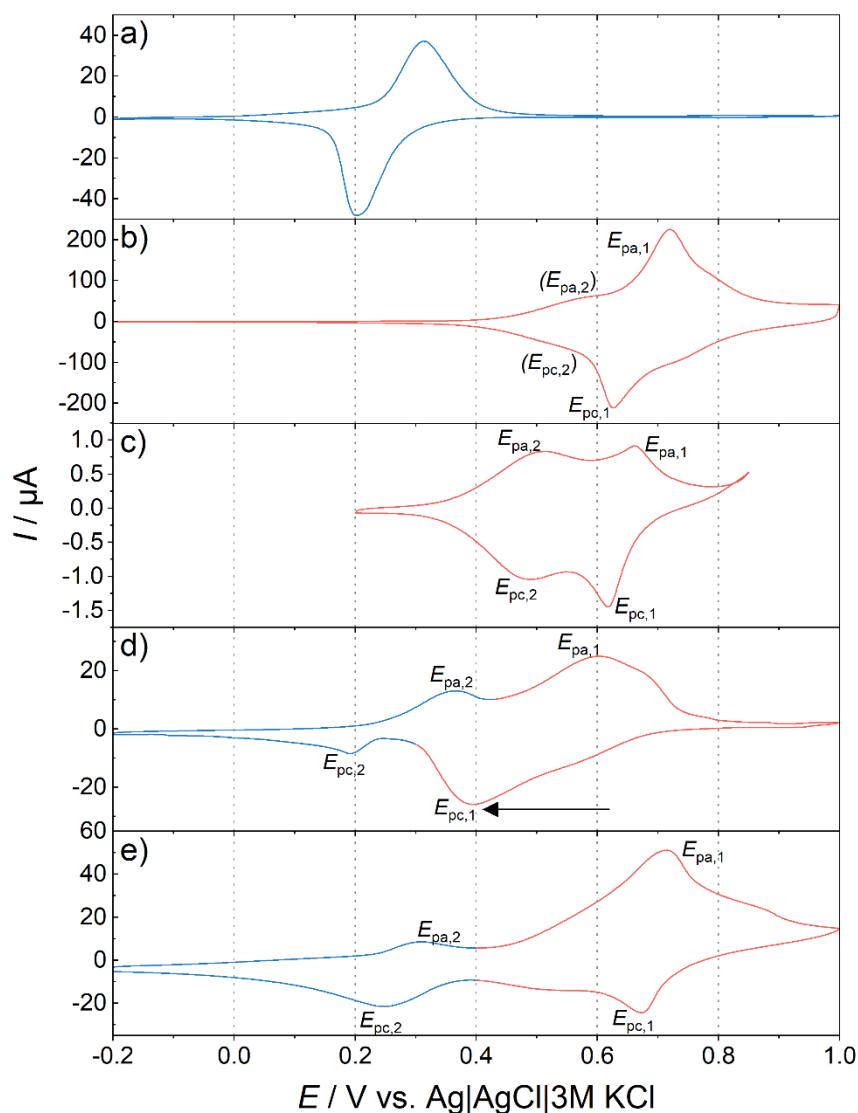


Figure 29. Electrochemical responses of a) electrodeposited Fe-HCR, b) electrodeposited Ni-HCF, c) Ni-HCF prepared by layer-by-layer deposition on a nitrile-modified Au surface, d) the mixed material of Fe-HCF and Ni-HCF and e) the layered Fe-HCR|Ni-HCF material. The cyclic voltammograms were recorded in 1 M KCl, $\nu = 0.1 \text{ V s}^{-1}$. The figure was adapted from Ref. 151.

The voltammogram in Figure 29d was obtained with the layered material of Fe-HCR as the inner and Ni-HCF as an outer layer. The peaks are at $E_{pa,1} = 0.60 \text{ V}$, $E_{pa,2} = 0.36 \text{ V}$, $E_{pc,1} = 0.39 \text{ V}$ and $E_{pc,2} = 0.19 \text{ V}$. The peaks associated with Fe-HCR ($E_{pa,2}$ and $E_{pc,2}$) do not shift significantly against the redox processes in the pure Fe-HCR film in Figure 29a. The estimated formal potential is only slightly more positive than the values found in Figure 29a ($E^{\circ} = 0.28 \text{ V}$ vs. 0.26 V). The anodic peak of Ni-HCF ($E_{pa,1}$) is also similar to the values reported for the pure Ni-HCF material in Figures 29b and 29c. It is noteworthy that the anodic peak is likely attributable to the insoluble form of Ni-HCF, which exhibits redox peaks at more negative

potentials. Additionally, the anodic peak $E_{pa,1}$ shows a shoulder at higher potentials at 0.68 V. This shoulder is close to the anodic peak reported for Ni-HCF in the material obtained by LbL deposition. Since Ni-HCF can be understood as a solid solution, defects in the structure arising during the deposition of the outer film probably caused the appearance of this anodic peak. However, the reduction peak in $E_{pc,1}$ corresponding to the redox reaction of $\text{Ni-C}\equiv\text{N-Fe}^{3+} \rightarrow \text{Ni-C}\equiv\text{N-Fe}^{2+}$ is shifted towards more negative potentials by 0.24 V. The main peak of this reduction process can be found at $E_{pc,1} = 0.39$ V. As the inner layer inhibits the redox reaction, a peak shift is expected for the cathodic peak ($E_{pc,1}$). The inner Fe-HCR layer cannot mediate the electron transfer. Equation 13 shows in a simplified way the reaction at the interface between both materials:



Figure 29e presents the CV of a film of the mixed material comprising Fe-HCR and Ni-HCF, prepared by alternating electrodeposition. The voltammogram exhibits additive signals for Fe-HCR (Figure 29a) and Ni-HCF (Figure 29b). The main redox features of Ni-HCF are observed at $E_{pa,1} = 0.71$ V and $E_{pc,1} = 0.67$ V. The peaks at $E_{pc,2} = 0.24$ and $E_{pa,2} = 0.31$ correspond to the reduction and oxidation of Fe-HCR, respectively. The voltammetric behavior of the mixed material supports the hypothesis that the electron transfer is not influenced by mixing these materials. In the CVs of the mixed material, both Fe-HCR and Ni-HCF exhibit behaviors similar to those observed in the pure material films shown in Figure 29a-c. These results highlight that the appearance of charge trapping critically depends on the the film's architecture.

Spectroelectrochemical PM IRRA spectra for a thin Fe-HCR film are shown in Figure 30. Fe-HCR is a solid solution of the 'soluble' and 'insoluble' structure with vacancies on the M^2 site,⁷ which can cause different signals in PM IRRA spectra even for the same material.¹⁶¹

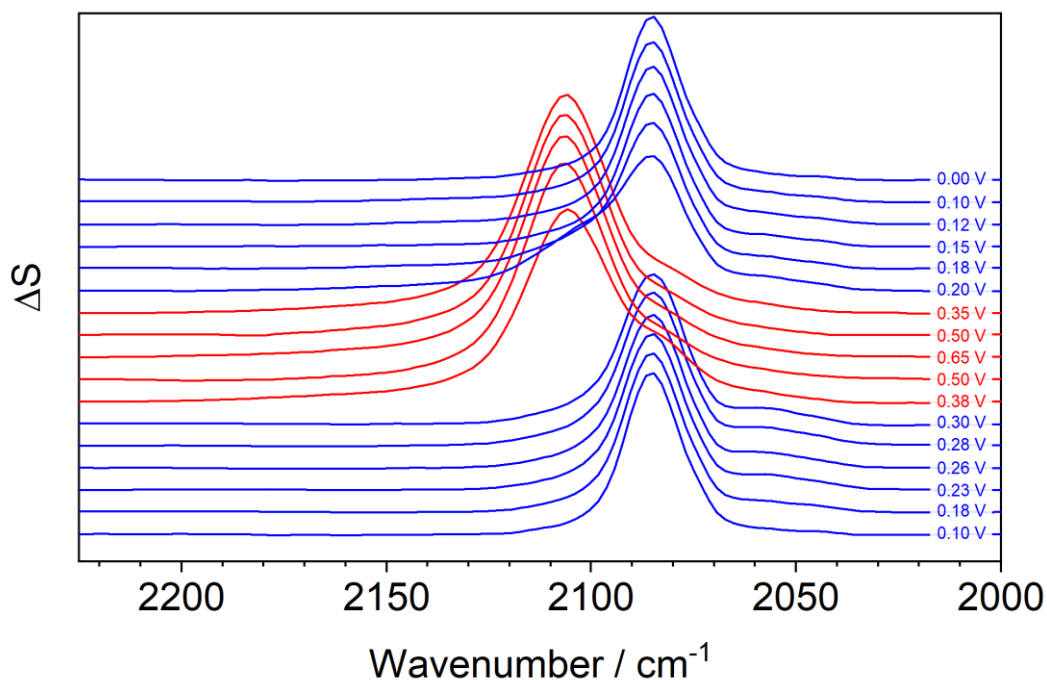


Figure 30. PM IRRA spectra in 2225- 2000 cm^{-1} region of Fe-HCR in positive and negative potential scans. The spectra were recorded in the electrolyte solution at half-wave retardation set to 2100 cm^{-1} . The figure was adapted from Ref. 151.

The PM IRRA spectra are dominated by a strong $\nu(\text{C}\equiv\text{N})$ absorption mode at $\sim 2080 \text{ cm}^{-1}$. This mode disappears in the potential range of 0.38 V – 0.65 V in the forward scan and 0.65 – 0.35 V in the back scan. Instead, a new $\nu(\text{C}\equiv\text{N})$ absorption mode appears at $\sim 2106 \text{ cm}^{-1}$. In accordance with literature¹²⁵ of other M-HCM with redox reactions at high-spin Fe, the IR absorption mode at around 2080 cm^{-1} can be assigned to $\text{Fe}^{2+}\text{-N}\equiv\text{C-Ru}^{2+}$, and the IR absorption mode at $\sim 2106 \text{ cm}^{-1}$ can be attributed to $\text{Fe}^{3+}\text{-N}\equiv\text{C-Ru}^{2+}$. The PM IRRA spectra of the oxidized material in Figure 30 still contain a shoulder at wavenumbers attributed to the reduced form. The position of this signal was found as a local minimum of the second derivative of the spectra at 2042 cm^{-1} and 2056 cm^{-1} , as shown in Figure 31a. The vibration mode can be attributed to defects in the structure, like vacancies and changes in the binding motif to $\text{Ru-N}\equiv\text{C-Fe}$, but also terminal cyanides.^{162,161} The assignments of the signals for the oxidized and reduced forms of Fe-HCR are compiled in Table 15.

Table 15. Wavenumber, intensity, and assignment of the $\nu(\text{C}\equiv\text{N})$ stretching mode in Fe-HCR thin films deposited on an Au electrode surface. The data was taken from Ref. 151.

| $\nu(\text{C}\equiv\text{N})/\text{cm}^{-1}$ | Mode intensity ^a | Assignment | References |
|--|-----------------------------|---|------------|
| 2042 | v.w. | Defects | 162,161 |
| 2056-2057 | v.w. | Defects | 162,161 |
| 2079-2085 | v.s. | $\text{Ru}^{2+}\text{-C}\equiv\text{N-Fe}^{2+}$ | 125 |
| 2106-2007 | v.s. | $\text{Ru}^{2+}\text{-C}\equiv\text{N-Fe}^{3+}$ | 125 |

^a v.w. – very weak; v.s. – very strong

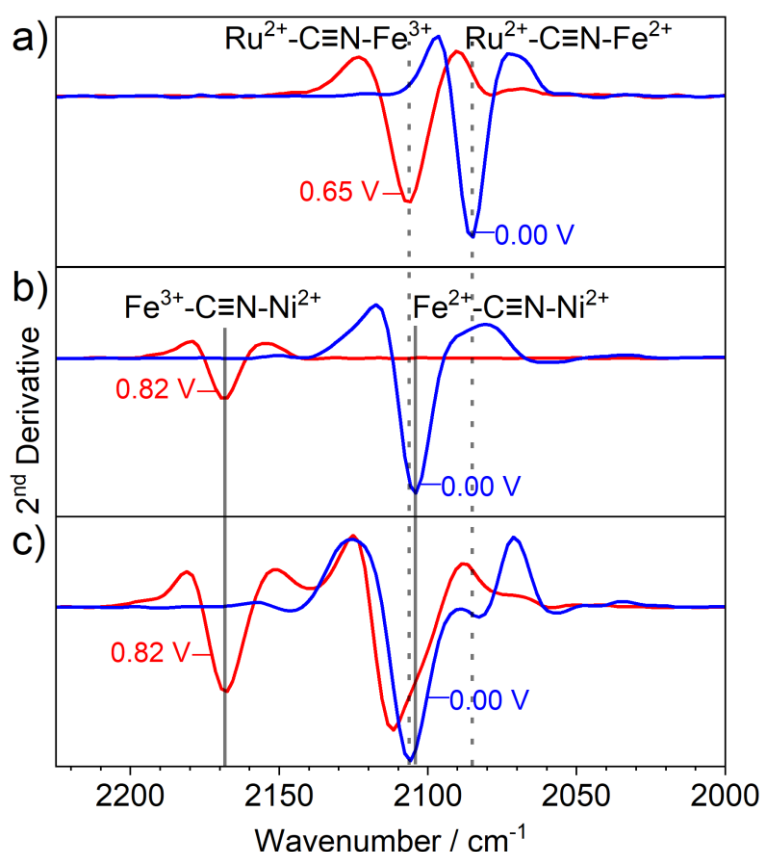


Figure 31. Second derivative of the in-situ PM IRRRA spectra of a) Fe-HCR, b) Ni-HCF and c) the Fe-HCR|Ni-HCF layered material. The spectra were recorded in the electrolyte solution at half-wave retardation set to 2100 cm^{-1} . The figure was adapted from Ref. 151.

PM IRRAS data from spectroelectrochemical in-situ measurements of a thin Ni-HCF film are presented in Figure 32. Electrochemical responses of the pure Ni-HCF thin film, as shown in the voltammograms in Figures 29b and 29c, indicate the presence of non-stoichiometric forms. The second derivative of the spectra is shown in Figure 31b. The defects associated with the non-stoichiometric structure, a solid solution of $\text{K}_2\text{Ni}[\text{Fe}(\text{CN})_6]$ and $\text{KNi}_{1.5}[\text{Fe}(\text{CN})_6]$, may

influence the PM IRRA spectra. In the PM IRRA spectra, a strong $\nu(\text{C}\equiv\text{N})$ absorption mode at approximately 2100 cm^{-1} is observed. This mode disappears completely at potentials of $E > 0.73\text{ V}$. Additionally, a new, rather weak absorption mode appears at 2163 cm^{-1} at potentials around $E > 0.55\text{ V}$. In accordance with the literature,¹²⁵ the strong IR absorption mode at around $\sim 2100\text{ cm}^{-1}$ can be assigned to $\text{Ni}^{2+}\text{-N}\equiv\text{C-Fe}^{2+}$. At oxidizing potentials, the IR absorption mode at approximately 2163 cm^{-1} can be attributed to $\text{Ni}^{2+}\text{-N}\equiv\text{C-Fe}^{3+}$.^{125,162-164}

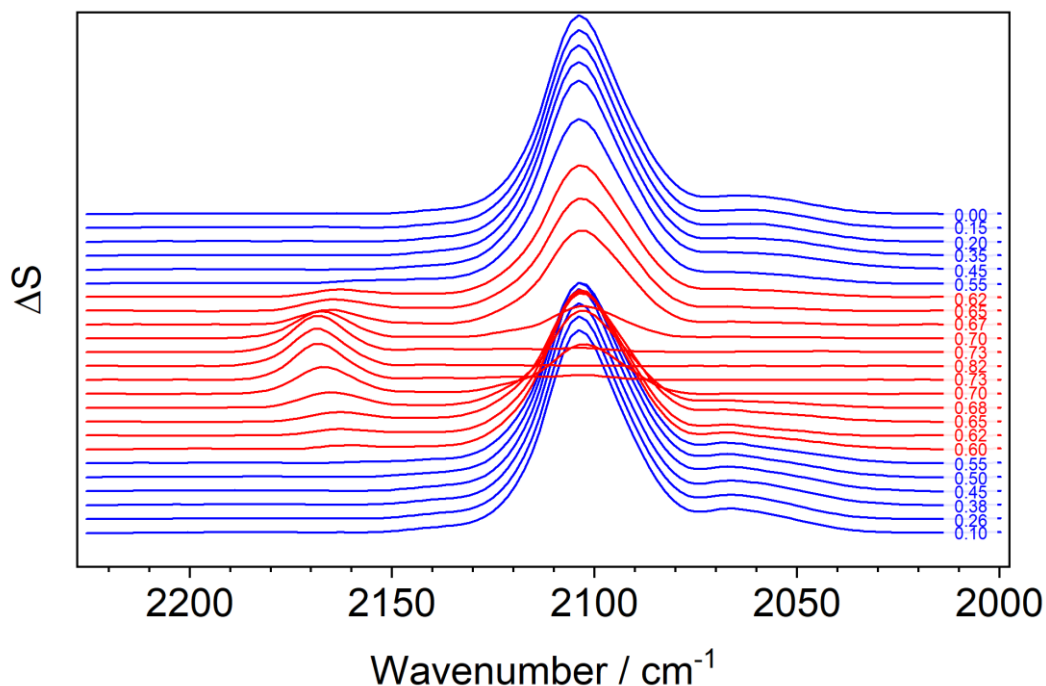


Figure 32. PM IRRA spectra in $2225\text{-}2000\text{ cm}^{-1}$ region of Ni-HCF in positive and negative potential scans. The spectra were recorded in the electrolyte solution at half-wave retardation set to 2100 cm^{-1} . The figure was adapted from Ref. 151.

Besides the main features, the second derivative of the spectra (not shown) revealed additional, very weak absorption modes at approximately 2050 cm^{-1} , 2065 cm^{-1} , 2125 cm^{-1} and 2140 cm^{-1} . These can be attributed to defects in the structure and/or also terminal cyanides.^{162,161} During the potential change, the intensities of the absorption modes at 2050 cm^{-1} and 2125 cm^{-1} change concomitantly. A similar observation is made for the modes at 2065 cm^{-1} and 2140 cm^{-1} . This allows their assignment to the oxidized and reduced forms in Table 16. In the negatively going potential scan, the absorption mode at around 2163 cm^{-1} assigned to $\text{Fe}^{3+}\text{-C}\equiv\text{N-Ni}^{2+}$ disappears at potentials of $E < 0.55\text{ V}$.

Table 16. Wavenumber, intensity, and assignment of the $\nu(\text{C}\equiv\text{N})$ stretching mode in Ni-HCF thin films deposited on an Au electrode surface. The data was taken from Ref. 151.

| $\nu(\text{C}\equiv\text{N})/\text{cm}^{-1}$ | Mode intensity ^a | Assignment | References |
|--|-----------------------------|---|-----------------|
| 2048-2053 | v.w. | Defects | 162,161 |
| 2063-2065 | w. | Defects | 162,161 |
| 2100-2104 | v.s. | $\text{Fe}^{2+}\text{-C}\equiv\text{N-Ni}^{2+}$ | 125,163,162,164 |
| 2124-2125 | v.w. | Defects | 162,161 |
| 2140-2141 | v.w. | Defects | 162,161 |
| 2163-2169 | s. | $\text{Fe}^{3+}\text{-C}\equiv\text{N-Ni}^{2+}$ | 125,164,162 |

^a v.w. – very weak; w. – weak; s. – strong; v.s. – very strong

The spectroelectrochemical PM IRRAS data of the layered Fe-HCR|Ni-HCF material are shown in Figure 33. The absorption modes of the two compounds in different oxidation states overlap for the oxidized form of Fe-HCR and the reduced form of Ni-HCF, leading to difficulties in a precise assignment (Table 17). Signals identified from the second derivative of the spectra in Figure 31c are listed in Table 17. Additional weak absorption modes can be found in Figure 33 at 2043 cm^{-1} , 2057 cm^{-1} and approximately 2140 cm^{-1} . These may be assigned to defects in the structure.^{161,162} The absorption mode for $\text{Fe}^{2+}\text{-C}\equiv\text{N-Ru}^{2+}$ appears at 2082 cm^{-1} , and the strong absorption mode for $\text{Fe}^{2+}\text{-C}\equiv\text{N-Ni}^{2+}$ appears at 2105 cm^{-1} .^{125,162–164} When Fe-HCR is oxidized at $E > 0.30\text{ V}$, the strong absorption mode shifts to 2111 cm^{-1} . With the ongoing oxidation of the system, this peak shifts slightly further to 2114 cm^{-1} . In this wavenumber range, overlap of different absorption modes is expected. The absorption modes of $\text{Fe}^{2+}\text{-C}\equiv\text{N-Ni}^{2+}$ occur here, as well as the absorption mode of $\text{Ru}^{2+}\text{-C}\equiv\text{N-Fe}^{3+}$. Indeed, the shift of the peak at potentials ($E > 0.30\text{ V}$) shows the influence of oxidation of $\text{Ru}^{2+}\text{-C}\equiv\text{N-Fe}^{3+}$ on this absorption mode.

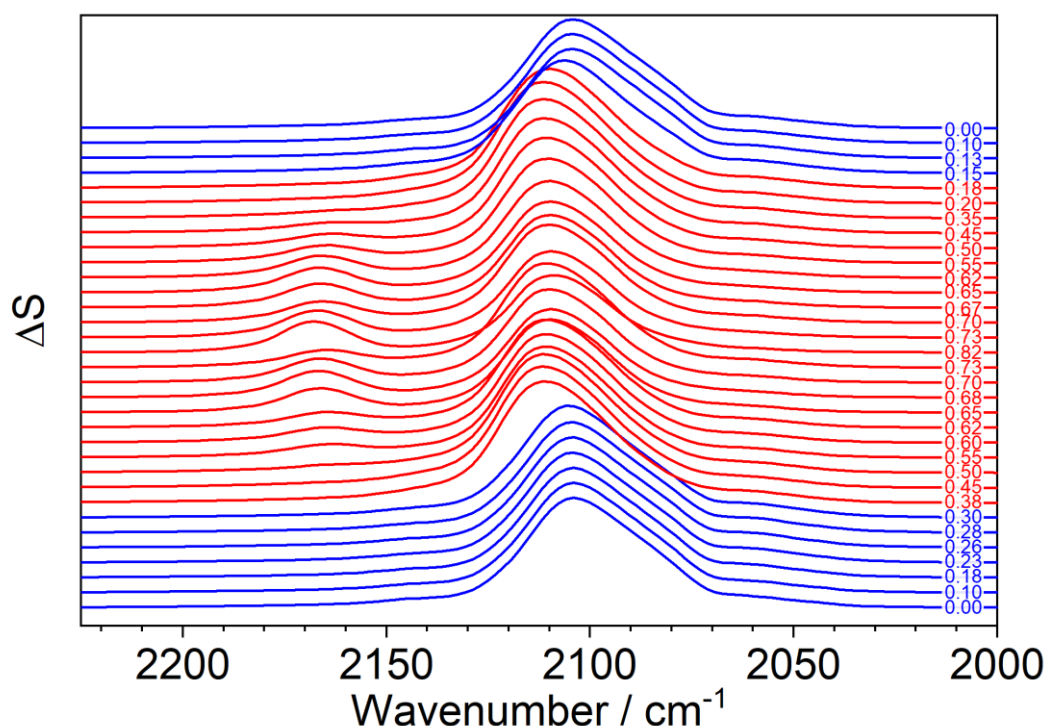


Figure 33. PM IRRA spectra in 2225- 2000 cm^{-1} region of Fe-HCR | Ni-HCF layered material in positive and negative potential scans. The spectra were recorded in the electrolyte solution at half-wave retardation set to 2100 cm^{-1} . The figure was adapted from Ref. 151.

Moreover, the peak intensity decreases with increasing potential, indicating the oxidation of $\text{Fe}^{2+}\text{-C}\equiv\text{N-Ni}^{2+}$. The resulting oxidized form, $\text{Fe}^{3+}\text{-C}\equiv\text{N-Ni}^{2+}$, is associated with the absorption mode at approximately 2165 cm^{-1} . As can be concluded from Figure 33, this absorption mode appears in the PM IRRA spectra at around 0.45 V.^{125,162,164} In the negatively going scan, the absorption mode at around 2165 cm^{-1} , which is assigned to $\text{Fe}^{3+}\text{-C}\equiv\text{N-Ni}^{2+}$, disappears at potentials of $E < 0.30$ V.

Table 17. Wavenumber, intensity, and assignment of the $\nu(\text{C}\equiv\text{N})$ stretching mode in Fe-HCR | Ni-HCF layered material thin films deposited on an Au electrode surface. The data was taken from Ref. 151.

| $\nu(\text{C}\equiv\text{N})/\text{cm}^{-1}$ | Mode Intensity ^a | Assignment | References |
|--|-----------------------------|--|-------------|
| 2043 | v.w. | Defects | 161,162 |
| 2057 | w | Defects | 161,162 |
| 2082 | m.s. | $\text{Ru}^{2+}\text{-C}\equiv\text{N-Fe}^{2+}$ | 125 |
| 2105 | v.s. | $\text{Fe}^{2+}\text{-C}\equiv\text{N-Ni}^{2+}$ | 125,162-164 |
| 2111-14 | v.s. | $\text{Fe}^{2+}\text{-C}\equiv\text{N-Ni}^{2+}$ / $\text{Ru}^{2+}\text{-C}\equiv\text{N-Fe}^{3+}$ | 125 |
| 2138-45 | w | Defects | 161,162 |
| 2164-67 | s | $\text{Fe}^{3+}\text{-C}\equiv\text{N-Ni}^{2+}$ | 125,162,164 |

^a v.w. – very weak; w. – weak; m.s. – medium strong; s. – strong; v.s. – very strong

6.5 Conductivity in Solid State

Experiments with M^1 -HCM²s in the solid state, conducted without a liquid electrolyte, are feasible due to mixed-valent redox centers within the network structure. These centers enable charge exchange and are stabilized by (partially solvated) counter cations that stabilize different redox states.³⁰ However, unlike in voltammetry with electrolyte solutions, there is no net flux of counterions to balance charge between the coordination networks and any adjacent ion-conducting phase. To gain more insight into the solid-state electrochemical behavior of these materials, measurements of I - V curves were recorded using conductive SFM tips (Figure 34). These tips enable the microscopic regions of the sample to be addressed. The voltage was applied across the films of coordination network compounds between a conducting SFM cantilever and the ITO substrate. For each sample, several I - V curves were recorded. The averaged curves are also discussed and shown in Figure 34 as a thick black line.

The I - V curves of pure Fe-HCR shown in Figure 34a exhibit symmetric behavior, similar to what was reported for the I - V characteristics of Fe-HCF,¹⁶⁵ where the curve was almost flat between -0.5 V and +0.5 V and decreased and increased linearly between this range and ± 3.0 V. For Fe-HCR a similar behavior was found, indicating an almost flat region in the range between -5 and 5 V and linear decrease and increase between this and ± 10 V.¹⁶⁶ In Figure 34a, I - V curve of Fe-HCR is almost linear between -1 V to +1 V followed by a section, where the curve rises exponentially in negative and positive directions. The appearance of the I - V characteristics changes drastically when the materials are arranged in stratified layers as shown in Figures 34b and 34c.

The sample for Figure 34b was a Fe-HCR thin film, onto which Ni-HCF nanoparticles (TEM images in Figure 25) were drop-cast. Such samples enable recording I - V curves on the uncovered Fe-HCR films (by placing the C-SFM tip in between nanoparticles) and on the layered system (with the C-SFM tip on an individual Ni-HCF nanoparticle). An overview scan of $15\ \mu\text{m} \times 15\ \mu\text{m}$ (Figure 24c) allowed the locating of single nanoparticles on the Fe-HCR film. To approach the nanoparticle, the scan area was stepwise reduced until the scanned area was smaller than the lateral extension of the nanoparticle. This was evident because the nanoparticle filled the entire image frame. The I - V curves in 34b remain flat in the voltage range between approximately -1 V and +2 V. This is a larger range than that observed for a

pure Fe-HCR film in Figure 34a. The further increase in current on both sides of the flat region is asymmetrical. At positive bias, the curve increases exponentially, while in the negative bias region, a leakage current is detected up to the breakdown voltage at around -4 V (Figure 34b). The I - V curves of the mixed material in Figure 34d show strong variations between different locations on the same sample, which is not observed in Figures 34a and 34b.

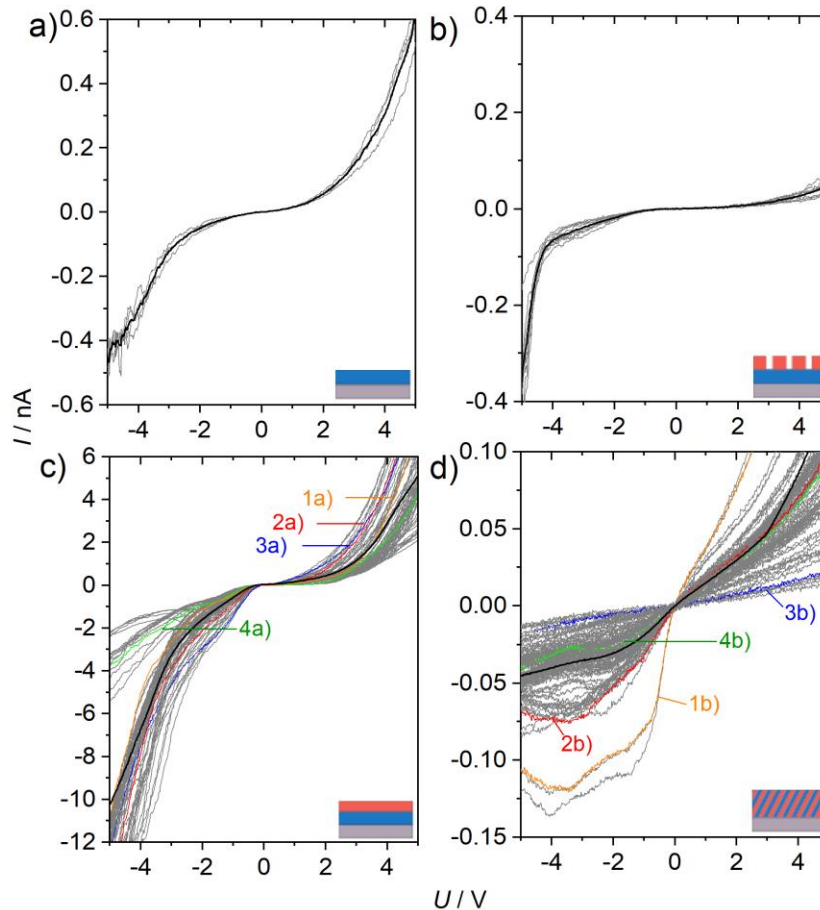


Figure 34. I - V curves of the M-HCM samples. a) Fe-HCR, b) layered material of Ni-HCF nanoparticles on a Fe-HCR film, c) layered material Fe-HCR|Ni-HCF, d) mixed material of Fe-HCF and Ni-HCF. For each material, several I - V curves were recorded at different locations of the same sample. They are shown in gray. The average of the curves for each sample is indicated by a black line. The colored curves 1-4 in panels c) and d) are selected curves shown with expanded scale in Figure 35. The figure was adapted from Ref. 151.

Representative individual curves are shown in Figure 35. Some curves in Figure 34d are similar those of the layered Fe-HCR|Ni-HCF material in Figure 34c and Figure 35 (curves 1a, 2a). In contrast, curve 4a and especially curve 3a are more resembling an ohmic behavior. This locally different behavior underlines the disordered architecture of the film.

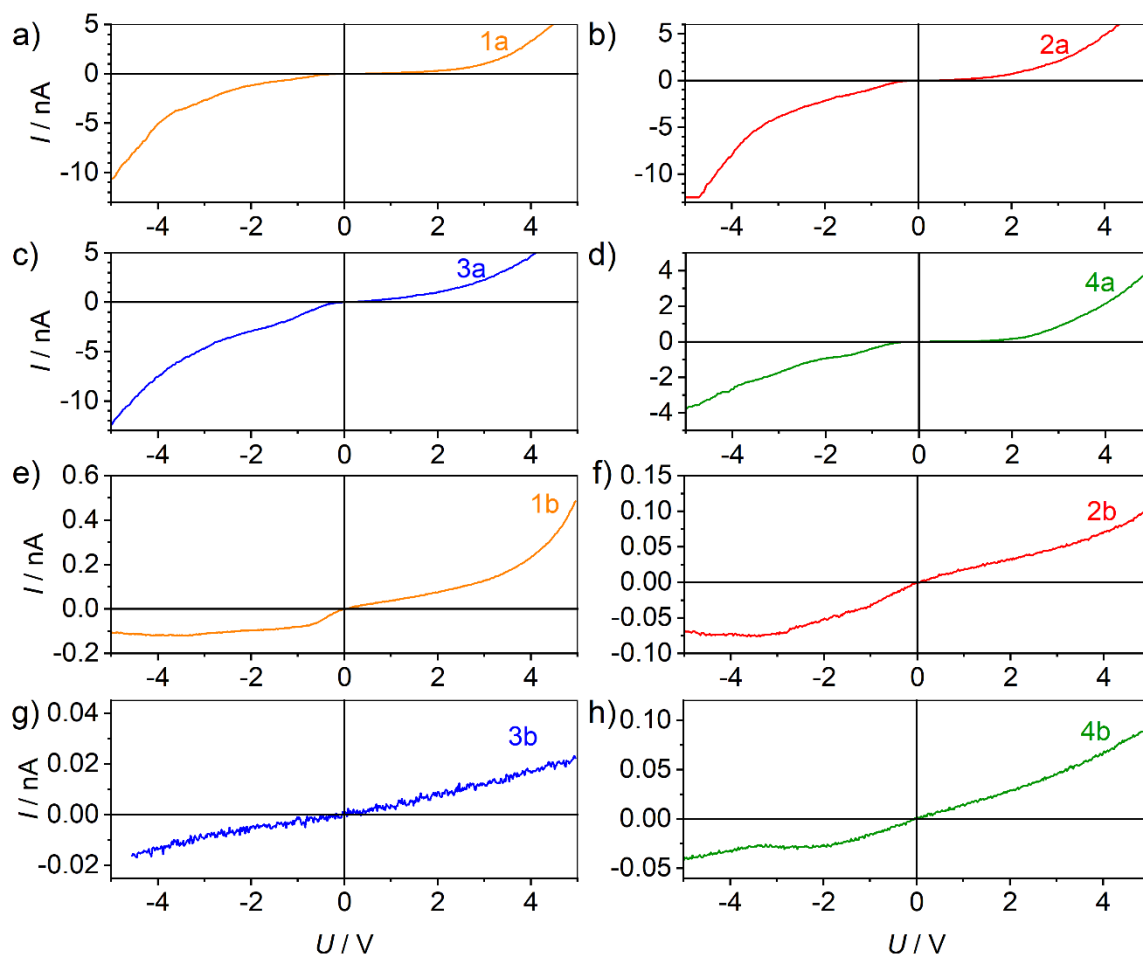


Figure 35. a)-d) Selected I - V curves of the layered material from Figure 34c. The numbers of the curves correspond to those in Figure 34c. e)-h) Selected I - V curves of the mixed material from Figure 34d. The numbers of the curves correspond to those in Figure 34d. The figure was adapted from Ref. 151.

The analysis of the I - V curves in solid-state (Figure 34b, c, Figure 35a-d) reveals the rectifying behavior of the layered material similar to the results obtained by cyclic voltammetry, where charge trapping was found (Figure 29d). This phenomenon is not observed if the same elements are processed in a mixed layer. The air-dried samples contain structural water.^{30,167} It is known that the mobility of K^+ counterions and, thus, the conductivity depends on the presence of structural water in M-HCM materials.³⁰ In the air-dried sample, this condition is met, and the inner Fe-HCR film, which is in direct contact with the back electrode, is easily reduced if a sufficiently negative potential is applied. The outer Ni-HCF material is in contact with the electrolyte solution or the tip of the cantilever. In both experiments, the Ni-HCF layer can only be reduced once the reduction of Fe-HCR has commenced. The I - V curve in Figure 34b confirms that Ni-HCF does not directly exchange electrons with the back electrode and

that the electronic contact between the inner Fe-HCR layer and the outer layer Ni-HCR nanoparticles is established due to the preparation method.

The role of film preparation is also evident from the comparison of the I - V curves for Fe-HCR in Figure 34a and the layered sample Fe-HCR | Ni-HCF in Figure 34c, which showed much higher currents, although the same tips and experimental parameters were used. It is assumed that this results from the differences in film morphologies. Electrodeposited Fe-HCR has a pronounced granular structure, as shown in Figure 23a. The granular structure makes it likely that the current is conducted through a limited number of grains, as schematically depicted in Figure 36a, because gaps between grains and grain boundaries are likely to have a much higher resistance than the material itself.

In contrast, the Ni-HCF layer in the layered structure Fe-HCR | Ni-HCF was obtained by the layer-by-layer procedure and had a distinctly different morphology, as shown in Figure 23b. This may be caused by the different growth mechanisms. The smoother appearance of the film implies less grain boundaries. Usually, the surface roughness decreases compared to the underlying Fe-HCR film. As such, Ni-HCF may contact several grains of the underlying Fe-HCR film and enables the distribution of the current over more grains than can be assessed by a direct contact of the conducting SFM tip, as demonstrated in Figure 36b.

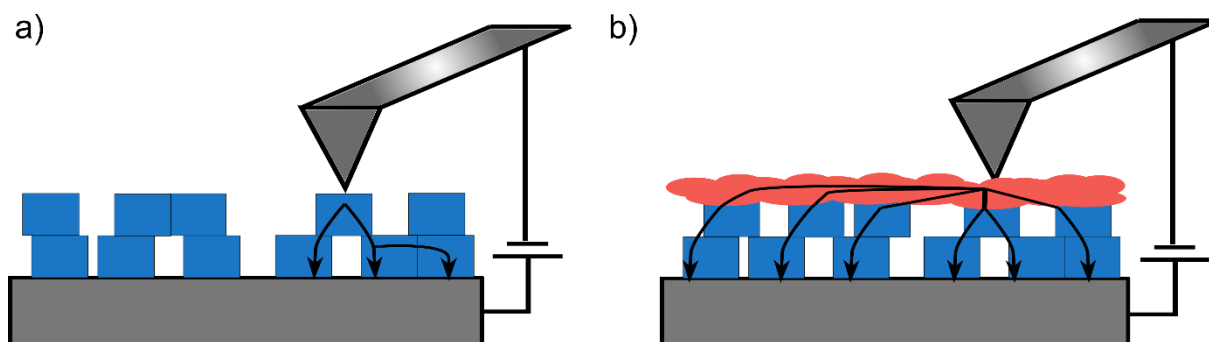


Figure 36. Schematic illustration of possible current path in I - V measurements in a) electrodeposited Fe-HCR and b) layered material of Fe-HCR|Ni-HCF. The scheme was adapted from Ref. 151.

This is also supported by the observation that dispersed Ni-HCF crystals used in Figure 34b do not show the current amplification, in agreement with the assumption that they contact only a limited number of Fe-HCR grains of the inner layer.

6.6 Attempts on other Layered Metal Hexacyanometallates Systems

Fe-HCF|Ni-HCF. The system of Fe-HCF|Ni-HCF, as presented by other authors,^{30,31} failed to demonstrate charge trapping when created using a mix of electrodeposition and LbL-deposition. Figure 37 presents the resulting cyclic voltammogram of the layered Fe-HCF|Ni-HCF system. The graph combines the individual signals of Fe-HCF and Ni-HCF with no evidence of charge trapping. This outcome aligns with the findings of Karpova et al.,¹⁵² where bilayers of Fe-HCF and Ni-HCF were prepared by electrodeposition without a binder between both layers.

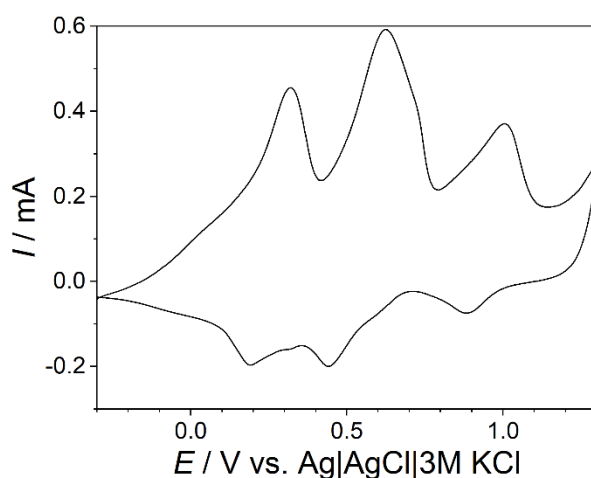


Figure 37. Cyclic voltammogram of layered Fe-HCF|Ni-HCF system on an ITO electrode; $\nu = 0.01 \text{ V s}^{-1}$. The figure was adapted from Ref. 151.

Fe-HCR|Cu-HCF. The bilayer system Fe-HCR|Cu-HCF displays a potential difference, suggesting that it may be suitable to achieve rectifying behavior and charge trapping. Conductive scanning force was employed to record I - V curves on a Cu-HCF thin film deposited on Fe-HCR, revealing an asymmetrical response (Figure 38).

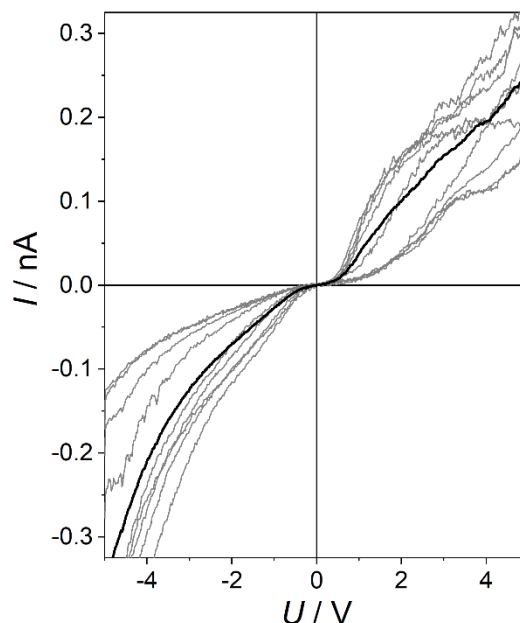


Figure 38. *I-V* curves on such films were recorded between the support electrode and a C-SFM tip on a layered Fe-HCR|Cu-HCF structure. The figure was adapted from Ref. 151.

However, the observed currents are like those measured for a Fe-HCR film (Figure 34a). Thus, the Cu-HCF most likely cannot electrically connect the different grains of the Fe-HCR film as the Ni-HCF film presented in Figure 36. The extent of asymmetry in the *I-V* curves is also less pronounced than in the layered Fe-HCR|Ni-HCF film (Figure 34d).

Systems with Zn-HCF. Due to the unique redox potential and the presence of abundant elements, Zn-HCF was explored as a potential component in bilayer systems. Electrodeposition of Zn-HCF, as shown in Figure 39, reveals that the process requires a larger potential window than compatible with aqueous electrolyte solutions and gold electrodes. For the studies of the layered systems using the methods used in this work, Au electrodes are preferred due to their compatibility with XPS analysis. In the case of ITO, the Sn 3p photoemission signal overlaps with the Fe 2p signal, complicating detailed XPS analysis.

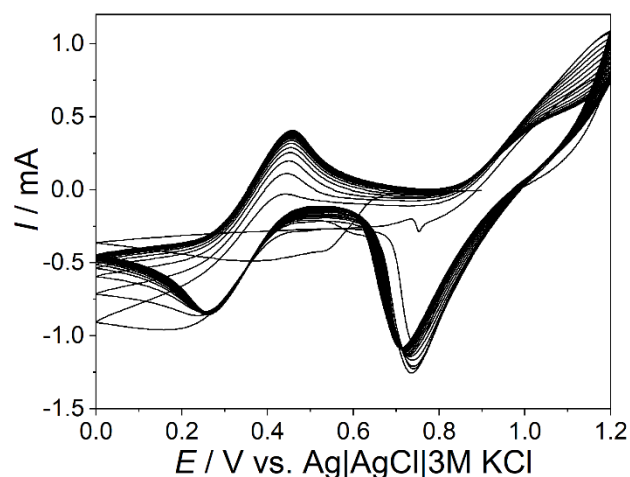


Figure 39. Electrochemical deposition of Zn-HCF on an ITO electrode in 0.1 M ZnCl_2 + 0.05 M $\text{K}_3[\text{Fe}(\text{CN})_6]$ + 0.5 M KCl + 0.1 M HCl; $\nu = 0.04 \text{ V s}^{-1}$. The figure was adapted from Ref. 151.

Electrodeposited Zn-HCF films exhibit non-uniform morphology, as evident from SEM images in Figure 40.

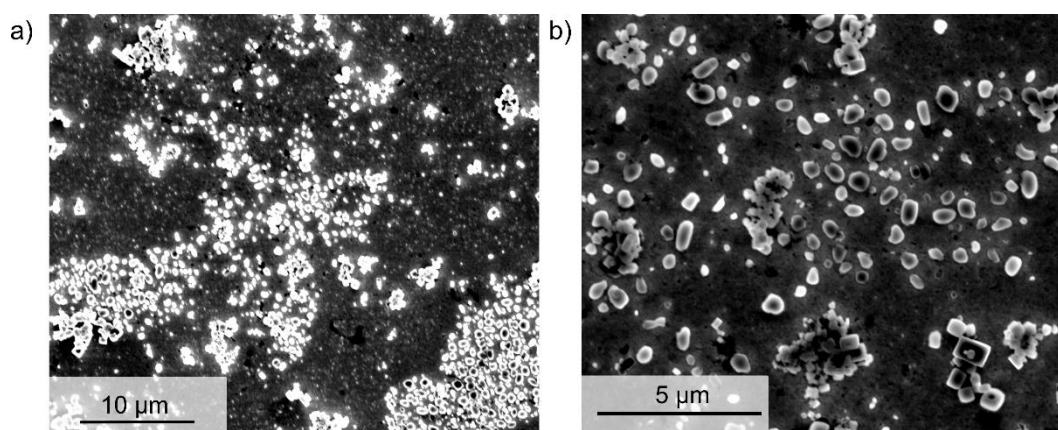


Figure 40. SEM images of a Zn-HCF thin film prepared by electrochemical deposition at different locations of the film. The figure was adapted from Ref. 151.

Another attempt to prepare Ni-HCF|Zn-HCF as a layered system by electrodeposited Ni-HCF followed by LbL-deposition of Zn-HCF was not successful because the material detached from the substrate during the LbL process, indicating limitations due to material incompatibility.

6.7 Conclusion

The electronic behavior and electrochemical properties of Fe-HCF and Ni HCF samples depend strongly on the nanoscale layer architecture. A “mixed layer”, which was obtained by

alternatingly performing an electrochemical synthesis by one oxidation-reduction potential cycle in the respective precursor solution, yields a film whose voltammetry exhibits a superposition of the signals found in the voltammograms of pure Fe-HCR or pure Ni-HCF films. Such mixed layers do not show a rectifying behavior in I - V curves recorded between the back Au electrode and a C-SFM tip.

However, rectifying behavior or charge trapping is observed in stratified layers. The layers are obtained by electrodeposition of granular Fe-HCR followed by overcoating Ni-HCF by an LBL approach. This yields a flaky morphology. In previous literature, M-HCM systems with rectifying behavior have been obtained by connecting and, at the same time, separating the different M-HCM layers by a polymer layer.³⁰ In this work, a direct connection between the two materials was achieved by first electrochemically depositing Fe-HCR and overcoating this by LbL deposition of Ni-HCF. Alternatively, the second layer can be applied as pre-synthesized Ni-HCF nanoparticles. The latter system allowed the comparison of I - V curves of the layered system Fe-HCR|Ni-HCF with those from Fe-HCR by placing the C-SFM tip either on a Ni-HCF nanoparticle or directly on the Fe-HCR layer. LbL deposition is a suitable method to form extended stratified layers because it has little impact on the previously deposited layer. This distinguishes this approach from electrodeposition, in which the redox state of the first film is periodically changed and may promote ion-exchanges processes at the interface between the two M^1 -HCM² materials. The electrochromic and electrocatalytic properties of Fe-HCR may thus be modulated not only by electronic communication with the supporting electrode but may also be integrated into a more sophisticated scheme for manipulating and reading the charging state of the material.

7 Isotope Effect in Metal Hexacyanometallates

The following Chapter is adapted from the own manuscript Gerhards, L.; Brand, I.; Wittstock, G. H/D Isotope Effects in the Electrochemistry of Electrochromic Iron Hexacyanoruthenate, *submitted*. L.G. conducted the experiments and analyzed the data. I.B. helped analyzing the PM IRRAS data. L.G., I.B. and G.W. discussed the analyzed data. All authors contributed to the writing of the manuscript.

7.1 Introduction

Isotope effects, which refer to variations in chemical and physical properties of the same compound depending on the isotopes of its constituting elements, are a topic of great interest in chemistry. This interest is partly due to the perception that these effects challenge one of the most fundamental laws of chemistry: that a pure compound exhibits identical chemical properties, irrespective of its origin or method of preparation.¹⁶⁸ In fact, even slight differences in the masses between isotopes of the same element can cause significant changes in the chemical properties of compounds containing these isotopes.¹⁶⁹ An example of this is observed in the substitution of ¹H (protium) for ²H (D, deuterium).¹⁶⁹ Isotope effects have broad applications in different fields, such as molecular spectroscopies as well as in provenience analyses in the fields of archeometry, environmental chemistry, food, cosmetics and pharmaceuticals.^{170,171} The underlying principle for these applications involves enhancing deviations from natural abundance through multiplicative distributions processed or by (bio)catalytic processes, which can result in strong and very specific preferences for certain isotope patterns in reagents.

Research into isotope effects in electrochemistry has remained limited in scope. A more negative potential is required for D₂ evolution compared to H₂, and there is a higher potential for O₂ evolution from D₂O compared to H₂O.¹⁷² These variances are fundamental for the production of D₂O by water electrolysis.¹⁷² Cai et al.¹⁷³ suggested utilizing this phenomenon to extend the usable potential range of supercapacitors with aqueous electrolytes.¹⁷³ Besides

reactions where deuterated compounds are either reagents or products of the electrode reaction, isotope effects are also well known for situations in which H₂O or D₂O serve as solvents in liquid electrolytes.

Studies indicate that the conductivity of electrolyte ions in H₂O is specified to be approximately 23% higher than in D₂O,¹⁷⁴ which correlated with the approximately 20% higher viscosity of D₂O compared to H₂O at constant temperature.¹⁷⁵ The conductivity of H⁺_(aq) in H₂O is reported to be 1.4 to 1.5 times higher than that of D⁺ in D₂O.¹⁷⁶ Additionally, H⁺ ions exhibit a significantly greater tendency to tunnel than D⁺. Large kinetic isotope effects are expected if H₂O/D₂O and H⁺/D⁺ are involved in rate-determining steps.¹⁷⁷ The *p*K_W values of H₂O and D₂O solutions are reported in literature with *p*K_W^H = 13.995, *p*K_W^D = 14.951.¹⁷⁸

Galagedera and Flechsig¹⁷⁹ reported a significant kinetic isotope effect in the reduction reaction



where [Co(NH₃)₆]³⁺_(aq) was electrostatically bound to the negatively charged backbone of single-stranded DNA (ssDNA) in a monolayer on an Au electrode. This effect was not observed for the structurally equivalent [Ru(NH₃)₆]³⁺_(aq). Galagedera and Flechsig¹⁷⁹ suggest that this difference is due to varying electron transport mechanisms within the ssDNA thin film and the involved transition metal complex. For [Ru(NH₃)₆]³⁺, the electron transfer mainly occurs via electron hopping, a process that is inhibited in [Co(NH₃)₆]³⁺ due to its spin structure. The necessity for physical diffusion of [Co(NH₃)₆]³⁺ within the ssDNA monolayer during the electrode reaction may render this reaction susceptible to a large isotope effect.¹⁷⁹

Expanding the potential window is a straightforward approach to enhancing electrochemical energy storage devices with aqueous electrolytes. This strategy could potentially suppress hydrogen or oxygen evolution side reactions in systems with intercalation electrodes in aqueous electrolytes. In this context, M-HCMs have recently received attention as active battery materials,^{180–183} in addition to their previously explored uses in scavenging radioactive and toxic metal cations,^{184,185} potentiometric sensors and electrocatalysts,^{186,41} and electrochromic materials.^{187,188} However, there are reports about significant differences in the intercalation chemistry when conducted in H₂O- or D₂O-based electrolytes.

Wang et al.³² reported a significant and reversible change in voltammograms of vanadium hexacyanoferrates (V-HCFs) in H₂O- and D₂O-containing electrolyte solutions. In this system, the redox reactions involve the formation of [VO₂]⁺ and VO⁺ on the V-sites, with H₂O/D₂O serving as a reagent. Lasky and Buttry¹⁸⁹ explored the redox processes of A₂Ni[Fe(CN)₆] (A = Cs⁺) using concurrent CV and EQCM experiments. They observed that the number of solvent molecules exchanged between the solution and the pore space of the coordination network varied between H₂O and D₂O, a difference that was only evident in the EQCM data, while the CV data appeared almost identical. However, a subsequent extensive study was unable to reproduce the difference in solvent transfer during redox reactions of A₂Ni[Fe(CN)₆] films in H₂O- and D₂O-based electrolytes.⁶¹

In this thesis, distinct voltammetric behaviors were noted for Fe-HCR films and solid Fe-HCR particles when using D₂O and H₂O electrolytes. Contrastingly, spectroscopic data reveals only minor differences between Fe-HCR films in H₂O- and D₂O-based electrolytes. Fe-HCR has been studied as an electrochromic material,¹³³ and as electrocatalysts for hydrogen evolution and hydrogen oxidation reactions.^{7,190} As of now, there have been no reports of isotope effects in this context to the best of current knowledge.

7.2 Electrodeposition of Fe-HCR Films in H₂O- and D₂O-Based

Electrolytes

Figure 41a illustrates the electrodeposition of Fe-HCR on a polycrystalline Au electrode in an H₂O-based electrolyte (labelled as Fe-HCR-H). The voltammogram obtained in H₂O displays a single broad anodic peak and two distinct cathodic peaks. The potentials of these two cathodic peaks, denoted as I_c and II_c, show a difference of 0.02 V in peak potential $E_{p,Ic}$ and $E_{p,IIc}$. The redox process is caused by a valence change of high-spin Fe^{II/III} and has often described by the Eq. 1 and Eq. 3.

The splitting of the voltammetric peaks, as seen in Figure 41a, has also been observed by Abe et al.,⁷ in experiments using a NaH₂PO₄ electrolyte. This phenomenon has been attributed to redox processes of Fe^{4III}[Ru^{II}(CN)₆]₃×kH₂O with charge compensation by H⁺ (peak I_c) and the

valence change in $\text{KFe}^{\text{III}}[\text{Ru}^{\text{II}}(\text{CN})_6] \times m\text{H}_2\text{O}$ with charge compensation by Na^+ (peak II_c).⁷ Similar to this, the splitting of peaks has also been explained for nickel hexacyanoferrate.¹⁹¹

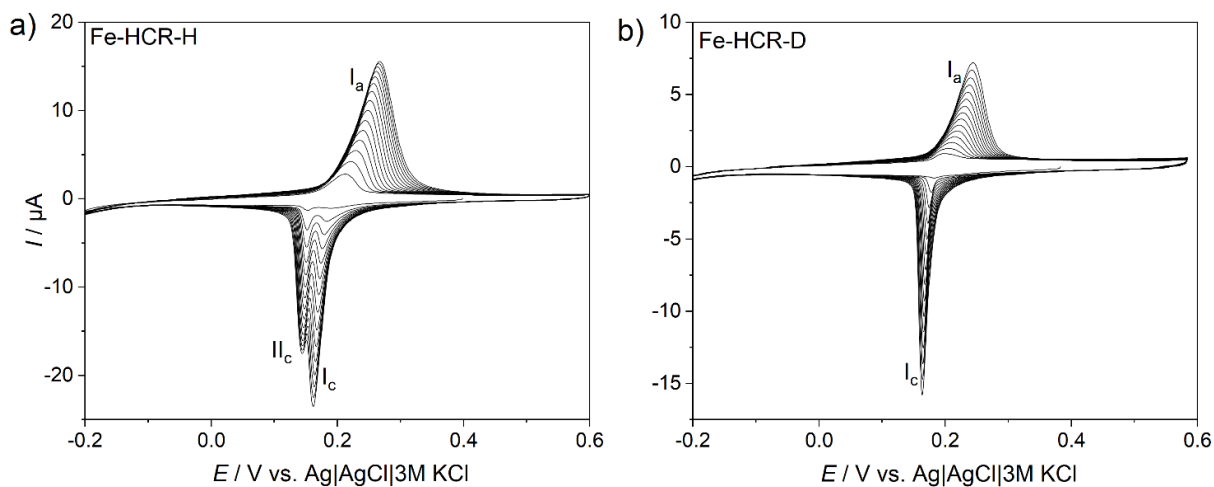


Figure 41. Deposition of Fe-HCR in 0.001 M $\text{FeCl}_3 \times 6 \text{H}_2\text{O}$, 0.001 M $\text{K}_4[\text{Ru}(\text{CN})_6] \times m\text{H}_2\text{O}$ and 0.07 M KCl in precursor solution made of a) H_2O and b) D_2O . Deposition was performed for 15 cycles at $\nu = 0.04 \text{ V s}^{-1}$ between -0.2 V and 0.6 V. The figure was adapted from the manuscript “H/D Isotope Effects in the Electrochemistry of Electrochromic Iron Hexacyanoruthenate”.

When the Fe-HCR film was prepared using the identical batch of chemicals but substituting H_2O with D_2O (Fe-HCR-D), there was a noticeable absence of cathodic peak splitting and the width of the anodic peak decreased, as shown in Figure 41b.

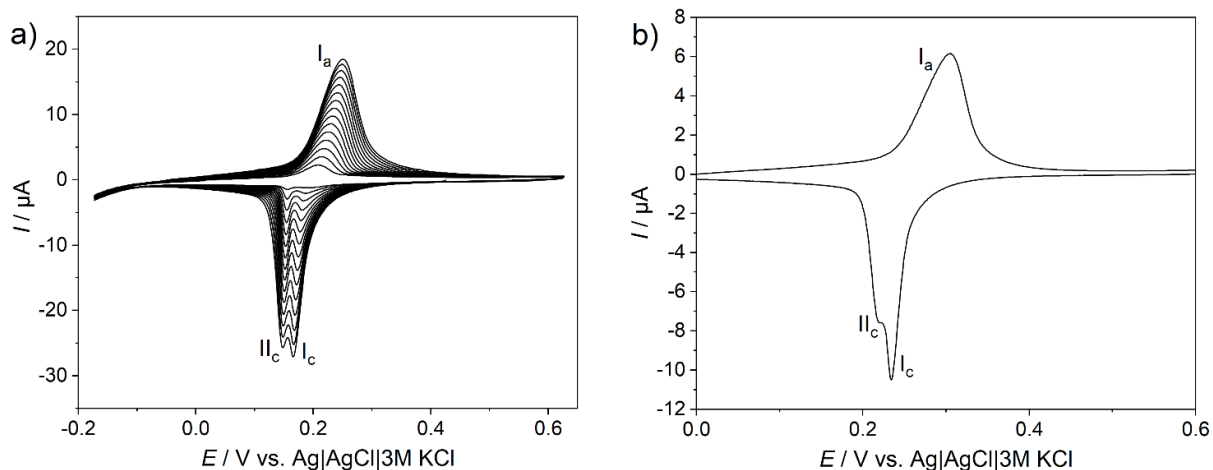


Figure 42. a) Electrochemical deposition of Fe-HCR from 0.001 M $\text{FeCl}_3 \times 6 \text{H}_2\text{O}$, 0.001 M $\text{K}_4[\text{Ru}(\text{CN})_6] \times m\text{H}_2\text{O}$ and 0.07 M KCl for 15 cycles at $\nu = 0.04 \text{ V s}^{-1}$ in high purity HPLC water and b) cyclic voltammetry of the deposited Fe-HCR film in 1 M KCl in high purity HPLC water at $\nu = 0.01 \text{ V s}^{-1}$. The figure was adapted from the manuscript “H/D Isotope Effects in the Electrochemistry of Electrochromic Iron Hexacyanoruthenate”.

To prove that the observed effects are not caused by a purity problem in the deionized water from the specific laboratory facility, commercially available high purity HPLC water was used for reference experiments. The presence of the two peaks was found to be consistent regardless of the H_2O source. Figure 42 demonstrates that two distinct reduction peaks are observable during the electrochemical deposition of Fe-HCR in an electrolyte solution prepared with commercially available, deionized, high-purity H_2O for HPLC. Similarly, cyclic voltammograms of the Fe-HCR film conducted in an electrolyte solution of high-purity H_2O for HPLC also display two reduction peaks. These peaks are similar to those in solutions prepared with water from the laboratory water purification system in Figure 43a.

7.3 Voltammetry of Electrodeposited Fe-HCR Films in H_2O - and D_2O -Based Electrolytes

The voltammetric behaviour of the Fe-HCR-H and Fe-HCR-D films exhibits reversible changes when an electrodeposited film (as shown in Figure 41a and b) is transferred between KCl solutions in H_2O and D_2O , as demonstrated in Figure 43. A film initially deposited in an H_2O electrolyte (Fe-HCR-H) and subsequently transferred to an H_2O -based 1 M KCl electrolyte

maintains its characteristic two distinct peaks (Figure 43a, curve 1). However, only a single sharp reduction peak is observed when the same film is transferred to a D₂O-based 1 M KCl solution (Fe-HCR-H-D), as evident in Figure 43a, curve 2. If the film is transferred back to a H₂O-based 1 M KCl solution (Fe-HCR-H-D-H), a voltammogram with two reduction peaks is recorded (Figure 43a, curve 3) similar to the voltammogram (c.f.) after preparation (Figure 43a, curve 1).

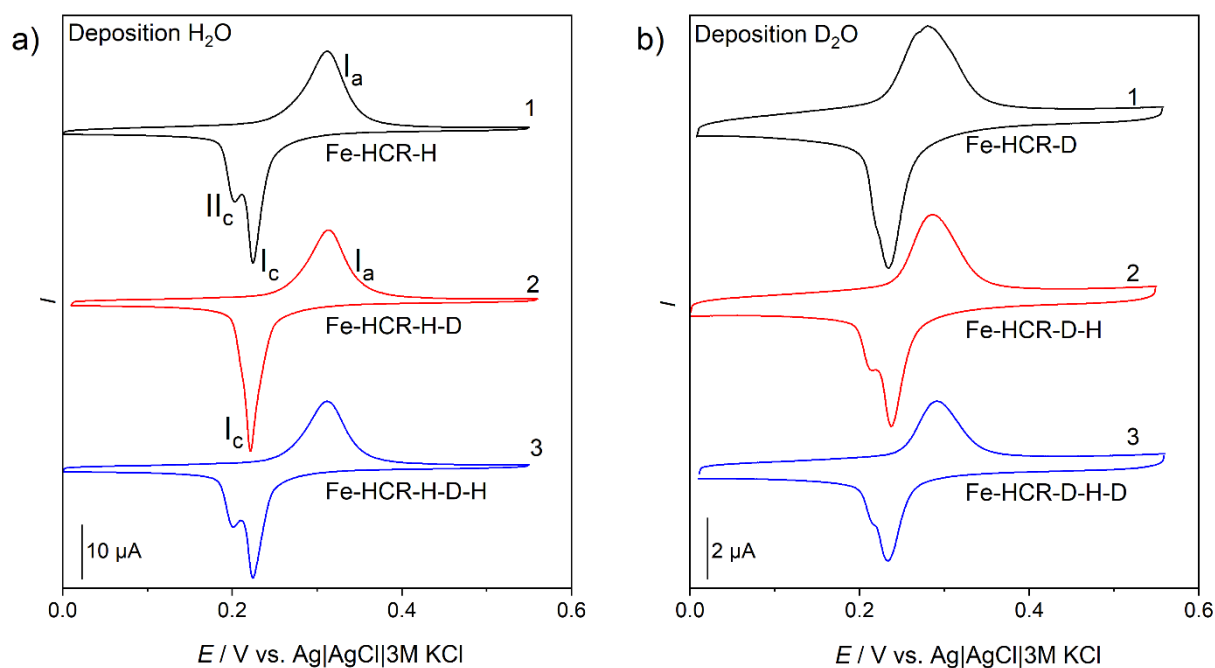


Figure 43. Cyclic voltammograms of electrochemically deposited Fe-HCR thin films with electrolyte exchange (H₂O / D₂O) in 1 M KCl at $\nu = 0.01 \text{ V s}^{-1}$. The films were deposited from 0.001 M FeCl₃ × 6 H₂O, 0.001 M K₄[Ru(CN)₆] × *m*H₂O and 0.07 M KCl for 15 cycles at $\nu = 0.04 \text{ V s}^{-1}$ in the range of -0.2 – 0.6 V in H₂O- or D₂O-containing solution. Panel a) film prepared in H₂O electrolyte, voltammograms recorded in electrolyte based on 1) H₂O, (2), D₂O, (3) H₂O; panel b) for film prepared in D₂O electrolyte, voltammograms recorded in electrolyte based on 1) D₂O, 2) H₂O, 3) D₂O. The figure was adapted from the manuscript “H/D Isotope Effects in the Electrochemistry of Electrochromic Iron Hexacyanoruthenate”.

Correspondingly, a Fe-HCR film initially deposited in a D₂O-based electrolyte (Fe-HCR-D, one cathodic peak), retains this characteristic upon transferring to a D₂O-based 1 M KCl solution (Figure 43b, curve 1). Transferring the Fe-HCR-D film to an H₂O-based 1 M KCl electrolyte (Fe-HCR-D-H) results in two cathodic peaks (Figure 43b, curve 2). A subsequent transfer back to D₂O-based 1 M KCl (Fe-HCR-D-H-D) leads to a reduction of the second

cathodic peak, which becomes barely discernable as a shoulder in Figure 43b, curve 3. The peak potentials are given in Table 18.

Table 18. Peak potentials of the redox peaks found in Figure 43. The films were deposited from 0.001 M $\text{FeCl}_3 \times 6 \text{H}_2\text{O}$, 0.001 M $\text{K}_4[\text{Ru}(\text{CN})_6] \times m\text{H}_2\text{O}$ and 0.07 M KCl for 15 cycles at $v = 0.04 \text{ V s}^{-1}$ in the range of -0.2 – 0.6 V in H_2O - or D_2O -containing solution.

| | Peak potential / V |
|------------|--------------------|
| a-1 | |
| Ia | 0.32 |
| Ic | 0.22 |
| IIc | 0.20 |
| a-2 | |
| Ia | 0.31 |
| Ic | 0.22 |
| IIc | - |
| a-3 | |
| Ia | 0.31 |
| Ic | 0.23 |
| IIc | 0.20 |
| b-1 | |
| Ia | 0.28 |
| Ic | 0.23 |
| IIc | - |
| b-2 | |
| Ia | 0.29 |
| Ic | 0.24 |
| IIc | 0.22 |
| b-3 | |
| Ia | 0.29 |
| Ic | 0.23 |
| IIc | 0.22 |

The split peaks in Figure 43 were fitted using a Voigt-profile as shown in Figure 44. For the Fe-HCR-H and Fe-HCR-H-D-H samples, approximately 22% of the charge is transferred in peak II_c , while for Fe-HCR-D-H, about 25% of the total cathodic charge is transferred in peak II_c . Given the inherent uncertainties associated with peak fitting procedures for voltammetric signals, the fraction of charge involved in the reduction processes of peak II_c can be considered relatively constant.

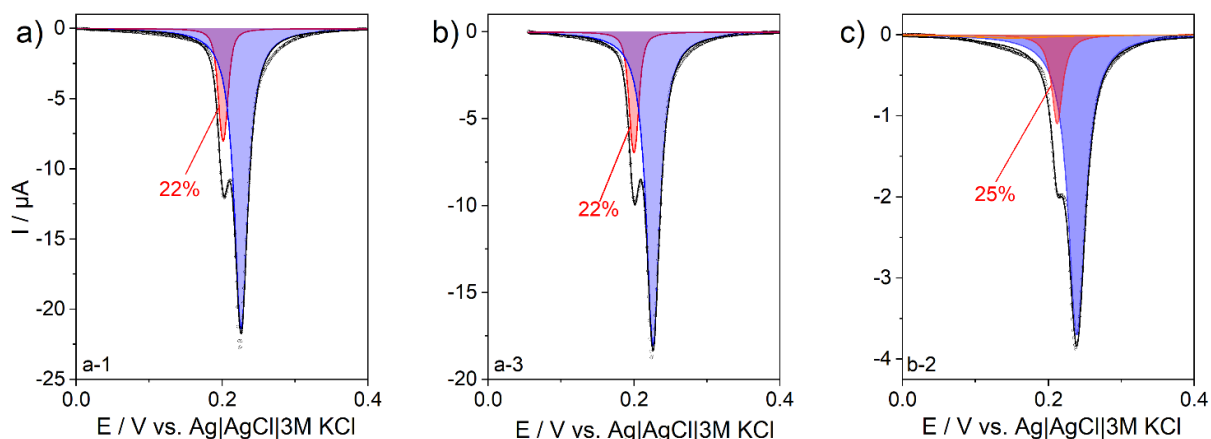


Figure 44. Estimation of associated charges of the split reduction peaks in Figure 43. a) data from Figure 43a, curve 1, b) data from Figure 43a, curve 3 and c) data from Figure 43b, curve 2. The figure was adapted from the manuscript “H/D Isotope Effects in the Electrochemistry of Electrochromic Iron Hexacyanoruthenate”.

Fe-HCR-H was deposited with an decrease in deposition cycles to investigate whether a second reduction peak appears in a D₂O-containing electrolyte solution. Figure 45 shows the CVs of Fe-HCR-H-D after 2 and 5 deposition cycles, and the absence of a second reduction peak can be clarified. The reduction peak can be found at 0.22 V and is similar to the reduction peaks I_c in the cyclic voltammogram of the cyclic voltammogram a-2 of Figure 43 (Table 18).

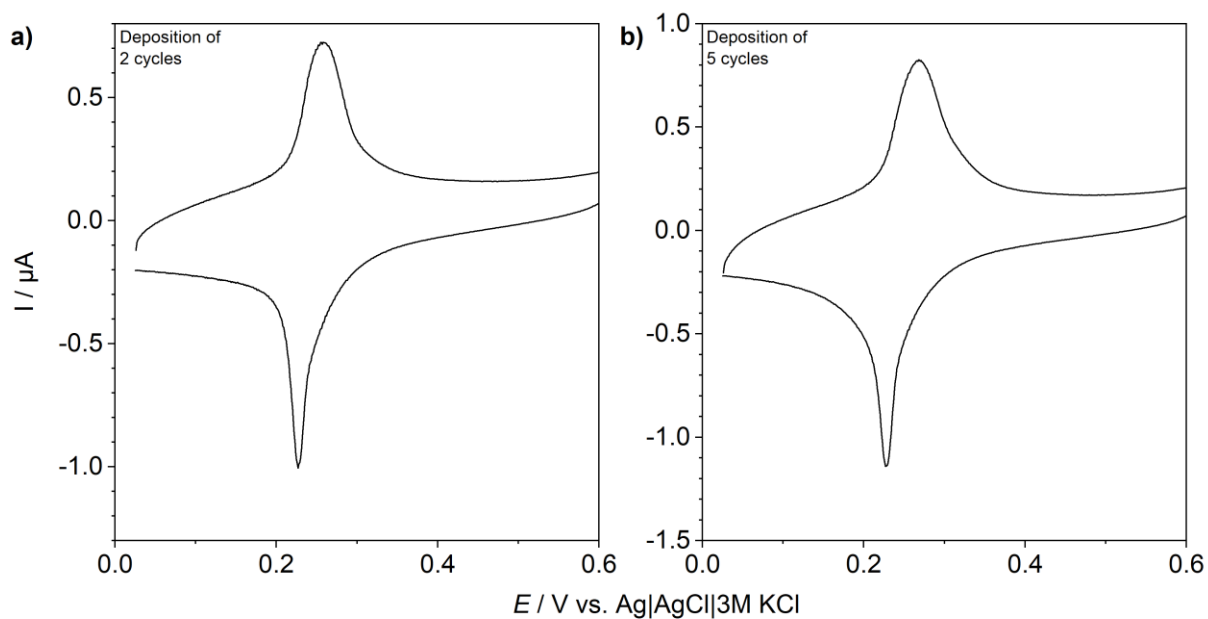


Figure 45. CVs of Fe-HCR thin films in 1 M KCl electrolyte solution at $\nu = 0.01 \text{ V s}^{-1}$ after deposition from 0.001 M $\text{FeCl}_3 \times 6 \text{ H}_2\text{O}$, 0.001 M $\text{K}_4[\text{Ru}(\text{CN})_6] \times m\text{H}_2\text{O}$ and 0.07 M KCl for 15 cycles at $\nu = 0.04 \text{ V s}^{-1}$ for a) 2 cycles and b) 5 cycles. The figure was adapted from the manuscript “H/D Isotope Effects in the Electrochemistry of Electrochromic Iron Hexacyanoruthenate”.

The long-term electrochemical behavior of Fe-HCR-H was tested by cycling the thin film in 1 M KCl in H_2O for 57 cycles, as can be seen in Figure 46.

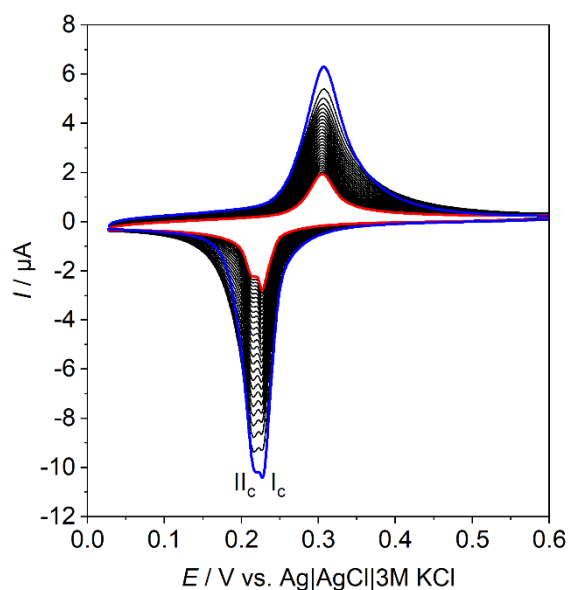


Figure 46. Long-time stability of Fe-HCR-H in 1 M KCl H₂O-based solution at $\nu = 0.01 \text{ V s}^{-1}$. The film was deposited from 0.001 M FeCl₃ × 6 H₂O, 0.001 M K₄[Ru(CN)₆] × *m*H₂O and 0.07 M KCl for 15 cycles at $\nu = 0.04 \text{ V s}^{-1}$. The figure was adapted from the manuscript “H/D Isotope Effects in the Electrochemistry of Electrochromic Iron Hexacyanoruthenate”.

The anodic peak can be found at 0.31 V and indicates no shift during cycling. The peak positions of the reduction peaks are at 0.23 V (I_c) and 0.22 V (II_c); here no shifting during cyclic can be found as well. Figure 43 and Table 18 also show that the peak splitting is approximately 0.01 V. Even though the current decreases due to material loss, the two reduction peaks from Fe-HCR remain throughout the cycling. This result suggests that no changes in the materials composition take place during cycling.

7.4 Voltammetry of Fe-HCR films in Electrolytes Made with H₂O-D₂O

Mixtures

CV experiments were conducted on a Fe-HCR-H sample using a series of H₂O-D₂O mixtures. These mixtures were prepared by adding *x* volume parts of H₂O to *y* volume parts of D₂O. The used mixtures, referred to as V(H₂O)+V(D₂O), included the following ratios: 10+0, 9+1, 8+2, 7+3, 6+4, 5+5, 4+6, 3+7, 2+8 and 0+10. Each of these solvent mixtures contained 1 M KCl. The same electrode was sequentially used across these varying electrolyte solutions.

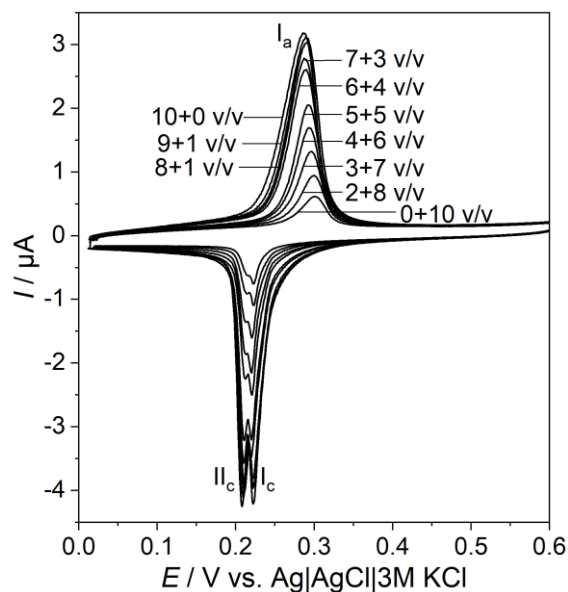


Figure 47. Cyclic voltammograms of Fe-HCR-H in 1 M KCl, with varying content of H₂O and D₂O $\nu = 0.01 \text{ V s}^{-1}$. The film was deposited from 0.001 M FeCl₃ × 6 H₂O, 0.001 M K₄[Ru(CN)₆] × *m*H₂O and 0.07 M KCl for 15 cycles at $\nu = 0.04 \text{ V s}^{-1}$. The mixtures, referred to as V(H₂O)+V(D₂O), included the following ratios: 10+0, 9+1, 8+2, 7+3, 6+4, 5+5, 4+6, 3+7, 2+8 and 0+10. The figure was adapted from the manuscript “H/D Isotope Effects in the Electrochemistry of Electrochromic Iron Hexacyanoruthenate”.

The CVs in Figure 47 show how the reduction peaks I_c and II_c change in response to the varying solvent composition V(H₂O)+V(D₂O). As the content of H₂O reduces, moving from a 10+0 to 4+6 electrolyte composition, there is a general trend of decreasing potential difference between the cathodic peaks I_c and II_c, as depicted in Figure 48. An exception to this trend is noted between the 3+7 and 2+8 [V(H₂O)+V(D₂O)] mixtures. The smallest potential difference is noted in the electrolyte composed of D₂O only (V(H₂O)+V(D₂O) = 0+10). The observed decrease in currents is associated with the partial detachment of the Fe-HCR thin film from the electrode, occurring during the transfer and rinsing stages of the experiment.

The largest area of II_c can be found at 100 % H₂O content; here the area of peak II_c reaches approximately 16%. As the H₂O content decreases, the fractional area of peak II_c in relation to the total peak tends to decrease. This experiment indicates a correlation between the H₂O content in the electrolyte solution and the voltammetric behavior of Fe-HCR films. The two distinct peaks observed in H₂O electrolytes tend to merge into a single peak at high mole fractions of D₂O.

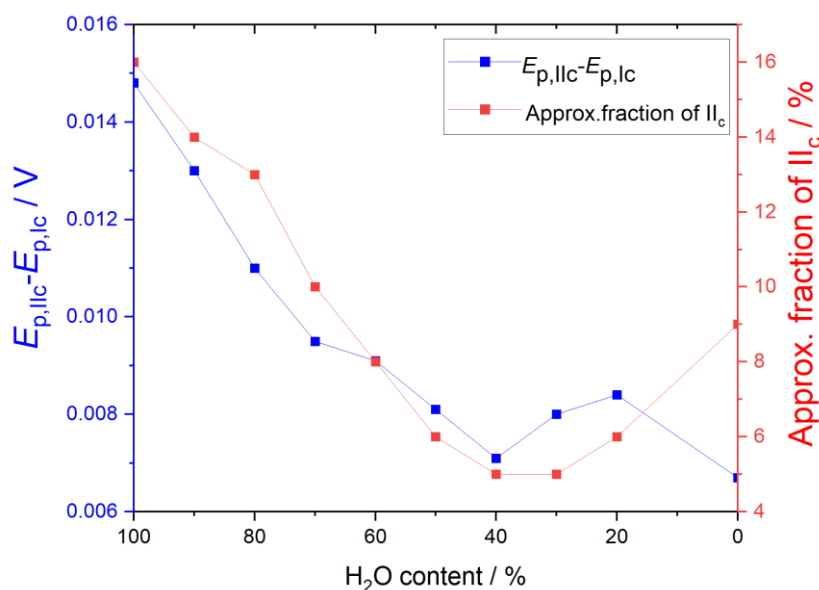


Figure 48. Analysis of the proportion of II_c in Fe-HCR-H sample of Figure 47 as well as the potential differences of I_c and II_c. The film was deposited from 0.001 M FeCl₃ × 6 H₂O, 0.001 M K₄[Ru(CN)₆] × *m*H₂O and 0.07 M KCl for 15 cycles at $\nu = 0.04 \text{ V s}^{-1}$. The figure was adapted from the manuscript “H/D Isotope Effects in the Electrochemistry of Electrochromic Iron Hexacyanoruthenate”.

Contrastingly to the findings in Figure 43a, curve 2, the experiment involving H₂O-D₂O mixtures maintained the two distinct signals. This difference is probably due to the multiple transfers between various electrolytes, as opposed to a single transfer between H₂O-based to D₂O-based electrolytes.

7.5 Voltammetry with Wave Clipping

Wave clipping experiments with Fe-HCR films in H₂O- and D₂O-based electrolytes were conducted to analyze the relationship between cathodic and anodic signals, as illustrated in Figure 49. In Figure 49a, the reduction peak of Fe-HCR-H increases as the positive vertex potential of the applied potential ramp is raised. Two cathodic signals are always present, even at very low positive vertex potentials. After scanning the entire scan range, the cathodic peak positions are found at $E_{p,Ic} = 0.23$ and $E_{p,IIc} = 0.22$ V. The peak corresponding to I_c is broader up to an anodic vertex potential of 0.3 V but becomes narrower beginning from a positive vertex potential of 0.31 V. It is important to note that all voltammograms in Figure 49a were recorded on the same film, indicating that the changes in peak shape are not due to structural variations caused by electrodeposition at different potentials. As the positive vertex potential increases,

$E_{p,lc}$ shifts in negative the direction (thus towards $E_{p,lc}$), while $E_{p,lc}$ remains relatively constant at 0.22 V.

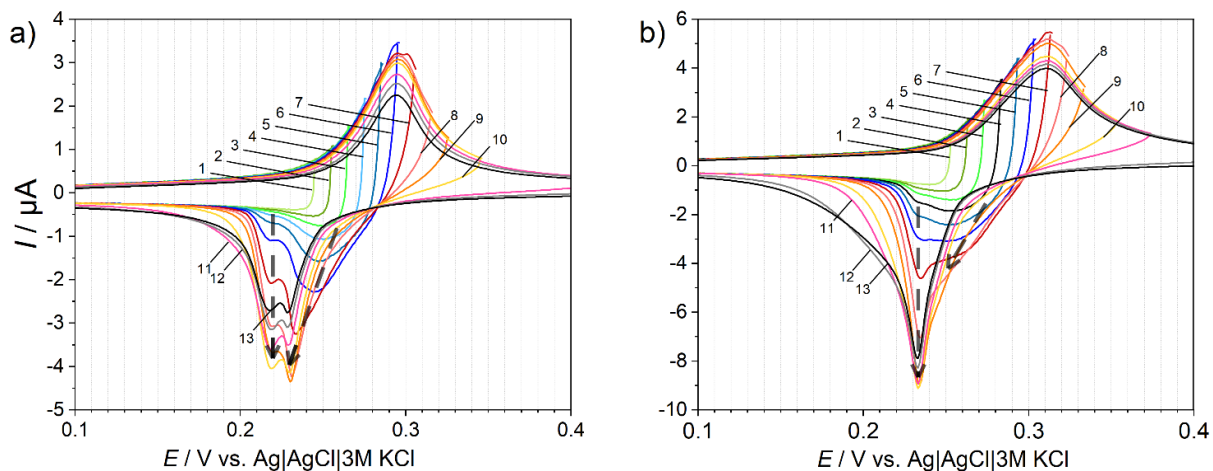


Figure 49. Wave clipping of a) Fe-HCR-H in H₂O-based 1 M KCl and b) Fe-HCR-D in D₂O-based 1 M KCl $\nu = 0.01 \text{ V s}^{-1}$. The films were deposited from 0.001 M FeCl₃ × 6 H₂O, 0.001 M K₄[Ru(CN)₆] × *m*H₂O and 0.07 M KCl for 15 cycles at $\nu = 0.04 \text{ V s}^{-1}$ in the range of -0.2 – 0.6 V in H₂O- or D₂O-containing solution. The figure was adapted from the manuscript “H/D Isotope Effects in the Electrochemistry of Electrochromic Iron Hexacyanoruthenate”.

In comparison, the redox signal of Fe-HCR-D in D₂O-based 1 M KCl electrolyte, as shown in Figure 49b, exhibits a broad signal comprised of several components. Both the position and shape of these components vary as the positive vertex potential is increased. The prominent peak, the main signal in Figure 43b, curve 1, initially appears as a shoulder and becomes more pronounced with an increase in positive vertex potential, particularly evident at an anodic vertex potential of 0.31 V. The broader signal at more positive potentials is only well-identified at relatively low vertex potentials and shifts to more negative values with increasing positive vertex potential. Eventually, at a positive vertex potential of 0.35 V, the two signals appear to “merge” or completely overlap. Notably, the signal component at approximately 0.23 V maintains its position, similar to Fe-HCR-H, while the other signal undergoes shifts and changes in peak shape.

7.6 Effect of Viscosity and Temperature

At 25 °C, the viscosity of H₂O is 0.8903 cP; whereas for D₂O, it is 1.100 cP; i.e., making D₂O about 20% more viscous.¹⁷⁵ This disparity in viscosity impacts the transport coefficients of

dissolved ions, thus influencing voltammetric curves that are dependent on interfacial kinetics and transport processes. Increasing the temperature of a D₂O-based solution to 35 °C can reduce its viscosity and match that of H₂O at 25 °C. If the variation in voltammetric signals of Fe-HCR in H₂O- and D₂O-based electrolytes is indeed due to transport effects, this difference should disappear when the viscosities of both electrolytes are matched by adjusting the temperature.

An experiment was conducted, where a Fe-HCR-H sample, which exhibited a voltammogram in an H₂O-based electrolyte, as shown in Figure 43a (curve 1), was transferred to a D₂O-based electrolyte at 35 °C, and another voltammogram was recorded (Fe-HCR-H.D, Figure 50). This led to a splitting in the reduction peak, a phenomenon absent in the same electrolyte at 25 °C. The voltammogram in Figure 50 closely resembles that in an H₂O-based electrolyte at 25 °C. The difference between the two cathodic peak potentials in Figure 50 is 0.01 V, aligning with the peak splitting in H₂O-based electrolyte at 25 °C (Figure 43a, curve 1). The result implies that the characteristics of the reduction peak are influenced by transport properties, typically the transport of the charge-compensating ion (K⁺), which may be limiting in the redox reaction of M^I-HCM².

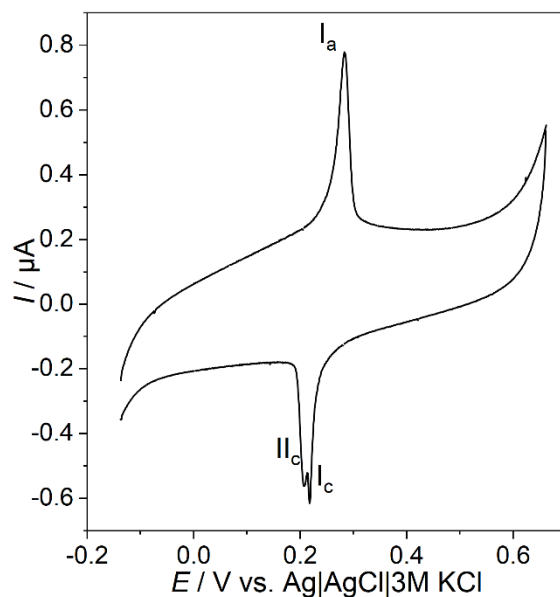


Figure 50. Cyclic voltammogram of Fe-HCR-H-D in 1 M KCl in D₂O at 35°C, $\nu = 0.01 \text{ V s}^{-1}$. The film was deposited from 0.001 M FeCl₃ × 6 H₂O, 0.001 M K₄[Ru(CN)₆] × *m*H₂O and 0.07 M KCl for 15 cycles at $\nu = 0.04 \text{ V s}^{-1}$. The figure was adapted from the manuscript “H/D Isotope Effects in the Electrochemistry of Electrochromic Iron Hexacyanoruthenate”.

7.7 Voltammetry of Fe-HCR Crystals in H₂O- and D₂O-Based

Electrolytes

The phenomenon of closely spaced cathodic peaks, as shown in Figure 43, can also be observed when studying bulk-synthesized Fe-HCR nanocrystals (Figure 51). These nanocrystals, transferred as solids to a paraffin-impregnated graphite electrode, were then alternated between H₂O-based and D₂O-based KCl electrolyte solutions.

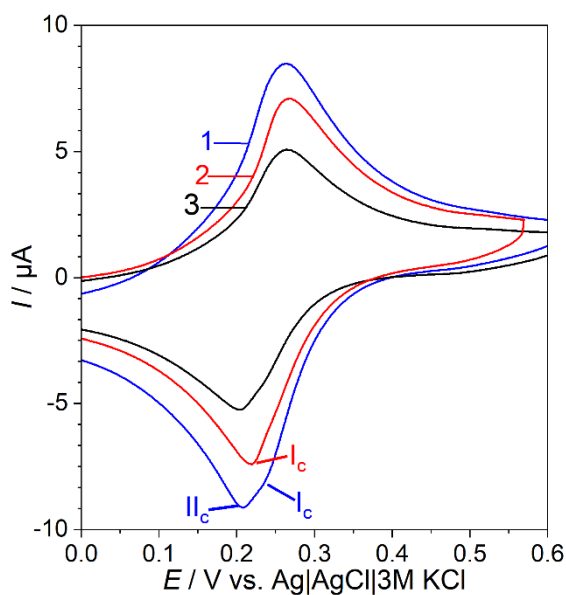


Figure 51. Cyclic voltammograms at $v = 0.01 \text{ V s}^{-1}$ were obtained for bulk-synthesized solid Fe-HCR microcrystals transferred to a paraffin-impregnated graphite electrode in 1 M KCl electrolyte. The electrolyte is based on 1) H_2O , 2) D_2O and 3) H_2O . The same electrode was used for all three voltammograms. The figure was adapted from the manuscript “H/D Isotope Effects in the Electrochemistry of Electrochromic Iron Hexacyanoruthenate”.

When the Fe-HCR crystals undergo cycling in an H_2O electrolyte, two cathodic peaks can be found at approximately 0.23 V and 0.21 V, as shown in curve 1 in Figure 51. However, the second peak is absent when the same electrode is transferred to a D_2O -containing electrolyte and cycled again (Figure 51, curve 2). This effect is reversible: transferring back to an H_2O -based electrolyte restores the shoulder at approximately 0.21 V (Figure 51, curve 3).

7.8 XPS Investigations of the Material

XPS analysis was conducted on electrodeposited films to obtain information about the binding states and elemental composition. For the discussion, three samples are considered: Fe-HCR deposited in H_2O both, in its oxidized (Fe-HCR-H-ox) and reduced (Fe-HCR-H-red) states; Fe-HCR deposited in H_2O with one additional cycle in D_2O electrolyte in both, the reduced and oxidized states (Fe-HCR-H-D-red and Fe-HCR-H-D-ox, respectively); and Fe-HCR deposited in a D_2O -based electrolyte solution, in the reduced and oxidized states (Fe-HCR-D-red and Fe-HCR-D-ox, respectively). Notable spectral differences between samples deposited or cycled in H_2O - versus D_2O -based electrolytes can be seen in the O 1s spectra in Figure 52.

In Figure 52a, c and e, the reduced forms of the Fe-HCR samples exhibit three distinct spectral components. The first component at 533.5 eV is associated with crystal water within the structure,¹⁵⁴ while the second component at 531.9 eV is ascribed to hydroxides.^{154,192} The third O 1s component, found at an even lower binding energy of 529.9 eV, corresponds to oxygen atoms bonded to metal centers, which will be referred to as coordinated O for brevity.¹⁹² Notably, this coordinated O signal is distinctly visible for the oxidized form of Fe-HCR-H-D in Figure 52d. In Figures 52b and 52f, which depict the oxidized forms of Fe-HCR-H and Fe-HCR-D, there is only a small third component at 530.4 eV (Fe-HCR-H-ox) and 529.8 eV (Fe-HCR-D-ox), which contributes to a good fit. The component at around 530.0 eV might be associated with an oxo-ruthenium species in the Fe-HCR network.¹⁵⁵

The reference material $K_4[Ru(CN)_6] \times mH_2O$ is analyzed in Figure 56c, and the positions of the fitted components can be found in Table 29. The component observed at low binding energies at 530.6 eV is attributed to metal-coordinated oxygen. The component at 532.2 eV is ascribed to (oxide-) hydroxides, as already reported by Cataldi et al.¹⁵⁴

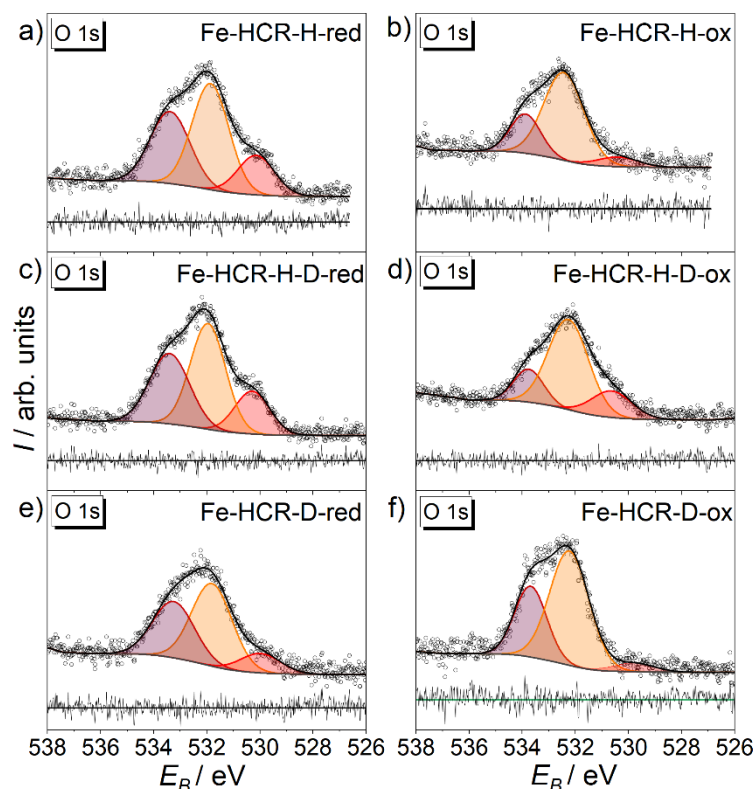


Figure 52. O 1s high-resolution XP spectra of Fe-HCR-H a) reduced, b) oxidized; Fe-HCR-H-D c) reduced, d) oxidized; Fe-HCR-D e) reduced, f) oxidized. The films were deposited from 0.001 M $\text{FeCl}_3 \times 6 \text{H}_2\text{O}$, 0.001 M $\text{K}_4[\text{Ru}(\text{CN})_6] \times m\text{H}_2\text{O}$ and 0.07 M KCl for 15 cycles at $\nu = 0.04 \text{ V s}^{-1}$ in H_2O - or D_2O -containing electrolyte solution. To receive the reduced or oxidized form, the deposition was stopped at -0.2 V (reduced form) or $+0.6 \text{ V}$ (oxidized form). The figure was adapted from the manuscript “H/D Isotope Effects in the Electrochemistry of Electrochromic Iron Hexacyanoruthenate”.

Table 19 presents elemental ratios for the studied compounds without distinguishing between the different components of the O 1s signal. Additionally, the table includes the ratio between Fe^{III} and Fe^{II} species. Overall, the reduced and oxidized samples show comparable relative Fe content when referenced to the N-content. However, the Ru-content varies depending on the samples and their respective oxidation state. The O : N ratio remains relatively consistent in most samples, except the oxidized Fe-HCR-H-D sample. These results suggest structural variations within the sample, as hypothesized by Abe et al.⁷ Similar changes have also been observed for other M-HCMs, like Ni-HCF.^{160,61} Such structural differences may account for the different electrochemical behavior observed.

Table 19. Quantitative analysis of XPS measurements of the samples presented in Figure 52. The films were deposited from 0.001 M $\text{FeCl}_3 \times 6 \text{H}_2\text{O}$, 0.001 M $\text{K}_4[\text{Ru}(\text{CN})_6] \times m\text{H}_2\text{O}$ and 0.07 M KCl for 15 cycles at $v = 0.04 \text{ V s}^{-1}$ in H_2O - or D_2O -containing electrolyte solution. The data was taken from the manuscript “H/D Isotope Effects in the Electrochemistry of Electrochromic Iron Hexacyanoruthenate”.

| Component | Fe:N | Ru:N | Ru:Fe | O:N | $\text{Fe}^{\text{III}}:\text{Fe}^{\text{II}}$ |
|--|------|------|-------|------|--|
| Fe-HCR-H-red | 0.18 | 0.23 | 1.29 | 0.24 | - |
| Fe-HCR-H-D-red | 0.20 | 0.30 | 1.51 | 0.23 | - |
| Fe-HCR-D-red | 0.19 | 0.15 | 0.80 | 0.24 | - |
| Fe-HCR-H-ox | 0.21 | 0.20 | 0.93 | 0.18 | 1.08 |
| Fe-HCR-H-D-ox | 0.45 | 0.28 | 0.60 | 0.60 | 2.34 |
| Fe-HCR-D-ox | 0.41 | 0.16 | 0.39 | 0.25 | 1.05 |
| $\text{K}_4[\text{Ru}(\text{CN})_6]^a$ | - | 0.18 | - | 0.07 | - |

^a Measured as a reference sample.

Considering that the oxygen species at 529.9 eV and 531.9 eV can be coordinated to the transition metals, the stoichiometry of the Fe-HCR films can be derived as shown in Table 20. To compare the different compositions, the ratios were normalized to represent five cyanide ligands. The intensities of the C 1s components have not been used due to disturbances from ubiquitous carbon contamination in samples from the ambient environment. In all samples, the Ru content is higher than expected from the stoichiometry of $\text{K}_4[\text{Ru}(\text{CN})_6] \times n\text{H}_2\text{O}$.

Additionally, there is a noticeable shift in the Fe : N ratio with changes in the oxidation state (Fe-HCR-D-red versus Fe-HCR-D-ox and Fe-HCR-H-D-red versus Fe-HCR-H-D-ox), which is also mirrored in the Ru : Fe content ratios. The ratio remains stable (within uncertainty margins) for the sample prepared in H_2O (Fe-HCR-H-red versus Fe-HCR-H-ox). The ratios of Ru : N are fairly stable for the different films and oxidation states.

Table 20. Calculated stoichiometries of Fe-HCR compounds deposited in electrolyte solutions based on H_2O , D_2O , and H_2O with additional oxidation/reduction in D_2O . The data was taken from the manuscript “H/D Isotope Effects in the Electrochemistry of Electrochromic Iron Hexacyanoruthenate”.

| Compound | Stoichiometry |
|----------------|--|
| Fe-HCR-H-red | $\text{K}_{3.1}\text{Fe}_{0.9}[\text{Ru}_{1.7}(\text{CN})_5(\text{OH}/\text{O})_{0.77}] \times x\text{H}_2\text{O}$ |
| Fe-HCR-H-ox | $\text{K}_{1.54}\text{Fe}_{1.1}[\text{Ru}_{1.64}(\text{CN})_5(\text{OH})_{0.8}] \times x\text{H}_2\text{O}$ |
| Fe-HCR-H-D-red | $\text{K}_{3.6}\text{Fe}_{0.95}[\text{Ru}_{1.67}(\text{CN})_5(\text{OH}/\text{O})_{0.76}] \times x\text{H}_2\text{O}$ |
| Fe-HCR-H-D-ox | $\text{K}_{1.81}\text{Fe}_{2.25}[\text{Ru}_{1.67}(\text{CN})_5(\text{OH}/\text{O})_{2.67}] \times x\text{H}_2\text{O}$ |
| Fe-HCR-D-red | $\text{K}_3\text{Fe}_{0.95}[\text{Ru}_{1.61}(\text{CN})_5(\text{OH})_{1.1}] \times x\text{H}_2\text{O}$ |
| Fe-HCR-D-ox | $\text{K}_{1.3}\text{Fe}_{2.1}[\text{Ru}_{1.64}(\text{CN})_5(\text{OH})_{0.87}] \times x\text{H}_2\text{O}$ |

In Figure 53-55a, b and 56a, the C 1s components observed at 285.9 - 286.6 eV can be assigned to sp^2 carbon species,¹²⁹ and the signal at 289.2 - 289.6 eV can be attributed to $\pi \rightarrow \pi^*$ shake-up satellite (further details are given in Tables 23-29).¹²⁹ However, C 1s XP spectra are not considered for quantitative analysis due to the challenge of differentiating between carbon atoms from the Fe-HCR coordination network and adventitious carbon.¹²¹ Table 21 displays the C : N ratios determined by XPS. These ratios indicate the presence of adventitious carbon, as the experimental C : N ratio consistently exceeds 1 : 1 expected for M-HCMs.

Table 21. Quantitative XPS analysis of C : N ratios found in the XPS samples. The data was taken from the manuscript "H/D Isotope Effects in the Electrochemistry of Electrochromic Iron Hexacyanoruthenate".

| Sample | Ratio C : N |
|----------------|-------------|
| Fe-HCR-H-red | 1.4 : 1.0 |
| Fe-HCR-H-ox | 1.5 : 1.0 |
| Fe-HCR-H-D-red | 1.3 : 1.0 |
| Fe-HCR-H-D-ox | 2.0 : 1.0 |
| Fe-HCR-D-red | 1.5 : 1.0 |
| Fe-HCR-D-ox | 1.2 : 1.0 |

In one of the few reports on XPS of Fe-HCR, Cataldi et al.¹⁵⁵ characterized the Ru $3d_{5/2}$ spectrum with only one component at 281.0 eV, associated with Ru-CN. The authors assumed the presence of an oxo-Ru^{IV} species at a binding energy very close to this value, consistent with the Ru $3d_{5/2}$ in Ru^{IV}O₂ reference samples observed at 280.7 eV.¹⁹³ However, Cataldi et al.¹⁵⁵ could not resolve the small difference in binding energy spectroscopically.

In the materials discussed in this work, the Ru : N elemental ratio consistently exceeds the expected value of 1 : 6 (Table 20, 22), indicating the presence of oxo-Ru^{IV} species. This trend is not only observed in Fe-HCR materials but is also found in K₄[Ru(CN)₆] (Table 22). The high-resolution spectra of Ru $3d_{5/2}$ spectrum show a slight asymmetry, which is unusual for Ru^{II} compound. Consequently, a fit with two components was attempted: one at the peak maximum (280.7 – 281.0 eV) and the other at a slightly higher binding energy (280.9 – 281.4 eV). Given that Ru^{II} is not expected to participate in a redox process within the studied potential range in this work (Eq. 1 and Eq. 3), the Ru $3d_{5/2}$ spectra for both the oxidized and reduced Fe-HCR materials appear similar.

Table 22. Stoichiometries of the Fe-HCR samples, referenced on N ($n = 6$), depending on the number of Ru compounds considered while fitting. The films were deposited from 0.001 M $\text{FeCl}_3 \times 6 \text{H}_2\text{O}$, 0.001 M $\text{K}_4[\text{Ru}(\text{CN})_6] \times m\text{H}_2\text{O}$ and 0.07 M KCl for 15 cycles at $v = 0.04 \text{ V s}^{-1}$ in H_2O - or D_2O -containing electrolyte solution. The data was taken from the manuscript “H/D Isotope Effects in the Electrochemistry of Electrochromic Iron Hexacyanoruthenate”.

| Fe-HCR sample | Stoichiometry with total Ru content | Stoichiometry considering only the Ru compound at $E_B = 280.7 - 281.0 \text{ eV}$ |
|---|---|--|
| Fe-HCR- H_2O red | $\text{K}_{3.7}\text{Fe}_{1.1}[\text{Ru}_{2.0}(\text{CN})_6]^b$ | $\text{K}_{3.7}\text{Fe}_{1.1}[\text{Ru}_{1.4}(\text{CN})_6]^a$ |
| Fe-HCR- H_2O ox | $\text{K}_{1.9}\text{Fe}_{1.3}[\text{Ru}_{1.9}(\text{CN})_6]^b$ | $\text{K}_{1.9}\text{Fe}_{2.3}[\text{Ru}_{1.2}(\text{CN})_6]^a$ |
| Fe-HCR- $\text{H}_2\text{O}/\text{D}_2\text{O}$ red | $\text{K}_{4.1}\text{Fe}_{1.1}[\text{Ru}_{1.9}(\text{CN})_6]^b$ | $\text{K}_{3.4}\text{Fe}_{1.2}[\text{Ru}_{1.8}(\text{CN})_6]^a$ |
| Fe-HCR- $\text{H}_2\text{O}/\text{D}_2\text{O}$ ox | $\text{K}_{2.2}\text{Fe}_{2.7}[\text{Ru}_{2.0}(\text{CN})_6]^b$ | $\text{K}_{2.3}\text{Fe}_{2.7}[\text{Ru}_{1.7}(\text{CN})_6]^a$ |
| Fe-HCR- D_2O red | $\text{K}_{3.6}\text{Fe}_{1.1}[\text{Ru}_{1.9}(\text{CN})_6]^b$ | $\text{K}_{3.6}\text{Fe}_{1.1}[\text{Ru}_{0.9}(\text{CN})_6]^a$ |
| Fe-HCR- D_2O ox | $\text{K}_{1.5}\text{Fe}_{2.5}[\text{Ru}_{2.0}(\text{CN})_6]^b$ | $\text{K}_{1.5}\text{Fe}_{2.9}[\text{Ru}_{1.0}(\text{CN})_6]^a$ |
| $\text{K}_4[\text{Ru}(\text{CN})_6] \times m\text{H}_2\text{O}$ | $\text{K}_4[\text{Ru}_{2.1}(\text{CN})_6]$ | $\text{K}_4[\text{Ru}_{1.1}(\text{CN})_6]$ |

The high-resolution K 2p spectra indicate two distinct components in all spectra (Figures 53-55a, b, Tables 23-28), particularly evident in Figure 54b. The occurrence of two peaks is not attributed to charging effects since no charging effects were found in the other spectra in Figure 54b. The other K 2p spectra are also consistently described with two strongly overlapping doublets. A fit with just one component fails to explain the asymmetry of the experimentally measured peaks. Even in Figure 56, $\text{K}_4[\text{Ru}(\text{CN})_6] \times n\text{H}_2\text{O}$, as a reference and a precursor for synthesizing Fe-HCR compounds, exhibits two K 2p_{3/2} components.

The binding energies for K 2p_{3/2} in Table 29 align with findings from previous research. Malik et al.¹²¹ found the K 2p_{3/2} compound of Fe-HCF on stainless steel at 293.3 eV (K 2p_{3/2}), while Emrich et al.¹⁹⁴ reported the K 2p_{3/2} signal for Fe-HCF at 293.9 eV. The presence of two K 2p_{3/2} peaks within a single spectrum remains not fully understood yet; most studies reported only a single K 2p_{3/2} compound in $\text{K}_4[\text{Ru}(\text{CN})_6]$,¹²⁸ and in many cases, the K 2p spectral region is not shown. However, Cano et al.¹²⁸ observed a shift in the K 2p_{3/2} for different potassium hexacyanometallate salts, attributing them to variations in crystal structures and electronic configurations.

N 1s spectra display one dominant component in the region of 397.7 – 398.9 eV (Figures 53-55e, f; Figure 56b; Tables 23-29). For a precise fit, two additional components are considered.

According to existing literature,¹⁵⁶ the main signal at 397.7 - 398.0 eV, can be assigned to $C\equiv N$ atoms. The exact binding energy of photoelectrons from cyanide nitrogen atoms varies depending on the oxidation states and the types of metal cations complexed.¹²⁹ In the current measurements, no significant peak shift was observed upon changing the Fe oxidation state.

The second compound identified in the N 1s spectra of Fe-HCR appears at 399.3 - 399.8 eV. This peak has also been observed in $K_2[Pd(CN)_4]$,¹⁵⁶ KCN¹⁵⁶ and $In_4[Fe(CN)_6]_3$ films.¹⁵⁷ It was attributed to decomposition products within the material, although the precise nature of these components remained unidentified.^{156,157} The signal found in the range of 402.5 - 403.0 eV can be assigned to $\pi\rightarrow\pi^*$ shake-up transitions, common in compounds with π electron systems near the emitter atom.¹²⁸ The energy difference between the $\pi\rightarrow\pi^*$ shake-up transitions and the main signal varies within the 3-5 eV range.¹²⁸

In the reduced forms of the Fe-HCR samples, as evident in Figures 53c, 54c and 55c, the Fe 2p_{3/2} spectra were fitted using the calculated intensity ratio within the multiplet¹²⁶ for free high-spin Fe²⁺ ions since N-coordinated Fe in Fe-HCR is in high-spin state.^{126,195} Additionally, a shake-up satellite and a surface peak were added in accordance with Grosvenor et al.¹²². This approach yielded a good fit for all three samples in the reduced state, as shown in Figures 53c, 54c and 55c. Notably, a peak at low binding energies was also added (708.1 eV in Figure 53c and Table 23, 708.5 eV in Figure 54c and Table 25, and 709.0 eV in Figure 55c and Table 27), which might be indicative of a minor presence of low-spin Fe²⁺ compounds in the samples.¹²³ This could arise from Ru-N \equiv C-Fe binding motifs within the network. Similar results were reported in studies of Cu-HCF thin films,¹⁶¹ where the binding motif can be denoted as Cu-N \equiv C-Fe, with a small fraction of the material potentially altering the motif to Fe-N \equiv C-Cu. A change to the C-coordination of some Fe centers in the network could lead to low-spin species within the material. Grosvenor et al.¹²² discussed the presence of a low binding energy 'pre-peak' in samples with high-spin Fe²⁺ of FeBr₂, FeCl₂, FeF₂, FeSO₄ and Fe_{1.1}O. The pre-peak was associated with the formation of Fe ions with a 'lower than normal' oxidation state due to the production of defects in neighboring sites.¹²²

In the case of oxidized Fe-HCR samples, as shown in Figures 53d, 54d and 55d, iron in oxidation state Fe³⁺ is expected, as can be concluded from Eq. 1 and Eq. 3. However, the presence of high-spin Fe²⁺ multiplets in Figures 53d, 54d, and 55d as well as in Tables 24, 26 and 28 suggests that the oxidation process may not be complete. This redox behavior was

previously observed in literature for $\text{K}_2\text{Ni}[\text{Fe}(\text{CN})_6]/\text{KNi}[\text{Fe}(\text{CN})_6]$ compounds.¹²³ Moreover, it has been observed that Fe-HCF does not always undergo complete oxidation of the N-coordinated Fe^{2+} .¹⁹⁶ The partial oxidation observed in $\text{Fe}_4[\text{Fe}(\text{CN})_6]_3$ was assumed to result from incomplete extraction of K^+ ions left in the structure from the precursor $\text{K}_3[\text{Fe}(\text{CN})_6]$. It was assumed that insufficient withdrawal of K^+ leads to residual Fe^{2+} in the oxidized structure.¹⁹⁶

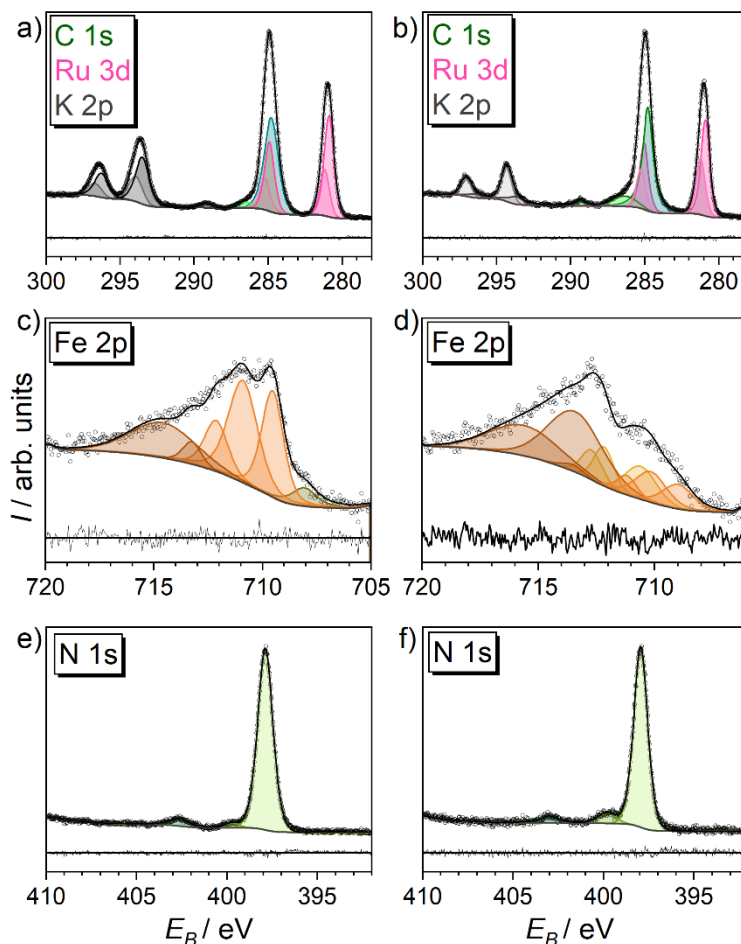


Figure 53. High-resolution XPS spectra of the reduced Fe-HCR-H a) C 1s, Ru 3d, K 2p; c) Fe 2p; e) N 1s; and high-resolution XPS spectra of oxidized Fe-HCR-H b) C 1s, Ru 3d, K 2p; d) Fe 2p and f) N 1s. The films were deposited from 0.001 M $\text{FeCl}_3 \times 6 \text{H}_2\text{O}$, 0.001 M $\text{K}_4[\text{Ru}(\text{CN})_6] \times m\text{H}_2\text{O}$ and 0.07 M KCl for 15 cycles at $\nu = 0.04 \text{ V s}^{-1}$ in H_2O -containing electrolyte solution. To receive the reduced or oxidized form, the deposition was stopped at -0.2 V (reduced form) or $+0.6 \text{ V}$ (oxidized form). The figure was adapted from the manuscript “H/D Isotope Effects in the Electrochemistry of Electrochromic Iron Hexacyanoruthenate”.

Table 23. Components in the high-resolution XP spectra of Fe-HCR-H red. The film was deposited from 0.001 M FeCl₃ × 6 H₂O, 0.001 M K₄[Ru(CN)₆] × *m*H₂O and 0.07 M KCl for 15 cycles at $v = 0.04 \text{ V s}^{-1}$ in H₂O-containing electrolyte solution. ls – low-spin, hs – high-spin. The data were taken from the manuscript “H/D Isotope Effects in the Electrochemistry of Electrochromic Iron Hexacyanoruthenate”.

| Fe-HCR-H-red | | |
|----------------------------------|---------------------|------------|
| Ru 3d | Binding Energy / eV | Literature |
| Ru 3d _{5/2} (Ru-CN) | 280.9 | 155 |
| Ru 3d _{3/2} (Ru-CN) | 284.9 | 155 |
| Ru 3d _{5/2} (Ru-O) | 281.2 | 155,193 |
| Ru 3d _{3/2} (Ru-O) | 285.2 | 155,193 |
| C 1s | | |
| Adventitious carbon / CN | 284.8 | 129 |
| sp ² | 286.5 | 129 |
| $\pi \rightarrow \pi^*$ shake-up | 289.2 | 129 |
| K 2p | | |
| K 2p _{3/2} | 293.5 | 121 |
| K 2p _{1/2} | 296.3 | 121 |
| K 2p _{3/2} | 294.0 | 121,194 |
| K 2p _{1/2} | 296.7 | 121,194 |
| Fe 2p _{3/2} | | |
| Fe ²⁺ ls / ‘pre-peak’ | 708.1 | 122,123 |
| Fe ²⁺ hs | 709.5 | 126,122 |
| Fe ²⁺ hs | 710.9 | 126,122 |
| Fe ²⁺ hs | 712.1 | 126,122 |
| Shake-up | 713.3 | 122 |
| Surface peak | 714.6 | 122 |
| N 1s | | |
| Fe ^{II} -NC | 397.9 | 156 |
| Decomposition product | 399.7 | 156,157 |
| $\pi \rightarrow \pi^*$ shake-up | 402.7 | 128 |
| O 1s | | |
| Absorbed water species | 533.4 | 154 |
| (oxide-) hydroxides | 531.9 | 154 |
| M-O | 530.1 | 192 |

Table 24. Components in the high-resolution XP spectra of Fe-HCR-H ox. The film was deposited from 0.001 M FeCl₃ × 6 H₂O, 0.001 M K₄[Ru(CN)₆] × mH₂O and 0.07 M KCl for 15 cycles at $\nu = 0.04 \text{ V s}^{-1}$ in H₂O-containing electrolyte solution. Is – low spin, hs – high spin. The data were taken from the manuscript “H/D Isotope Effects in the Electrochemistry of Electrochromic Iron Hexacyanoruthenate”.

| Fe-HCR-H-ox | | |
|----------------------------------|---------------------|------------|
| Ru3d | Binding Energy / eV | Literature |
| Ru 3d _{5/2} (Ru-CN) | 280.9 | 155 |
| Ru 3d _{3/2} (Ru-CN) | 285.0 | 155 |
| Ru 3d _{5/2} (Ru-O) | 281.2 | 155,193 |
| Ru 3d _{3/2} (Ru-O) | 285.3 | 155,193 |
| C 1s | | |
| Adventitious carbon / CN | 284.8 | 129 |
| sp ² | 286.4 | 129 |
| $\pi \rightarrow \pi^*$ shake-up | 289.4 | 129 |
| K 2p | | |
| K 2p _{3/2} | 293.7 | 121 |
| K 2p _{1/2} | 296.4 | 121 |
| K 2p _{3/2} | 294.3 | 121,194 |
| K 2p _{1/2} | 297.1 | 121,194 |
| Fe 2p _{3/2} | | |
| Fe ²⁺ hs | 709.0 | 126,122 |
| Fe ²⁺ hs | 710.2 | 126,122 |
| Fe ²⁺ hs | 711.2 | 126,122 |
| Fe ²⁺ hs shake-up | 713.5 | 126,122 |
| Fe ³⁺ hs | 710.6 | 126,122 |
| Fe ³⁺ hs | 712.2 | 126,122 |
| Fe ³⁺ hs | 712.7 | 126,122 |
| Sattelite | 713.4 | 122 |
| Sattelite | 715.6 | 122 |
| N 1s | | |
| Fe ^{II} -NC | 398.0 | 156 |
| Decomposition product | 399.8 | 156,157 |
| $\pi \rightarrow \pi^*$ shake-up | 403.00 | 128 |
| O 1s | | |
| Absorbed water species | 533.9 | 154 |
| (oxide-) hydroxides | 532.4 | 154 |
| M-O | 530.4 | 192 |

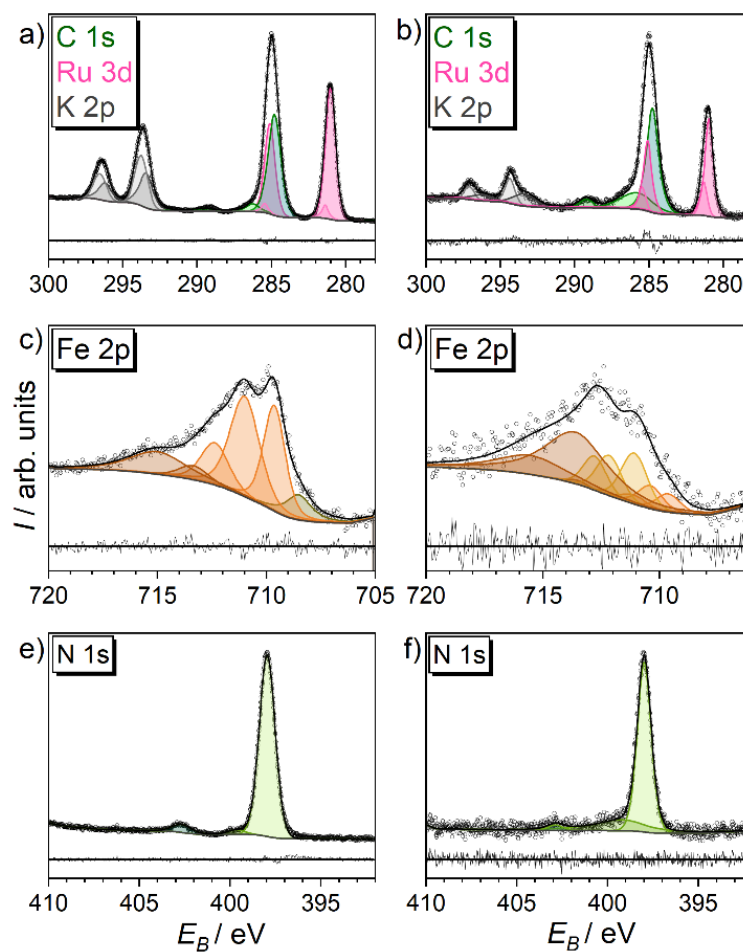


Figure 54. High-resolution XPS spectra of the reduced Fe-HCR-H-D a) C 1s, Ru 3d, K 2p; c) Fe 2p; e) N 1s; and high-resolution XPS spectra of oxidized Fe-HCR-H-D b) C 1s, Ru3d, K 2p; d) Fe 2p and f) N 1s. The films were deposited from 0.001 M $\text{FeCl}_3 \times 6 \text{H}_2\text{O}$, 0.001 M $\text{K}_4[\text{Ru}(\text{CN})_6] \times m\text{H}_2\text{O}$ and 0.07 M KCl for 15 cycles at $\nu = 0.04 \text{ V s}^{-1}$ in H_2O -containing electrolyte solution with a subsequent cycle in 1 M KCl in D_2O -containing electrolyte solution. To receive the reduced or oxidized form, the deposition was stopped at -0.2 V (reduced form) or +0.6 V (oxidized form). The figure was adapted from the manuscript “H/D Isotope Effects in the Electrochemistry of Electrochromic Iron Hexacyanoruthenate”.

Isotope Effect in Metal Hexacyanometallates

Table 25. Components in the high-resolution XP spectra of Fe-HCR-H-D-red. The film was deposited from 0.001 M FeCl₃ × 6 H₂O, 0.001 M K₄[Ru(CN)₆] × mH₂O and 0.07 M KCl for 15 cycles at $v = 0.04$ V s⁻¹ in H₂O-containing electrolyte solution with a subsequent cycle in 1 M KCl in D₂O. ls – low spin, hs – high spin. The data was taken from the manuscript “H/D Isotope Effects in the Electrochemistry of Electrochromic Iron Hexacyanoruthenate”.

| Fe-HCR-H-D-red | | |
|----------------------------------|--------|---------|
| Ru3d | | |
| Ru 3d _{5/2} (Ru-CN) | 281.0 | 155 |
| Ru 3d _{3/2} (Ru-CN) | 285.1 | 155 |
| Ru 3d _{5/2} (Ru-O) | 281.4 | 155,193 |
| Ru 3d _{3/2} (Ru-O) | 285.44 | 155,193 |
| C 1s | | |
| Adventitious carbon / CN | 284.8 | 129 |
| sp ² | 286.3 | 129 |
| π→π* shake-up | 289.6 | 129 |
| K 2p | | |
| K 2p _{3/2} | 293.5 | 121 |
| K 2p _{1/2} | 296.2 | 121 |
| K 2p _{3/2} | 293.8 | 121,194 |
| K 2p _{1/2} | 296.46 | 121,194 |
| Fe 2p_{3/2} | | |
| Fe ²⁺ ls / 'pre-peak' | 708.5 | 122,123 |
| Fe ²⁺ hs | 709.6 | 126,122 |
| Fe ²⁺ hs | 711.0 | 126,122 |
| Fe ²⁺ hs | 712.4 | 126,122 |
| Shake-up | 713.4 | 122 |
| Surface peak | 715.0 | 122 |
| N 1s | | |
| Fe ^{II} -NC | 398.0 | 156 |
| Decomposition product | 399.7 | 156,157 |
| π→π* shake-up | 402.6 | 128 |
| O 1s | | |
| Absorbed water species | 533.4 | 154 |
| (oxide-) hydroxides | 532.0 | 154 |
| M-O | 530.3 | 192 |

Table 26. Components in the high-resolution XP spectra of Fe-HCR-H-D-ox. The film was deposited from 0.001 M FeCl₃ × 6 H₂O, 0.001 M K₄[Ru(CN)₆] × *m*H₂O and 0.07 M KCl for 15 cycles at $\nu = 0.04$ V s⁻¹ in H₂O-containing electrolyte solution with a subsequent cycle in 1 M KCl in D₂O. ls – low spin, hs – high spin. The data were taken from the manuscript “H/D Isotope Effects in the Electrochemistry of Electrochromic Iron Hexacyanoruthenate”.

| Fe-HCR-H-D-ox | | |
|----------------------------------|---------------------|------------|
| Ru3d | Binding Energy / eV | Literature |
| Ru 3d _{5/2} (Ru-CN) | 281.0 | 155 |
| Ru 3d _{3/2} (Ru-CN) | 285.1 | 155 |
| Ru 3d _{5/2} (Ru-O) | 281.4 | 155,193 |
| Ru 3d _{3/2} (Ru-O) | 285.5 | 155,193 |
| C 1s | | |
| Adventitious carbon / CN | 284.8 | 129 |
| sp ² | 285.9 | 129 |
| $\pi \rightarrow \pi^*$ shake-up | 289.3 | 129 |
| K 2p | | |
| K 2p _{3/2} | 293.4 | 121 |
| K 2p _{1/2} | 296.3 | 121 |
| K 2p _{3/2} | 294.4 | 121,194 |
| K 2p _{1/2} | 297.1 | 121,194 |
| Fe 2p _{3/2} | | |
| Fe ²⁺ hs | 709.7 | 126,122 |
| Fe ²⁺ ls | 710.4 | 126,122 |
| Fe ²⁺ hs | 711.1 | 126,122 |
| Fe ²⁺ shake-up | 713.5 | 126,122 |
| Fe ³⁺ hs | 711.1 | 126,122 |
| Fe ³⁺ ls | 712.2 | 126,122 |
| Fe ³⁺ hs | 712.8 | 126,122 |
| Sattelite | 713.6 | 126,122 |
| Sattelite | 715.6 | 126,122 |
| N 1s | | |
| Fe ^{II} -NC | 398.0 | 156 |
| Decomposition product | 399.3 | 156,157 |
| $\pi \rightarrow \pi^*$ shake-up | 402.9 | 128 |
| O 1s | | |
| Absorbed water species | 533.8 | 154 |
| (oxide-) hydroxides | 532.3 | 154 |
| M-O | 530.6 | 192 |

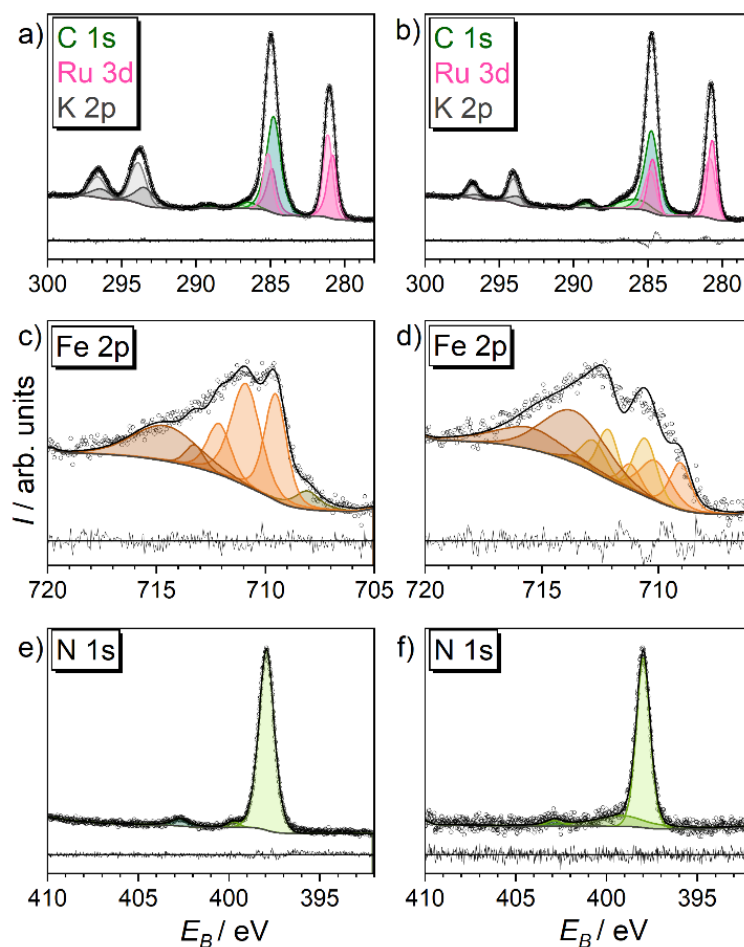


Figure 55. High-resolution XPS spectra of the reduced Fe-HCR-D a) C 1s, Ru 3d, K 2p; c) Fe 2p; e) N 1s; and high-resolution XPS spectra of the oxidized Fe-HCR-D b) C 1s, Ru3d, K 2p; d) Fe 2p and f) N1s. The films were deposited from 0.001 M $\text{FeCl}_3 \times 6 \text{H}_2\text{O}$, 0.001 M $\text{K}_4[\text{Ru}(\text{CN})_6] \times m\text{H}_2\text{O}$ and 0.07 M KCl for 15 cycles at $\nu = 0.04 \text{ V s}^{-1}$ in D_2O -containing electrolyte solution. To receive the reduced or oxidized form, the deposition was stopped at -0.2 V (reduced form) or $+0.6 \text{ V}$ (oxidized form). The figure was adapted from the manuscript “H/D Isotope Effects in the Electrochemistry of Electrochromic Iron Hexacyanoruthenate”.

Table 27. Components in the high-resolution XP spectra of Fe-HCR-D red. The films were deposited from 0.001 M $\text{FeCl}_3 \times 6 \text{H}_2\text{O}$, 0.001 M $\text{K}_4[\text{Ru}(\text{CN})_6] \times m\text{H}_2\text{O}$ and 0.07 M KCl for 15 cycles at $v = 0.04 \text{ V s}^{-1}$ in D_2O -containing electrolyte solution. ls – low spin, hs – high spin. The data were taken from the manuscript “H/D Isotope Effects in the Electrochemistry of Electrochromic Iron Hexacyanoruthenate”.

| Fe-HCR-D-red | | |
|----------------------------------|---------------------|------------|
| Ru3d | Binding Energy / eV | Literature |
| Ru 3d _{5/2} (Ru-CN) | 280.8 | 155 |
| Ru 3d _{3/2} (Ru-CN) | 284.9 | 155 |
| Ru 3d _{5/2} (Ru-O) | 281.1 | 155,193 |
| Ru 3d _{3/2} (Ru-O) | 285.2 | 155,193 |
| C 1s | | |
| Adventitious carbon / CN | 284.8 | 129 |
| sp ² | 286.5 | 129 |
| $\pi \rightarrow \pi^*$ shake-up | 289.2 | 129 |
| K 2p | | |
| K 2p _{3/2} | 293.5 | 121 |
| K 2p _{1/2} | 296.4 | 121 |
| K 2p _{3/2} | 293.9 | 121,194 |
| K 2p _{1/2} | 296.6 | 121,194 |
| Fe 2p _{3/2} | | |
| Fe ²⁺ ls / ‘pre-peak’ | 709.0 | 122,123 |
| Fe ²⁺ hs | 709.9 | 126,122 |
| Fe ²⁺ hs | 711.2 | 126,122 |
| Fe ²⁺ hs | 712.6 | 126,122 |
| Shake-up | 713.6 | 122 |
| Surface peak | 714.5 | 122 |
| N 1s | | |
| Fe ^{II} -NC | 398.0 | 156 |
| Decomposition product | 399.8 | 156,157 |
| $\pi \rightarrow \pi^*$ shake-up | 402.7 | 128 |
| O 1s | | |
| Absorbed water species | 533.3 | 154 |
| (oxide-) hydroxides | 531.8 | 154 |
| M-O | 530.0 | 192 |

Table 28. Components in the high-resolution XP spectra of Fe-HCR-D-ox. The films were deposited from 0.001 M FeCl₃ × 6 H₂O, 0.001 M K₄[Ru(CN)₆] × mH₂O and 0.07 M KCl for 15 cycles at $v = 0.04$ V s⁻¹ in D₂O-containing electrolyte solution. ls – low spin, hs – high spin. The data were taken from the manuscript “H/D Isotope Effects in the Electrochemistry of Electrochromic Iron Hexacyanoruthenate”.

| Fe-HCR-D-ox | | |
|------------------------------|---------------------|------------|
| Ru3d | Binding Energy / eV | Literature |
| Ru 3d _{5/2} (Ru-CN) | 280.7 | 155 |
| Ru 3d _{3/2} (Ru-CN) | 284.7 | 155 |
| Ru 3d _{5/2} (Ru-O) | 280.9 | 155,193 |
| Ru 3d _{3/2} (Ru-O) | 284.9 | 155,193 |
| C 1s | | |
| Adventitious carbon / CN | 284.8 | 129 |
| sp ² | 285.9 | 129 |
| π→π* shake-up | 289.3 | 129 |
| K 2p | | |
| K 2p _{3/2} | 293.8 | 121 |
| K 2p _{1/2} | 296.6 | 121 |
| K 2p _{3/2} | 294.1 | 121,194 |
| K 2p _{1/2} | 296.8 | 121,194 |
| Fe 2p _{3/2} | | |
| Fe ²⁺ hs | 709.1 | 126,122 |
| Fe ²⁺ ls | 710.2 | 126,122 |
| Fe ²⁺ hs | 711.2 | 126,122 |
| Fe ²⁺ shake-up | 713.5 | 126,122 |
| Fe ³⁺ hs | 710.6 | 126,122 |
| Fe ³⁺ ls | 712.2 | 126,122 |
| Fe ³⁺ hs | 712.8 | 126,122 |
| Sattelite | 713.6 | 122 |
| Sattelite | 715.6 | 122 |
| N 1s | | |
| Fe-NC | 397.7 | 156 |
| Decomposition product | 399.4 | 156,157 |
| π→π* shake-up | 402.7 | 128 |
| O 1s | | |
| Absorbed water species | 533.7 | 154 |
| (oxide-) hydroxides | 532.2 | 154 |
| M-O | 529.8 | 192 |

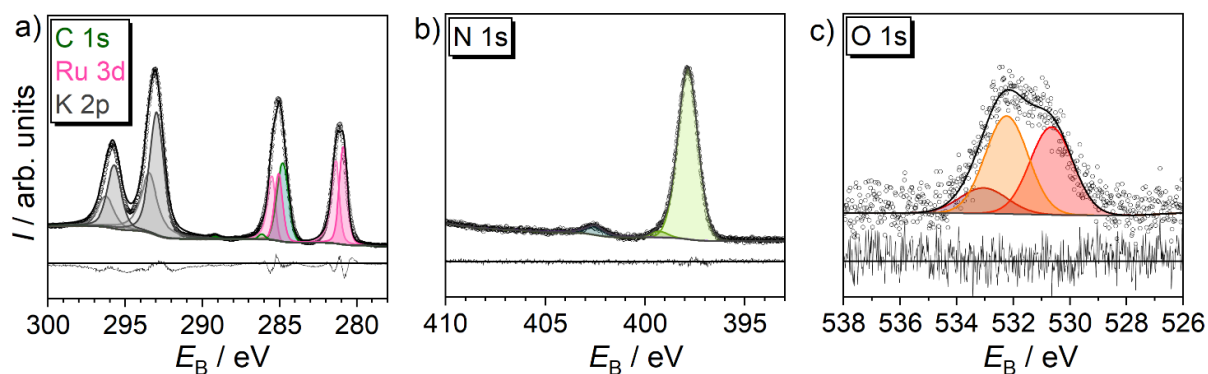


Figure 56. High-resolution XP spectra of $K_4[Ru(CN)_6] \times mH_2O$; a) Ru 3d, C 1s and K 2p; b) N 1s; c) O 1s. The figure was adapted from the manuscript “H/D Isotope Effects in the Electrochemistry of Electrochromic Iron Hexacyanoruthenate”.

Table 29. Components in the high-resolution XP spectra of $K_4[Ru(CN)_6] \times mH_2O$. The data were taken from the manuscript “H/D Isotope Effects in the Electrochemistry of Electrochromic Iron Hexacyanoruthenate”.

| $K_4[Ru(CN)_6] \times nH_2O$ | | |
|----------------------------------|---------------------|------------|
| Ru3d | Binding Energy / eV | Literature |
| Ru 3d _{5/2} (Ru-CN) | 280.9 | 155,128 |
| Ru 3d _{3/2} (Ru-CN) | 285.1 | 155,128 |
| Ru 3d _{5/2} (Ru-O) | 281.3 | 155,193 |
| Ru 3d _{3/2} (Ru-O) | 285.5 | 155,193 |
| C 1s | | |
| Adventitious carbon / CN | 284.8 | 129 |
| sp ² | 286.2 | 129 |
| $\pi \rightarrow \pi^*$ shake-up | 289.2 | 129 |
| K 2p | | |
| K 2p _{3/2} | 293.0 | 121 |
| K 2p _{1/2} | 295.7 | 121 |
| K 2p _{3/2} | 293.5 | 121,194 |
| K 2p _{1/2} | 296.3 | 121,194 |
| N 1s | | |
| Ru ^{II} -CN | 397.9 | 156 |
| Decomposition product | 399.3 | 156,157 |
| $\pi \rightarrow \pi^*$ shake-up | 402.5 | 128 |
| O 1s | | |
| (oxide-) hydroxides | 532.2 | 154 |
| M-O | 530.6 | 192 |

7.9 Polarization Modulation Infrared Reflection Absorption

Spectroscopy

Figure 57 presents the $\nu(\text{C}\equiv\text{N})$ absorption modes of the reduced and oxidized forms of the Fe-HCR materials, prepared, and measured in either H_2O - or D_2O -based solutions and recorded by PM IRRAS. In the reduced state of $\text{Fe}^{2+}\text{-N}\equiv\text{C-Ru}^{2+}$, a pronounced $\nu(\text{C}\equiv\text{N})$ absorption mode is observed at $(2088.7 \pm 0.6) \text{ cm}^{-1}$. In contrast, this mode appears at $(2114 \pm 2) \text{ cm}^{-1}$ for the oxidized form, denoted as $\text{Fe}^{3+}\text{-N}\equiv\text{C-Ru}^{2+}$. These values are in general agreement with those reported for Fe-HCF, featuring similar N-coordination of high-spin $\text{Fe}^{\text{II/III}}$.¹²⁵ The use of either H_2O or D_2O as the solvent, whether during the film preparation or spectroelectrochemical analysis, did not significantly influence the spectra of Fe-HCR film on the Au surface.

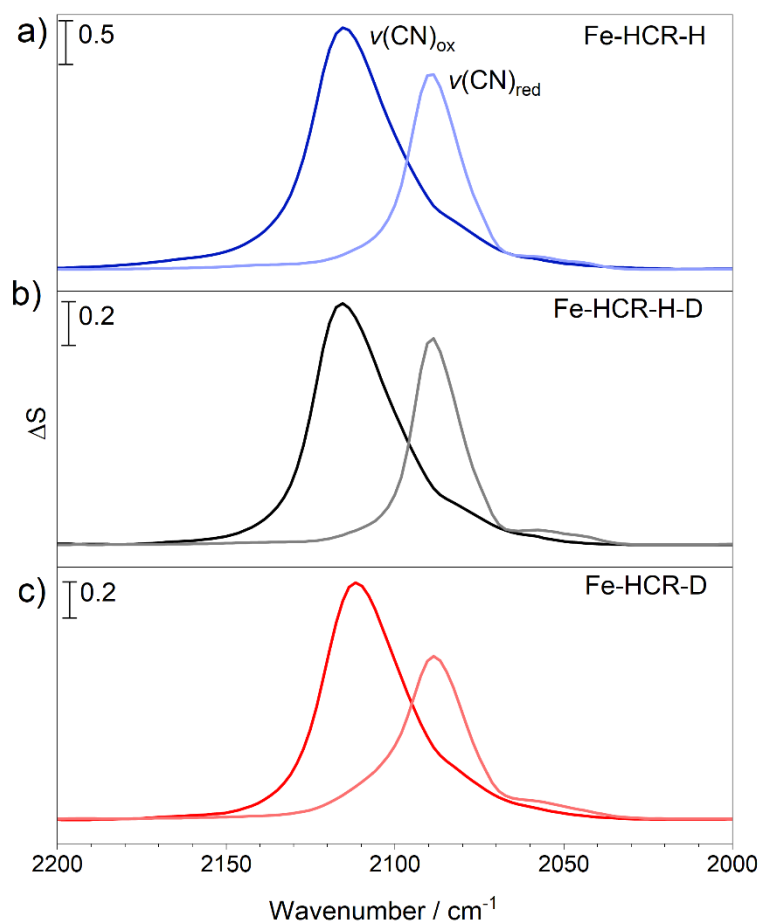


Figure 57. PM IRRAS spectra in the $\nu(\text{C}\equiv\text{N})$ stretching mode region of the Fe-HCR samples on Au substrates a) Fe-HCR-H in 1 M KCl in H_2O , b) Fe-HCR-H in 1 M KCl in D_2O and c) Fe-HCR-D in 1 M KCl in D_2O . The spectra were recorded in the electrolyte solution at half-wave retardation set to 2200 cm^{-1} at $E = 0.38\text{ V}$ (a) or $E = 0.34\text{ V}$ (b, c) for the oxidized forms and at $E = 0.0\text{ V}$ (a) and $E = 0.06\text{ V}$ (b, c) for the reduced forms. The films were deposited from $0.001\text{ M FeCl}_3 \times 6\text{ H}_2\text{O}$, $0.001\text{ M K}_4[\text{Ru}(\text{CN})_6] \times m\text{H}_2\text{O}$ and 0.07 M KCl for 15 cycles at $\nu = 0.04\text{ V s}^{-1}$ in H_2O - or D_2O -containing electrolyte solution. The figure was adapted from the manuscript “H/D Isotope Effects in the Electrochemistry of Electrochromic Iron Hexacyanoruthenate”.

While no spectroscopic differences are noted in the spectral region of the $\nu(\text{C}\equiv\text{N})$ absorption mode of Fe-HCR prepared and cycled in H_2O - or D_2O -based electrolytes, PM IRRAS can be used to distinguish between absorption modes involving $\text{H}_2\text{O}/\text{D}_2\text{O}$ and OH^-/OD^- . Such groups are expected to be present in hydrated Fe-HCR films.¹²⁵ Figure 58 shows the $\nu(\text{OH})$ and $\delta(\text{HOH})$ absorption bands in Fe-HCR material deposited on an Au electrode and measured in air. The $\nu(\text{OH})$ band is broad and comprises two or three absorption modes. In line with the preparation method, the Fe-HCR sample made in H_2O shows stronger intensities for the $\nu(\text{OH})$ and $\delta(\text{HOH})$ modes than the Fe-HCR sample prepared in D_2O . An absorption band at 3600

cm^{-1} , assigned to $\nu(\text{OH})$ in hydroxides, is observed regardless of the solvent used for preparation.^{197,198} The presence of hydroxides suggests the presence of structural defects where hydroxides are coordinated to transition metal cations, a conclusion supported by the O 1s XP spectra shown in Figure 52.

Samples prepared in H_2O (Fe-HCR-H and Fe-HCR-H-D in Figure 52a, b, respectively) display two broad $\nu(\text{OH})$ modes centered at 3400 cm^{-1} and 3200 cm^{-1} . The absorption band at 3400 cm^{-1} is assigned to water coordinated to the Fe-HCR structure or to water within a disrupted network of hydrogen bonds.¹⁹⁹ According to the structure in Figure 1b, these water molecules are likely bound to the high-spin Fe at anionic vacancies within the structure. Surprisingly, this observation also applies to the Fe-HCR-H-D sample (Figure 52b), which indicates that OH^- coordinated during preparation exchanges only slowly with D_2O .

The $\delta(\text{HOH})$ absorption band is asymmetric and centered at 1615 cm^{-1} . The shoulder of this $\delta(\text{HOH})$ band, appearing at higher wavenumbers around 1650 cm^{-1} , indicated water within a hydrogen bond network.²⁰⁰ This assignment is also made for $\nu(\text{OH})$ at 3200 cm^{-1} .¹⁹⁹ The absorption mode at 1615 cm^{-1} in Figure 52 is attributed to coordinated water within the Fe-HCR structure.²⁰⁰ Notably, these two absorption bands were only detected in samples in contact with H_2O during their preparation process. In contrast, when D_2O was used as the solvent in the preparation process, this type of water was not observed.

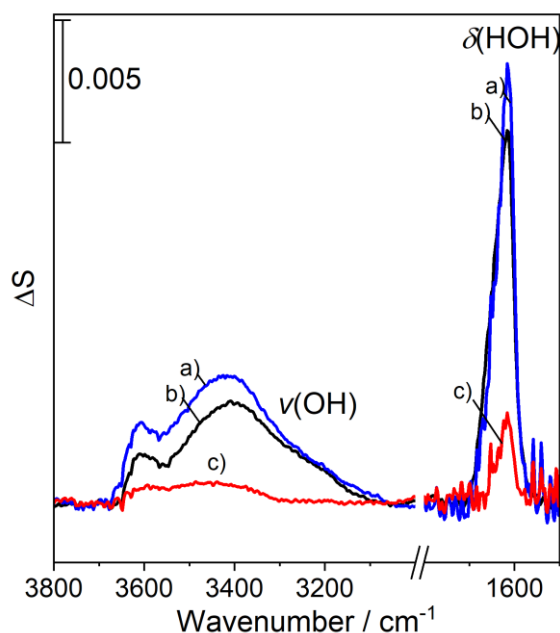


Figure 58. PM IRRA spectra of the Fe-HCR samples deposited onto a gold surface from a) Fe-HCR-H (blue line), b) Fe-HCR-H-D (black line) and c) Fe-HCR-D (red line). The composition of the electrolyte was 1 M KCl. The spectra were recorded at the air | gold interface at the half-wave retardation set to 3500 cm^{-1} and 1600 cm^{-1} . ΔS corresponds to the background-corrected intensity of the PM IRRA spectra. The films were deposited from 0.001 M $\text{FeCl}_3 \times 6 \text{H}_2\text{O}$, 0.001 M $\text{K}_4[\text{Ru}(\text{CN})_6] \times m\text{H}_2\text{O}$ and 0.07 M KCl for 15 cycles at $v = 0.04 \text{ V s}^{-1}$ in H_2O - or D_2O -containing electrolyte solution. The figure was adapted from the manuscript “H/D Isotope Effects in the Electrochemistry of Electrochromic Iron Hexacyanoruthenate”.

The $\nu(\text{OH})$ and $\nu(\text{OD})$ modes are generally broad, and subtracting the background for these peaks is complicated due to the non-linear background caused by the photoelastic modulator in PM IRRAS, which complicates the detection of the broad and weak $\nu(\text{OD})$ absorption modes.

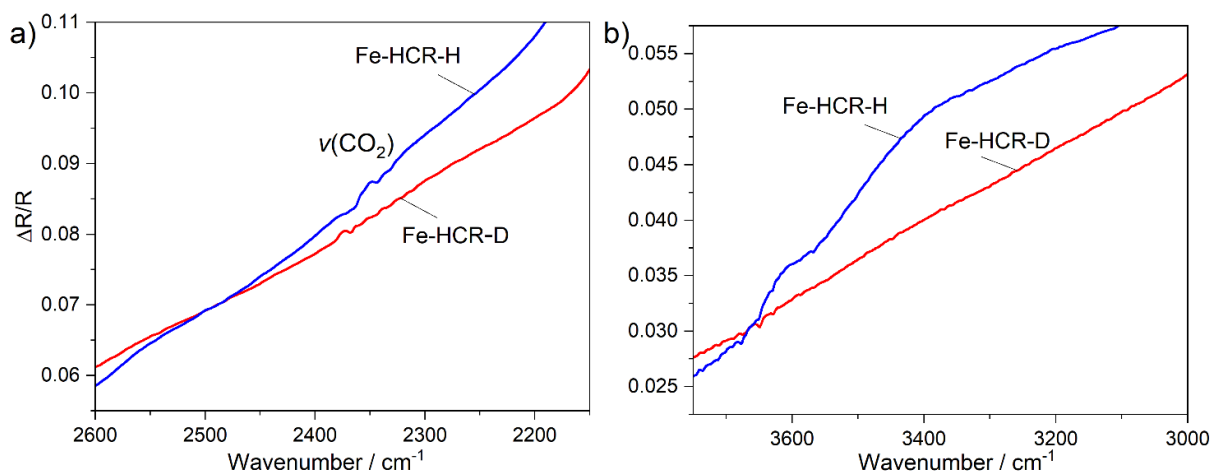


Figure 59. Original spectra of Fe-HCR-H and Fe-HCR-D at the air | gold interface a) in the range of 2600 – 2150 cm^{-1} at half-wave retardation set to 2200 cm^{-1} and b) in the range of 3750 – 3000 cm^{-1} at half-wave retardation set to 3500 cm^{-1} . The figure was adapted from the manuscript “H/D Isotope Effects in the Electrochemistry of Electrochromic Iron Hexacyanoruthenate”.

Figure 59 displays the raw spectra (without any background correction) of the Fe-HCR samples in the $\nu(\text{OH})$ and $\nu(\text{OD})$ region of the Fe-HCR-H and Fe-HCR-D samples. While the $\nu(\text{OH})$ mode can be identified, the corresponding $\nu(\text{OD})$ mode cannot be subtracted from the background. It is important to note, that the relatively lower quantity of Fe-HCR-D presents a challenge in differentiating the $\nu(\text{OD})$ bands from the background spectrum.

7.10 Discussion on the H/D Isotope Effect

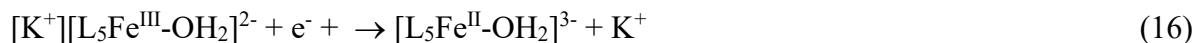
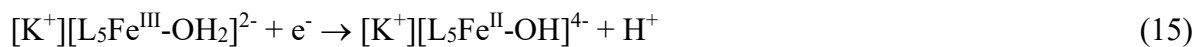
In different studies of Fe-HCR and Fe-HCF, the split of the cathodic peak in the voltammetry of the high-spin Fe is associated with different influences as reviewed in Chapter 2.3. As discussed in Chapter 7.1, changes in the voltammetric behavior of M-HCMs in H₂O- and D₂O-based electrolyte solutions are only known for V-HCF.³² For V-HCF, the change of the redox peaks depending on the electrolyte solution is related to the formation of [VO₂]⁺ and VO⁺ on the V-sites, with H₂O/D₂O serving as a reagent.

In other M^I-HCM² compounds, isotope effects are generally not found. Although there has not been a comprehensive search for such effects, the case of A₂Ni[Fe(CN)₆] remains a subject of debate.^{61,189} In own studies, no significant isotope effect was found for K₂Ni[Fe(CN)₆] (see Appendix 9.2). It is possible, that in other systems, isotope effects remain undetected due to broader and distorted voltammetric signals.

A mechanistic explanation for the observed phenomenon in this work is not immediately evident. It might be assumed that the Fe^{II/III} centers, which are partially coordinated by OH⁻/H₂O as shown in Figure 1b, exhibit slightly different redox potentials compared to those Fe^{II/III} centers partially coordinated to OD⁻/D₂O and the complete cyanide-coordinated Fe^{II/III} centers in Figure 1a. Assuming further that the partially OD⁻/D₂O-coordinated Fe^{II/III} centers have similar redox potentials as the complete cyanide-coordinated centers, the shoulder in the reduction signal with a roughly constant relative intensity could be explained. This would indicate a thermodynamic isotope effect. However, this hypothesis would not explain the observed change in voltammetric shape with temperature changes and the resulting change in viscosity of D₂O. It is also challenging to determine whether other variants of kinetic isotope effects could explain the observed changes in voltammetry with temperature.

The behavior observed in Fe-HCR is more likely attributable to a kinetic isotope effect. Fe-HCR is a solid solution comprising both the 'soluble' and 'insoluble' structures, as illustrated in Figure 1. Two potential mechanisms, which might even act simultaneously, can be proposed. Firstly, OH⁻/H₂O and OD⁻/D₂O coordinated to high-spin Fe^{II/III} centers, as identified by XPS (Figure 52) and PM IRRAS (Figure 58), could potentially be involved in

charge compensation during valence change in the ‘insoluble’ form of the solid material. This can be represented by the following simplified reaction, where L represents N-coordinated cyanide:



It is plausible that H⁺ and D⁺ ions might exhibit different properties for charge compensation due to the distinct conductivities and acidities of H₂O and D₂O. The kinetics of transport could be affected in various ways by viscosity. For instance, when the viscosity of D₂O is adjusted to match that of H₂O at room temperature, a second reduction peak becomes evident in D₂O electrolytes, as demonstrated in Figure 50.

Another potential explanation involves deviations between the bulk and the surface structures in Fe-HCR. This could involve incomplete coordination, particularly of the Fe^{II/III} centers, or amorphous layers lacking long-range order. The transport of K⁺ through these layers could be more restricted compared to its transport in channels of crystalline Fe-HCR, potentially playing a significant role in transport resistance. The K⁺ transfer across the interface between Fe-HCR and the liquid electrolyte involves partial solvation or desolvation processes that might be influenced by the presence of coordinated OH⁻/H₂O and OD⁻/D₂O at the crystal surface. Moreover, the viscosity of the solvent is also likely to impact this transfer process.

7.11 Summary and Conclusion

The voltammetric curves for Fe-HCR thin films are influenced by the type of electrolyte used, showing variations between H₂O- or D₂O-based electrolytes. Mixtures of H₂O and D₂O yield intermediate voltammograms. Adjusting the temperature in D₂O electrolytes to match the viscosity of H₂O results in voltammograms similar to those in H₂O electrolytes at room temperature. These changes are reversible when samples are transferred between the two electrolytes. XPS and PM IRRAS could detect coordinated water and hydroxide ions in the material. The temperature-dependent modulation of the effect (and the associated decrease in viscosity) suggests a kinetic isotope effect in this system. The examined Fe-HCR films consist of a solid solution of two forms: Fe⁴⁺[Ru^{II}(CN)₆]₃ × *k*H₂O ('insoluble') and K₂Fe^{II}[Ru^{II}(CN)₆] × *m*H₂O ('soluble'). The 'insoluble' form contains coordinated water, which may participate in the charge compensation process.

The behavior of coordinated OH⁻/H₂O and OD⁻/D₂O could be significantly different, impacting the voltammetric signals observed. It remains unclear whether the observed behavior is common in many M¹-HCM² compounds or unique to Fe-HCR, as many M¹-HCM² compounds display broad voltammetric signals, which might obscure minor shifts in voltammetric signals. This challenges a wider search for isotope effects in other M¹-HCM² compounds. Ni-HCF, despite showing sharp voltammetric signals, does not show this isotope effect, possibly due to the absence of the N-coordinated high-spin Fe centers, typically present in systems with pronounced peak splitting. It is tempting to assume that these centers play a crucial role in the observed isotope effect, but conclusive evidence is yet to be established.

8 Summary and Outlook

As already mentioned in the introduction of this work, metal hexacyanometallates have been known for more than 200 years and intensive research is still being conducted on these materials. Due to the versatile (electro-)chemical properties of these materials, new applications but also properties of these compounds are found till today. Besides preparation of powders, this work shows, that substrates can be modified by metal hexacyanometallates using electrochemical deposition but also chemical deposition techniques, which widens the window for possible applications of M-HCM films.

In this work, a combination of electrochemical deposition and layer-by-layer deposition was used to deposit multilayer M-HCM films on conductive substrates to create rectifying material. The electrochemical deposition was used to deposit Fe-HCR as the inner layer. Ni-HCF was prepared using layer-by-layer deposition as the outer film. This material combination showed the most promising rectifying behaviour.

To highlight the rectifying behaviour of the layered material, a mixed material was prepared and used as a control besides the pure materials. Fe-HCR and Ni-HCF were deposited alternately to prepare a film presenting the same transition metal ions in the same coordination environment but without a phase boundary between Fe-HCR and Ni-HCF. In cyclic voltammetry, the mixed material reflected a superposition of the redox behaviour of the pure materials Fe-HCR and Ni-HCF. In contrast, the layered material demonstrates charge trapping by a shift of the reduction peak of Ni-HCF.

I-V characteristics of the layered material underline the rectifying behaviour by an asymmetrical curve displaying a plateau with increasing and decreasing currents in forward and negatively biased regions. Additionally, there is a breakdown current, which is common for unidirectional current flow. To verify that this *I-V* characteristics is due to the behaviour of the layered material, an additional layered system was prepared comprising an electrodeposited Fe-HCR thin film with Ni-HCF nanoparticles dropcasted on this film. This system allows to measure the *I-V* characteristics of layered material and the pure Fe-HCF film on the very same substrate and sample. Also, here, the rectifying behaviour was proven, and

the differences between the pure Fe-HCR film and the layered material highlighted the other results of this work.

XPS measurements confirmed the complete coverage of the inner Fe-HCR layer by the outer Ni-HCF layer, cracks within the film or other defects can be ruled out since no Ru was detected. The Ru signal enables safe distinction between the inner and outer layer, since only the inner layer is constituted of this transition metal centre.

The investigated H/D isotope effect in Fe-HCR is an interesting discovery. It is worth noting that these results are fundamental electrochemical results, which are rare, especially for this material class nowadays. Since isotope effects are only known for V-HCF in the class of M-HCMs, the behaviour of Fe-HCR in H₂O- and D₂O-containing electrolytes is unexpected. The appearance of a second cathodic peak in the CV of Fe-HCR in H₂O-based electrolyte and, contrastingly, the disappearance of the second reduction peak in CVs in D₂O-based electrolyte is not only found for thin films of Fe-HCR but also for solid crystals of the material attached to paraffin-impregnated graphite electrodes. Control experiments using commercially available H₂O in HPLC quality also reveal the second peak in the CV, and thus, contamination of the commonly used distilled H₂O can be excluded as the source of the effect. Fe-HCR forms solid solutions, consisting of the 'soluble' and the 'insoluble' form of the material. XPS revealed differences in the oxygen compounds in the oxidized and reduced states of the three different samples Fe-HCR-H, Fe-HCR-H-D and Fe-HCR-D. Ex situ PM IRRAS measurements revealed different water species depending on the origin of the sample. In the case of the samples Fe-HCR-H and Fe-HCR-H-D, not only coordinated but also zeolitic water can be found, indicating that even if the Fe-HCR-H sample undergoes an additional cycle in D₂O, the H₂O molecules are not completely exchanged by D₂O molecules.

These results suggest that oxygen coordinated as hydroxides in the 'insoluble' form may influence the electrochemistry of Fe-HCR in the different isotopic electrolyte environments. Temperature-dependent measurements suggest a kinetic isotope effect in the system.

The research presented in this work highlights the diverse electrochemical properties of M-HCMs. Although these compounds have been known for a long time, numerous new and/or unexplained phenomena remain. This class of materials demonstrates significant potential, especially for thin film applications. Various deposition methods can be employed for film fabrication, thus broadening the range of potential substrates and application areas.

To expand the field of unidirectional current flow in thin films, the next step would be the translation of the findings to flexible substrates, as used for nano- and microdevices. Since the Fe-HCR|Cu-HCF system has already presented promising behavior in *I-V* characteristics, preparation of this layered material using other methods is suggested. Also, searching for new materials in the coordination network compound family might be interesting. For instance, in the research field of metal-organic-frameworks, many electrically conductive compounds are investigated.^{201,202}

To gain a deeper insight into the redox chemistry of high-spin Fe in M-HCMs in H₂O- and D₂O-based electrolytes, further studies of Fe-HCMs would be interesting with another C-coordinated transition metal ion. Additionally, pH- and pD-adjusted measurements will help to understand, whether the two reduction peaks are pH (pD) dependent, as already discussed in literature. Furthermore, the investigation of the behaviour of Fe-HCR under the same conditions as in this work (WE, temperature, concentration of electrolyte solution) with different electrolytes like NaCl, LiCl, RbCl and CsCl but also different anions is suggested. These studies could yield insights about the influence on the isotope effect by other ions.

9 Appendix

9.1 Software Modification of the Dipping Robot

The software used for conducting layer-by-layer deposition relies on G-Code, which is also used for 3D printers. An MS Excel spreadsheet containing a macro is used to translate experimental parameters into G-Code. The position of the reservoirs, number of dipping cycles, and residence time in each beaker are the input parameters for the dipping operation. The spreadsheet is open for extensions to implement more beakers or devices that can control illumination or gas flow. The 3D printer interprets the G-Code and reacts consequently with hardware control signals to each part of the setup. The open-source firmware of the 3D printer was downloaded and modified using the Arduino IDE.

Modification of the Permanent Control Code of the 3D Printer to Manipulate the Temperature Sensor. In this step, the temperature sensor should be manipulated to control the pump, the changes are shown in Table A1. There is a need for changes in the temperature control as well as changes in the thermal runaway control protection of the printer. The latter is implemented in the software to switch off the heating if the target temperature is not reached within a specified time span. If the pump (the rinsing of the substrate) should be used for a longer time, this protection needs to be disabled for the dipping procedure. Otherwise, the operation would stop.

Table A1. Changes in the firmware of the 3D printer to manipulate the temperature sensor behavior.

| File in open-source firmware: Configuration.h | |
|---|-----------------------------------|
| Original code line | Modified code line |
| #define TEMP_SENSOR_0 1 | #define TEMP_SENSOR_0 998 |
| Comment. This code line sets the temperature sensor type at the extruder. The modification selects the dummy. | |
| #define TEMP_SENSOR_BED 1 | #define TEMP_SENSOR_BED 998 |
| Comment. This code line sets the time of the temperature sensor at the printing bed. This modification selects the dummy. | |
| #define THERMAL_PROTECTION_HOTENDS | /// THERMAL_PROTECTION_HOTENDS |
| Comment. The modification turns off the thermal protection of the extruder. | |
| #define THERMAL_PROTECTION_BED | /// THERMAL_PROTECTION_BED |
| Comment. This modification turns off the thermal protection of the printing bed. | |

Modification of the Permanent Control Code of the 3D Printer to Decrease the Acceleration of the Printing Bed. In the ‘homing’ procedure, the 3D printer calibrates all axes by moving them to the extreme positions / zero positions. In the commercial printing procedure, this process is conducted fast. For the preparation of the dipping process, softer movements of the printing bed are required to prevent spilling of the precursor or rinsing solutions from the beakers. The changes in the firmware are given in Table A2.

Table A2. Change in software to soften the calibration procedure (homing) after starting the 3D printer.

| File in open-source firmware: Configuration.h | |
|---|---------------------------------------|
| Original code line | Modified code line |
| #define HOMING_FEEDRATE_XY (50*60) | #define HOMING_FEEDRATE_XY (20*60) |
| Comment. This modification lowers the translation rate for calibration. | |
| File in open-source firmware: Configuration adv.h | |
| #define HOMING_BUMP_DIVISOR {2, 2,4} | #define HOMING_BUMP_DIVISOR {5, 5, 4} |
| Comment. This code line is the re-bump speed divisor, which divides the homing feed rate. | |

Upload of the Modified Software. Before executing this step, it is important to understand that modifying the firmware of the 3D printer is likely to infringe on the original device's warranty. A new bootloader is required to upload the modified software to the control unit of the 3D printer. An ISP Programmer (Paradisetronic.com, Tinkerly GmbH, Berlin, Germany) was used for this. The ISP Programmer allows the transfer of an alternative bootloader (part of the Arduino IDE) from the Arduino IDE to the 3D printer ("burn bootloader"). This part was connected to the ISP port on the mainboard of the 3D printer and, via USB, to a PC (personal computer). After this step, the 3D printer can receive new firmware by the direct USB connection of the 3D printer. A detailed step-by-step description is given in Table A3.

Table A3. Step-by-step procedure to modify and upload the firmware of the printer for the dipping operation.

| Installation of a compatible driver on the ISP programmer | |
|---|--|
| 1 | Download the software “zadig” to the PC. ²⁰³ |
| 2 | Connect the ISP programmer to the PC via USB. |
| 3 | Install the driver “libusbK v3.1.0.0” to the ISP programmer using the “zadig”-software. |
| Burning of the bootloader | |
| 4 | Install the Arduino software to the PC. |
| 5 | Connect the ISP programmer to the mainboard of the 3D printer as well as to the PC. |
| 6 | “Sanguino board” is a required component of the Arduino Software. Select in Arduino software: Tools → Board → Boards Manager Search for ‘Sanguino’ and install it |
| 7 | Make the following selections in the Arduino software: Tools → Board → Sanguino Tools → Processor → ATmega 1284 or ATmega 1284P (16 MHz) Tools → Programmer → USBasp |
| 8 | Run the bootloader and select from the Arduino software. Tools → Burn Bootloader |
| 9 | Remove the ISP programmer from the PC and the mainboard of the 3D printer. |
| Direct connection of PC and 3D printer | |
| 10 | Download and install the driver “CH341SER.exe” for the 3D printer on the PC. |
| 11 | After step 10, the 3D printer can be recognized by a computer and can communicate with the PC via a serial port. |
| Modify the firmware and upload it to the 3D printer | |
| 12 | Download the firmware of the 3D printer to the PC. |
| 13 | Run the firmware in Arduino software. |
| 14 | Edit the firmware as shown in Table A1 and Table A2. |
| 15 | Make the following selections in the Arduino software: Tools → Board → Sanguino Tools → Processor → ATmega 1284 or ATmega 1284P (16 MHz) Tools → Port → Choose the port of the 3D printer Tools → Programmer → AVRISP mkll |
| 16 | Upload the edited firmware to the 3D printer by selecting the Arduino software: Sketch → upload |

9.2 Section Analysis of Fe-HCR, the layered Fe-HCR|Ni-HCF material and the mixed material.

The section analysis of the materials was performed on the respective sample, which was scratched as described in Chapter 4.1.

Fe-HCR. For Fe-HCR the analyzed area is shown in Figure A1, the vertical distance analyzed from the material is given in Table 4.

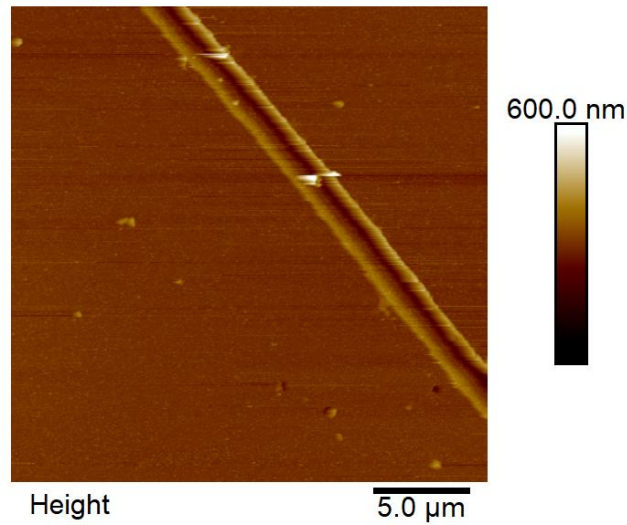


Figure A1. A scratch of the Fe-HCR surface used for thickness analysis in SFM.

Table A4. Vertical distances determined by SFM from the Fe-HCR surface.

| Number of analyzed points | Vertical Distance/nm |
|---------------------------|----------------------|
| 1 | 84.4 |
| 2 | 73.9 |
| 3 | 82.4 |
| 4 | 94.6 |
| 5 | 63.4 |
| 6 | 79.7 |
| Mean standard deviation | 79.9 ± 9.6 |

Layered Material. For the Fe-HCR|Ni-HCF layered material, the analyzed area is shown in Figure 2, and the vertical distance analyzed from the material is given in Table 5.

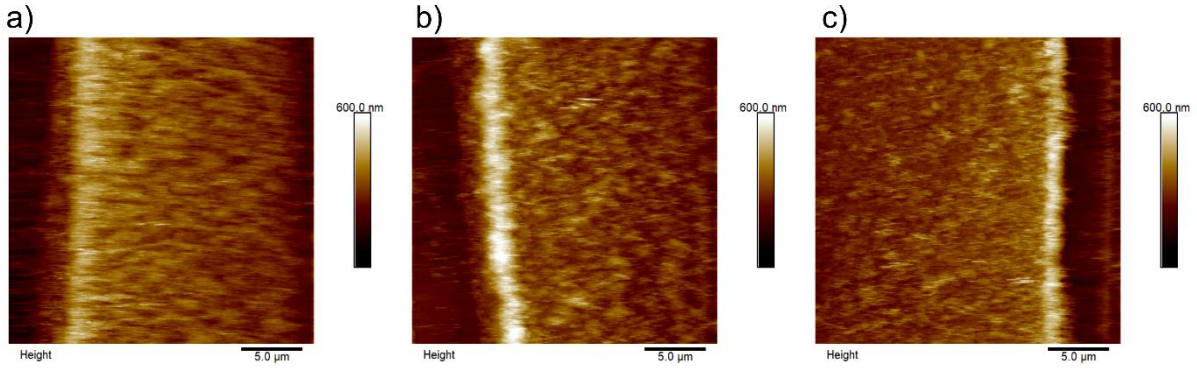


Figure A2. Scratch of the Fe-HCR|Ni-HCF layered material surface used for thickness analysis in SFM.

Table A5. Vertical distances determined by SFM from the Fe-HCR|Ni-HCF layered material surface.

| Number of analyzed points in Figure 53a | Vertical Distance/nm |
|---|----------------------|
| 1 | 218.5 |
| 2 | 222.7 |
| 3 | 252.6 |
| 4 | 218.3 |
| 5 | 227.6 |
| Number of analyzed points in Figure 53b | Vertical Distance/nm |
| 1 | 263.6 |
| 2 | 121.0 |
| 3 | 155.8 |
| 4 | 161.8 |
| 5 | 211.5 |
| 6 | 118.0 |
| Number of analyzed points in Figure 53c | Vertical Distance/nm |
| 1 | 165.1 |
| 2 | 154.6 |
| 3 | 195.5 |
| 4 | 223.1 |
| 5 | 213.8 |
| 6 | 140.7 |
| Mean standard deviation | 192.0 ± 43.2 |

Mixed Material. For the mixed material of Fe-HCR and Ni-HCF, the analyzed area is shown in Figure 3, and the vertical distance analyzed from the material is given in Table 6.

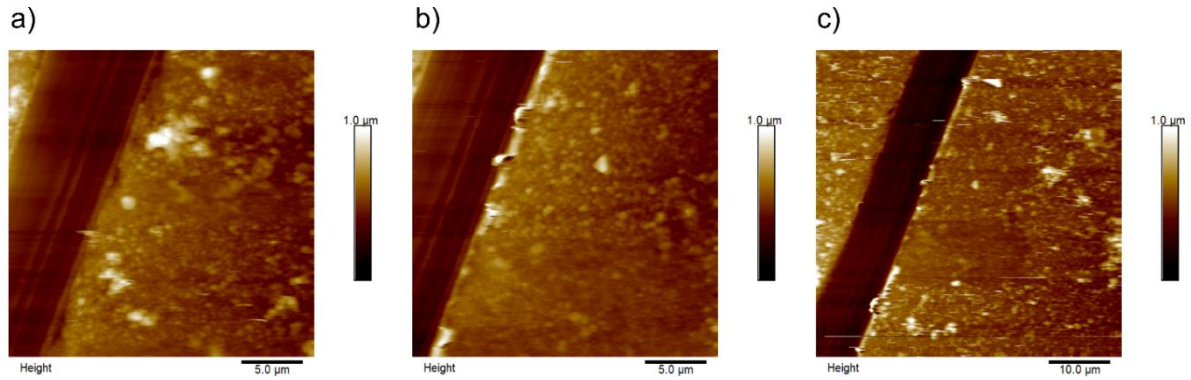


Figure A3. Scratch of the Fe-HCR|Ni-HCF mixed material surface used for thickness analysis in SFM.

Table A6. Vertical distances determined by SFM from the Fe-HCR|Ni-HCF layered material surface.

| Number of analyzed points in Figure A3a | Vertical Distance/nm |
|---|----------------------|
| 1 | 238.2 |
| 2 | 270.1 |
| 3 | 259.3 |
| 4 | 226.1 |
| 5 | 266.8 |
| 6 | 329.8 |
| Number of analyzed points in Figure A3b | Vertical Distance/nm |
| 1 | 232.0 |
| 2 | 279.1 |
| 3 | 324.8 |
| 4 | 281.4 |
| 5 | 248.4 |
| 6 | 170.5 |
| Number of analyzed points in Figure A3c | Vertical Distance/nm |
| 1 | 220.3 |
| 2 | 243.0 |
| 3 | 178.1 |
| 4 | 160.7 |
| 5 | 189.6 |
| 6 | 179.6 |
| Mean standard deviation | 242.2 ± 47.7 |

9.3 H/D Exchange Experiments in Ni-HCF

The electrochemical deposition of Ni-HCF was carried out according to the procedure described in Chapter 5.3. A Ni-HCF film, initially deposited in an H₂O-based electrolyte, was subsequently transferred to H₂O-based 1 M KCl electrolyte (Ni-HCF-H). The redox process for this sample, as shown in Figure A4, can be associated with the soluble form (Eq. 2) and insoluble form (Eq 4).³⁰ The pronounced peak pair at approximately 0.64 V is related to the soluble form, but the broader peak pair at lower potentials is connected to the insoluble form.^{69,160} When this film is transferred to a D₂O-based 1 M KCl solution (Ni-HCF-H-D), the voltammogram retains its shape. Furthermore, upon transferring the sample back to H₂O-based 1 M KCl solution (Ni-HCF-H-D-H), the voltammogram remains unchanged.

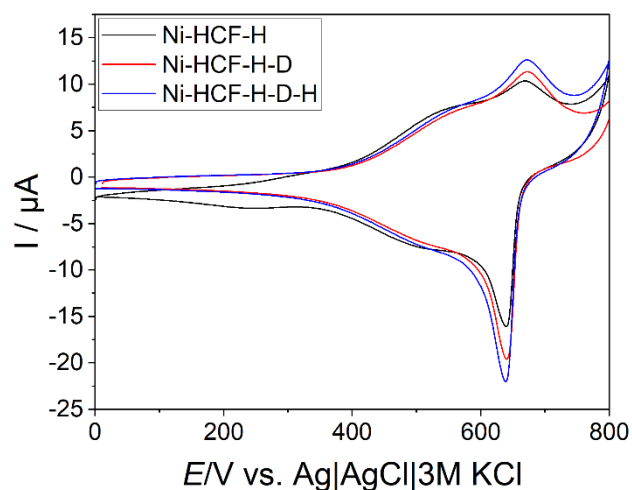


Figure A4. Cyclic voltammograms of electrochemically deposited Ni-HCF thin films with electrolyte exchange from H₂O (Ni-HCF-H) to D₂O (Ni-HCF-H-D) back to H₂O (Ni-HCF-H-D-H) in 1 M KCl at $\nu = 0.01 \text{ V s}^{-1}$.

9.4 List of Abbreviations

The term metal hexacyanometallates is abbreviated as M-HCM (M^1 -HCM 2) for reasons of simplicity, where M^1 refers to the N-coordinated transition metal and M^2 refers to the C-coordinated transition metal.

| | |
|----------------------------------|---|
| 3D | three dimensional |
| AFM | Atomic force microscopy |
| CE | Counter electrode |
| Co HCF | Cobalt hexacyanoferrate |
| C-SFM | Conductive scanning force microscopy |
| CV | Cyclic voltammetry, cyclic voltammogram |
| EQCM | Electrochemical quartz crystal microbalance |
| fcc | Face-centered cubic |
| FDA | Food and Drug Administration |
| Fe HCCo | Iron hexacyanocobaltate |
| Fe HCR | Iron hexacyanoruthenate |
| GI XRD | Grazing incidence X-ray diffraction |
| HCl | Hydrochloric acid |
| HOMO | Highest occupied molecular orbital |
| IR | Infrared |
| ITO | Indium tin oxide |
| <i>I-V</i> characteristic curves | Current-voltage characteristic curves |
| LbL | Layer-by-layer |
| LUMO | Lowest unoccupied orbital |
| Ni HCF | Nickel hexacyanoferrate |
| p | Parallel |
| PAH | Poly(allylamine hydrochloride) |
| PDADMA | Poly(diallyl-dimethylammonium chloride) |
| PEM | Polarization modulator |

Appendix

| | |
|----------|---|
| PM IRRAS | Polarization modulation infrared reflection absorption spectroscopy |
| PSS | Poly(styrene sulfonate) |
| PXRD | Powder X-ray diffraction |
| RE | Reference electrode |
| Ru HCR | Ruthenium hexacyanoruthenate |
| s | Perpendicular |
| SAM | Self-assembled monolayer |
| SCE | Saturated calomel electrode |
| SEM | Scanning electron microscopy |
| SFM | Scanning force microscopy |
| STM | Scanning tunneling microscopy |
| SURMOF | Surface-mounted metal-organic frameworks |
| TEM | Transmission electron microscopy |
| UHV | Ultra high vacuum |
| V-HCF | Vanadium Hexacyanoferrate |
| WE | Working electrode |
| XPS | X-ray photoelectron spectroscopy |
| XRD | X-ray diffraction |
| Zn HCF | Zinc Hexacyanoferrate |

9.5 Symbols

| | |
|--------------|-------------------------------------|
| λ | Wavelength of incident X-rays (XRD) |
| Γ | Surface excess |
| θ | Angle of incidence, Braggs law |
| I_p | Peak current |
| A | Area |
| E_λ | Switching potential CV |
| $E^{\circ'}$ | Formal potential / V |
| E_{pa} | Anodic peak potential / V |
| E_{pc} | Cathodic peak potential / V |
| F | Faraday constant |
| I | Current / A |
| n | Number of transferred electrons |
| R | Gas constant |
| T | Temperature |
| t | Time |
| v | Scan rate / V s ⁻¹ |

10 Literature

- (1) Peng, J.; Zhang, W.; Liu, Q.; Wang, J.; Chou, S.; Liu, H.; Dou, S. Prussian Blue Analogues for Sodium-Ion Batteries: Past, Present, and Future. *Adv. Mater.* **2022**, *34*, 2108384. <https://doi.org/10.1002/adma.202108384>.
- (2) Muñoz, M. J. P.; Martínez, E. C. *Prussian Blue Based Batteries*; Springer International Publishing, 2018. <https://doi.org/10.1007/978-3-319-91488-6>.
- (3) Mortimer, R. J. Electrochromic Materials. *Annu. Rev. Mater. Res.* **2011**, *41*, 241–268. <https://doi.org/10.1146/annurev-matsci-062910-100344>.
- (4) Hu, J.; Tao, H.; Chen, M.; Zhang, Z.; Cao, S.; Shen, Y.; Jiang, K.; Zhou, M. Interstitial Water Improves Structural Stability of Iron Hexacyanoferrate for High-Performance Sodium-Ion Batteries. *ACS Appl. Mater. Interfaces* **2022**, *14*, 12234–12242. <https://doi.org/10.1021/acsami.1c23762>.
- (5) Rudola, A.; Du, K.; Balaya, P. Monoclinic Sodium Iron Hexacyanoferrate Cathode and Non-Flammable Glyme-Based Electrolyte for Inexpensive Sodium-Ion Batteries. *J. Electrochem. Soc.* **2017**, *164*, A1098. <https://doi.org/10.1149/2.0701706jes>.
- (6) Sitnikova, N. A.; Komkova, M. A.; Khomyakova, I. V.; Karyakina, E. E.; Karyakin, A. A. Transition Metal Hexacyanoferrates in Electrocatalysis of H₂O₂ Reduction: An Exclusive Property of Prussian Blue. *Anal. Chem.* **2014**, *86*, 4131–4134. <https://doi.org/10.1021/ac500595v>.
- (7) Abe, T.; Toda, G.; Tajiri, A.; Kaneko, M. Electrochemistry of Ferric Ruthenocyanide (Ruthenium Purple), and Its Electrocatalysis for Proton Reduction. *J. Electroanal. Chem.* **2001**, *510*, 35–42. [https://doi.org/10.1016/S0022-0728\(01\)00539-3](https://doi.org/10.1016/S0022-0728(01)00539-3).
- (8) Tian, F.; Llaudet, E.; Dale, N. Ruthenium Purple-Mediated Microelectrode Biosensors Based on Sol-Gel Film. *Anal. Chem.* **2007**, *79*, 6760–6766. <https://doi.org/10.1021/ac070822f>.
- (9) Husmann, S.; Zarbin, A. J. G. Multifunctional Carbon Nanotubes/ruthenium Purple Thin Films: Preparation, Characterization and Study of Application as Sensors and Electrochromic Materials. *Dalton Trans.* **2015**, *44*, 5985–5995. <https://doi.org/10.1039/C4DT02784A>.

- (10) Chi, B.-Z.; Zeng, Q.; Jiang, J.-H.; Shen, G.-L.; Yu, R.-Q. Synthesis of Ruthenium Purple Nanowire Array for Construction of Sensitive and Selective Biosensors for Glucose Detection. *Sens. Actuators, B* **2009**, *140*, 591–596. <https://doi.org/10.1016/j.snb.2009.05.025>.
- (11) Hu, M.; Belik, A. A.; Imura, M.; Mibu, K.; Tsujimoto, Y.; Yamauchi, Y. Synthesis of Superparamagnetic Nanoporous Iron Oxide Particles with Hollow Interiors by Using Prussian Blue Coordination Polymers. *Chem. Mater.* **2012**, *24*, 2698–2707. <https://doi.org/10.1021/cm300615s>.
- (12) Hu, M.; Yamauchi, Y. Synthesis of a Titanium-Containing Prussian-Blue Analogue with a Well-Defined Cube Structure and Its Thermal Conversion into a Nanoporous Titanium-Iron-Based Oxide. *Chem. Asian J.* **2011**, *6*, 2282–2286. <https://doi.org/10.1002/asia.201100075>.
- (13) Wang, F.; Liu, Y.; Wei, H.-J.; Li, T.-F.; Xiong, X.-H.; Wei, S.-W.; Ren, F.-Z.; Volinsky, A. Recent Advances and Perspective in Metal Coordination Materials-Based Electrode Materials for Potassium-Ion Batteries. *Rare Met.* **2021**, *40*, 448–470. <https://doi.org/10.1007/s12598-020-01649-1>.
- (14) Li, W.-J.; Han, C.; Cheng, G.; Chou, S.-L.; Liu, H.-K.; Dou, S.-X. Chemical Properties, Structural Properties, and Energy Storage Applications of Prussian Blue Analogues. *Small* **2019**, *15*, 1900470. <https://doi.org/10.1002/smll.201900470>.
- (15) Tacconi, N. R. de; Rajeshwar, K.; Lezna, R. O. Metal Hexacyanoferrates: Electrosynthesis, in Situ Characterization, and Applications. *Chem. Mater.* **2003**, *15*, 3046–3062. <https://doi.org/10.1021/cm0341540>.
- (16) Long, X.; Chen, R.; Yang, S.; Wang, J.; Huang, T.; Lei, Q.; Tan, J. Preparation, Characterization and Application in Cobalt Ion Adsorption Using Nanoparticle Films of Hybrid Copper–nickel Hexacyanoferrate. *RSC Adv.* **2019**, *9*, 7485–7494. <https://doi.org/10.1039/C9RA00596J>.
- (17) Fitta, M.; Prima-Garcia, H.; Czaja, P.; Korzeniak, T.; Krupiński, M.; Wojtyniak, M.; Bałanda, M. Magnetic and Magneto-Optical Properties of Nickel Hexacyanoferrate/chromate Thin Films. *RSC Adv.* **2017**, *7*, 1382–1386. <https://doi.org/10.1039/C6RA25775E>.

- (18) Bie, X.; Kubota, K.; Hosaka, T.; Chihara, K.; Komaba, S. Synthesis and Electrochemical Properties of Na-Rich Prussian Blue Analogues Containing Mn, Fe, Co, and Fe for Na-Ion Batteries. *J. Power Sources* **2018**, *378*, 322–330. <https://doi.org/10.1016/j.jpowsour.2017.12.052>.
- (19) Avila, Y.; Acevedo-Peña, P.; Reguera, L.; Reguera, E. Recent Progress in Transition Metal Hexacyanometallates: From Structure to Properties and Functionality. *Coord. Chem. Rev.* **2022**, *453*, 214274. <https://doi.org/10.1016/j.ccr.2021.214274>.
- (20) Kitchamsetti, N. A Review on Recent Advances in Prussian Blue, Its Analogues, and Their Derived Materials as Electrodes for High Performance Supercapacitors. *J. Energy Storage* **2023**, *73*, 108958. <https://doi.org/10.1016/j.est.2023.108958>.
- (21) Neff, V. D. Electrochemical Oxidation and Reduction of Thin Films of Prussian Blue. *J. Electrochem. Soc.* **1978**, *125*, 886–887. <https://doi.org/10.1149/1.2131575>.
- (22) Millward, R. C.; Madden, C. E.; Sutherland, I.; Mortimer, R. J.; Fletcher, S.; Marken, F. Directed Assembly of Multilayers--the Case of Prussian Blue. *Chem. Commun.* **2001**, 1994–1995. <https://doi.org/10.1039/b106616c>.
- (23) Hosseini, P.; Wolkersdörfer, K.; Wark, M.; Redel, E.; Baumgart, H.; Wittstock, G. Morphology and Conductivity of Copper Hexacyanoferrate Films. *J. Phys. Chem. C* **2020**, *124*, 16849–16859. <https://doi.org/10.1021/acs.jpcc.0c06114>.
- (24) Li, C. H.; Nanba, Y.; Asakura, D.; Okubo, M.; Talham, D. R. Li-Ion and Na-Ion Insertion into Size-Controlled Nickel Hexacyanoferrate Nanoparticles. *RSC Adv.* **2014**, *4*, 24955–24961. <https://doi.org/10.1039/C4RA03296A>.
- (25) Liu, Y.; Wei, G.; Ma, M.; Qiao, Y. Role of Acid in Tailoring Prussian Blue as Cathode for High-Performance Sodium-Ion Battery. *Chemistry (Weinheim an der Bergstrasse, Germany)* **2017**, *23*, 15991–15996. <https://doi.org/10.1002/chem.201703081>.
- (26) Zacher, D.; Shekhah, O.; Wöll, C.; Fischer, R. A. Thin Films of Metal-Organic Frameworks. *Chem. Soc. Rev.* **2009**, *38*, 1418–1429. <https://doi.org/10.1039/b805038b>.
- (27) Kong, B.; Selomulya, C.; Zheng, G.; Zhao, D. New Faces of Porous Prussian Blue: Interfacial Assembly of Integrated Hetero-Structures for Sensing Applications. *Chem. Soc. Rev.* **2015**, *44*, 7997–8018. <https://doi.org/10.1039/c5cs00397k>.

- (28) Matos-Peralta, Y.; Antuch, M. Review—Prussian Blue and Its Analogs as Appealing Materials for Electrochemical Sensing and Biosensing. *J. Electrochem. Soc.* **2020**, *167*, 37510. <https://doi.org/10.1149/2.0102003JES>.
- (29) Abruña, H. D.; Denisevich, P.; Umaña, M.; Meyer, T. J.; Murray, R. W. Rectifying Interfaces Using Two-Layer Films of Electrochemically Polymerized Vinylpyridine and Vinylbipyridine Complexes of Ruthenium and Iron on Electrodes. *J. Am. Chem. Soc.* **1981**, *103*, 1–5. <https://doi.org/10.1021/ja00391a001>.
- (30) Miecznikowski, K.; Chojak, M.; Steplowska, W.; Malik, M.; Kulesza, P. Microelectrochemical Electronic Effects in Two-Layer Structures of Distinct Prussian Blue Type Metal Hexacyanoferrates. *J. Solid State Electrochem.* **2004**, *8*, 868–875. <https://doi.org/10.1007/s10008-004-0555-4>.
- (31) Ono, K.; Ishizaki, M.; Soma, S.; Kanaizuka, K.; Togashi, T.; Kurihara, M. A Low-Temperature Sintered Heterostructure Solid Film of Coordination Polymer Nanoparticles: An Electron-Rectifier Function Based on Partially Oxidised/reduced Conductor Phases of Prussian Blue. *RSC Adv.* **2015**, *5*, 96297–96304. <https://doi.org/10.1039/C5RA18678A>.
- (32) Wang, Y.; Zhu, G.; Wang, E. Electrochemical Quartz Crystal Microbalance Study for Vanadium Hexacyanoferrates: Monitoring of Film Growth and Ion Effects During Redox Reactions. *J. Electroanal. Chem.* **1997**, *430*, 127–132. [https://doi.org/10.1016/S0022-0728\(97\)00104-6](https://doi.org/10.1016/S0022-0728(97)00104-6).
- (33) Kraft, A. What a Chemistry Student Should Know about the History of Prussian Blue. *ChemTexts* **2018**, *4*, 16. <https://doi.org/10.1007/s40828-018-0071-2>.
- (34) Ivanov, V. D. Four Decades of Electrochemical Investigation of Prussian Blue. *Ionics* **2020**, *26*, 531–547. <https://doi.org/10.1007/s11581-019-03292-y>.
- (35) Woodward, J. Praeparatio Caerulei Prussiaci ex Germania missa ad Johannem Woodward. *Philos. Trans. R. Soc. London* **1724**, *33*, 15–17.
- (36) Samain, L.; Grandjean, F.; Long, G. J.; Martinetto, P.; Bordet, P.; Sanyova, J.; Strivay, D. Synthesis and Fading of Eighteenth-Century Prussian Blue Pigments: A Combined Study by Spectroscopic and Diffractive Techniques Using Laboratory and Synchrotron Radiation Sources. *J. Synchrotron Radiat.* **2013**, 460–473. <https://doi.org/10.1107/s0909049513004585>.

- (37) Keggin, J. F.; Miles, F. D. Structures and Formulae of the Prussian Blues and Related Compounds. *Nature* **1936**, *137*, 577–578. <https://doi.org/10.1038/137577a0>.
- (38) Liu, X.; Zhou, A.; Dou, Y.; Pan, T.; Shao, M.; Han, J.; Wei, M. Ultrafast Switching of an Electrochromic Device Based on Layered Double Hydroxide/Prussian Blue Multilayered Films. *Nanoscale* **2015**, *7*, 17088–17095. <https://doi.org/10.1039/C5NR04458H>.
- (39) Department of Health and Human Service. Guidance for Industry on Prussian Blue for Treatment of Internal Contamination with Thallium or Radioactive Cesium. *Fed. Regist.* **2003**, *68*, 5645–5648.
- (40) Karyakin, A. A.; Gitelmacher, O. V.; Karyakina, E. E. A High-Sensitive Glucose Amperometric Biosensor Based on Prussian Blue Modified Electrodes. *Anal. Lett.* **1994**, *27*, 2861–2869. <https://doi.org/10.1080/00032719408000297>.
- (41) Karyakin, A. A. Prussian Blue and Its Analogues: Electrochemistry and Analytical Applications. *Electroanalysis* **2001**, *13*, 813–819. [https://doi.org/10.1002/1521-4109\(200106\)13:10<813:AID-ELAN813>3.0.CO;2-Z](https://doi.org/10.1002/1521-4109(200106)13:10<813:AID-ELAN813>3.0.CO;2-Z).
- (42) Hurlbutt, K.; Giustino, F.; Pasta, M.; Volonakis, G. Electronic Structure and Electron-Transport Properties of Three Metal Hexacyanoferrates. *Chem. Mater.* **2021**. <https://doi.org/10.1021/acs.chemmater.1c02183>.
- (43) Ojwang, D. O.; Grins, J.; Wardecki, D.; Valvo, M.; Renman, V.; Häggström, L.; Ericsson, T.; Gustafsson, T.; Mahmoud, A.; Hermann, R. P.; Svensson, G. Structure Characterization and Properties of K-Containing Copper Hexacyanoferrate. *Inorg. Chem.* **2016**, *55*, 5924–5934. <https://doi.org/10.1021/acs.inorgchem.6b00227>.
- (44) Dunbar, K. R.; Heintz, R. A. Chemistry of Transition Metal Cyanide Compounds: Modern Perspectives. In *Progress in Inorganic Chemistry*; Karlin, K. D., Ed.; Progress in Inorganic Chemistry, Vol. 45; Interscience Publishers: New York, 1997; pp 282–391.
- (45) Buser, H. J.; Schwarzenbach, D.; Petter, W.; Ludi, A. The Crystal Structure of Prussian Blue: $\text{Fe}_4[\text{Fe}(\text{CN})_6]_3x\text{H}_2\text{O}$. *Inorg. Chem.* **1977**, *16*, 2704–2710. <https://doi.org/10.1021/ic50177a008>.

- (46) Momma, K.; Izumi, F. VESTA 3 for Three-Dimensional Visualization of Crystal, Volumetric and Morphology Data. *J. Appl. Crystallogr.* **2011**, *44*, 1272–1276. <https://doi.org/10.1107/S0021889811038970>.
- (47) Liebig, J. von. Handbuch der Chemie: Mit Rücksicht auf Pharmacie; Als neue Bearbeitung des ersten Bandes von Geiger's Handbuch der Pharmacie, Heidelberg, 1843.
- (48) Ellis, D.; Eckhoff, M.; Neff, V. D. Electrochromism in the Mixed-Valence Hexacyanides. 1. Voltammetric and Spectral Studies of the Oxidation and Reduction of Thin Films of Prussian Blue. *J. Phys. Chem.* **1981**, *85*, 1225–1231.
- (49) Kulesza, P. J.; Malik, M. A.; Berrettoni, M.; Giorgetti, M.; Zamponi, S.; Schmidt, R.; Marassi, R. Electrochemical Charging, Counterion Accommodation, and Spectrochemical Identity of Microcrystalline Solid Cobalt Hexacyanoferrate. *J. Phys. Chem. B* **1998**, *102*, 1870–1876. <https://doi.org/10.1021/jp9726495>.
- (50) Widmann, A.; Kahlert, H.; Petrovic-Prelevic, I.; Wulff, H.; Yakhmi, J. V.; Bagkar, N.; Scholz, F. Structure, Insertion Electrochemistry, and Magnetic Properties of a New Type of Substitutional Solid Solutions of Copper, Nickel, and Iron Hexacyanoferrates/Hexacyanocobaltates. *Inorg. Chem.* **2002**, *41*, 5706–5715. <https://doi.org/10.1021/ic0201654>.
- (51) Lundgren, C. A.; Murray, R. W. Observations on the Composition of Prussian Blue Films and Their Electrochemistry. *Inorg. Chem.* **1988**, *27*, 933–939. <https://doi.org/10.1021/ic00278a036>.
- (52) Chen, S.-M.; Hsueh, S.-H. Iron Hexacyanoruthenate Films and Their Electrocatalytic Properties with Nitrite and Dopamine. *J. Electrochem. Soc.* **2003**, *150*, D175–D183. <https://doi.org/10.1149/1.1604113>.
- (53) Itaya, K.; Ataka, T.; Toshima, S. Spectroelectrochemistry and Electrochemical Preparation Method of Prussian Blue Modified Electrodes. *J. Am. Chem. Soc.* **1982**, *104*, 4767–4772. <https://doi.org/10.1021/ja00382a006>.
- (54) Marcus, Y. Are Ionic Stokes Radii of Any Use? *J. Solution Chem.* **2012**, *41*, 2082–2090. <https://doi.org/10.1007/s10953-012-9922-4>.

- (55) Crumbliss, A. L.; Lugg, P. S.; Childers, J. W.; Palmer, R. A. Fourier Transform Infrared Photothermal Spectroscopic Characterization of Prussian Blue Surface Modified Electrodes. Countercation Effects. *J. Phys. Chem.* **1985**, *89*, 482–488. <https://doi.org/10.1021/j100249a023>.
- (56) Crumbliss, A. L.; Lugg, P. S.; Morosoff, N. Alkali Metal Cation Effects in a Prussian Blue Surface Modified Electrode. *Inorg. Chem.* **1984**, *23*, 4701–4708. <https://doi.org/10.1021/ic00194a057>.
- (57) Bocarsly, A. B.; Sinha, S. Effects of Surface Structure on Electrode Charge Transfer Properties. *J. Electroanal. Chem. Interfacial Electrochem.* **1982**, *140*, 167–172. [https://doi.org/10.1016/0368-1874\(82\)85310-0](https://doi.org/10.1016/0368-1874(82)85310-0).
- (58) Malik, M. A.; Kulesza, P. J.; Marassi, R.; Nobili, F.; Miecznikowski, K.; Zamponi, S. Countercation Intercalation and Kinetics of Charge Transport During Redox Reactions of Nickel Hexacyanoferrate. *Electrochim. Acta* **2004**, *49*, 4253–4258. <https://doi.org/10.1016/j.electacta.2004.04.021>.
- (59) Schneemeyer, L. F.; Spengler, S. E.; Murphy, D. W. Ion Selectivity in Nickel Hexacyanoferrate Films on Electrode Surfaces. *Inorg. Chem.* **1985**, *24*, 3044–3046. <https://doi.org/10.1021/ic00213a034>.
- (60) Wang, L.; Song, J.; Qiao, R.; Wray, L. A.; Hossain, M. A.; Chuang, Y.-D.; Yang, W.; Lu, Y.; Evans, D.; Lee, J.-J.; Vail, S.; Zhao, X.; Nishijima, M.; Kakimoto, S.; Goodenough, J. B. Rhombohedral Prussian White as Cathode for Rechargeable Sodium-Ion Batteries. *J. Am. Chem. Soc.* **2015**, *137*, 2548–2554. <https://doi.org/10.1021/ja510347s>.
- (61) Bácskai, J.; Martinusz, K.; Cziráok, E.; Inzelt, G.; Kulesza, P. J.; Malik, M. A. Polynuclear Nickel Hexacyanoferrates: Monitoring of Film Growth and Hydrated Counter-Cation Flux/storage During Redox Reactions. *J. Electroanal. Chem.* **1995**, *385*, 241–248. [https://doi.org/10.1016/0022-0728\(94\)03788-5](https://doi.org/10.1016/0022-0728(94)03788-5).
- (62) Inzelt, G. A Quartz Crystal Microbalance Study of the Sorption of Ions and Solvent Molecules in Poly(Tetracyanoquinodimethane) Electrodes. *J. Electroanal. Chem.* **1990**, *287*, 171–177. [https://doi.org/10.1016/0022-0728\(90\)87167-I](https://doi.org/10.1016/0022-0728(90)87167-I).
- (63) Rutgers, A. J.; Hendrikx, Y. Ionic Hydration. *Trans. Faraday Soc.* **1962**, *58*. <https://doi.org/10.1039/TF9625802184>.

- (64) Feldman, B. J.; Melroy, O. R. Ion Flux During Electrochemical Charging of Prussian Blue Films. *J. Electroanal. Chem. Interfacial Electrochem.* **1987**, *234*, 213–227. [https://doi.org/10.1016/0022-0728\(87\)80173-0](https://doi.org/10.1016/0022-0728(87)80173-0).
- (65) Chang, L.; Chang, S.; Chen, W.; Han, W.; Li, Z.; Zhang, Z.; Dai, Y.; Da, C. Facile One-Pot Synthesis of Magnetic Prussian Blue Core/shell Nanoparticles for Radioactive Cesium Removal. *RSC Adv.* **2016**, *6*, 96223–96228. <https://doi.org/10.1039/C6RA17525B>.
- (66) Weidinger, D.; Brown, D. J.; Owrutsky, J. C. Transient Absorption Studies of Vibrational Relaxation and Photophysics of Prussian Blue and Ruthenium Purple Nanoparticles. *J. Chem. Phys.* **2011**, *134*, 124510. <https://doi.org/10.1063/1.3564918>.
- (67) Malik, M. A.; Miecznikowski, K.; Kulesza, P. J. Quartz Crystal Microbalance Monitoring of Mass Transport During Redox Processes of Cyanometallate Modified Electrodes: Complex Charge Transport in Nickel Hexacyanoferrate Films. *Electrochim. Acta* **2000**, *45*, 3777–3784.
- (68) Kulesza, P. J.; Galus, Z. Mixed-Valence Electron Hopping, Redox Conduction and Migration Effects in Solid-State Electrochemistry of Transition Metal Hexacyanoferrates. *J. Electroanal. Chem.* **1992**, *323*, 261–274. [https://doi.org/10.1016/0022-0728\(92\)80015-V](https://doi.org/10.1016/0022-0728(92)80015-V).
- (69) Zamponi, S.; Berrettoni, M.; Kulesza, P. J.; Miecznikowski, K.; Malik, M. A.; Makowski, O.; Marassi, R. Influence of Experimental Conditions on Electrochemical Behavior of Prussian Blue Type Nickel Hexacyanoferrate Film. *Electrochim. Acta* **2003**, *48*, 4261–4269. <https://doi.org/10.1016/j.electacta.2003.08.001>.
- (70) Ono, K.; Ishizaki, M.; Kanaizuka, K.; Togashi, T.; Yamada, T.; Kitagawa, H.; Kurihara, M. Grain-Boundary-Free Super-Proton Conduction of a Solution-Processed Prussian-Blue Nanoparticle Film. *Angew. Chem. Int. Ed.* **2017**, *56*, 5531–5535. <https://doi.org/10.1002/anie.201701759>.
- (71) Feldman, B. J.; Murray, R. W. Electron Diffusion in Wet and Dry Prussian Blue Films on Interdigitated Array Electrodes. *Inorg. Chem.* **1987**, *26*, 1702–1708. <https://doi.org/10.1021/ic00258a014>.
- (72) Mortimer, R. J.; Varley, T. S. Synthesis, Characterisation and in Situ Colorimetry of Electrochromic Ruthenium Purple Thin Films. *Dyes Pigm.* **2011**, *89*, 169–176. <https://doi.org/10.1016/j.dyepig.2010.10.009>.

- (73) Liu, S.-Q.; Xu, J.-J.; Chen, H.-Y. Electrochemical Behavior of Nanosized Prussian Blue Self-Assembled on Au Electrode Surface. *Electrochem. Commun.* **2002**, *4*, 421–425. [https://doi.org/10.1016/S1388-2481\(02\)00336-3](https://doi.org/10.1016/S1388-2481(02)00336-3).
- (74) Rajan, K. P.; Neff, V. D. Electrochromism in the Mixed-Valence Hexacyanides. 2. Kinetics of the Reduction of Ruthenium Purple and Prussian Blue. *J. Phys. Chem.* **1982**, *86*, 4361–4368. <https://doi.org/10.1021/j100219a017>.
- (75) Ohkoshi, S.-I.; Nakagawa, K.; Tomono, K.; Imoto, K.; Tsunobuchi, Y.; Tokoro, H. High Proton Conductivity in Prussian Blue Analogues and the Interference Effect by Magnetic Ordering. *J. Am. Chem. Soc.* **2010**, *132*, 6620–6621. <https://doi.org/10.1021/ja100385f>.
- (76) Davidson, D.; Welo, L. A. The Nature of Prussian Blue. *J. Phys. Chem.* **1928**, *32*, 1191–1196. <https://doi.org/10.1021/j150290a007>.
- (77) Pajerowski, D. M.; Watanabe, T.; Yamamoto, T.; Einaga, Y. Electronic Conductivity in Berlin Green and Prussian Blue. *Phys. Rev. B: Solid State* **2011**, *83*, 153202. <https://doi.org/10.1103/PhysRevB.83.153202>.
- (78) Chopra, K. L.; Kaur, I. *Thin Film Device Applications*; Springer New York, 2012.
- (79) Biswas, A.; Bayer, I. S.; Biris, A. S.; Wang, T.; Dervishi, E.; Faupel, F. Advances in Top-down and Bottom-up Surface Nanofabrication: Techniques, Applications & Future Prospects. *Adv. Colloid Interface Sci.* **2012**, *170*, 2–27. <https://doi.org/10.1016/j.cis.2011.11.001>.
- (80) Rao, M. C.; Shekhawat, M. S. A Brief Survey on Basic Properties of Thin Films for Device Application. *Int. J. Mod. Phys. Conf.* **2013**, *22*, 576–582.
- (81) Azzaroni, O.; Alvarez, M.; Abou-Kandil, A. I.; Yameen, B.; Knoll, W. Tuning the Unidirectional Electron Transfer at Interfaces with Multilayered Redox-Active Supramolecular Bionanoassemblies. *Adv. Funct. Mater.* **2018**, *18*, 3487–3496. <https://doi.org/10.1002/adfm.200800764>.
- (82) Janes, D. Rectifying Current Behaviours. *Nat. Chem.* **2009**, *1*, 601–603. <https://doi.org/10.1038/nchem.429>.
- (83) Weddigen, C.; Jüngst, W. *Elektronik: Eine Einführung für Naturwissenschaftler und Ingenieure mit Beispielen zur Computer-Simulation*, 2nd ed.; Springer-Lehrbuch; Springer Berlin, Heidelberg, 2013. <https://doi.org/10.1007/978-3-642-84959-6>.

- (84) Oh, S.-K.; Baker, L. A.; Crooks, R. M. Electrochemical Rectification Using Mixed Monolayers of Redox-Active Ferrocenyl Dendrimers and *N*-Alkanethiols. *Langmuir* **2002**, *18*, 6981–6987. <https://doi.org/10.1021/la020382h>.
- (85) Liu, Y.; Offenhäusser, A.; Mayer, D. Electrochemical Current Rectification at Bio-Functionalized Electrodes. *Bioelectrochemistry* **2010**, *77*, 89–93. <https://doi.org/10.1016/j.bioelechem.2009.06.015>.
- (86) Shekhah, O.; Liu, J.; Fischer, R. A.; Wöll, C. MOF Thin Films: Existing and Future Applications. *Chem. Soc. Rev.* **2011**, *40*, 1081–1106. <https://doi.org/10.1039/C0CS00147C>.
- (87) Campagnol, N.; van Assche, T. R. C.; Li, M.; Stappers, L.; Dincă, M.; Denayer, J. F. M.; Binnemans, K.; Vos, D. E. de; Fransaer, J. On the Electrochemical Deposition of Metal–Organic Frameworks. *J. Mater. Chem. A* **2016**, *4*, 3914–3925. <https://doi.org/10.1039/c5ta10782b>.
- (88) Itaya, K.; Akahoshi, H.; Toshima, S. Electrochemistry of Prussian Blue Modified Electrodes: An Electrochemical Preparation Method. *J. Electrochem. Soc.* **1982**, *129*, 1498–1500. <https://doi.org/10.1149/1.2124191>.
- (89) McCormac, T.; Cassidy, J.; Cameron, D. Electrochemical Deposition of Prussian Blue Films Across Interdigital Array Electrodes and Their Use in Gas Sensing. *Electroanalysis* **1996**, *8*, 195–198. <https://doi.org/10.1002/elan.1140080219>.
- (90) Isfahani, V. B.; Dizaji, H. R.; Memarian, N.; Arab, A. Electrodeposition of Prussian Blue Films: Study of Deposition Time Effect on Electrochemical Properties. *Mater. Res. Express* **2019**, *6*, 096449. <https://doi.org/10.1088/2053-1591/ab0989>.
- (91) Ledo, A.; Fernandes, E.; Brett, C. M.; Barbosa, R. M. Enhanced Selectivity and Stability of Ruthenium Purple-Modified Carbon Fiber Microelectrodes for Detection of Hydrogen Peroxide in Brain Tissue. *Sens. Actuators, B* **2020**, *311*, 127899. <https://doi.org/10.1016/j.snb.2020.127899>.
- (92) Cataldi, T. R. I.; Benedetto, G. E. de; Campa, C. Electrochemical Quartz Crystal Microbalance Study and Electrochromic Behavior of a Novel Ruthenium Purple Film. *J. Electroanal. Chem.* **1997**, *437*, 93–98.
- (93) Richardson, J.; Björnmalm, M.; Caruso, F. Technology-Driven Layer-by-Layer Assembly of Nanofilms. *Science* **2015**, *348*, aaa2491. <https://doi.org/10.1126/science.aaa2491>.

- (94) Hidalgo-Acosta, J. C.; Scanlon, M. D.; Méndez, M. A.; Amstutz, V.; Vrabel, H.; Opallo, M.; Girault, H. H. Boosting Water Oxidation Layer-by-Layer. *Phys. Chem. Chem. Phys.* **2016**, *18*, 9295–9304. <https://doi.org/10.1039/c5cp06890h>.
- (95) Shen, Y.; Liu, J.; Jiang, J.; Liu, B.; Dong, S. Fabrication of Metalloporphyrin-Polyoxometalate Hybrid Film by Layer-by-Layer Method and Its Catalysis for Dioxygen Reduction. *Electroanalysis* **2002**, *14*, 1557–1563. [https://doi.org/10.1002/1521-4109\(200211\)14:22<1557:AID-ELAN1557>3.0.CO;2-1](https://doi.org/10.1002/1521-4109(200211)14:22<1557:AID-ELAN1557>3.0.CO;2-1).
- (96) Shimomura, H.; Gemici, Z.; Cohen, R. E.; Rubner, M. F. Layer-by-Layer-Assembled High-Performance Broadband Antireflection Coatings. *ACS Appl. Mater. Interfaces* **2010**, *2*, 813–820. <https://doi.org/10.1021/am900883f>.
- (97) DeLongchamp, D. M.; Hammond, P. T. Multiple-Color Electrochromism from Layer-by-Layer-Assembled Polyaniline/Prussian Blue Nanocomposite Thin Films. *Chem. Mater.* **2004**, *16*, 4799–4805. <https://doi.org/10.1021/cm0496624>.
- (98) Tang, Z.; Wang, Y.; Podsiadlo, P.; Kotov, N. A. Biomedical Applications of Layer-by-Layer Assembly: From Biomimetics to Tissue Engineering. *Adv. Mater.* **2006**, *18*, 3203–3224. <https://doi.org/10.1002/adma.200600113>.
- (99) Wang, Z.; Wöll, C. Fabrication of Metal-Organic Framework Thin Films Using Programmed Layer-by-Layer Assembly Techniques. *Adv. Mater. Technol.* **2019**, *4*, 1800413. <https://doi.org/10.1002/admt.201800413>.
- (100) Pyrasch, M.; Toutianoush, A.; Jin, W.; Schnepf, J.; Tiede, B. Self-Assembled Films of Prussian Blue and Analogues: Optical and Electrochemical Properties and Application as Ion-Sieving Membranes. *Chem. Mater.* **2003**, *15*, 245–254. <https://doi.org/10.1021/cm021230a>.
- (101) Haugstad, G. *Atomic Force Microscopy: Understanding Basic Modes and Advanced Applications*; John Wiley & Sons, Inc., 2012.
- (102) Tararam, R.; Garcia, P. S.; Deda, D. K.; Varela, J. A.; Lima Leite, F. de. Atomic Force Microscopy: A Powerful Tool for Electrical Characterization. In *Nanocharacterization Techniques: A Volume in Micro and Nano Technologies*; Da Roz, A. L., Ferreira, M., Lima Leite, F. de, Oliveira, O. N., Eds.; William Andrew; Elsevier, 2017; pp 37–64.

- (103) Voigtländer, B. *Atomic Force Microscopy*, 2nd ed.; Nanoscience and technology; Springer Cham, 2019.
- (104) Ted Limpoco, F.; Beck, D. E. How to Choose the Right AFM Probe for Your Experiment. *Microscopy Today* **2023**, *31*, 22–27. <https://doi.org/10.1093/mictod/qaad055>.
- (105) Schirmeisen, A.; Anczykowski, B.; Fuchs, H. Dynamic Modes of Atomic Force Microscopy. In *Springer Handbook of Nanotechnology*; Bhushan, B., Ed.; Springer Handbook; Springer: Berlin, 2004; pp 737–766.
- (106) García, R.; Pérez, R. Dynamic Atomic Force Microscopy Methods. *Surf. Sci. Rep.* **2002**, *47*, 197–301. [https://doi.org/10.1016/S0167-5729\(02\)00077-8](https://doi.org/10.1016/S0167-5729(02)00077-8).
- (107) Jandt, K. D. Atomic Force Microscopy of Biomaterials Surfaces and Interfaces. *Surf. Sci.* **2001**, *491*, 303–332. [https://doi.org/10.1016/S0039-6028\(01\)01296-1](https://doi.org/10.1016/S0039-6028(01)01296-1).
- (108) Assis, L. M. N.; Andrade, J. R.; Santos, L. H. E.; Motheo, A. J.; Hajduk, B.; Lapkowski, M.; Pawlicka, A. Spectroscopic and Microscopic Study of Prussian Blue Film for Electrochromic Device Application. *Electrochim. Acta* **2015**, *175*, 176–183. <https://doi.org/10.1016/j.electacta.2015.01.178>.
- (109) Pajerowski, D. M.; Gardner, J. E.; Frye, F. A.; Andrus, M. J.; Dumont, M. F.; Knowles, E. S.; Meisel, M. W.; Talham, D. R. Photoinduced Magnetism in a Series of Prussian Blue Analogue Heterostructures. *Chem. Mater.* **2011**, *23*, 3045–3053. <https://doi.org/10.1021/cm2003337>.
- (110) Avlyanov, J. K.; Josefowicz, J. Y.; MacDiarmid, A. G. Atomic Force Microscopy Surface Morphology Studies of 'In Situ' Deposited Polyaniline Thin Films. *Synth. Met.* **1995**, *73*, 205–208.
- (111) Yuan, W.-L.; O'Rear, E. A.; Cho, G.; Funkhouser, G. P.; Glatzhofer, D. T. Thin Polypyrrole Films Formed on Mica and Alumina with and Without Surfactant Present: Characterization by Scanning Probe and Optical Microscopy. *Thin Solid Films* **2001**, *385*, 96–108. [https://doi.org/10.1016/S0040-6090\(01\)00755-6](https://doi.org/10.1016/S0040-6090(01)00755-6).
- (112) Cho, G. Preparation of Electronically Conducting Ultra-Thin Polymer Films. *Bull. Chem. Soc. Jpn.* **1997**, *70*, 2309–2316. <https://doi.org/10.1246/bcsj.70.2309>.

- (113) Teichert, C.; Beinik, I. Conductive Atomic-Force Microscopy Investigation of Nanostructures in Microelectronics. In *Scanning Probe Microscopy in Nanoscience and Technology 2*; Bhushan, B., Ed.; Nanoscience and Technology; Springer Berlin, Heidelberg, 2010; pp 691–721.
- (114) Stiny, L. *Schnelleinführung Elektronik*, 1st ed.; Springer Vieweg Wiesbaden, 2021. <https://doi.org/10.1007/978-3-658-33462-8>.
- (115) Bard, A. J.; Faulkner, L. R. *Electrochemical Methods. Fundamentals and Applications*, 2nd ed.; John Wiley & Sons, 2004.
- (116) Wittstock, G. *Lehrbuch Der Elektrochemie: Grundlagen, Methoden, Materialien, Anwendungen*; Wiley-VCH GmbH, Weinheim, 2023.
- (117) Vickerman, J. C.; Gilmore, I. S., Eds. *Surface Analysis: The Principal Techniques*, 2nd ed.; Wiley, Chichester, 2009.
- (118) Stevie, F. A.; Donley, C. L. Introduction to x-Ray Photoelectron Spectroscopy. *J. Vac. Sci. Technol., A* **2020**, *38*, 063204. <https://doi.org/10.1116/6.0000412>.
- (119) Ilton, E. S.; Post, J. E.; Heaney, P. J.; Ling, F. T.; Kerisit, S. N. XPS Determination of Mn Oxidation States in Mn (Hydr)Oxides. *Appl. Surf. Sci.* **2016**, *366*, 475–485. <https://doi.org/10.1016/j.apsusc.2015.12.159>.
- (120) Scheurle, P. I.; Mähringer, A.; Haug, T.; Biewald, A.; Axthammer, D.; Hartschuh, A.; Harms, L.; Wittstock, G.; Medina, D. D.; Bein, T. Helical Anthracene–Ethyne-Based MOF-74 Analogue. *Cryst. Growth Des.* **2022**, *22*, 2849–2853. <https://doi.org/10.1021/acs.cgd.1c01145>.
- (121) Malik, M. A.; Kulesza, P. J.; Wlodarczyk, R.; Wittstock, G.; Szargan, R.; Bala, H.; Galus, Z. Formation of Ultra-Thin Prussian Blue Layer on Carbon Steel that Promotes Adherence of Hybrid Polypyrrole Based Protective Coating. *J. Solid State Electrochem.* **2005**, *9*, 403–411. <https://doi.org/10.1007/s10008-005-0654-x>.
- (122) Grosvenor, A. P.; Kobe, B. A.; Biesinger, M. C.; McIntyre, N. S. Investigation of Multiplet Splitting of Fe 2p XPS Spectra and Bonding in Iron Compounds. *Surf. Interface Anal.* **2004**, *36*, 1564–1574. <https://doi.org/10.1002/sia.1984>.
- (123) Sauter, S.; Wittstock, G.; Szargan, R. Localisation of Electrochemical Oxidation Processes in Nickel and Cobalt Hexacyanoferrates Investigated by Analysis of the Multiplet Patterns in

x-Ray Photoelectron Spectra. *Phys. Chem. Chem. Phys.* **2001**, *3*, 562–569. <https://doi.org/10.1039/b008430l>.

(124) Biesinger, M. C.; Payne, B. P.; Grosvenor, A. P.; Lau, L. W.; Gerson, A. R.; Smart, R. S. Resolving Surface Chemical States in XPS Analysis of First Row Transition Metals, Oxides and Hydroxides: Cr, Mn, Fe, Co and Ni. *Appl. Surf. Sci.* **2011**, *257*, 2717–2730. <https://doi.org/10.1016/j.apsusc.2010.10.051>.

(125) Gerber, S. J.; Erasmus, E. Electronic Effects of Metal Hexacyanoferrates: An XPS and FTIR Study. *Mater. Chem. Phys.* **2018**, *203*, 73–81. <https://doi.org/10.1016/j.matchemphys.2017.09.029>.

(126) Gupta, R. P.; Sen, S. K. Calculation of Multiplet Structure of Core *p*-Vacancy Levels. II. *Phys. Rev. B: Solid State* **1975**, *12*, 15–19. <https://doi.org/10.1103/PhysRevB.12.15>.

(127) Schönherr, M. I.; Scheurle, P. I.; Frey, L.; Martínez-Abadía, M.; Döblinger, M.; Mähringer, A.; Fehn, D.; Gerhards, L.; Santourin, I.; Schirmacher, A.; Quast, T.; Wittstock, G.; Bein, T.; Meyer, K.; Mateo-Alonso, A.; Medina, D. D. An Electrically Conducting 3D Coronene Based Metal-Organic Framework. *J. Mater. Chem.* **2024**, *12*, 10044. <https://doi.org/10.1039/d3ta07120k>.

(128) Cano, A.; Reguera, L.; Avila, M.; Velasco-Arias, D.; Reguera, E. Charge Redistribution Effects in Hexacyanometallates Evaluated from XPS Data. *Eur. J. Inorg. Chem.* **2020**, *2020*, 137–145. <https://doi.org/10.1002/ejic.201900907>.

(129) Cano, A.; Rodríguez-Hernández, J.; Reguera, L.; Rodríguez-Castellón, E.; Reguera, E. On the Scope of XPS as Sensor in Coordination Chemistry of Transition Metal Hexacyanometallates. *Eur. J. Inorg. Chem.* **2019**, *2019*, 1724–1732. <https://doi.org/10.1002/ejic.201801556>.

(130) Kiani, D. X-Ray Diffraction (XRD). In *Springer Handbook of Advances Catalyst Characterization*; Wachs, I. E., Banares, M. A., Eds.; Springer Cham, 2023; pp 519–539. https://doi.org/10.1007/978-3-031-07125-6_25.

(131) Artioli, G. X-Ray Diffraction (XRD). In *Encyclopedia of Geoarchaeology. Encyclopedia of Earth Science Series*; Gilbert, A. S., Ed.; Springer, Dordrecht, 2016.

(132) Sakata, O.; Nakamura, M. Grazing Incidence x-Ray Diffraction. In *Surface Science Techniques*, 1st ed.; Bracco, G., Holst, B., Eds.; Springer Berlin, Heidelberg, 2013; pp 165–190.

- (133) Jain, V.; Sahoo, R.; Jinschek, J. R.; Montazami, R.; Yochum, H. M.; Beyer, F. L.; Kumar, A.; Heflin, J. R. High Contrast Solid State Electrochromic Devices Based on Ruthenium Purple Nanocomposites Fabricated by Layer-by-Layer Assembly. *Chem. Commun.* **2008**, 3663–3665. <https://doi.org/10.1039/B803915A>.
- (134) Behera, J. N.; D'Alessandro, D. M.; Soheilnia, N.; Long, J. R. Synthesis and Characterization of Ruthenium and Iron–Ruthenium Prussian Blue Analogues. *Chem. Mater.* **2009**, *21*, 1922–1926. <https://doi.org/10.1021/cm900230p>.
- (135) Assumpcao Pereira-da-Silva, M. de; Ferri, F. A. Scanning Electron Microscopy. In *Nanocharacterization Techniques: A Volume in Micro and Nano Technologies*; Da Roz, A. L., Ferreira, M., Lima Leite, F. de, Oliveira, O. N., Eds.; William Andrew; Elsevier, 2017; pp 1–35.
- (136) Ul-Hamid, A. *A Beginners' Guide to Scanning Electron Microscopy*, 1st ed.; Springer Cham. <https://doi.org/10.1007/978-3-319-98482-7>.
- (137) Reimer, L. *Scanning Electron Microscopy: Physics of Image Formation and Microanalysis*, 2nd ed.; Springer Berlin, Heidelberg, 2013. <https://doi.org/10.1007/978-3-540-38967-5>.
- (138) Baggio, B. F.; Vicente, C.; Pelegrini, S.; Cid, C. C. P.; Brandt, I. S.; Tumelero, M. A.; Pasa, A. A. Morphology and Structure of Electrodeposited Prussian Blue and Prussian White Thin Films. *Materials* **2019**, *12*, 1103. <https://doi.org/10.3390/ma12071103>.
- (139) Qui, P.; Wang, L.; Mao, C. B. TEM Characterization of Biological and Inorganic Nanocomposites. In *Transmission Electron Microscopy Characterization of Nanomaterials*, 1st ed.; Kumar, C. S. S. R., Ed.; Springer Berlin, Heidelberg; pp 1–41. https://doi.org/10.1007/978-3-642-38934-4_1.
- (140) Nie, P.; Shen, L.; Luo, H.; Ding, B.; Xu, G.; Wang, J.; Zhang, X. Prussian Blue Analogues: A New Class of Anode Materials for Lithium Ion Batteries. *J. Mater. Chem. A* **2014**, *2*, 5852–5857. <https://doi.org/10.1039/C4TA00062E>.
- (141) Allara, D.; Stapleton, J. Methods of IR Spectroscopy for Surfaces and Thin Films. In *Surface Science Techniques*, 1st ed.; Bracco, G., Holst, B., Eds.; Springer Berlin, Heidelberg, 2013; pp 59–98.

- (142) Brand, I. *Application of Polarization Modulation Infrared Reflection Absorption Spectroscopy in Electrochemistry*; Monographs in Electrochemistry; Springer, Cham, 2020. <https://doi.org/10.1007/978-3-030-42164-9>.
- (143) Golden, W. G.; Dunn, D. S.; Overend, J. A Method for Measuring Infrared Reflection-Absorption Spectra of Molecules Adsorbed on Low-Area Surfaces at Monolayer and Submonolayer Concentrations. *J. Catal.* **1981**, *71*, 395–405. [https://doi.org/10.1016/0021-9517\(81\)90243-8](https://doi.org/10.1016/0021-9517(81)90243-8).
- (144) Greenler, R. G. Infrared Study of Adsorbed Molecules on Metal Surfaces by Reflection Techniques. *J. Chem. Phys.* **1966**, *44*, 310–315. <https://doi.org/10.1063/1.1726462>.
- (145) Scholz, F.; Lange, B. Abrasive Stripping Voltammetry - an Electrochemical Solid State Spectroscopy of Wide Applicability. *TrAC, Trends Anal. Chem.* **1992**, *11*, 359–367.
- (146) Harms, L.; Roth, N.; Wittstock, G. A New Programmable Dipping Robot. *Electrochem. Sci. Adv.* **2022**, *3*. e2100177. <https://doi.org/10.1002/elsa.202100177>.
- (147) *Polyethylene (PETG/PET) Labware | Thermo Fisher Scientific - DE*. <https://www.thermofisher.com/de/de/home/life-science/lab-plasticware-supplies/plastic-material-selection/polyethylene-pet-petg-labware.html> (accessed 2023-12-18).
- (148) Gupta, R. P.; Sen, S. K. Calculation of Multiplet Structure of Core *p*-Vacancy Levels. *Phys. Rev. B: Solid State* **1974**, *10*, 71–77. <https://doi.org/10.1103/PhysRevB.10.71>.
- (149) Schneider, C. A.; Rasband, W. S.; Eliceiri, K. W. NIH Image to ImageJ: 25 Years of Image Analysis. *Nat. Methods* **2012**, *9*, 671–675. <https://doi.org/10.1038/nmeth.2089>.
- (150) Rasband, W. S. *Image J*; U. S. National Institutes of Health, Bethesda, Maryland, USA, 1997. <https://imagej.nih.gov/ij/>.
- (151) Gerhards, L.; Wittstock, G. Unidirectional Current in Layered Metal Hexacyanometallate Thin Films: Implications for Alternative Wet-Processed Electronic Materials. *ACS Omega* **2023**, *8*, 44139–44147. <https://doi.org/10.1021/acsomega.3c06447>.
- (152) Karpova, E. V.; Karyakina, E. E.; Karyakin, A. A. Iron–nickel Hexacyanoferrate Bilayer as an Advanced Electrocatalyst for H₂O₂ Reduction. *RSC Adv.* **2016**, *6*, 103328–103331. <https://doi.org/10.1039/C6RA24128J>.

(153) Wessells, C. D.; Peddada, S. V.; Huggins, R. A.; Cui, Y. Nickel Hexacyanoferrate Nanoparticle Electrodes for Aqueous Sodium and Potassium Ion Batteries. *Nano Lett.* **2011**, *11*, 5421–5425. <https://doi.org/10.1021/nl203193q>.

(154) Benedetto, G. E. de; Guascito, M. R.; Ciriello, R.; Cataldi, T. R. I. Analysis by x-Ray Photoelectron Spectroscopy of Ruthenium Stabilised Polynuclear Hexacyanometallate Film Electrodes. *Anal. Chim. Acta* **2000**, *410*, 143–152. [https://doi.org/10.1016/S0003-2670\(00\)00724-8](https://doi.org/10.1016/S0003-2670(00)00724-8).

(155) Cataldi, T. R. I.; Salvi, A. M.; Centonze, D.; Sabbatini, L. Voltammetric and XPS Investigations of Polynuclear Ruthenium-Containing Cyanometallate Film Electrodes. *J. Electroanal. Chem.* **1996**, *406*, 91–99. [https://doi.org/10.1016/0022-0728\(95\)04426-4](https://doi.org/10.1016/0022-0728(95)04426-4).

(156) Cano, A.; Monroy, I.; Ávila, M.; Velasco-Asrias, D.; Rodríguez-Hernández, J.; Reguera, E. Relevant Electronic Interactions Related to the Coordination Chemistry of Tetracyanometallates. An XPS Study. *New J. Chem.* **2019**, *43*, 18384–18393. <https://doi.org/10.1039/C9NJ04173G>.

(157) Cataldi, T. R. I.; Benedetto, G. E. de; Bianchini, A. X-Ray Photoelectron Spectroscopic Investigation and Electrochemistry of Polynuclear Indium (III) Hexacyanoferrate Films. *J. Electroanal. Chem.* **1998**, *448*, 111–117. [https://doi.org/10.1016/S0022-0728\(98\)00030-8](https://doi.org/10.1016/S0022-0728(98)00030-8).

(158) Ahn, W.; Park, M. G.; Lee, D. U.; Seo, M. H.; Jiang, G.; Cano, Z. P.; Hassan, F. M.; Chen, Z. Hollow Multivoid Nanocuboids Derived from Ternary Ni–Co–Fe Prussian Blue Analog for Dual-Electrocatalysis of Oxygen and Hydrogen Evolution Reactions. *Adv. Funct. Mater.* **2018**, *28*, 1802129. <https://doi.org/10.1002/adfm.201802129>.

(159) Cano, A.; Lartundo-Rojas, L.; Shchukarev, A.; Reguera, E. Contribution to the Coordination Chemistry of Transition Metal Nitroprussides: A Cryo-XPS Study. *New J. Chem.* **2019**, *43*, 4835–4848. <https://doi.org/10.1039/C9NJ00141G>.

(160) Chen, W.; Tang, J.; Xia, X.-H. Composition and Shape Control in the Construction of Functional Nickel Hexacyanoferrate Nanointerfaces. *J. Phys. Chem. C* **2009**, *113*, 21577–21581. <https://doi.org/10.1021/jp908112u>.

(161) Hosseini, P.; Wittstock, G.; Brand, I. Infrared Spectroelectrochemical Analysis of Potential Dependent Changes in Cobalt Hexacyanoferrate and Copper Hexacyanoferrate

Films on Gold Electrodes. *J. Electroanal. Chem.* **2018**, *812*, 199–206. <https://doi.org/10.1016/j.jelechem.2017.12.029>.

(162) Pajerowski, D. M.; Gardner, J. E.; Talham, D. R.; Meisen, M. W. Tuning the Sign of Photoinduced Changes in Magnetization: Spin Transitions in the Ternary Metal Prussian Blue Analogue $\text{Na}_\alpha\text{Ni}_{1-x}\text{Co}_x[\text{Fe}(\text{CN})_6]_\beta \cdot n\text{H}_2\text{O}$. *J. Am. Chem. Soc.* **2009**, *131*, 12927–12936. <https://doi.org/10.1021/ja9012672>.

(163) Goberna-Ferrón, S.; Hernández, W. Y.; Rodríguez-García, B.; Galán-Mascarós, J. R. Light-Driven Water Oxidation with Metal Hexacyanometallate Heterogeneous Catalysts. *ACS Catal.* **2014**, *4*, 1637–1641. <https://doi.org/10.1021/cs500298e>.

(164) Banavath, R.; Abhinav, A.; Srivastava, R.; Bhargava, P. Highly Sensitive Ascorbic Acid Sensors from EDTA Chelation Derived Nickel Hexacyanoferrate/ Graphene Nanocomposites. *Electrochim. Acta* **2022**, *419*, 140335. <https://doi.org/10.1016/j.electacta.2022.140335>.

(165) Xidis, A.; Neff, V. D. On the Electronic Conduction in Dry Thin Films of Prussian Blue, Prussian Yellow, and Everitt's Salt. *J. Electrochem. Soc.* **1991**, *138*, 3637–3642. <https://doi.org/10.1149/1.2085472>.

(166) Sydam, R.; Deepa, M.; Shivaprasad, S. M.; Srivastava, A. K. A WO_3 -Poly(Butyl Viologen) Layer-by-Layer Film/ruthenium Purple Film Based Electrochromic Device Switching by 1 Volt Application. *Solar Energy Materials and Solar Cells* **2015**, *132*, 148–161. <https://doi.org/10.1016/j.solmat.2014.08.034>.

(167) Kulesza, P. J. Solid-State Electrochemistry of Iron Hexacyanoferrate (Prussian Blue Type) Powders: Evidence for Redox Transitions in Mixed-Valence Ionically Conducting Microstructures. *J. Electroanal. Chem. Interfacial Electrochem.* **1990**, *289*, 103–116. [https://doi.org/10.1016/0022-0728\(90\)87209-3](https://doi.org/10.1016/0022-0728(90)87209-3).

(168) Wöhler, F. Ueber die künstliche Bildung des Harnstoffs. *Ann. Phys. Chem.* **1828**, *12*, 253–256.

(169) Wiberg, K. B. The Deuterium Isotope Effect. *Chem. Rev.* **1955**, *55*, 713–743. <https://doi.org/10.1021/cr50004a004>.

(170) Katerinopoulou, K.; Kontogeorgos, A.; Salmas, C. E.; Patakas, A.; Ladavos, A. Geographical Origin Authentication of Agri-Food Products: A Review. *Foods* **2020**, *9*, 498. <https://doi.org/10.3390/foods9040489>.

(171) Daniele, G.; Wytrychowski, M.; Batteau, M.; Guibert, S.; Casabianca, H. Stable Isotope Ratio Measurements of Royal Jelly Samples for Controlling Production Procedures: Impact of Sugar Feeding. *Rapid Commun. Mass Spectrom.* **2011**, *25*, 1929–1932. <https://doi.org/10.1002/rcm.5070>.

(172) Rae, H. K. Selecting Heavy Water Processes. In *Separation of Hydrogen Isotopes*; Rae, H. K., Ed.; ACS Symposium Series, Vol. 68; American Chemical Society, 1978; pp 1–26. <https://doi.org/10.1021/bk-1978-0068.ch001>.

(173) Cai, S.; Bai, T.; Chen, H.; Fang, W.; Xu, Z.; Lai, H.; Huang, T.; Xu, H.; Chu, X.; Ling, J.; Gao, C. Heavy Water Enables High-Voltage Aqueous Electrochemistry via the Deuterium Isotope Effect. *J. Phys. Chem. Lett.* **2020**, *11*, 303–310. <https://doi.org/10.1021/acs.jpcclett.9b03267>.

(174) Swain, C. G.; Evans, D. F. Conductance of Ions in Light and Heavy Water at 25°. *J. Am. Chem. Soc.* **1966**, *88*, 383–390. <https://doi.org/10.1021/ja00955a001>.

(175) Cho, C. H.; Urquidi, J.; Singh, S.; Robinson, G. W. Thermal Offset Viscosities of Liquid H₂O, D₂O, and T₂O. *J. Phys. Chem. B* **1999**, *103*, 1991–1994. <https://doi.org/10.1021/jp9842953>.

(176) DeCoursey; T. E.; Cherny, V. V. Deuterium Isotope Effects on Permeation and Gating of Proton Channels in Rat Alveolar Epithelium. *J. Gen. Physiol.* **1997**, *109*, 415–434. <https://doi.org/10.1085/jgp.109.4.415>.

(177) Dongmo, S.; Wittstock, G.; Christoffers, J.; Brand, I. In Situ Determination of Potential-Driven Structural Changes in a Redox-Active Plumbagin Polymer Film on a Glassy Carbon Electrode Using pm IRRAS Under Electrochemical Control. *Electrochim. Acta* **2017**, *255*, 298–308. <https://doi.org/10.1016/j.electacta.2017.09.152>.

(178) Lide, D. R., Ed. *CRC Handbook of Chemistry and Physics*, 85th ed.; CRC Press, Boca Raton, FL, 2005.

(179) Galagedera, S. K. K.; Flechsig, G.-U. Voltammetric H/D Isotope Effects on Redox-Active Small Molecules Conjugated with DNA Self-Assembled Monolayers. *ChemElectroChem* **2019**, *6*, 4781–4788. <https://doi.org/10.1002/celec.201901151>.

- (180) Neff, V. D. Some Performance Characteristics of a Prussian Blue Battery. *J. Electrochem. Soc.* **1985**, *132*, 1382–1384. <https://doi.org/10.1149/1.2114121>.
- (181) Wessells, C. D.; Huggins, R. A.; Cui, Y. Copper Hexacyanoferrate Battery Electrodes with Long Cycle Life and High Power. *Nat. Commun.* **2011**, *2*, 550. <https://doi.org/10.1038/ncomms1563>.
- (182) Paulitsch, B.; Yun, J.; Bandarenka, A. S. Electrodeposited $\text{Na}_2\text{VO}_x\text{Fe}(\text{CN})_6$ Films as a Cathode Material for Aqueous Na-Ion Batteries. *ACS Appl. Mater. Interfaces* **2017**, *9*, 8107–8112. <https://doi.org/10.1021/acsami.6b15666>.
- (183) Wang, B.; Han, Y.; Wang, X.; Bahlawane, N.; Pan, H.; Yan, M.; Jiang, Y. Prussian Blue Analogs for Rechargeable Batteries. *iScience* **2018**, *3*, 110–133. <https://doi.org/10.1016/j.isci.2018.04.008>.
- (184) Nigrović, V. Enhancement of the Excretion of Radiocaesium in Rats by Ferric Cyanoferrate (II). *Int. J. Radiat. Biol. Relat. Stud. Phys., Chem. Med.* **1963**, *7*, 307–309. <https://doi.org/10.1080/09553006314551221>.
- (185) Parajuli, D.; Kitajima, A.; Takahashi, A.; Tanaka, H.; Ogawa, H.; Hakuta, Y.; Yoshino, K.; Funahashi, T.; Yamaguchi, M.; Osada, M.; Kawamoto, T. Application of Prussian Blue Nanoparticles for the Radioactive Cs Decontamination in Fukushima Region. *J. Environ. Radioact.* **2016**, *151*, 233–237. <https://doi.org/10.1016/j.jenvrad.2015.10.014>.
- (186) Narayanan, S. S.; Scholz, F. A Comparative Study of the Electrocatalytic Activities of Some Metal Hexacyanoferrates for the Oxidation of Hydrazine. *Electroanalysis* **1999**, *11*, 465–469. [https://doi.org/10.1002/\(SICI\)1521-4109\(199906\)11:7<465:AID-ELAN465>3.0.CO;2-%23](https://doi.org/10.1002/(SICI)1521-4109(199906)11:7<465:AID-ELAN465>3.0.CO;2-%23).
- (187) DeLongchamp, D. M.; Hammond, P. T. High-Contrast Electrochromism and Controllable Dissolution of Assembled Prussian Blue/Polymer Nanocomposites. *Adv. Funct. Mater.* **2004**, *14*, 224–232. <https://doi.org/10.1002/adfm.200304507>.
- (188) Paoletta, A.; Faure, C.; Timoshevskii, V.; Marras, S.; Bertoni, G.; Guerfi, A.; Vijn, A.; Armand, M.; Zaghib, K. A Review on Hexacyanoferrate-Based Materials for Energy Storage and Smart Windows: Challenges and Perspectives. *J. Mater. Chem. A* **2017**, *5*, 18919–18932. <https://doi.org/10.1039/c7ta05121b>.

- (189) Lasky, S. J.; Buttry, D. A. Mass Measurements Using Isotopically Labeled Solvents Reveal the Extent of Solvent Transport During Redox in Thin Films on Electrodes. *J. Am. Chem. Soc.* **1988**, *110*, 6258–6260. <https://doi.org/10.1021/ja00226a058>.
- (190) Abe, T.; Nagasaka, T.; Taijri, A. Electrocatalysis Characteristics of a Polynuclear Cyanide Complex, Ruthenium Purple, for Dihydrogen Oxidation. *J. Inorg. Organomet. Polym. Mater.* **2004**, *14*. <https://doi.org/10.1023/B:JOIP.0000039365.88800.1b>.
- (191) Zeng, B.; Zhao, F.; Ding, X. Electrochemical Characteristics of Thin Nickel Hexacyanoferrate Films Formed on Gold and Thiol Self-Assembled Monolayers Modified Gold Electrodes. *Anal. Sci.* **2001**, *17*, 259–264. <https://doi.org/10.2116/analsci.17.259>.
- (192) Huang, L.; Ge, X.; Dong, S. A Facile Conversion of a Ni/Fe Coordination Polymer to a Robust Electrocatalyst for the Oxygen Evolution Reaction. *RSC Adv.* **2017**, *7*, 32819–32825. <https://doi.org/10.1039/C7RA04280A>.
- (193) Bianchi, C. L.; Ragaini, V.; Cattania, M. G. An XPS Study on Ruthenium Compounds and Catalysts. *Mater. Chem. Phys.* **1991**, *29*, 297–306. [https://doi.org/10.1016/0254-0584\(91\)90025-P](https://doi.org/10.1016/0254-0584(91)90025-P).
- (194) Emrich, R. J.; Traynor, L.; Gambogi, W.; Buhks, E. Surface Analysis of Electrochromic Displays of Iron Hexacyanoferrate Films by x-Ray Photoelectron Spectroscopy. *J. Vac. Sci. Technol., A* **1987**, *5*, 1307–1310. <https://doi.org/10.1116/1.574797>.
- (195) Grandjean, F.; Samain, L.; Long, G. J. Characterization and Utilization of Prussian Blue and Its Pigments. *Dalton Trans.* **2016**, *45*, 18018–18044. <https://doi.org/10.1039/C6DT03351B>.
- (196) Shen, L.; Wang, Z.; Chen, L. Prussian Blue as a Cathode Material for Lithium Ion Batteries. *Chem. Eur. J.* **2014**, *20*, 12559–12562. <https://doi.org/10.1002/chem.201403061>.
- (197) Hall, D. S.; Lockwood, D. J.; Poirier, S.; Bock, C.; MacDougall, B. R. Raman and Infrared Spectroscopy of A and B Phases of Thin Nickel Hydroxide Films Electrochemically Formed on Nickel. *J. Phys. Chem. A* **2012**, *116*, 6771–6784.
- (198) Harms, L.; Brand, I. Application of PMIRRAS to Study Structural Changes of the Magnesium Surface in Corrosive Environments. *Vib. Spectrosc.* **2018**, *97*, 106–113. <https://doi.org/10.1016/j.vibspec.2018.06.006>.

- (199) Wittmar, J.; Meyer, S.; Sieling, T.; Kunte, J.; Smiatek, J.; Brand, I. What Does Ectoine Do to DNA? A Molecular-Scale Picture of Compatible Solute–Biopolymer Interactions. *J. Phys. Chem. B* **2020**, *124*, 7999–8011. <https://doi.org/10.1021/acs.jpccb.0c05273>.
- (200) Andonova, S.; Akbari, S. S.; Karadas, F.; Spassova, I.; Paneva, D.; Hadjiivanov, K. Structure and Properties of KNi–hexacyanoferrate Prussian Blue Analogues for Efficient CO₂ Capture: Host–Guest Interaction Chemistry and Dynamics of CO₂ Adsorption. *J. CO₂ Util.* **2021**, *50*, 101593. <https://doi.org/10.1016/j.jcou.2021.101593>.
- (201) Mähringer, A.; Döblinger, M.; Hennemann, M.; Gruber, C.; Fehn, D.; Scheurle, P. I.; Hosseini, P.; Santourian, I.; Schirmacher, A.; Rotter, J. M.; Wittstock, G.; Meyer, K.; Clark, T.; Bein, T.; Medina, D. D. An Electrically Conducting Three-Dimensional Iron-Catecholate Porous Framework. *Angew. Chem. Int. Ed.* **2021**, *60*, 18065–18072. <https://doi.org/10.1002/anie.202102670>.
- (202) Xie, L. S.; Skorupskii, G.; Dincă, M. Electrically Conductive Metal–Organic Frameworks. *Chem. Rev.* **2020**, *120*, 8536–8580. <https://doi.org/10.1021/acs.chemrev.9b00766>.
- (203) Zadig - USB Driver Installation Made Easy. <https://zadig.akeo.ie/> (accessed 2023-12-22).

11 Own Publications and Conference Contributions

11.1 Own Publications

(1) **Gerhards, L.**; Brand, I.; Wittstock, G. H/D Isotope Effects in the Electrochemistry of Electrochromic Iron Hexacyanoruthenate. *Submitted*.

(2) Schönherr, M. I.; Scheurle, P. I.; Frey, L.; Martínez-Abadía, M.; Döblinger, M.; Mähringer, A.; Fehn, D.; **Gerhards, L.**; Santourin, I.; Schirmacher, A.; Quast, T.; Wittstock, G.; Bein, T.; Meyer, K.; Mateo-Alonso, A.; Medina, D. D. An Electrically Conducting 3D Coronene based Metal-Organic Framework. *J. Mater. Chem.* **2024**, *12*, 10044. DOI: 10.1039/d3ta07120k.

(3) **Gerhards, L.**; Wittstock, G. Unidirectional Current in Layered Metal Hexacyanometallate Thin Films: Implications for Alternative Wet-processed Electronic Materials. *ACS Omega* **2023**, *8* (46), 44139–44147. DOI: 10.1021/acsomega.3c06447.

(4) Scheurle, P. I.; Mähringer, A.; Haug, T.; Biewald, A.; Axthammer, D.; Hartschuh, A.; **Harms, L.**; Wittstock, G.; Medina, D. D.; Bein, T. Helical Anthracene–Ethyne-Based MOF-74 Analogue. *Cryst. Growth Des.* **2022**, *22* (5), 2849–2853. DOI: 10.1021/acs.cgd.1c01145.

(5) **Harms, L.**; Roth, N.; Wittstock, G. A new programmable dipping robot. *Electrochem. Sci. Adv.* **2023**, *3* (2), e2100177. DOI: 10.1002/elsa.202100177.

(6) Baues, S.; Vocke, H.; **Harms, L.**; Rücker, K. K.; Wark, M.; Wittstock, G. Combinatorial Screening of Cu-W Oxide-Based Photoanodes for Photoelectrochemical Water Splitting. *ACS Appl. Mater. Interfaces* **2022**, *14* (5), 6590–6603. DOI: 10.1021/acsami.1c20837.

11.2 Oral Presentations in National and International Conferences

Harms, L., Wittstock, G., Analysis of Multi-layer Thin Films of Metal Hexacyanometallates, 8th Regional Symposium of Electrochemistry for South-East Europe, 11.-15.07.2022, Graz, Austria.

Harms, L., Wittstock G. Multi-layer Thin Film Architectures of Metal Hexacyanometallates, 72nd Annual Meeting of the International Society of Electrochemistry, 29.08.-03.09.2021, Hybrid: Online Meeting, Jeju Island, Republic Korea (South Korea).

Harms, L., Wittstock, G. Multi-layer Thin Films of Metal Hexacyanometallates, Coordination Networks: Building Blocks for Functional Systems (COORNETs), WebCon 2021, 19.-20.01.2021, Online Meeting.

11.3 Posters in National and International Conferences

Gerhards, L.; Wittstock, G., Isotope Effect in the Voltammetry of Iron Hexacyanometallates, 74th Annual Meeting of the International Society of Electrochemistry, 03.-08.09.2023, Lyon, France.

Harms, L.; Wittstock, G. Analysis of Multi-layer Thin Film Structures of Metal Hexacyanometallates, 8th International Conference on Metal-Organic Frameworks and Open Framework Compounds, 04.-07.09.2022, Dresden, Germany.

Harms, L.; Wittstock, G., Analysis of Layered Metal Hexacyanometallates, 73rd Annual Meeting of the International Society of Electrochemistry, 12.-16.09.2022, Online Meeting.

Harms, L.; Wittstock, G. Metal Hexacyanometallate Multilayer Thin Film Architectures, Summer School 2021, Conductive Metal-Organic Frameworks – From Synthesis To Functions, 06.-08.09.2021, Online Meeting.

12 Erklärung

Hiermit erkläre ich, Lena Gerhards (geb. Harms), geboren am 24.07.1995 in Delmenhorst, dass ich die vorliegende Dissertation selbstständig verfasst und die hierfür benutzten Hilfsmittel vollständig angegeben habe. In Teilen wurde die vorliegende Arbeit bereits veröffentlicht. Diese Teile betreffen die im Kapitel 11.1 „Own Publications“ aufgelisteten Veröffentlichungen 2-6. Die im Kapitel 11.1 aufgeführten Publikation 1 ist zum Peer-Reviewing-Prozess bei einer Fachzeitschrift eingereicht. Ich erkläre außerdem, dass die Dissertation weder in ihrer Gesamtheit noch in Teilen einer anderen Hochschule zur Begutachtung in einem Promotionsverfahren vorliegt oder vorgelegen hat. Die Leitlinien guter wissenschaftlicher Arbeit der Carl von Ossietzky Universität Oldenburg wurden befolgt und im Zusammenhang mit dem Promotionsvorhaben sind keine kommerziellen Vermittlungs- oder Beratungsdienste (Promotionsberatung) in Anspruch genommen worden.

Oldenburg, den 06.05.2024

Lena Gerhards